

AD \_\_\_\_\_

Award Number: W81XWH-05-1-0291

TITLE: A Partnership Training Program in Breast Cancer Research Using Molecular Imaging Techniques

PRINCIPAL INVESTIGATOR: Paul C. Wang, Ph.D.

CONTRACTING ORGANIZATION: Howard University  
Washington, DC 20059

REPORT DATE: July 2008

TYPE OF REPORT: Annual

PREPARED FOR: U.S. Army Medical Research and Materiel Command  
Fort Detrick, Maryland 21702-5012

DISTRIBUTION STATEMENT: Approved for Public Release;  
Distribution Unlimited

The views, opinions and/or findings contained in this report are those of the author(s) and should not be construed as an official Department of the Army position, policy or decision unless so designated by other documentation.

REPORT DOCUMENTATION PAGE				Form Approved OMB No. 0704-0188	
Public reporting burden for this collection of information is estimated to average 1 hour per response, including the time for reviewing instructions, searching existing data sources, gathering and maintaining the data needed, and completing and reviewing this collection of information. Send comments regarding this burden estimate or any other aspect of this collection of information, including suggestions for reducing this burden to Department of Defense, Washington Headquarters Services, Directorate for Information Operations and Reports (0704-0188), 1215 Jefferson Davis Highway, Suite 1204, Arlington, VA 22202-4302. Respondents should be aware that notwithstanding any other provision of law, no person shall be subject to any penalty for failing to comply with a collection of information if it does not display a currently valid OMB control number. <b>PLEASE DO NOT RETURN YOUR FORM TO THE ABOVE ADDRESS.</b>					
1. REPORT DATE 01-07-2008		2. REPORT TYPE Annual		3. DATES COVERED 1 Jul 2007 – 30 Jun 2008	
4. TITLE AND SUBTITLE  A Partnership Training Program in Breast Cancer Research Using Molecular Imaging Techniques				5a. CONTRACT NUMBER	
				5b. GRANT NUMBER W81XWH-05-1-0291	
				5c. PROGRAM ELEMENT NUMBER	
6. AUTHOR(S)  Paul C. Wang, Ph.D.  Email: pwang@howard.edu				5d. PROJECT NUMBER	
				5e. TASK NUMBER	
				5f. WORK UNIT NUMBER	
7. PERFORMING ORGANIZATION NAME(S) AND ADDRESS(ES)  Howard University Washington, DC 20059				8. PERFORMING ORGANIZATION REPORT NUMBER	
9. SPONSORING / MONITORING AGENCY NAME(S) AND ADDRESS(ES) U.S. Army Medical Research and Materiel Command Fort Detrick, Maryland 21702-5012				10. SPONSOR/MONITOR'S ACRONYM(S)	
				11. SPONSOR/MONITOR'S REPORT NUMBER(S)	
12. DISTRIBUTION / AVAILABILITY STATEMENT Approved for Public Release; Distribution Unlimited					
13. SUPPLEMENTARY NOTES					
14. ABSTRACT In the third year, Howard faculty from Departments of Biology, Radiology, and Radiation Oncology at Howard University were further trained in molecular imaging through seminars and workshops, and by conducting two research projects with the faculty at the Johns Hopkins University. We have established three breast cancer tumor models, and further optimized the imaging probes for MRI and fluorescent optical imaging of breast cancers. We have determined how the interactions between MCF-7 cells and macrophages are affected by tamoxifen and aspirin. We have also identified the phenotypic changes that may render TAMs selectively vulnerable to pharmacological agents. In this report period, we have published 11 papers and given 24 presentations. Based on the data we obtained, we have submitted 5 new grant proposals to NIH and DoD. The Molecular Imaging Lab continuously serves as a synergic center on campus to promote molecular imaging research. Six new research collaborations were established with the faculty members at Howard, as well as with the scientists from other institutes.					
15. SUBJECT TERMS training, molecular imaging, breast cancer, optical imaging, magnetic resonance imaging					
16. SECURITY CLASSIFICATION OF:			17. LIMITATION OF ABSTRACT  UU	18. NUMBER OF PAGES  113	19a. NAME OF RESPONSIBLE PERSON USAMRMC
a. REPORT U	b. ABSTRACT U	c. THIS PAGE U			19b. TELEPHONE NUMBER (include area code)

## Table of Contents

<b>Introduction.....</b>	<b>4</b>
<b>Body.....</b>	<b>5</b>
<b>Key Research Accomplishments.....</b>	<b>11</b>
<b>Reportable Outcomes.....</b>	<b>12</b>
<b>Conclusions.....</b>	<b>15</b>
<b>References.....</b>	<b>16</b>
<b>Appendices.....</b>	<b>17</b>

## **A Partnership Training Program In Breast Cancer Research Using Molecular Imaging Techniques**

### **I. INTRODUCTION**

Advances in molecular and cell biology techniques in recent years have had a marked effect on our understanding of the cellular and molecular mechanisms of cancers, including breast cancer. Significant strides have also been made in the development of a noninvasive, high-resolution, in vivo imaging technology such as positron emission tomography (PET), magnetic resonance imaging (MRI), and optical imaging techniques for better imaging of tumors. In vivo molecular imaging, which utilizes these two fronts, opens up an extraordinary opportunity for studying diseases noninvasively, and in many cases, quantitatively at the molecular level (1-4). Molecular imaging is a growing research discipline aimed at developing and testing novel tools, reagents, and methods to image specific molecular pathways in vivo, particularly those that are key targets in disease processes.

The current assessment of breast cancer depends on anatomic and physiological changes of the disease. These changes are a late manifestation of the molecular changes that truly underlie the disease. If imaging of these early molecular changes is possible, it will directly affect patient care by allowing much earlier detection of the disease. Potentially, clinicians may be able to image molecular changes that currently are defined as “predisease states”. This will allow intervention at a time when the outcome will be most likely affected. In addition, by directly imaging the underlying alterations of disease, the effects of therapy may be monitored shortly after therapy has been initiated in contrast to the many months often required(5).

In this proposed training program, a partnership between Howard University (HU) and the In Vivo Cellular Molecular Imaging Center (ICMIC) at Johns Hopkins University (JHU) will be established to pursue the molecular imaging research of breast cancer. At Howard University, this partnership will involve a multidisciplinary consortium of five departments. The program is composed of two components: a research component and a broad training component. Howard University faculty will obtain training through conducting collaborative research and by participating in a broad based training program. Experts from Johns Hopkins will participate in training by offering laboratory internships, mentoring research efforts, and conducting seminars and workshops. Through this program, a core facility will also be established to support sustainable long-term molecular imaging research at Howard University.

Our goal for this program is to provide faculty trainees at Howard University with basic and updated molecular imaging techniques that they can employ while conducting breast cancer research. The program objectives are:

1. Train new researchers in the breast cancer imaging using molecular imaging techniques.
2. Offer molecular imaging and breast cancer-related lectures, seminars, workshops, and laboratory internships.
3. Conduct two proposed research projects:
  - a. Magnetic resonance (MR) image enhancement by tumor cell targeted immunoliposome complex delivered contrast agent.
  - b. Imaging the effects of macrophage function on tumor progression.
4. Establish a molecular imaging core to support long-term sustainable research.
5. Research concept development and submit grants in breast cancer imaging.

## II. BODY

This training program consists of two components: a research component and a broad based training component. The research component includes research in molecular imaging of breast cancer and the establishment of a molecular imaging core facility at Howard University.

### II.1 Research Projects

#### *Project 1: MR Image Enhancement by Tumor Cell Targeted Immunoliposome Complex Delivered Contrast Agent*

Contrast-enhanced MRI is one of the best noninvasive methodologies available today in clinical medicine for assessing anatomy and function of tissues (6). High spatial resolution and high soft tissue contrast are desirable features of noninvasive MRI. However, due to intrinsically low sensitivity, a large amount of CA has to be used due to the non-specific uptake by tumors *in vivo*. In recent years, targeted CA delivery systems have been developing based on the concept that molecular imaging can increase the signal to noise ratio by detecting the difference in 'molecular properties' between cancer and normal tissues (7-9). This should, in theory, allow for detection of smaller tumors. As one strategy, monoclonal antibodies or antibody fragments have been coupled with CA directly or linked with CA through liposome (Lip) carriers. High concentrations of antibody-mediated CA such as Gd provides high T1 positive contrast *in vivo*, but insufficient direct linkage of Gd with antibodies or the large molecular size of antibody-Lip-Gd particles may limit its use for imaging cell-surface receptors in solid tumors because of inefficient extravasation and very slow diffusion in the interstitial compartment (10,11). Furthermore, antibody immunogenicity, poor stability of the conjugates and a potential change of the antibody binding ability due to changes in surface antigens are still problematic for *in vivo* applications. A ligand with less toxic, high binding specificity for tumors, relative small size and without immunogenicity is required to target the CA to tumors.

Optical imaging offers several advantages over other imaging techniques. Among these are simplicity of technique, high sensitivity and absence of ionizing radiation. There is a general increase in the development of techniques for *in vivo* evaluation of gene expression, monitoring of gene delivery and real-time intraoperative visualization of tumor margins and metastatic lesions to improve surgical outcomes (12-14). Limited depth of light penetration and lack of tomographic information prevent *in vivo* efficiency of optical imaging. In order to overcome the limitations of various imaging modalities, multimodal probes have been developed for detection using multiple imaging devices (15-17).

Transferrin receptor (TfR) is a cell-surface internalizing receptor responsible for almost all iron sequestration in mammalian cells. Overexpression of TfR is reported on human cancers from various tissues including breast and is of great value in grading tumors and determining prognosis (18). TfR has been successfully applied as a molecular target to direct therapeutic agents to tumor cells (19). Transferrin (Tf), the TfR ligand, is a monomeric glycoprotein that binds  $\text{Fe}^{3+}$  atoms for delivery to vertebrate cells through receptor-mediated endocytosis. Fluorescently labeled Tf has greatly aided the investigation of endocytosis *in vitro*. *In vivo* use of the physiological serum protein Tf is less likely to cause adverse reactions. Indeed, Tf has been successfully used in targeted gene therapy (20,21). We hypothesized that near-infrared dye (NIR) labeled Tf ( $\text{Tf}^{\text{NIR}}$ ) would be an ideal ligand and would selectively increase the cellular uptake of MRI and optical reporters *in vivo*, resulting in contrast-enhanced MRI and NIR-based optical detection.

We have first developed a Tf- and Lip-mediated dual molecular probe with both fluorescent and magnetic reporter groups ( $\text{Tf}^{\text{NIR}}\text{-Lip}^{\text{NBD}}\text{-CA}$ ). The nanoparticles were constructed with Tf on the surface of Lip as a ligand for specific targeting and CA (Magnevist) inside as the payload. These components together formed a liposomal nanocomplex,  $\text{Tf}^{\text{NIR}}\text{-Lip}^{\text{NBD}}\text{-CA}$ , with a diameter less than 100 nm. The feasibility of the nanoparticles was tested both *in vitro* and in animal models. *In vitro* analysis demonstrated that the  $\text{Tf}^{\text{NIR}}\text{-Lip}^{\text{NBD}}\text{-CA}$  nanocomplex dramatically improved the uptake of CA in monolayer cultures of MDA-MB-231-luc human breast cancer cells through both receptor- and Lip-mediated endocytosis. *In vivo*, the probe significantly enhanced the MRI signals, and was superior to the use of clinical MRI CA alone. The DCE-MRI exhibited heterogeneous signal enhancement by the liposomal nanocomplex probe and was correlated well with the pathology of the tumors.

To visualize tumors using the optical imaging technique, the Tf was labeled with NIR fluorescent dye ( $\text{Tf}^{\text{NIR}}$ ). NIR dyes were encapsulated in the Lip, instead of MRI CA, to yield targeted fluorescent liposome nanoparticles ( $\text{Tf}^{\text{NIR}}\text{-Lip}^{\text{NBD}}\text{-dye}$ ) in some experiments. Confocal microscopy showed endocytosis of the fluorescent reporters from Tf, liposome particles and encapsulated dyes, separately, following incubation of the MDA-MB-231-luc cells with the nanoparticles. Pretreatment with Tf blocked the cellular uptake of the reporters indicating the importance and specificity of the Tf moiety for targeting. Quantification using flow cytometry revealed a 1.8, 7.0 and 16 fold higher fluorescence intensity in cells incubated for 1 hour with  $\text{Tf}^{\text{NIR}}$ ,  $\text{Lip}^{\text{NBD}}\text{-dye}$ , and  $\text{Tf}^{\text{NIR}}\text{-Lip}^{\text{NBD}}\text{-dye}$ , separately, than in control cells without probes (all  $p < 0.05$ ). Systemic administration of  $\text{Tf}^{\text{NIR}}$  alone showed a preferential accumulation of the fluorescent signal in tumor xenografts in nude mice. The fluorescent signal was clearly detectable at 10 min in tumors and reached the maximum intensity at 90-120 min after injection. The ratio of the signal from tumor to background from muscle ranged from 1.64 to 3.14, depending on the tumor sizes. Application of the  $\text{Tf}^{\text{NIR}}\text{-Lip}^{\text{NBD}}\text{-dye}$  nanoparticles further increased the signal from tumor to background ratio by up to 30 % compared to  $\text{Tf}^{\text{NIR}}$  alone. Importantly,  $\text{Tf}^{\text{NIR}}\text{-Lip}^{\text{NBD}}\text{-dye}$  system is superior to  $\text{Tf}^{\text{NIR}}$  alone for imaging small tumors (<3 mm in diameter).

To increase the sensitivity of optical imaging in early diagnosis of cancers, we have further designed QDs conjugated with Tf as an optical imaging agent. QD is chosen to improve detection sensitivity due to its great extinction coefficient and emission of bright light in comparison to the organic fluorescent dyes. Two step carbodiimide chemistry process was used to obtain the QDs-transferrin conjugation. First, Carboxylated QDs were activated by excess EDC and sulfo-NHS at pH 6.5. Then the excess EDC and sulfo-NHS was removed by Sephadex<sup>TM</sup>. Later, the activated QDs were conjugated with transferrin at pH 8.3, and further purified by gel filtration. A controlled experiment from Tf-Alexa Fluor conjugate was used to confirm the conjugation. The successful linkage of transferrin to QDs was demonstrated by SDS-PAGE gel electrophoresis. *In vitro* uptake of QDs-Tf by MDA-MB-231 cells was confirmed by cellular labeling combined with flow cytometry. In addition, to further stabilize quantum dots, a novel kind of tri-block copolymer as a multi-dentate ligand has been successfully synthesized. The block copolymer has a polycarboxylic acid and polythiol block at both ends and a intermediate poly(styrene/divinyl benzene) block. The multiple mercapto groups of polythiol block will act as multi-dentate ligands to stabilize quantum dots nanoparticles, while the polycarboxylic acid block offers reaction sites to modify or conjugate quantum dots with biomolecules. The densely compacted hydrophobic intermediate shell formed from cross-linked poly(styrene/divinyl benzene) block will efficiently prohibit the diffusion of other molecules through the macromolecular shell, resulting in decomposition of quantum dots. The QDs can be coated and stabilized with this multi-dentate

block copolymer in water. It is expected that the novel multi-dentate ligand can improve the stability and biocompatibility of QDs under harsh in vivo conditions.

In addition, we have also developed a bioluminescence assay system for rapid measurement of tumor cell death using Xenogen IVIS digital camera system and luciferase-transfected MDA-MB-231-luc cells. The system was tested when cells were subjected to 43°C hyperthermia and compared with traditional methods including MTT and colony formation assays. The luminescence using the bioluminescence assay system was related to the number of viable cells over a wide range ( $10^2$  to  $10^5$  cells per well). The decrease in luminescence was detectable immediately after heat treatment. This decrease was related to the duration of heating at 43°C. Relative to the gold standard of clonogenic assay, MTT assay overestimated viability, while bioluminescence underestimated viability of cells subjected to hyperthermia. Bioluminescence assay of response to hyperthermia is rapid in bioluminescent cells, but is not closely related to the clonogenic potential. This suggests that other ATP based assays of cell viability will also overestimate cytotoxicity when compared to clonogenicity assays. Nonetheless bioluminescence estimate of ATP in cells can be used for rapid screening of cytotoxic regimens.

## *Project 2: Imaging the Effects of Macrophage Function on Tumor Promotion*

Accumulating evidence implicates tumor-associated macrophages (TAMs) in tumor progression. Recent reports indicate that key modifier genes of tumor progression are expressed in TAMs. Macrophage ablation has been proposed as a therapeutic strategy; however, context-specific targeting of TAMs would be preferable. We used a pathway-focused gene array, RT-PCR, and Western blot analyses of inflammation- and angiogenesis-related gene expression in co-cultured MCF-7 cells and macrophages, to determine how interactions between the two cell types are affected by tamoxifen and aspirin. We also sought to identify phenotypic changes that may render TAMs selectively vulnerable to pharmacological agents.

THP-1 (human monocytic leukemia), MCF-10A (nontumorigenic mammary epithelial), MCF-7 (mammary adenocarcinoma) and MDA-MB-231 (mammary adenocarcinoma) were used in this study. THP-1 monocytes were differentiated to macrophages with PMA (100 nM) for 3 d; differentiated macrophages were activated with LPS (20 ng/ml) for 5 h. THP-1 were cultured in RPMI medium 1640 supplemented with 7.5% FBS, 100 U/ml penicillin, 100 µg/ml streptomycin, and 50 µM 2-mercaptoethanol. Breast cell lines were propagated in MEM supplemented with 8% FBS and antibiotics.  $1 \times 10^6$  THP-1 cells/well were seeded in the inserts (3-µm pore size) of 6-well Transwell™ chambers, and differentiated 1 d later with PMA, and then activated with LPS.  $2.5 \times 10^5$  MCF-7 cells/ml were seeded in a 2-ml volume in lower wells (separately) 2 d after THP-1 cells were seeded. The medium of both cell types was changed and inserts (activated macrophages) were placed in the lower wells. Chambers were incubated for 3 d. Tamoxifen, aspirin, and rhMIF were used at final concentrations of 10 µM (24 h), 1 mM (24 h), and 10 ng/ml (6 h), respectively. The results showed that all cells expressed MIF RNA. In co-culture, *MIF* expression was upregulated in MCF-7, but downregulated in macrophages. MCF-7-induced reduction of MIF expression in TAMs may be associated with partial M2 polarization; therefore, co-culture produced macrophage phenotypes that were intermediate between M1 and M2. Reduction of MIF expression may also produce context-specific vulnerability of macrophages to therapeutic agents. Aspirin induced *IL-10* expression in both macrophages and MCF-7 grown separately. MCF-7 cells did not express *IL-10* when grown separately or in co-culture. However, aspirin induced *IL-10* expression in MCF-7 and in tamoxifen-pretreated MCF-7. Moreover, aspirin-pretreated

macrophages potently induced *IL-10* expression in MCF-7 cells and pretreatment of MCF-7 with tamoxifen did not prevent this induction. Two molecular variants of MIF were identified: a larger, macrophage-type and a smaller, MCF-7-type; both variants were present in co-cultured MCF-7 cells. Co-culture of MCF-7 with LPS-activated THP-1 macrophages induced a change in MCF-7 morphology reminiscent of an epithelial-to-mesenchymal transition.

## **II.2 Broad Based Training Components**

The Molecular Imaging Lab has regular group meetings, journal club, and seminars. The faculty trainees have also attended special workshops on molecular imaging and imaging instrumentation. The PI and the partnership leader at JHU have been coordinating the training efforts through meetings and emails.

### ***II.2.a. Seminars and workshops at Howard University:***

1. Quantum Dots Bioconjugates as Imaging Agents.  
Tongxin Wang, PhD. Molecular Imaging Laboratory  
HUH Cancer Center, September 21, 2007
2. Potential of QDs Targeted Delivery by QD-streptavidin-biotin-Tf Complexes.  
Alexandru Korotcov, Ph.D. Molecular Imaging Laboratory  
HUH Cancer Center, Nov. 13, 2007
3. Optical Imaging System Training: Acquisition and Analysis in Living Image 3.0. 3D Reconstructions (DLIT).  
Dustin H. Whittemore, Advanced Imaging Training Manager, Caliper Life Sciences, Inc.,  
HUH Cancer Center, September 21, 2007
4. Fluorescent and Confocal Endomicroscopy, Optical Imaging and Potential Combination for Detection of Precancerous Lesions.  
Liang Shan, M.D., Ph.D. Molecular Imaging Laboratory  
HUH Cancer Center, Nov. 21, 2007
5. ABC Transporters As Multidrug Resistance Mechanisms and the Development of Chemosensitizers.  
Yanfei Zhou, Ph.D. Department of Radiation Oncology, Howard University  
HUH Cancer Center, Dec. 21, 2007
6. Validating of *in vivo* Bioluminescence Imaging as a Quantitative Modality for Solid Tumor Xenografts.  
Alexandru Korotcov, Ph.D. Molecular Imaging Laboratory  
HUH Cancer Center, Dec. 21, 2007
7. Expression of Recombinant Antibodies and Immunotoxins  
Yuanyi Liu, Ph.D., National Institute of Mental Health, NIH, Bethesda, Maryland  
HUH Cancer Center, Feb. 5, 2008
8. Analysis of Mass Spectrometry Data for Serum Biomarker Discovery  
Habtom Ressim, Ph.D., Co-Director of the LCCC Macromolecular Analysis Shared Resource Georgetown Lombardi Comprehensive Cancer Center, Washington, DC  
HU Seeley G. Mudd Building, Feb. 28, 2008
9. Animal Handling Workshop  
Songping Wang, BS, Liang Shan, M.D., Ph.D.  
HUH Cancer Center, May 9, 2008



10. IVIS Spectrum Optical Imaging System Workshop.  
Dustin H. Whittemore, Advanced Imaging Training Manager, Caliper Life Sciences, Inc.,  
HUH Cancer Center, May 20, 2008

II.2.b. Seminars and workshops at John Hopkins University and other institutes:

1. Exploring New Routes for Paramagnetic Lanthanide Complexes in MR-Molecular Imaging Investigations  
Silvio Aime, Ph.D. Director NMR Laboratory Center of Excellence on Molecular Imaging  
University of Torino, Italy.  
JHU, Darner Conference Room Ross G-007, April 9, 2008
2. Beyond FDG: Moving New Imaging PET Probes to the Clinic.  
Jerry M. Collins, Ph.D., Director, Developmental Therapeutics Program, NCI  
JHU Radiology Building – Hospital, Stoll Conference Room, March 26, 2008
3. NMR Concepts & Operating Techniques, the Traficante Series.  
Mar 30 – April 5, 2008  
University of Rhode Island, Kingston, RI
4. 2008 PerkinElmer Inorganic Workshop  
Tuesday, April 8, 2008  
The Inn and Conference Center, Adelphi, MD 20783
5. Service and Maintenance Course  
April 15 – April 18, 2008  
Bruker Biospin MRI, Inc., Billerica, MA 01821

**II.3 Statement of Work** (The bold typed accomplishments are occurred in this reporting period).

*Task 1. To conduct the study “MR Image Enhancement by Tumor Cell Targeted immunoliposome Complex Delivered Contrast Agent”*

- a. Purchase supplies for cell culture and materials for construction of liposome (Months 1-2) (completed)
- b. Construct and measure the size of liposome (Months 3-4) (completed)
- c. Attach ligands (single chain variable fragment of transferring antibody) to liposome (TfR-scFv-Lip) (Months 5-8) (completed).
- d. Make TfR-scFv-Lip-contrast agent complex. Measure the size of complex and amount of contrast agent encapsulated in the liposome (Month 9-12) (completed).
- e. In vitro imaging of transfected MDA-MB-231 breast cancer cells in pellet (Month 13-24) (completed)
- f. Verify the transfection efficiency by MRI and optical imaging (Month 19-24) (completed)
- g. Animal Study: Grow tumor xenografts on nude mice. In vivo MRI imaging of 120 tumor-bearing mice administered TfR-scFv-Lip-CA, Lip-CA, and CA only, using T1 and T2 weighted MRI imaging techniques (Months 27-45) (**completed**)
- h. Quantify the contrast enhancement. Image data analysis (Months 27-45).

*Task 2. To conduct the study “Imaging the Effects of Macrophage Function on Tumor Promotion”*

- Determine the effects of macrophages on metastasis-related gene expression in breast cancer cells (Months 1 – 24) (**completed**).
  - a. Measure migratory and invasive properties of breast cell lines that are co-cultured with macrophages: changes in anchorage-dependent cell growth, invasion through matrigel (Months 1 – 12) (**completed**).
  - b. Isolate RNA for gene expression analysis using gene arrays. Monitor expression of proinvasive integrins, MMPs, and TIMPs, etc. (Months 6 – 18) (**completed**).
  - c. Transfect MCF-12A (mammary epithelial cells), MDA-MB-231, and MDA-MB-468 cancer cells with luciferase construct. Screen luciferase-expressing cells and isolate stable clones by limiting dilution (Months 8 – 24) (**completed**).
- Determine the effects of co-culture with macrophages on the growth of Luc<sup>+</sup> mammary epithelial cells and breast cancer cells in 20 athymic nu/nu mice (Months 24 – 48).
  - a. Luc<sup>+</sup> MCF-7 cells (in development) and MDA-MB-231 cells will be obtained from Xenogen. Luc<sup>+</sup> mammary epithelial and breast cancer cells co-cultured with macrophages (LPS activated or unactivated). Inject breast cells into athymic mice and monitor with the Xenogen IVIS™ Imaging System. (Month 24-48). (**in progress**)
  - b. Repeat gene expression experiments in Luc<sup>+</sup> cells to correlate gene expression patterns with *in vivo* growth (Months 36 – 48) (**in progress**).

*Task 3. To establish a molecular imaging core facility.*

- a. Purchase laboratory supplies (months 1-4) (completed).
- b. Purchase Xenogen IVIS imaging system (months 3-9) (completed).
- c. Establish the designated Molecular Imaging Core Facility in Cancer Center (Rm B103). Install incubator and hood. (Months 3-9) (completed).
- d. Relocate/centralize all the molecular biology instruments to the Molecular Imaging Core Facility (Months 3-9) (completed).
- e. Training on Xenogen IVIS imaging system (Month 10) (completed).
- f. Molecular Imaging Core Facility open house (Month 10) (completed).

*Task 4. To train faculty trainees in molecular imaging research.*

- a. Biweekly group meetings (organized by research leaders) (Months 1-48) (**in progress**).
- b. Monthly journal clubs (Months 1-48) (**in progress**).
- c. Seminar series (nine seminars each year) (Months 1-48) (**in progress**).
- d. Six workshops (chaired by Dr. Wang and Dr. Bhujwalla) (months 1-18) (**completed**).
- e. Laboratory Internships (2 days to one week each) (Months 1-18) (**completed**).
- f. Research concepts development (**in progress**).
- g. Research grants submission (**in progress**).

*Task 5. Administrative and communication affairs (coordinated by Dr. Wang and Dr. Bhujwalla). (Months 1-48) (**in progress**).*

- a. Status reports (monthly, quarterly, and annual reports).
- b. Research progress review (quarterly).
- c. Administrative meetings (biannually meetings).
- d. Coordination of seminars, workshops, and laboratory internships.

### III. Key Research Accomplishments

#### *Project 1: MR Image Enhancement by Tumor Cell Targeted Immunoliposome Complex Delivered Contrast Agent*

- We have constructed liposome (Lip) nanoparticles modified with Tf on the surface as a ligand for specific targeting and CA (Magnevist) inside as the payload ( $\text{Tf}^{\text{NIR}}\text{-Lip}^{\text{NBD}}\text{-CA}$ ). In vitro analysis demonstrated that the nanocomplex dramatically improved the uptake of CA in monolayer cultures of MDA-MB-231-luc human breast cancer cells. In vivo, the probe significantly enhanced the MRI signals, and was superior to the use of clinical MRI CA alone. The heterogeneous signal enhancement by the liposomal nanocomplex probe correlates well with the pathology of the tumors.
- For optical imaging of human breast cancers, we have constructed targeted fluorescent liposome nanoparticles using near-infrared (NIR) fluorescent transferrin conjugate ( $\text{Tf}^{\text{NIR}}$ ), NIR fluorescent dyes and fluorescently labeled (NBD) cationic liposomes ( $\text{Lip}^{\text{NBD}}$ ) ( $\text{Tf}^{\text{NIR}}\text{-Lip}^{\text{NBD}}\text{-dye}$ ). *In vitro* and *in vivo* analysis indicates that both  $\text{Tf}^{\text{NIR}}$  and  $\text{Tf}^{\text{NIR}}\text{-Lip}^{\text{NBD}}\text{-dye}$  are potentially useful for visualizing human breast cancer in clinic.  $\text{Tf}^{\text{NIR}}\text{-Lip}^{\text{NBD}}\text{-dye}$  is superior to  $\text{Tf}^{\text{NIR}}$  alone for imaging small tumors because of better delivery of fluorescent contrast agents to the tumors.
- To increase the sensitivity of optical detection of breast cancer, we have synthesized QDs and conjugated QDs with Tf as an optical imaging agent. *In vitro* targeted uptake of QDs-Tf by MDA-MB-231 cells was confirmed using flow cytometry. In addition, to further stabilize QDs, a novel kind of tri-block copolymer as a multi-dentate ligand has been successfully synthesized. It is expected that the novel multi-dentate ligand can improve the stability and biocompatibility of QDs under harsh *in vivo* conditions.
- We have also developed a bioluminescence assay for rapid measurement of cell death using Xenogen Optical Imaging System and luciferase transfected MDA-MB-231-luc human breast cancer cells. The assay was tested when cells were subjected to 43°C hyperthermia and compared with traditional methods including MTT and colony formation assays. The results indicate that this assay may be used for rapid screening of cytotoxic regimens.

#### *Project 2: Imaging the Effects of Macrophages on Breast Cancer Metastasis*

- We have analyzed how interactions between the MCF-7 and macrophages are affected by tamoxifen and aspirin, and the phenotypic changes that may render TAMs selectively vulnerable to pharmacological agents.
- All cells expressed MIF RNA. In co-culture, *MIF* expression was upregulated in MCF-7, but downregulated in macrophages. MCF-7-induced reduction of MIF expression in TAMs may be associated with partial M2 polarization; therefore, co-culture produced macrophage phenotypes that were intermediate between M1 and M2. Reduction of MIF expression may also produce context-specific vulnerability of macrophages to therapeutic agents.
- Aspirin induced *IL-10* expression in both macrophages and MCF-7 grown separately. MCF-7 cells did not express *IL-10* when grown separately or in co-culture. However, aspirin induced *IL-10* expression in MCF-7 and in tamoxifen-pretreated MCF-7. Moreover, aspirin-pretreated macrophages potently induced *IL-10* expression in MCF-7 cells and pretreatment of MCF-7 with tamoxifen did not prevent this induction.

- Two molecular variants of MIF were identified: a larger, macrophage-type and a smaller, MCF-7-type; both variants were present in co-cultured MCF-7 cells.
- Co-culture of MCF-7 with LPS-activated THP-1 macrophages induced a change in MCF-7 morphology reminiscent of an epithelial-to-mesenchymal transition.

#### IV. REPORTABLE OUTCOMES

##### Publications

1. Shan L, Hao Y, Wang S, Korotcov A, Zhang R, Wang T, Califano J, Gu X, Sridhar R, Bhujwalla ZM, Wang PC. Visualizing Head and Neck Tumors *In Vivo* Using Near-infrared Fluorescent Transferrin Conjugate. *Mol. Imaging* 7:42-49, 2008
2. Shan L, Wang S, Korotcov A, Sridhar R, Wang PC: Bioluminescent Animal Models of Human Breast Cancer for Tumor Biomass Evaluation and Metastasis Detection. *Ethn. Dis.* 18:S2-65-69, 2008
3. Ross, S, Ejofodomi O, Jendoubi A, Kinnard L, Chouikha M, Lo B, Wang P, Zheng J. A Mammography Database and View System for the African American Patients. *J. Dig. Imaging* 21:18-26, 2008.
4. Cheng KT, Wang PC, and Shan L. Alexa Fluor 680-labeled Transferrin-cationic (NBD-labeled DOPE-DOTAP) Liposome-encapsulated Gadopentetate Dimeglumine Complex (Abbreviated name: Tf<sup>NIR</sup>-Lip<sup>NBD</sup>-CA complex) Targeting to Transferrin Receptors (TfR). In: *Molecular Imaging and Contrast Agent Database (MICAD)* [database online]. National Library of Medicine (US), NCBI; 2008. Available from: <http://micad.nih.gov>.
5. Gu, X., Song, X., Dong, Y., Cai, H., Walters, E., Zhang, R., Pang, X., Xie, T., Guo, Y., Sridhar, R., Califano, J.A. Vitamin E succinate induces ceramide-mediated apoptosis in head and neck squamous cell carcinoma in vitro and in vivo. *Clin. Cancer Res.* 14: 1840-1848, 2008.
6. Shan L, Wang S, Sridhar R, Bhujwalla ZM, Paul C. Wang PC: A Dual Probe with Fluorescent and Magnetic Properties for Imaging Solid Tumor Xenografts. *Mol. Imaging* 6:85-95, 2007
7. Chung DWY, Tsai YS, Miaou SG, Chang WH, Chang YJ, Chen SC, Hong YY, Chyang CS, Chang QS, Hsu HY, Hsu J, Yao WC, Hsu MS, Chen MC, Lee SC, Hsu C, Miao L, Byrd K, Chouikha MF, Gu XB, Wang PC, Szu H. Non-invasive methodology for wellness baseline profiling. *Proceedings of SPIE "Independent Component Analyses, Wavelets, Unsupervised Nano-Biomimetic Sensors, and Neural Networks V"*, 6576:OR1-17, 2007.
8. Velan, S.S., Lemieux, S.K., Raylman, R.R., Boling, W., Sridhar, R., Kuppusamy, P. and Thomas, M.A. Detection of cerebral metabolites by single – voxel based PRESS and COSY techniques at 3T. *J. Magn. Reson. Imaging* 26: 405-409, 2007.
9. Velan, S.S., Durst, C.L., Lemieux, S.K., Raylman, R.R., Sridhar, R., Spencer, R.G., Hobbs, G.R. and Thomas, M.A. Investigation of muscle lipid metabolism by localized one- and two-dimensional MRS techniques using a clinical 3T MRI/MRS scanner. *J. Magn. Reson. Imaging.* 25: 192-199, 2007.
10. Zhou, Y., Gu, X., Ashayeri, E., Zhang, R. and Sridhar R. Nicotine decreases the cytotoxicity of doxorubicin towards MCF-7 and KB-3.1 human cancer cells in culture. *J.*

Natl. Med. Assoc. 99: 319-327, 2007

11. Burnett GT, Weathersby DC, Taylor TE, Bremner TA. Regulation of inflammation- and angiogenesis-related gene expression and breast cancer cell and co-cultured macrophages. Anticancer Res. 28, July 15 online first, 2008 (in press)

### **Meeting Abstracts/Presentations**

1. Wang PC, Shan L, Hao Y, Zhang D, Zhang R, Korotcov A, Wang TX, Califano J, Gu X. Optical Imaging of Head and Neck Squamous Cell Carcinoma Xenografts Using Near-infrared Fluorescent Transferrin Conjugate. Joint Molecular Imaging Conference, pp.318, Providence, RI, Sep 8-11, 2007
2. Wang PC. Molecular Imaging of Solid Tumor Xenografts Using a Dual Fluorescent and MR Probe. Progress in Biochemistry and Biophysics. 34(1):95, Beijing, China, 2007
3. Liang XJ, Wang PC. Circumventing Malignant Tumors by Innovative and Effective Nanoparticle as Novel Chemotherapeutic Agent. Progress in Biochemistry and Biophysics. 34(1):104, Beijing, China, 2007
4. Wang PC. Molecular Imaging of Solid Tumor Xenografts Using a Dual Fluorescent and MR Probe. National Center for Nanoscience and Technology, Beijing, China. Oct 9, 2007.
5. Wang PC. Molecular Imaging of Tumor in Small Animals. NanChang, JiangXi, China. Oct 12, 2007.
6. Wang PC. Molecular Imaging of Solid Tumor Xenografts Using a Dual Fluorescent and MRI Probe. Fu Jen Catholic University, Taipei, Taiwan. Oct 24, 2007.
7. Wang PC. Studying of Solid Tumor in Small Animals Using Various Imaging Modalities. National Chung Shing University, TaiChung, Taiwan. Oct 26, 2007.
8. Wang PC. Molecular Imaging Laboratory. Howard University Nanotechnology Symposium. Nov 5-6, 2007. Washington DC
9. Shan L. Transferrin targeted fluorescent liposome nanoparticles for visualization of human breast cancer xenografts in mouse. Howard University Nanotechnology Symposium. Nov 5-6, 2007, Washington DC
10. Wang TX. Encapsulation and bioconjugation of quantum dots for non-invasive detection of tumor. Howard University Nanotechnology Symposium. Nov 5-6, 2007, Washington DC.
11. Korotcov AV. Targeted MR imaging for solid tumor xenografts using liposomal nanocomplex. Howard University Nanotechnology Symposium. Nov 5-6, 2007, Washington DC.
12. Sridhar R. Quality control and safety issues in nanomedicine. Howard University Nanotechnology Symposium. Nov 5-6, 2007, Washington DC.
13. Wang PC. Howard University Molecular Imaging Laboratory, National Children's Hospital, Washington, DC, January 9, 2008, Washington DC.
14. Wang PC. Molecular Imaging of Solid Tumor Xenografts Using a Dual Fluorescent and MRI Probe. Howard University Biochemistry and Molecular Biology Department, February 14, 2008, Washington DC.

15. Wang PC, Wang TX, Shan L, Wang SP, Korotcov A. Molecular Imaging of Solid Tumor in Small Animal Using a Dual Fluorescent and MRI Probe. BIROW, Jan 17-19, 2008, Rockville, MD
16. Shan L, Korotcov A, Wang SP, Wang TX, Wang PC. Molecular Imaging of Solid Tumor in Small Animal Using a Dual Fluorescent and MRI Probe. Cancer Nanobiology Think Tank, NCI, May 24, 2008, Fredrick, MD.
17. Wang PC. Molecular Imaging Laboratory at Howard University. Era of Hope: Building Networks Symposium. June 24-25, 2008, Baltimore, MD.
18. Wang TX, Shan L, Korotcov A, Wang SP, Zhou YF, Wang PC. Surface Coating and Bioconjugating of Quantum Dots for Non-invasive Detection of Breast Cancer. Era of Hope. June 25-28, 2008, Baltimore, MD
19. Shan L, Wang SP, Zhou YF, Korotcov A, Zhang RS, Wang TX, Sridhar R, Bhujwalla ZM, Wang PC. Targeted Fluorescent Liposome Nanoparticles for Molecular Imaging of Breast Cancer Xenografts in Mouse. Era of Hope. June 25-28, 2008, Baltimore, MD
20. Korotcov A, Shan L, Wang SP, Wang TX, Sridhar R, Bhujwalla ZM, Wang PC. Targeted DCE-MRI for Imaging and Characterization of Solid Tumor Xenografts. Era of Hope. June 25-28, 2008, Baltimore, MD
21. Burnett G, Bremner T. Breast Cancer Cells Down-regulate Tristetraprolin in Co-cultured Macrophages: A Possible Mechanism for Sustaining Inflammation and Angiogenesis in the Tumor Microenvironment. Era of Hope. June 25-28, 2008, Baltimore, MD
22. Burnett GT, Weathersby DC, Taylor TE, Bremner TA. MCF-7 breast cancer cells down-regulate macrophage migration inhibitory factor in co-cultured macrophages: Implications for context-specific modulation of tumor-associated macrophages. Era of Hope. June 25-28, 2008, Baltimore, MD
23. Sridhar R, Beyene D, Zhou Y, Kassa A, Zhang R, Ashayeri E. Cytotoxicity, cell cycle effects and mutagenicity of etidronic acid towards MCF-7 human breast cancer cells. Era of Hope. June 25-28, 2008, Baltimore, MD
24. Sridhar R, Zhang R, Zhou Y, Shan L, Ashayeri E, Wang PC. Bioluminescence Imaging for Monitoring the Response of a Luciferase Transfected Human Breast Cancer Cell Line Subjected to Hyperthermia. Era of Hope. June 25-28, 2008, Baltimore, MD

#### Submitted Grants

1. NIH/NCI 03/11/2008, pending  
Application of Targeted Contrast Agent for Pathological Evaluation of Solid Tumor  
PI: Dr. Paul C. Wang (Dr. Zaver Bhujwalla/JHU, as Co-PI)
2. NIH 03/31/2008, pending  
Multiple Targeted Gene Expression Display and Establishment of a Database Bank of Targets and Probes for Detection of Epithelial Precancers  
PI: Dr. Liang Shan
3. DoD (PI: Dr. Hill-Williams) 05/21/2008, pending  
Targeting specific alteration in phosphatidylinositol 3-kinase signal transduction pathway for prostate cancer preventive and/or curative therapy  
Collaborator: Dr. Paul C. Wang
4. DoD 06/30/2008, pending

Targeting specific alteration in phosphatidylinositol 3-kinase signal transduction pathway for prostate cancer preventive and/or curative therapy

PI: Dr. Rajagopalan Sridhar

5. DoD 06/30/2008, pending  
Transrectal Targeted Optical Imaging and Light-guided Sampling for Detection of Early Prostate Cancer  
PI: Dr. Liang Shan

### **On Going Grants**

1. 2G12 RR003048 (Taylor) 08/05/03 - 05/31/08  
NIH/NCRR/RCMI  
Biomedical Imaging and Molecular Structural Studies-RCMI  
To serve as the director of the Biological NMR Laboratory and to coordinate the research activities using this core laboratory.  
Role: Project PI
2. USAMCAA W81XWH-05-1-0291 (Wang) 07/01/05-06/30/09  
US Army Medical Command  
A Partnership Training Program in Breast Cancer Research Using Molecular Imaging Techniques  
This is a training partnership program with Dr. Zaver M. Bhujwalla at Johns Hopkins University to train faculty at Howard University in the molecular imaging field. This program has two components: a collaborative research component and a training component. The research component includes two projects using MRI and optical imaging techniques to study the functions of macrophage in tumor bearing animals. The training component includes organizing workshops, symposiums and lab internships for the trainees.  
Role: PI
3. 2U54 CA 091431-06A1 (Adams-Campbell) 08/31/06-09/30/09  
NIH  
Tumor-targeted MR Contrast Enhancement Using Molecular Imaging Techniques  
This is a full research project included in the Howard University Cancer Center / Johns Hopkins University Cancer Center Partnership grant.  
Role: Project PI

## **V. CONCLUSIONS**

In the third year, this training grant continuously progressed well. Faculty members from Departments of Biology, Radiology, and Radiation Oncology at Howard University were further trained in molecular imaging through seminars and workshops, and by conducting research with the faculty at the Johns Hopkins University.

We have established three breast cancer tumor models, and further optimized the imaging probes for MRI and fluorescent optical imaging of breast cancers. We have determined how the interactions between MCF-7 cells and macrophages are affected by tamoxifen and aspirin. We

have also identified the phenotypic changes that may render TAMs selectively vulnerable to pharmacological agents.

In this reporting period, we have published 11 papers and given 24 presentations in conferences. Based on the data we obtained, we have submitted 5 new proposals for the NIH and DoD grant applications. The Molecular Imaging Lab continuously serves as a synergic center on campus for promoting molecular imaging research. New research collaborations were established among the faculty at Howard, as well as with the scientists from the Children's National Medical Center and Georgetown University.

## VI. REFERENCES

- [1] Pautler RG (2004). Mouse MRI: concepts and applications in physiology. *Physiol.* 19:168-175.
- [2] Artemov D (2003). Molecular magnetic resonance imaging with targeted contrast agent. *J Cell Biochem.* 90: 518-524.
- [3] Massoud TF, Gambhir SS (2003). Molecular imaging in living subjects: seeing fundamental biological processes in a new light. *Gene Dev.* 17:545-580.
- [4] Persigehl T, Heindel W, Bremer C (2005). MR and optical approaches to molecular imaging. *Abdom Imaging.* 30:342-354.
- [5] Blasberg RG (2003). Molecular imaging and cancer. *Mol Cancer Ther.* 2:335-345.
- [6] Artemov D, Mori N, Okollie B, Bhujwalla ZM (2003). MR molecular imaging of HER-2/neu receptor in breast cancer cells using targeted iron oxide nanoparticles, *Magn Reson Med.* 49:403-408.
- [7] Mulder WJM, Strijkers GJ, Griffioen AW, van Bloois L, Molema G, Storm G, Koning GA, Nicolay K (2004). A liposomal system for contrast-enhanced magnetic resonance imaging of molecular targets. *Bioconjugate Chem.* 15:799-806.
- [8] Jones DT, Trowbridge IS, Harris AL (2006). Effects of transferrin receptor blockade on cancer cell proliferation and hypoxia-inducible factor function and their differential regulation by ascorbate. *Cancer Res.* 66:2749-2756.
- [9] Hogemann-Savellano D, Bos E, Blondet C, Sato F, Abe T, Josephson L, Weissleder R, Gaudet J, Sgroi D, Peters PJ, Basilion JP (2003). The transferrin receptor: a potential molecular imaging marker for human cancer. *Neoplasia.* 5:495-506.
- [10] Batra JK, Fitzgerald DJ, Chaudhary VK, Pastan I (1991). Single-chain immunotoxins directed at the human transferrin receptor containing Pseudomonas exotoxin A or diphtheria toxin: Anti-TFR(Fv)-PE40 and DT388-anti-TFR(Fv). *MolCellBiol.* 11:2200-2205.
- [11] Jain RK, Baxter LT (1988). Mechanisms of heterogeneous distribution of monoclonal antibodies and other macro-molecules in tumors: Significance of elevated interstitial pressure. *CancerRes.* 48:7022-7032.
- [12] Xu L, Tang WH, Huang CC, Alexander W, Xiang LM, Pirollo KF, Rait A, Chang EH (2001). Systemic p53 gene therapy of cancer with immunolipoplexes targeted by anti-transferrin receptor scFv. *MolMed.* 7:723-734.
- [13] Xu L, Huang C-C, Huang W-Q, Tang W-H, Rait A, Yin Y, Cruz I, Xiang L-M, Pirollo K, Chang EH (2002). Systemic tumor-targeted gene delivery by anti-transferrin receptor scFv-immunolipo-somes. *MolCancerTher.* 1:337-346.



- [14] Xu L, Pirollo KF, Tang Wh, Rait A, Chang EH (1999). Transferrin-liposome-mediated systemic p53 gene therapy in combination with radiation results in regression of human head and neck cancer xenographs. *Hum Gene Ther.* 10:2941-2952.
- [15] Schellenberger EA, Sosnovik D, Weissleder R, Josephson L (2004). Magneto/optical annexin V, a multimodal protein. *Bioconjugate Chem.* 15:1062-1067.
- [16] Blasberg RG (2003). In vivo molecular-genetic imaging: multi-modality nuclear and optical combinations. *Nucl Med Biol.* 30:879-888.
- [17] Veisheh O, Sun C, Gunn J, Kohler N, Gabikian P, Lee D, Bhattarai N, Ellenbogen R, Sze R, Hallahan A, Olson J, Zhang M (2005). Optical and MRI multifunctional nanoprobe for targeting gliomas. *Nano Lett.* 5:1003-1008.
- [18] Jones DT, Trowbridge IS, Harris AL (2006). Effects of transferrin receptor blockade on cancer cell proliferation and hypoxia-inducible factor function and their differential regulation by ascorbate. *Cancer Res.* 66:2749-2756.
- [19] Hogemann-Savellano D, Bos E, Blondet C, Sato F, Abe T, Josephson L, Weissleder R, Gaudet J, Sgroi D, Peters PJ, Basilion JP (2003). The transferrin receptor: a potential molecular imaging marker for human cancer. *Neoplasia.* 5:495-506.
- [20] Xu L, Pirollo KF, Tang Wh, Rait A, Chang EH (1999). Transferrin-liposome-mediated systemic p53 gene therapy in combination with radiation results in regression of human head and neck cancer xenographs. *Hum Gene Ther.* 10:2941-2952.
- [21] Bellocq NC, Pun SH, Jensen GS, Davis ME (2003). Transferrin-containing, cyclodextrin polymer-based particles for tumor-targeted gene delivery. *Bioconjugate Chem.* 14:1122-1132.

## VII. APPENDICES

1. Shan L, Hao Y, Wang S, Korotcov A, Zhang R, Wang T, Califano J, Gu X, Sridhar R, Bhujwalla ZM, Wang PC. Visualizing Head and Neck Tumors *In Vivo* Using Near-infrared Fluorescent Transferrin Conjugate. *Mol. Imaging* 7:42-49, 2008
2. Shan L, Wang S, Korotcov A, Sridhar R, Wang PC: Bioluminescent Animal Models of Human Breast Cancer for Tumor Biomass Evaluation and Metastasis Detection. *Ethn. Dis.* 18:S2-65-69, 2008
3. Ross, S, Ejofodomi O, Jendoubi A, Kinnard L, Chouikha M, Lo B, Wang P, Zheng J. A Mammography Database and View System for the African American Patients. *J. Dig. Imaging* 21:18-26, 2008.
4. Cheng KT, Wang PC, and Shan L. Alexa Fluor 680-labeled Transferrin-cationic (NBD-labeled DOPE-DOTAP) Liposome-encapsulated Gadopentetate Dimeglumine Complex (Abbreviated name: Tf<sup>NIR</sup>-Lip<sup>NBD</sup>-CA complex) Targeting to Transferrin Receptors (TfR). In: *Molecular Imaging and Contrast Agent Database (MICAD)* [database online]. National Library of Medicine (US), NCBI; 2008.
5. Shan L, Wang S, Sridhar R, Bhujwalla ZM, Paul C, Wang PC: A Dual Probe with Fluorescent and Magnetic Properties for Imaging Solid Tumor Xenografts. *Mol. Imaging* 6:85-95, 2007
6. Chung DWY, Tsai YS, Miaou SG, Chang WH, Chang YJ, Chen SC, Hong YY, Chyang CS, Chang QS, Hsu HY, Hsu J, Yao WC, Hsu MS, Chen MC, Lee SC, Hsu C, Miao L, Byrd K, Chouikha MF, Gu XB, Wang PC, Szu H. Non-invasive methodology for wellness baseline profiling. *Proceedings of SPIE "Independent Component Analyses, Wavelets, Unsupervised*

Nano-Biomimetic Sensors, and Neural Networks V", 6576:OR1-17, 2007.

7. Zhou, Y., Gu, X., Ashayeri, E., Zhang, R. and Sridhar R. Nicotine decreases the cytotoxicity of doxorubicin towards MCF-7 and KB-3.1 human cancer cells in culture. *J. Natl. Med. Assoc.* 99: 319-327, 2007
8. Gu, X., Song, X., Dong, Y., Cai, H., Walters, E., Zhang, R., Pang, X., Xie, T., Guo, Y., Sridhar, R., Califano, J.A. Vitamin E succinate induces ceramide-mediated apoptosis in head and neck squamous cell carcinoma in vitro and in vivo. *Clin. Cancer Res.* 14: 1840-1848, 2008.
9. Velan, S.S., Lemieux, S.K., Raylman, R.R., Boling, W., Sridhar, R., Kuppusamy, P. and Thomas, M.A. Detection of cerebral metabolites by single – voxel based PRESS and COSY techniques at 3T. *J. Magn. Reson. Imaging* 26: 405-409, 2007.
10. Velan, S.S., Durst, C.L., Lemieux, S.K., Raylman, R.R., Sridhar, R., Spencer, R.G., Hobbs, G.R. and Thomas, M.A. Investigation of muscle lipid metabolism by localized one- and two-dimensional MRS techniques using a clinical 3T MRI/MRS scanner. *J. Magn. Reson. Imaging.* 25: 192-199, 2007.
11. Wang PC, Wang TX, Shan L, Wang SP, Korotcov A. Molecular Imaging of Solid Tumor in Small Animal Using a Dual Fluorescent and MRI Probe. BIROW, Rockville, MD, Jan 17-19, 2008.
12. Wang PC, Wang SP, Korotcov A, Wang TX, Shan L, Sridhar R, Bhujwalla ZM. A Molecular Probe  $Tf^{NIR}$ -Lip $^{NBD}$ -CA for MRI and Optical Imaging of Breast Cancer. Cancer Nanobiology Think Tank, NCI, Fredrick, MD, May 24, 2008.
13. Korotcov A, Shan L, Wang SP, Wang TX, Sridhar R, Bhujwalla ZM, Wang PC. Targeted DCE-MRI for Imaging and Characterization of Solid Tumor Xenografts. Era of Hope. Baltimore, MD, June 25-28, 2008.
14. Shan L, Wang SP, Zhou YF, Korotcov A, Zhang RS, Wang TX, Sridhar R, Bhujwalla ZM, Wang PC. Targeted Fluorescent Liposome Nanoparticles for Molecular Imaging of Breast Cancer Xenografts in Mouse. Era of Hope. Baltimore, MD, June 25-28, 2008.
15. Wang TX, Shan L, Korotcov A, Wang SP, Zhou YF, Wang PC. Surface Coating and Bioconjugating of Quantum Dots for Non-invasive Detection of Breast Cancer. Era of Hope. Baltimore, MD, June 25-28, 2008.
16. Sridhar R, Beyene D, Zhou Y, Kassa A, Zhang R, Ashayeri E. Cytotoxicity, cell cycle effects and mutagenicity of etidronic acid towards MCF-7 human breast cancer cells. Era of Hope. June 25-28, 2008, Baltimore, MD
17. Sridhar R, Zhang R, Zhou Y, Shan L, Ashayeri E, Wang PC. Bioluminescence Imaging for Monitoring the Response of a Luciferase Transfected Human Breast Cancer Cell Line Subjected to Hyperthermia. Era of Hope. June 25-28, 2008, Baltimore, MD
18. Burnett G, Bremner T. Breast Cancer Cells Down-regulate Tristetraprolin in Co-cultured Macrophages: A Possible Mechanism for Sustaining Inflammation and Angiogenesis in the Tumor Microenvironment. Era of Hope. June 25-28, 2008, Baltimore, MD
19. Burnett GT, Weathersby DC, Taylor TE, Bremner TA. MCF-7 breast cancer cells down-regulate macrophage migration inhibitory factor in co-cultured macrophages: Implications for context-specific modulation of tumor-associated macrophages. Era of Hope. June 25-28, 2008, Baltimore, MD

# Visualizing Head and Neck Tumors In Vivo Using Near-Infrared Fluorescent Transferrin Conjugate

Liang Shan, Yubin Hao, Songping Wang, Alexandru Korotcov, Renshu Zhang, Tongxin Wang, Joseph Califano, Xinbin Gu, Rajagopalan Sridhar, Zaver M. Bhujwalla, and Paul C. Wang

## Abstract

Transferrin receptor (TfR) is overexpressed in human head and neck squamous cell carcinomas (HNSCCs). This study was carried out to investigate the feasibility of imaging HNSCC by targeting TfR using near-infrared fluorescent transferrin conjugate (Tf<sup>NIR</sup>). Western blot analysis of four HNSCC cell lines revealed overexpression of TfR in all four lines compared with that in normal keratinocytes (OKFL). Immunocytochemistry further confirmed the expression of TfR and endocytosis of Tf<sup>NIR</sup> in JHU-013 culture cells. Following intravenous administration of Tf<sup>NIR</sup> (200  $\mu$ L, 0.625  $\mu$ g/ $\mu$ L), fluorescent signal was preferentially accumulated in JHU-013 tumor xenografts grown in the lower back ( $n = 14$ ) and oral base tissues ( $n = 4$ ) of nude mice. The signal in tumors was clearly detectable as early as 10 minutes and reached the maximum at 90 to 120 minutes postinjection. The background showed an increase, followed by a decrease at a much faster pace than tumor signal. A high fluorescent ratio of the tumor to muscle was obtained (from 1.42 to 4.15 among tumors), usually achieved within 6 hours, and correlated with the tumor size ( $r = .74$ ,  $p = .002$ ). Our results indicate that TfR is a promising target and that Tf<sup>NIR</sup>-based optical imaging is potentially useful for noninvasive detection of early HNSCC in the clinic.

A CHALLENGE IN NEOPLASTIC DIAGNOSTICS is noninvasive detection of tumors at an early stage and providing information on treatment selection and its outcome. Molecular imaging provides opportunities to fulfill the clinical needs.<sup>1–3</sup> Its advancement benefits from the identification of hundreds of biomarkers that are highly expressed in tumors.<sup>4,5</sup> In theory, by detecting the differences in “molecular properties” between cancer and surrounding normal tissues, the signal to noise ratio can be significantly increased, and that should allow for detection of smaller tumors. Relative to other imaging techniques, near-infrared (NIR) fluorescence-based optical imaging

offers unique advantages for diagnostic imaging of solid tumors. Newly developed fluorescent contrast agents and highly sensitive light detection systems have made it possible to monitor the biologic activity of a wide variety of molecular targets, such as intracellular enzymes, cell surface receptors, and antigens in living subjects. NIR optical imaging is highly sensitive, with a capability to detect a molecular probe at  $10^{-9}$  to  $10^{-12}$  mol/L without much interference from background and does not require the use of radioactive materials.<sup>1</sup> Because water and biologic tissues have minimal absorbance and autofluorescence in the NIR window (650–980 nm), efficient photon penetration into and out of tissue with low intratissue scattering can be achieved with a depth of about 1 cm for reflectance and 2 to 6 cm for tomographic fluorescence.<sup>1,6</sup> Although clinical application of optical imaging is limited owing to poor tissue penetration, the notable theoretical advantages include imaging a variety of molecular features based on versatile fluorescent probe design, providing dynamic, real-time in vivo images, monitoring of gene delivery, noninvasive detection of early tumors from accessible lumina by endoscopy, and real-time intraoperative visualization of tumor margins.<sup>7,8</sup>

In the United States, more than 55,000 Americans develop head and neck cancer each year. Squamous cell carcinoma accounts for 90% of the head and neck

From the Departments of Radiology, Oral Diagnostic Service, and Radiation Oncology, Howard University, Washington, DC, and Departments of Otolaryngology and Radiology, Johns Hopkins University, Baltimore, MD.

This work was supported in part by Department of Defense grant USAMRMC W81XWH-05-1-0291, the Charles and Mary Latham Fund (7023185), and National Institutes of Health National Center for Research Resources/Research Centers in Minority Institutions Program grants 2G12 RR003048, 5P20 CA118770, and 5U 54CA091431.

Address reprint requests to: Paul C. Wang, PhD, Department of Radiology, Howard University, 2041 Georgia Avenue, NW, Washington, DC 20060; e-mail: pwang@howard.edu.

DOI 10.2310/7290.2008.0006

© 2008 BC Decker Inc

cancers.<sup>9</sup> Head and neck squamous cell cancer (HNSCC) develops through a series of well-defined clinical and pathologic stages from atypia to carcinoma in situ and invasive lesions.<sup>10,11</sup> These lesions locate superficially, which makes them ideal for early detection and evaluation of biomarker expression using optical imaging. Transferrin receptor (TfR) is a cell-membrane internalizing receptor that is responsible for almost all of the iron sequestration in mammalian cells. It is overexpressed in various malignant tumors.<sup>12–14</sup> Previous work using radiolabeled transferrin (Tf) has demonstrated the feasibility of imaging mammary gland tumor xenografts with high sensitivity.<sup>15,16</sup> However, targeted detection methods based on radiolabeled probes have been hampered by relatively low spatial resolution and the risk of ionizing radiation exposure. Positron emission tomography (PET) involves the generation of positron-emitting short-lived radioisotopes using a cyclotron. This limits the accessibility of PET in many locations. There are also problems associated with the time necessary for conjugating a short-lived positron emitter to biomolecules. We hypothesized that TfR would be a promising target and NIR fluorescent Tf conjugate (Tf<sup>NIR</sup>) would be an ideal optical reporter for imaging HNSCC because TfR is expressed only in the parabasal and basal layers of normal squamous epithelium at a very low level and rarely in benign lesions. Importantly, TfR is overexpressed in the majority of HNSCC.<sup>17–19</sup> Since HNSCCs are superficial tumors, they are ideal for early detection and evaluation of biomarker expression using optical imaging. In the present study, we investigated the feasibility of imaging HNSCC xenografts using Tf<sup>NIR</sup>. A preferential accumulation of fluorescent signal was observed in tumors, and the tumor was clearly detectable in Tf<sup>NIR</sup>-based optical imaging.

## Materials and Methods

### Cell Culture

Four HNSCC cell lines (John Hopkins University, Baltimore, MD) were analyzed for TfR expression. These cell lines were originally established from human HNSCC arising from the base of the tongue (JHU-06), larynx (JHU-011 and 022), and neck node (JHU-013) metastasis. All four cell lines were routinely maintained in RPMI 1640 medium supplemented with 10% heat-inactivated fetal bovine serum and 50 µg/mL each of penicillin, streptomycin, and neomycin (Invitrogen, Carlsbad, CA). A normal human keratinocyte line (OKFL) was used as a control and cultured in keratinocyte serum-free medium (Invitrogen, Carlsbad, CA).<sup>20</sup>

### Western Blot Analysis

Cells were washed twice with Dulbecco's phosphate buffered saline (DPBS) and collected in protein lysis buffer containing 50 mM Tris (pH 8.0), 150 mM NaCl, 0.1% sodium dodecyl sulfate (SDS), 0.5% sodium deoxycholate, 1% NP40, 100 µg/mL of phenylmethylsulfonyl fluoride, 2 µg/mL of aprotinin, 1 µg/mL of pepstatin, and 10 µg/mL of leupeptin. The mixture was placed on ice for 30 minutes. Following centrifugation at 15,000 rpm for 15 minutes at 4°C, the supernatant was collected. Protein concentration was determined using the Bio-Rad Protein Assay Dye Reagent Concentrate (Bio-Rad, Hercules, CA). Whole-cell lysate (30 µg) was resolved in 8% SDS-polyacrylamide gel, transferred to polyvinylidene difluoride membrane (Immobilon, Amersham Corp., Arlington Heights, IL), and probed sequentially with antibodies against TfR (Invitrogen) and β-actin (Sigma, St. Louis, MO) at 4°C overnight, separately. Blots were washed thrice (10 minutes each) with PBS + 0.1% Tween 20 and incubated with horseradish peroxidase-conjugated anti-mouse antibody (Santa Cruz Biotech, Santa Cruz, CA) for 1 hour at room temperature. Blots were developed using the ECL detection system (Bio-Rad).

### Endocytosis of Tf and Immunocytochemistry of TfR

JHU-013 tumor cells at 40 to 50% confluence growing on four-chamber glass slides were used for endocytosis analysis. Cells were incubated with 6.25 µL of Alexa Fluor 488-labeled Tf (Tf<sup>488</sup>) (5 mg/mL) in 500 µL of complete medium for different durations (from 1 minute to 4 hours). After removal of the media, cells were completely washed thrice using DPBS. Cells were then fixed with 10% neutralized formalin for 10 minutes and mounted for fluorescent microscopic observation. For immunocytochemical staining of TfR, cells were first fixed using 10% neutralized formalin for 10 minutes and then incubated with anti-TfR monoclonal antibody for 2 hours at room temperature. The antibody was prepared in DPBS with a dilution of 1:200. After DPBS washing (three times, 5 minutes each), cells were incubated with Alexa Fluor 588-labeled goat antimouse immunoglobulin G (Invitrogen) for 1 hour. Negative control was stained similarly except the anti-TfR antibody was replaced by DPBS.

### Animal Models and Optical Imaging of Tumors

Two solid tumor xenograft models were developed by subcutaneous inoculation of  $1 \times 10^7$  subconfluent cells of

JHU-013 in 100  $\mu\text{L}$  of DPBS in the lower back or oral base tissues of athymic nude mice (8–10 weeks old; Harlan, Indianapolis, IN). Tumors were imaged when they reached certain sizes (2.4–9 mm in diameter). Fourteen tumors grown in the lower back of 12 mice, including 2 with tumors in both sides, were tested for the feasibility and fluorescent signal dynamics of  $\text{Tf}^{\text{NIR}}$ -based optical imaging. To verify the results, four tumors produced in the oral base tissues of four mice were further analyzed. Five healthy mice without tumors were used as the control.

$\text{Tf}^{\text{NIR}}$ -based fluorescent optical imaging was performed using the IVIS 200 Imaging System (Caliper Life Sciences, Hopkinton, MA). Imaging and quantification of the signals were controlled by the acquisition and analysis software *Living Image* (Caliper Life Sciences). Mice were placed onto the warmed stage inside a light-tight camera box with continuous exposure to 2% isoflurane. Animals were given 200  $\mu\text{L}$  (0.625  $\mu\text{g}/\mu\text{L}$ ) of the conjugate  $\text{Tf}^{\text{NIR}}$  through the tail vein. The entire animal was imaged every 10 to 30 minutes for at least 6 hours. The acquisition time for each image was 1 second. The light emitted from the mouse was detected, integrated, digitized, and displayed. Regions of interest from displayed images were identified and measured around the tumor sites. The signal intensity was expressed as mean flux (photons per second per centimeter squared per steradian,  $\text{p/s}/\text{cm}^2/\text{sr}$ ). Contralateral leg muscle was selected as normal background.

### Statistical Analysis

The tumor sizes were measured using calipers, and the relationship between fluorescent signal and tumor sizes was evaluated using the statistical software *OriginPro 7.0* (OriginLab, Northampton, MA). A significant correlation was inferred if a  $p$  value was  $< .05$  by correlation analysis.

## Results

### Expression of TfR in HNSCC Cell Lines

To better understand the expression status of TfR in HNSCC, TfR levels were analyzed in four HNSCC cell lines and one normal squamous cell line. A significantly high expression level of TfR was detected in all four HNSCC cell lines compared with that in the normal squamous cell line (Figure 1, A and B). Immunocytochemistry further confirmed the expression of TfR in JHU-013 cells. An immunoreactive signal was clearly seen in the cell

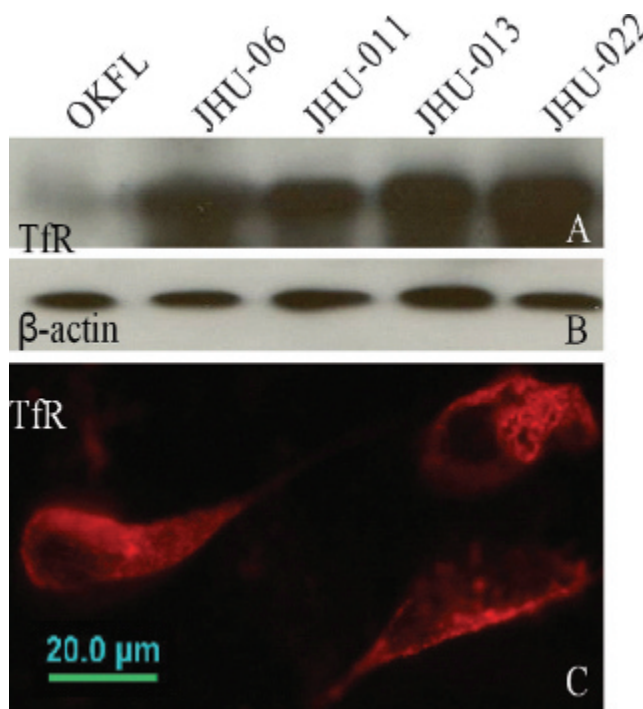


**Figure 1.** Transferrin receptor (TfR) expression. A, Western blot analysis of TfR expression showing overexpression of TfR in head and neck squamous cell carcinoma cell lines (JHU-06, 011, 013, 022) relative to that in a normal squamous cell line (OKFL). B, Same membrane re-probed with  $\beta$ -actin antibody. C, Immunocytochemistry in JHU-013 culture cells showing immunoreactive signal in cell membrane and cytoplasm.

membrane and cytoplasm (Figure 1C). Almost all of the tumor cells showed strong immunoreaction against TfR antibody. No signal was observed in the negative controls without primary antibody (data not shown).

### Endocytosis and Exocytosis of Tf

The kinetics of endocytosis of Tf in JHU-013 cells was examined following incubation of fluorescence-labeled Tf ( $\text{Tf}^{488}$ ) with monolayer cell cultures (Figure 2). Binding of  $\text{Tf}^{488}$  with TfR on the cell membrane was observed as early as 1 to 2 minutes after incubation. With prolonged incubation,  $\text{Tf}^{488}$  signal was seen in the cytoplasm and cell membrane. The maximum signal in the cytoplasm was observed after 1 to 2 hours of incubation, and the signal was distributed evenly within cytoplasm. With increased incubation time (3–4 hours), signal accumulation was observed in the regions surrounding the nuclei and regions close to the cell membrane. The total fluorescence decreased gradually thereafter, indicating exocytosis of  $\text{Tf}^{488}$ .



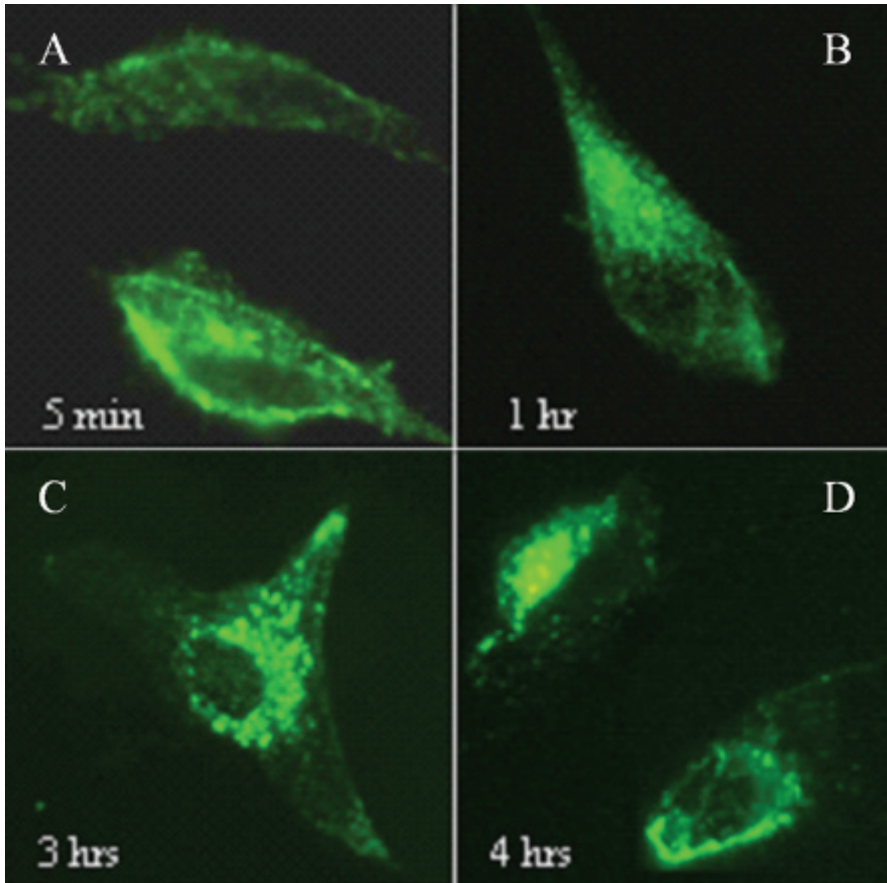


**Figure 2.** Different stages of transferin (Tf) endocytosis. Cells were incubated with Tf for varied times and imaged, and representative images are presented. *A*, Tf signal mainly in cell membrane (5 minutes). *B*, Signal in both cell membrane and cytoplasm with an evenly distributed pattern (1 hour incubation). Signal mainly in the perinuclear area (*C*; 3-hour incubation) and the peripheral area (*D*; 4-hour incubation). Tf was labeled with Alexa Fluor 488. The original magnification was  $\times 400$ .

### Tf<sup>NIR</sup>-Based Tumor Imaging in Animal Models of Human HNSCC

The Tf<sup>NIR</sup> conjugate contains 3 mol NIR fluorescent dye (Alexa Fluor 680)/mol Tf (Invitrogen). Two hundred microliters (0.625  $\mu\text{g}/\mu\text{L}$ ) of the Tf conjugate as a single bolus was administered via the tail vein of mice, and the whole animal was then imaged at different times. We first tested the imaging efficiency of Tf<sup>NIR</sup> in human tumor xenografts ( $n = 14$ ) grown in the lower back of athymic nude mice (Figure 3). The tumor sizes varied from 2.4 to 9 mm in diameter. A preferential accumulation of the fluorescence was detectable as early as 10 minutes in most tumors. The fluorescent signal in the tumors showed a rapid increase followed by a gradual decrease over time. The signal was still detectable after 48 hours. Interestingly, the time to reach the maximum fluorescence varied from 90 to 300 minutes, showing significant differences among tumors in different animals. In comparison with the tumor signal, the background fluorescence increased immediately after tail vein injection of the Tf<sup>NIR</sup> and decayed much faster than tumor signal. The background fluorescence was observed mainly arising from the liver, bone marrow,

brain tissue, and spleen. The fluorescent signal intensity ( $\text{p/s}/\text{cm}^2/\text{sr}$ ) was measured from the tumors and muscles in the opposite leg. The maximum tumor to muscle fluorescent signal ratio was reached within 6 hours in the majority of the tumors. The maximum ratio varied among tumors, ranging from 1.42 to 4.15. A positive correlation was observed between this ratio and the tumor sizes (2.4–9 mm in diameter) ( $r = .74$ ,  $p = .002$ ) (Figure 4).

To further test the *in vivo* imaging feasibility of Tf<sup>NIR</sup> in HNSCC, tumor xenografts were also established in the oral base tissues in four mice (Figure 5). In healthy mice without tumor, the fluorescent signal was observed immediately in the neck and head following administration of Tf<sup>NIR</sup>. The background fluorescent signal was observed arising mainly from the large blood vessels in the neck and brain tissue (Figure 5D). The background fluorescent signal was still detectable at 2 hours after injection. Importantly, in animals with tumors, although both background and tumor fluorescent signal were observed following injection, the background fluorescence decreased rapidly and was weak, whereas the tumor signal decreased slowly and was much stronger than background. The tumor in the oral base could be clearly imaged as those

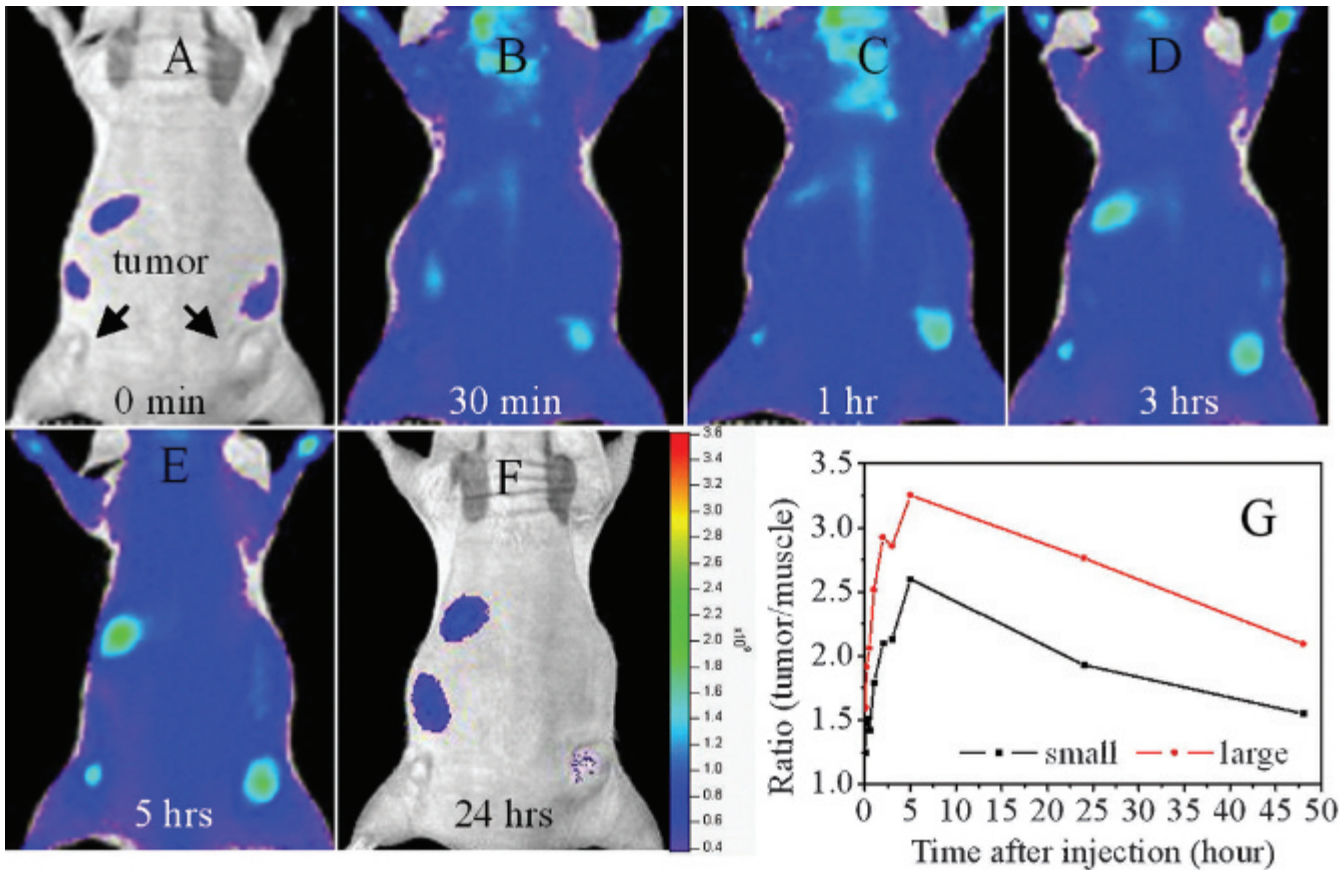


**Figure 3.** Whole-animal imaging following intravenous injection of near-infrared transferrin showing preferential accumulation of fluorescent signals in tumors. A to F show images taken at 0, 30 minutes, and 1, 3, 5, and 24 hours, separately. G shows change in the ratio of tumor to muscle fluorescence signal in small and large tumors over time.

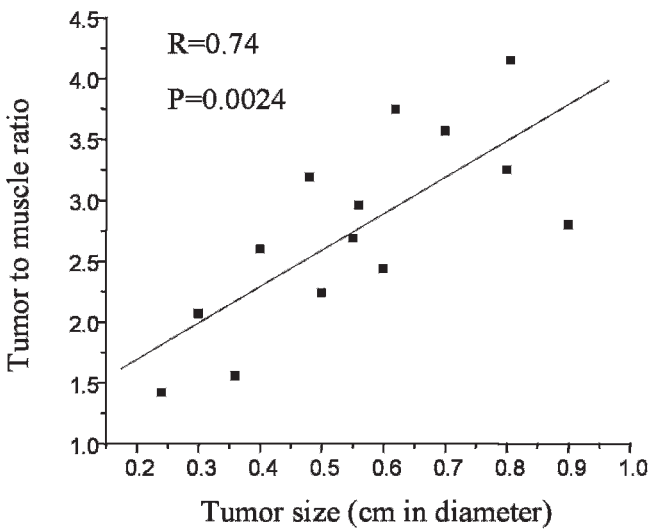


**Figure 4.** Positive correlation between the tumor size and the ratio of fluorescence signals from tumors to that from muscles.

in the lower back (Figure 5A–C). The background fluorescence appeared less problematic for detection of neck tumors owing to significantly weak intensity of the background compared with tumor signal.

**Discussion**

Theoretically, malignant tumor cells could be detected by imaging overexpressed biomarkers by taking advantage of specific binding of ligands with biomarkers and high sensitivity of optical imaging.<sup>1,3</sup> Furthermore, optical assessment of the biomarker expression level is potentially helpful in assessment of tumor prognosis and drug sensitivity.<sup>21,22</sup> Keeping these in mind, we tested the feasibility of tumor detection by targeted imaging of TfR using the fluorescent ligand Tf<sup>NIR</sup>. TfR expression is found only in the basal layer of normal oral squamous epithelium at an extremely low level and is rarely detected in benign lesions.<sup>17–19</sup> Importantly, TfR is expressed strongly in HNSCC, and a high expression level of TfR indicates high

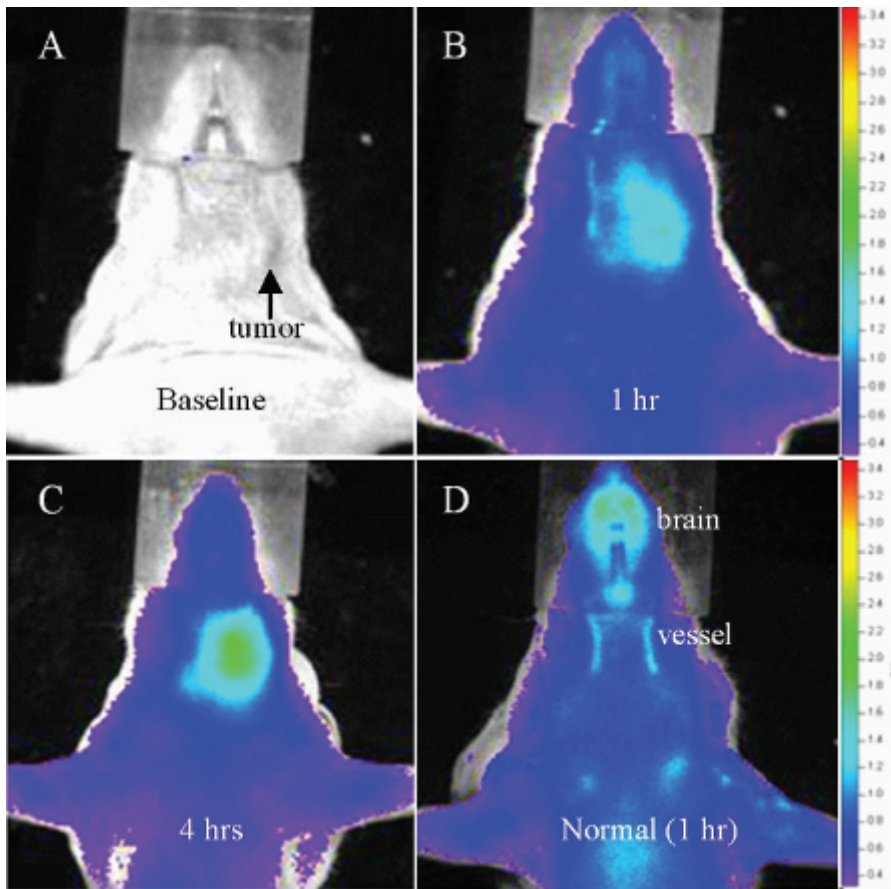


**Figure 5.** Near-infrared transferrin receptor ( $Tf^{NIR}$ )-based imaging in healthy mice and mice with oral base tumor xenografts. A to C show images taken at 0, 1, and 4 hours, separately, following intravenous injection of  $Tf^{NIR}$ . Note the significant difference in fluorescence signals and kinetics of signal decay between tumors and background over time. D shows a healthy mouse with background signal from carotid arteries and brain tissue. The color intensity scale is the same for A, B, and C (minimum =  $3.31 \times 10^8$  and maximum =  $3.45 \times 10^9$ ). The color intensity scale for the healthy mouse in D is different (minimum =  $3.83 \times 10^8$  and maximum =  $2.59 \times 10^9$ ).

tumor malignancy and a poor prognosis.<sup>17–19</sup> This specific expression pattern of TfR makes it an ideal candidate to image HNSCC. We hypothesized that the normal epithelia or benign lesions can be differentiated from malignant cells by exploring the differential expression of TfR. In the present study, overexpression of TfR was demonstrated in all HNSCC cell lines using Western blot analysis. Microscopic findings for the rapid binding of  $Tf^{NIR}$  with TfR and endocytotic activity of  $Tf^{NIR}$  in cell cultures further provided the rationale to image HNSCC in vivo using  $Tf^{NIR}$ . Specificity is critical for molecular imaging in vivo. Our previous work using MDA-MB-231 human breast cancer cells has shown that pretreatment of the cells with a threefold higher amount of unlabeled Tf (375  $\mu$ g Tf/dish) than the probe (125  $\mu$ g  $Tf^{NIR}$ /dish) resulted in a 66% decrease in the fluorescent signal.<sup>13</sup> Specificity of the Tf moiety for targeting has also been demonstrated by other investigators.<sup>23</sup> In an in vitro study using  $^{125}I$ -Tf in a K562 cell line, preincubation with 100-fold excess of unlabeled Tf for 5 minutes resulted in a dramatic inhibition of subsequent  $^{125}I$ -Tf binding. A 100-fold excess of bovine serum albumin or asialo-orosomucoid (a glycoprotein) had no effect on  $^{125}I$ -Tf binding.<sup>23</sup>

To test our hypothesis, we first imaged HNSCC xenografts grown in the lower back of mice.  $Tf^{NIR}$  accumulated preferentially in the tumor xenografts. The maximum tumor signal to background ratio reached to 1.42 to 4.15 and could be observed within 6 hours in the majority of the tumors. The significantly high ratio enabled early detection of tumors with high sensitivity and specificity. Interestingly, the time to reach the highest signal in tumors varied among tumors and was not related to tumor sizes. This phenomenon is also observed in bioluminescent imaging following D-luciferin administration in tumors established with luciferase-expressing tumor cell lines (data not shown). The in vivo dynamic difference of  $Tf^{NIR}$  accumulation might be related to both animal individual and tumor characteristics such as tumor volume, tumor cell proliferation, vascular supply, and hypoxia.<sup>24</sup> The tumor fluorescent signal is a sum of photons from specific binding of the ligand with its receptor and nonspecific presence of the fluorescent conjugate in blood vessels and interstitial space. However, the nonspecific signal was cleared more rapidly than true tumor cell-bound signal and appeared less significant in tumor detection. Previous studies using



radiolabeled Tf showed a significant decrease in tumor signal by pretreatment with a large amount of unlabeled Tf.<sup>15</sup> These results further indicate the importance and specificity of the Tf moiety for targeting *in vivo*. One major concern is the hypoxia and necrosis frequently presenting in large tumors.<sup>25</sup> Hypoxia and necrosis might affect both the expression of TfR and the entry, settling, and binding of Tf<sup>NIR</sup>. These factors might become evident if quantitative assessment of biomarker expression or comparative analysis among tumors is performed using optical imaging, although we obtained a close correlation between the tumor to muscle fluorescent ratio and tumor size.

To further test the feasibility of HNSCC detection, we imaged the animals with and without oral base tumors. In healthy mice, fluorescent signal was observed from the large blood vessels in the neck and from brain tissue. The carotids and their branches and aorta arch are located superficially in the neck. Normal brain tissue is known to express TfR at a high level. The fluorescent background might adversely affect the detection of metastatic lesions in neck lymph nodes. Metastatic lesions might be too small to produce a stronger signal than the vessels in animal models (further study is necessary). Primary tumors can be clearly detected through the neck owing to a much stronger signal and delayed signal fading relative to background. Human HNSCC is developed and progressed through atypia to carcinoma *in situ* and then to invasive squamous cell carcinoma. These early lesions locate superficially in the wall of the oral cavity, pharynx, and esophagus. The difference in TfR expression among normal squamous epithelial cells, atypical cells, and carcinoma cells may be significant enough for optical differentiation among them through the use of Tf<sup>NIR</sup>. Furthermore, development of confocal laser endomicroscopy enables analysis of *in vivo* microarchitecture.<sup>26</sup> The combination of a fluorescently labeled probe such as Tf<sup>NIR</sup> and fluorescent confocal laser endomicroscopy will enable identification of early lesions, including squamous cell atypia and carcinoma *in situ*, as well as early invasive carcinomas. Our results in animal models of human HNSCC indicate that TfR is a promising target and Tf<sup>NIR</sup>-based optical imaging is potentially useful for detection and localization of early HNSCC and atypical lesions in clinical practice.

Under physiologic conditions, iron-loaded Tf binds TfR on the surface of actively dividing cells. Subsequently, the Tf-TfR complex is internalized, first transported to early endosomes and then delivered to recycling endosomes. The apo-Tf is released only after the complex reaches the cell surface and then circulates until it again

comes in contact with free iron. It has been estimated that one Tf molecule could participate in this transport cycle as many as 100 times.<sup>27</sup> In the present study, the Tf was labeled with NIR fluorescent dye and the tumor was imaged based on the fluorescence of the optical reporter. The details of Tf<sup>NIR</sup> recycling in tumors are unknown, and further analysis would be necessary for understanding the pharmacokinetics of Tf<sup>NIR</sup> in mice.

## References

1. Massoud TF, Gambhir SS. Molecular imaging in living subjects: seeing fundamental biological processes in a new light. *Gene Dev* 2003;17:545–80.
2. Graves EE, Weissleder R, Ntziachristos V. Fluorescence molecular imaging of small animal tumor models. *Curr Mol Med* 2004;4: 419–30.
3. Ntziachristos V, Bremer C, Weissleder R. Fluorescence imaging with near-infrared light: new technological advances that enable *in vivo* molecular imaging. *Eur Radiol* 2003;13:195–208.
4. Hogemann-Savellano D, Bos E, Blondet C, et al. The transferrin receptor: a potential molecular imaging marker for human cancer. *Neoplasia* 2003;5:495–506.
5. Stefflova K, Chen J, Zheng G. Using molecular beacons for cancer imaging and treatment. *Front Biosci* 2007;12:4709–21.
6. Hoffman RM. The multiple uses of fluorescent proteins to visualize cancer *in vivo*. *Nature* 2005;5:796–806.
7. Veiseh M, Gabikian P, Bahrami SB, et al. Tumor paint: a chlorotoxin: Cy5.5 bioconjugate for intraoperative visualization of cancer foci. *Cancer Res* 2007;67:6882–8.
8. Kaijzel EL, van der Pluijm G, Lowik CW. Whole-body optical imaging in animal models to assess cancer development and progression. *Clin Cancer Res* 2007;13:3490–7.
9. Greenlee RT, Hill-Harmon MB, Murray T, Thun M. Cancer statistics, 2001. *CA Cancer J Clin* 2001;51:15–36.
10. Forastiere A, Koch W, Trotti A, Sidransky D. Head and neck cancer. *N Engl J Med* 2001;345:1890–900.
11. Westra WH, Califano J. Toward early oral cancer detection using gene expression profiling of saliva: a thoroughfare or dead end? *Clin Cancer Res* 2004;10:8130–1.
12. Pirolo K, Dagata J, Wang P, et al. A tumor-targeted nanodelivery system to improve early MRI detection of cancer. *Mol Imaging* 2006;5:41–52.
13. Shan L, Wang S, Sridhar R, et al. A dual probe with fluorescent and magnetic properties for imaging solid tumor xenografts. *Mol Imaging* 2007;6:85–95.
14. Belloccq NC, Pun SH, Jensen GS, Davis ME. Transferrin-containing, cyclodextrin polymer-based particles for tumor-targeted gene delivery. *Bioconjug Chem* 2003;14:1122–32.
15. Smith TA, Perkins AC, Walton PH. 99mTc-labelled human serum transferrin for tumour imaging: an *in vitro* and *in vivo* study of the complex. *Nucl Med Commun* 2004;25:387–91.
16. Vavere AL, Welch MJ. Preparation, biodistribution, and small animal PET of 45Ti-transferrin. *J Nucl Med* 2005;46:683–90.
17. Miyamoto T, Tanaka N, Eishi Y, Amagasa T. Transferrin receptor in oral tumors. *Int J Oral Maxillofac Surg* 1994;23:430–3.

18. Kearsley JH, Furlong KL, Cooke RA, Waters MJ. An immunohistochemical assessment of cellular proliferation markers in head and neck squamous cell cancers. *Br J Cancer* 1990;61:821–7.
19. Tanaka N, Miyamoto T, Saito M, et al. Transferrin receptor expression in oral tumors. *Bull Tokyo Med Dent Univ* 1991;38:19–26.
20. Dickson M, Hahn W, Ino Y, et al. Human keratinocytes that express hTERT and also bypass a p16INK4a-enforced mechanism that limits life span become immortal yet retain normal growth and differentiation characteristics. *Mol Cell Biol* 2000;20:1436–47.
21. Klausner RD, Renswoude JV, Ashwell G, et al. Receptor-mediated endocytosis of transferrin in K562 cells. *J Biol Chem* 1982;258:4715–24.
22. Zhang W, Moorthy B, Chen M, et al. A Cyp1a2-luciferase transgenic CD-1 mouse model: responses to aryl hydrocarbons similar to the humanized AhR mice. *Toxicol Sci* 2004;82:297–307.
23. Pillon A, Servant N, Vignon F, et al. *In vivo* bioluminescent imaging to evaluate estrogenic activities of endocrine disrupters. *Analyt Biochem* 2005;340:295–302.
24. Raman V, Artemov D, Pathak AP, et al. Characterizing vascular parameters in hypoxic regions: a combined magnetic resonance and optical imaging study of a human prostate cancer model. *Urol Oncol* 2007;25:358–9.
25. Kanematsu M, Semelka R, Osada S, Amaoka N. Magnetic resonance imaging and expression of vascular endothelial growth factor in hepatocellular nodules in cirrhosis and hepatocellular carcinomas. *Top Magn Reson Imaging* 2005;16:67–75.
26. Hoffman A, Goetz M, Vieth M, et al. Confocal laser endomicroscopy: technical status and current indications. *Endoscopy* 2006;38:1275–83.
27. Gomme PT, McCann KB, Bertolini J. Transferrin: structure, function and potential therapeutic actions. *Drug Discov Today* 2005;10:267–73.

# BIOLUMINESCENT ANIMAL MODELS OF HUMAN BREAST CANCER FOR TUMOR BIOMASS EVALUATION AND METASTASIS DETECTION

Liang Shan, MD, PhD; Songping Wang, PhD;  
Alexandru Korotcov, PhD; Rajagopalan Sridhar, PhD;  
Paul C. Wang, PhD

**Introduction:** Convenient animal models are needed to study the progression and treatment of human tumors in vivo. Luciferase-based bioluminescent imaging (BLI) enables researchers to monitor tumors noninvasively and is sensitive to subtle changes in tumors.

**Methods:** Three human breast cancer models in nude mice were established by using luciferase-expressing MDA-MB-231-luc cells. They were subcutaneous xenografts ( $n=8$ ), mammary gland xenografts ( $n=5$ ), and lung metastases ( $n=3$ ). The tumors were imaged in live mice by using a highly sensitive BLI system. The relationship between the intensity of bioluminescence from the tumor was analyzed with respect to tumor volume. Bioluminescent signals from lung metastases were studied to determine the threshold of detectability.

**Results:** Tumors growing in the mice's backs and mammary gland fat pads were imaged dynamically after administration of D-luciferin. The bioluminescent intensity from the tumors gradually increased and then decreased in a one-hour span. The time to reach maximum signal intensity differed significantly among tumors and was independent of tumor volume and unrelated to maximum signal intensity. A significant correlation was observed between tumor volume and maximum signal intensity in tumors from both sites. Lung metastatic lesions of .3–.5 mm in diameter were clearly detectable through the entire animal imaging process.

**Conclusion:** The animal models established with luciferase-expressing cancer cells in combination with BLI provide a system for rapid, noninvasive, and quantitative analysis of tumor biomass and metastasis. This biosystem simplifies in vivo monitoring of tumors and will be useful for noninvasive investigation of tumor growth and response to therapy. (*Ethn Dis.* 2008;18[Suppl 2]:S2-65–S2-69)

**Key Words:** Bioluminescent Imaging, Luciferase, Animal Models, Bbreast Cancer

From the Department of Radiology (LS, SW, AK, PCW), Department of Radiation Oncology (RS), Howard University, Washington, DC.

Address correspondence and reprint requests to: Paul C. Wang, PhD; Department of Radiology, Howard University; 2041 Georgia Ave, NW; Washington, DC 20060; 202-865-3711; 202-865-3722 (fax); pwang@howard.edu

## INTRODUCTION

Bioluminescent imaging (BLI) is an optical imaging modality that enables rapid in vivo analyses of a variety of cellular and molecular events with extreme sensitivity.<sup>1–3</sup> This imaging technique is based on light-emitting enzymes, such as luciferase, as internal biological light sources that can be detected externally as biological indicators. As a result of recent developments in techniques for high-sensitivity detection of bioluminescence, BLI has been recently tested in the detection and real-time observation of primary tumor growth and metastasis in living subjects.<sup>4–6</sup> Luciferase-based light-emitting animal models have also been used to develop therapeutics that target the molecular basis of disease.<sup>7</sup> Importantly, BLI provides a biosystem to test the spatial-temporal expression patterns of both target and therapeutic genes in living animals where the contextual influences of whole biological systems are intact.<sup>8,9</sup> In this study, we established three bioluminescent animal models of human breast cancer using MDA-MB-231-luc cell line, which has been stably transfected with the luciferase gene. The primary and metastatic lesions were analyzed through whole-animal imaging, and the tumor volume was evaluated in relationship with the bioluminescent signal intensity.

## MATERIALS AND METHODS

### Cell culture and animal models

MDA-MB-231-luc human breast cancer cell line and D-luciferin were obtained from Xenogen (Alameda, Calif). This cell line has been stably transfected with

luciferase gene for luciferase-based BLI. Cells were routinely maintained in Dulbecco minimal essential medium/F-12 medium supplemented with 10% heat inactivated fetal bovine serum and 50 µg/mL each penicillin, streptomycin, and neomycin (Invitrogen, Carlsbad, Calif). Female athymic nude mice of 8–10 weeks of age ( $N=16$ ) were purchased from Harlan (Indianapolis, Ind). Three animal models were developed. The subcutaneous solid tumor xenograft model was developed by subcutaneous injection of  $1 \times 10^7$  subconfluent cells in 100 µL Dulbecco phosphate buffered saline (DPBS) in the right lower back of each mouse ( $n=8$ ). The mammary gland fat pad tumor model was developed by injection of  $1 \times 10^7$  subconfluent cells in 100 µL DPBS into the right fifth mammary gland fat pad ( $n=5$ ). Matrigel or other anchoring matrix was not used to produce the tumors. The lung metastasis model of breast cancer was developed by tail vein injection of  $1 \times 10^6$  tumor cells ( $n=3$ ). The tumors in subcutaneous tissue and mammary gland fat pad were imaged and analyzed when they reached a certain size (3–11 mm diameter). For lung metastatic model, whole animals were checked weekly and autopsied when tumor signal from the lung region was detected.

### In vivo BLI

Luciferase-based BLI was performed with a highly sensitive, cooled charge-coupled device camera mounted in a light-tight specimen box (Xenogen IVIS 200 imaging system). Imaging and quantification of signals were controlled by the acquisition and analysis software Living Image (Xenogen). Mice were placed onto the warmed stage inside the light-tight camera box with continuous exposure to 2% isoflurane. After a

baseline image was taken, animals were given the substrate D-luciferin by intraperitoneal injection at 150 mg/kg in DPBS. Then the whole animal was imaged at an interval of 2 minutes for more than one hour. Imaging time was one minute. The light emitted from the mouse was detected, integrated, digitized, and displayed by the IVIS camera system. Regions of interest from the displayed images were identified and measured around the tumor sites. The signal was quantified and expressed as photons per second by using Living Imaging software (Xenogen).

All animal protocols were conducted according to National Institutes of Health guidelines for humane use and care of animals. The animal protocols were approved by the institutional animal care and use committee of Howard University.

### Histopathology

To confirm whether the detected signal from whole-animal imaging originated from the metastatic lesions in the lung, the animal was autopsied as soon as the signal was detected. The lung was examined and fixed by intrabronchial perfusion of 10% neutralized formalin solution. Paraffin-embedded sections were stained using hematoxylin and eosin) for microscopic evaluation.

### Statistical Analysis

Statistical analysis was performed by using statistical software OriginPro 7.0 (OriginLab, Northampton, Mass). A  $P$  value  $<.05$  was considered to be a significant difference between any two sets of data.

## RESULTS

### Individual Difference in Dynamics of Tumor Bioluminescent Signals

After inoculation of the tumor cells into the subcutaneous tissue and mammary gland fat pads of the mouse,

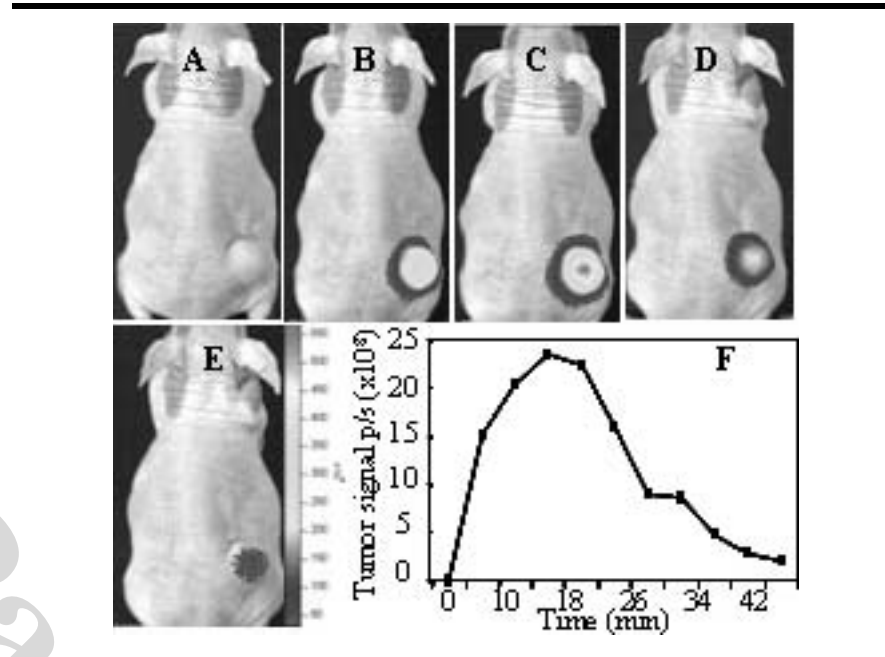


**Fig 1.** Dynamic change of the bioluminescent signal in tumors after administration of D-luciferin, showing gradual increase and then decrease over time. Panels A to E represent the whole animal images taken separately at 0, 10, 15, 30, and 40 minutes after luciferin administration. Panel F shows the plot of signal intensity from tumor as a function of time after injection of luciferin

≈90% of the mice developed tumor nodules at the inoculated sites within one month. To a certain degree, the tumors varied with respect to size and rate of growth. In the present study, the tumors were allowed to grow to a desired size and used for BLI. A total of eight tumors in the subcutaneous tissue in the backs and five tumors in the mammary gland fat pads of athymic nude mice were analyzed. The maximum diameter of the 13 tumors was 3–11 mm. After administration of D-luciferin, the bioluminescent signal in tumors was clearly detectable as early as two minutes and showed a dynamic change of gradual increase and then decrease over time (Figure 1). In most of the tumors, the signal became very weak or undetectable within 60 minutes. There was a significant difference among tumors for the peak intensity time, which is defined as the time for luminescence intensity of tumor to reach the maximum, ranging from 5 to 24 minutes. A similar phenomenon

was observed for tumors located in the backs and mammary fat pads. There was no correlation between the peak intensity time and tumor volume ( $R = -.13$ ,  $P = .76$  in subcutaneous and  $R = .67$ ,  $P = .21$  in mammary gland xenografts). Also, there was no correlation between the peak intensity time and maximum tumor signal intensity ( $R = -.18$ ,  $P = .67$  in subcutaneous and  $R = .74$ ,  $P = .15$  in mammary gland xenografts). These results indicate that the dynamic change of tumor bioluminescent signal after D-luciferin administration might be related to the differences of individual mice.

### Close Correlation between Bioluminescent Signal Intensity and Tumor Volume

The maximum tumor signal measured at the peak intensity time point was selected for further analysis because of the significant difference in the dynamics of tumor bioluminescent signals among mice. There was a

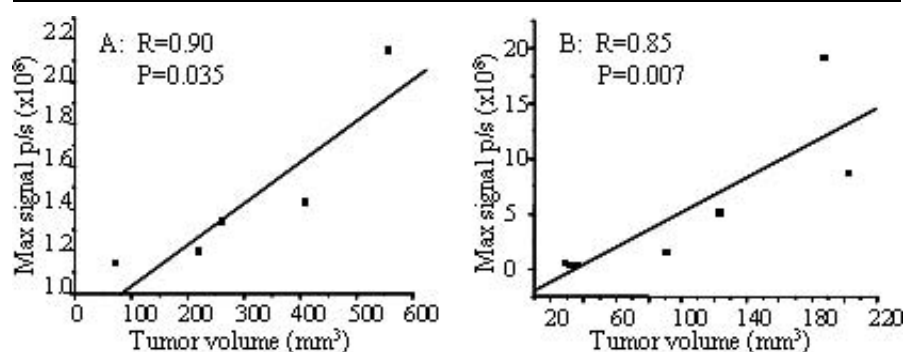


**Fig 2.** Close correlation between maximum signal of tumors and tumor volume. A) Solid tumor xenografts in the mammary gland fat pads of mice. B) Subcutaneous tumors in the backs of mice

significant correlation between the maximum signal and the tumor volume for tumors located both subcutaneously ( $R=.85$ ,  $P=.007$ , Figure 2B) and at the mammary gland fat pad ( $R=.90$ ,  $P=.035$ , Figure 2A). This result indicates that the bioluminescent signal intensity reflects tumor size. The maximum signal intensity could be used as an indicator of tumor growth. The background signal was at a negligible level and significantly less than the signal from the tumor (Figure 1).

### Highly Sensitive in vivo Detection of Lung Metastatic Lesions

In three mice, the tumor cells were injected through the tail vein, and whole animal imaging was performed every week. Clear signal of the tumors was first detected in the lung area at approximately one month after tail vein injection of tumor cells. After recording the images, the mice were autopsied immediately, and pathology studies of the lung were performed. In one mouse, two distinct tumor signals were observed bilaterally (Figure 3A). However, many lesions with different sizes and distributed in bilateral sides of the lung were observed under microscopy. The largest lesion located at the right lower lobe was .5 mm in diameter, corresponding to the signal on the right side

of the bioluminescent image, and the second largest lesion located at the left upper lobe was .3 mm in diameter, corresponding to the left side tumor signal in whole animal imaging (Figure 3C). In another mouse, a single tumor signal was detected, and pathology examination revealed a tumor mass of .6 mm in diameter located near the left pulmonary hilus (Figure 3B). Multiple microscopic metastatic lesions were also observed in the third mouse with very weak tumor signals. Identifying lesions <.3 mm in diameter and differ-

entiating one small lesion from another based on imaging alone was difficult.

## DISCUSSION

Luciferase has served as a reporter in a number of targeted gene expression experiments in the last two decades.<sup>1,2</sup> In recent years, luciferase-based BLI is becoming an important and rapidly advancing field to visualize and quantify the proliferation of tumor cells in animal models.<sup>10,11</sup> Luciferase labeling is superior to other reporters, such as green fluorescent protein for tracing the progression of neoplastic growth from a few cells to extensive metastasis.<sup>12,13</sup> In spite of the remarkable progress made, much more remains to be done with luciferase-based visualization of tumors in vivo. In the present study, we established three animal models of human breast cancer using stably luciferase-transfected cells. Regardless of the tumor sites in subcutaneous tissue or in mammary gland fat pad, the tumors could be clearly imaged with extremely low background by whole-animal imaging. Interestingly, the dynamics of the tumor signal intensity were significantly

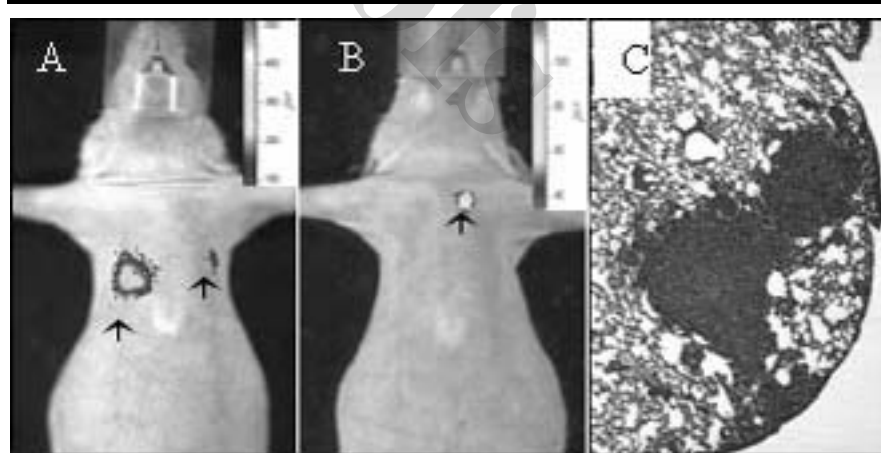


**Fig 3.** Detection of lung metastasis through whole animal imaging. Panel A is the image from one mouse showing signals in bilateral sides of the lung. Panel B is the image from a mouse with signal from one tumor in the left upper lobe of the lung. Panel C represents the pathologic finding of the left tumor in panel A (hematoxylin-eosin stain,  $\times 40$ )

different among tumors. Some tumors quickly reached the maximum intensity, whereas others took more time. The time to reach the maximum signal was independent of tumor volume and was also not related to the maximum tumor signal. Individual differences in light emission appeared to follow administration of D-luciferin. The tumor heterogeneity with respect to size, vascular density, blood supply, and other factors may affect accessibility and retention of luciferin and consequently the kinetics of light emission. Hypoxia and necrosis that are commonly observed in large tumors can lead to decreased synthesis of luciferase and ATP. The signal intensity is largely dependent on ATP and luciferase levels in the tumor and the tumor volume. In small tumors, the influence from hypoxia and necrosis may be less significant. In the present animal models, tumors <1.2 cm are more suitable for BLI because excessive necrosis was not observed under microscope. A significant correlation was observed between bioluminescent signal and tumor volume. The bioluminescent signal could be used as an indicator of tumor biomass. However, as tumors become larger, the correlation between tumor volume and bioluminescent signal becomes inferior. Another issue of concern is the selection of the time point to measure the signal intensity after luciferin administration. In the previous studies, the bioluminescent signal at the five-minute time point was arbitrarily used to represent the tumor in various analyses.<sup>4,5</sup> Based on our dynamic analysis, it was clear that the signal at five-minute time point was less likely to reflect the real signal intensity of the tumors. The maximum signals at peak intensity time point may be a better indicator for tumor volume because of the strong correlation between the maximum intensity and the volume.

One potential use of BLI is the detection of metastasis in animals. The

animals can be monitored through whole-animal imaging. Wetterwald et al showed by using a bone metastasis model, that micrometastasis of .5-mm<sup>3</sup> volume can be detected, which reveals greater sensitivity than radiographic methods.<sup>14</sup> A study by Edinger et al using luciferase-expressing HeLa cells demonstrated that  $1 \times 10^3$  cells in the peritoneal cavity,  $1 \times 10^4$  cells at subcutaneous sites, and  $1 \times 10^6$  circulating cells could be observed immediately after injection of the cells.<sup>15</sup> In the present study, clear signaling from metastatic lesions could be detected when pulmonary metastatic lesions approached .3 mm in diameter. The lesions at this stage were still difficult to differentiate from the vessel spots in magnetic resonance imaging (data not shown). All of these studies with different models confirmed the high detection sensitivity of metastatic lesions using BLI. To date, the conventional methods used to test the efficacy of novel therapies on primary tumors and metastasis in vivo are labor intensive and time consuming. Luciferase-based BLI is highly sensitive, real-time, noninvasive, and significantly correlated with the tumor growth. These characteristics simplify such kinds of in vivo analysis that rely on animals.<sup>16</sup> The therapeutic efficacy of a drug can be assessed without having to sacrifice the mice to search for tumor growth at primary and metastatic sites. Statistically significant results can be achieved by using a small number of mice, since multiple measurements can be made over time. Although metastatic lesions above a certain critical size in the lung can be detected using BLI, a major limitation of BLI is the difficulty in quantification of multiple micrometastatic lesions and comparative analysis of lesions in different parts of the body due to the photon characteristics as well as the tissue differences along the photon pathway.

#### ACKNOWLEDGMENTS

This work was supported in part by DoD USAMRMC W81XWH-05-1-0291 and DAMD 17-03-1-0759, DAMD 17-03-1-0123, NIH 5U54CA091431 and grant 2G12 RR003048 from the RCMI Program, Division of Research Infrastructure, National Center for Research Resources, NIH.

#### REFERENCES

1. Massoud TF, Gambhir SS. Molecular imaging in living subjects: seeing fundamental biological processes in a new light. *Genes Develop.* 2003;17:545-580.
2. Greer IILF, Szalay AA. Imaging of light emission from the expression of luciferases in living cells and organisms: a review. *Luminescence.* 2002;17:43-74.
3. Yu YA, Shabahang S, Timiryasova TM, et al. Visualization of tumors and metastases in live animals with bacteria and vaccinia virus encoding light-emitting proteins. *Nat Biotech.* 2003;22:313-320.
4. Jenkins DE, Hornig YS, Oei Y, Dusich J, Purchio T. Bioluminescent human breast cancer cell lines that permit rapid and sensitive in vivo detection of mammary tumors and multiple metastases in immune deficient mice. *Breast Cancer Res.* 2005;7:R444-R454.
5. Nogawa M, Yuasa T, Kimura S, et al. Monitoring luciferase-labeled cancer cell growth and metastasis in different in vivo models. *Cancer Lett.* 2005;217:243-253.
6. Sarraf-Yazdi S, Mi J, Dewhirst MW, Clary BM. Use of in vivo bioluminescence imaging to predict hepatic tumor burden in mice. *J Surg Res.* 2004;120:249-255.
7. Zhang W, Moorthy B, Chen M, et al. A Cyp1a2-luciferase transgenic CD-1 mouse model: responses to aryl hydrocarbons similar to the humanized AhR mice. *Toxicol Science.* 2004;82:297-307.
8. Pillon A, Servant N, Vignon F, Balaguer P, Nicolas JC. In vivo bioluminescent imaging to evaluate estrogenic activities of endocrine disrupters. *Analyt Biochem.* 2005;340:295-302.
9. Vooijs M, Jonkers J, Lyons S, Berns A. Noninvasive imaging of spontaneous retinoblastoma pathway-dependent tumors in mice. *Cancer Res.* 2002;62:1862-1867.
10. Ghosh M, Gambhir SS, De A, Nowels K, Goris M, Wapnir I. Bioluminescent monitoring of NIS-mediated (131)I ablative effects in MCF-xenografts. *Mol Imaging.* 2006;5:76-84.
11. Paulmurugan R, Massoud TF, Huang J, Gambhir SS. Molecular imaging of drug-modulated protein-protein interactions in living subjects. *Cancer Res.* 2004;64:2113-2119.
12. Choy G, O'Connor S, Diehn FE, et al. Comparison of noninvasive fluorescent and

- bioluminescent small animal optical imaging. *Biotechniques*. 2003;35:1022–1026.
13. Troy T, Jekic-McMullen D, Sambucetti L, Rice B. Quantitative comparison of the sensitivity of detection of fluorescent and bioluminescent reporters in animal models. *Mol Imaging*. 2004;3:9–23.
  14. Wetterwald A, van der Pluijm G, Sijmons B, et al. Optical imaging of cancer metastasis to bone marrow: a mouse model of minimal residual disease. *Am J Pathol*. 2002;160:1143–1153.
  15. Edinger M, Sweeney TJ, Tucker AA, Olomu AB, Negrin RS, Contag CH. Noninvasive assessment of tumor cell proliferation in animal models. *Neoplasia*. 1999;1:303–310.
  16. Hardy J, Edinger M, Bachmann MH, Negrin RS, Fathman CG, Contag CH. Bioluminescence imaging of lymphocyte trafficking in vivo. *Exp Hematol*. 2001;29:1353–1360.

Page Proofs



## A Mammography Database and View System for African-American Patients

Shani Ross,<sup>1,2</sup> O'tega Ejofodomi,<sup>2</sup> Ahmed Jendoubi,<sup>2</sup> Lisa Kinnard,<sup>3</sup> Mohamed Chouika,<sup>2</sup> Ben Lo,<sup>3</sup>  
Paul Wang,<sup>4</sup> and Jianchao Zeng<sup>2</sup>

We have digitized mammography films of African-American patients treated in the Howard University Hospital Radiology Department and have developed a database using these images. Two hundred and sixty cases totaling more than 5,000 images have been scanned with a high resolution Kodak LS85 laser scanner. The database system and web-based search engine were developed using MySQL and PHP. The database has been evaluated by medical professionals, and the experimental results obtained so far are promising with high image quality and fast access time. We have also developed an image viewing system, D-Viewer, to display these digitized mammograms. This viewer is coded in Microsoft Visual C# and is intended to help medical professionals view and retrieve large data sets in near real time. Finally, we are currently developing an image content-based retrieval function for the database system to provide improved search capability for the medical professionals.

**KEY WORDS:** African-American women, breast cancer, database, mammography, mammogram, digitization, image viewer, Howard University

### INTRODUCTION

The American Cancer Society estimates that in the United States alone, approximately 40,000 women die each year from breast cancer and that over 200,000 new breast cancer cases are diagnosed each year.<sup>1,2</sup> Typically, there are four main types of breast cancer: ductal carcinoma in situ (DCIS) where the cancer is confined within the ducts of the breast, lobular carcinoma in situ (LCIS) where the cancer is confined within the lobules or glands of the breast, invasive ductal carcinoma (IDC), and invasive lobular carcinoma (ILC).<sup>1,3</sup> IDC and ILC refer to the type of breast cancer where the tumor has spread from the ducts

or lobules it originated from, respectively, into the surrounding tissue of the breast. Other less common breast cancers include medullary carcinoma, mucinous carcinoma, Paget's disease of the nipple, Phyllodes Tumor, and tubular carcinoma.<sup>3</sup>

Breast cancer is grouped into stages which indicate the invasiveness of the disease. There are four stages—I, II, III, IV—defined by the American Joint Committee on Cancer<sup>1,3</sup> based on a combination of tumor size, lymph node involvement, and presence or absence of distant metastasis. There is also a more general classification: early/local stage where tumor is confined to the breast, late/regional stage where cancer has spread to the surrounding tissue or nearby lymph nodes, and advanced/distant stage where cancer has spread to other organs beside the breast.<sup>1,4</sup>

There has been a decline in breast cancer mortality rates of about 2.3% over the last decade<sup>1,2</sup> due to improved screening techniques leading to earlier detection, increased awareness,

---

<sup>1</sup>From the Biomedical Engineering, University of Michigan, Ann Arbor, MI, USA.

<sup>2</sup>From the Electrical and Computer Engineering, Howard University, Washington, DC, USA.

<sup>3</sup>From the Radiology, Georgetown University, Washington, DC, USA.

<sup>4</sup>From the Radiology, Howard University Hospital, Washington, DC, USA.

Correspondence to: Mohamed Chouika, 2300 Sixth St., NW, Rm 1022, Washington DC 20059; tel: 202-806-4816; fax: 202-332-3152; e-mail: mchouika@howard.edu

Copyright © 2007 by Society for Imaging Informatics in Medicine

Online publication 29 March 2007

doi: 10.1007/s10278-007-9019-6



and improved treatments. Improved screening techniques include regular self breast examination, breast physical examination by a doctor, and regular mammogram examinations. In a mammogram, a radiologist looks for any unusual signs. These include asymmetry between the two breasts, any irregular areas of increased density, or any areas of skin thickening all of which can indicate whether there is a mass, or lump, in the breast tissue.<sup>1,3</sup> As this mass can either be cancerous or benign, further tests such as a biopsy of the suspicious area are done to differentiate between the two. In addition, doctors look for calcifications which are tiny calcium deposits that indicate changes within the breast possibly pointing to cancer. Microcalcifications especially are usually associated with cancer.

Despite improved screening techniques, this decline has been much smaller in African-American women compared to Caucasian-American women even with increased participation by African-Americans in routine mammography screening since 1980.<sup>5</sup> Furthermore, statistics have shown that although Caucasian-American women have an overall higher incident rate of breast cancer than African-American women, African-American women have a slightly higher incident rate of breast cancer before the age of 35 and are more likely to die of breast cancer at any age.<sup>1,6</sup> Also, in comparison to Caucasian women, African-American women are less likely to be diagnosed with tumors of diameter less than or equal to 2.0 cm and in the early stage of breast cancer, but more likely to be diagnosed with tumors of diameters greater than 2.0 cm and in later and advanced stages of the cancer.<sup>1,6,7</sup> Some of this disparity could be explained by an overall lower socioeconomic status, unequal access to medical care, and additional illnesses,<sup>8-10</sup> which results in a much smaller percentage of African-American women getting early and regular mammograms compared to Caucasian women. Hence, they are usually not diagnosed with cancer until at a much later date when the cancer is at an advanced stage, which increases their mortality risk.

Some studies have also reported differences in breast cancer histology in African-American women and Caucasian women, although they noted that these results are not conclusive. Some of these studies found that African-American women had a greater chance of developing ductal tumors, whereas Caucasian women had a greater

chance of developing more lobular tumors.<sup>11,12</sup> This could be significant in the difference in outlook for the two racial groups, as lobular carcinoma is usually less aggressive. Other studies reported that African-American women had a greater frequency of medullary carcinoma than Caucasian women.<sup>5,7</sup> Medullary carcinoma is similar to ductal carcinoma but has a clearer distinction between the cancerous and normal cells.

Perhaps the most statistically significant differences seen between the two racial groups are the steroid receptor status of the tumor and the tumor proliferation rates. These differences are evident even when comparisons were adjusted for age, stage, treatment and screening opportunities, and risk factors. Typically African-American women had more estrogen- and progesterone-receptor negative tumors. Such tumors are generally unaffected by changing levels of these hormones and are thus less responsive to antihormonal treatments. African-American women also tended to have more poorly defined tumors, increased cell growth, and marked tumor necrosis. All these factors contribute to more aggressive tumors for African-American women.<sup>5,7,11,12</sup>

The epidemiological and tumor biology differences seen in African-American women compared to Caucasian women, leading to higher mortality rates, stress the particular importance in trying to fully understand why these disparities arise. One possible step towards addressing these issues is to have a larger number of African-American breast cancer cases available for study. Currently, there are no breast cancer databases primarily developed for African-American patients, although general breast cancer database systems do exist.<sup>13,14</sup> Hence, the main objective of this research is to develop the first major African-American Breast Cancer Mammography database for the use of training radiologists and other personnel involved in the detection and treatment of breast cancer. This could thus help in further understanding the nature of the breast cancer in African-American women. Part of this study also includes developing a view system that will allow radiologists to retrieve and view the digital imaging and communications (DICOM)-formatted images in the database in near real time.

This research is divided into three main parts. The first part is the collection of actual data for the

database, which includes the obtaining, scanning, and organization of the mammography films. The second part is the development of the database and web-search engine using database management software and webpage development programming languages. The third part is the development of the viewing software.

## METHODS

This study is in collaboration between the Howard University Electrical and Computer Engineering Department, the Howard University Hospital Radiology Department, and the Georgetown University Radiology Department. The database and viewing software development are being done through the Howard University Electrical Engineering Department with the films being supplied by the Howard University Hospital Radiology Department. Consulting support is provided by the Georgetown University Radiology Department. Before conducting the study, approval was obtained from the Institutional Review Board. The primary investigators, who worked directly with the films, took the Human Participants Protection Education for Research Teams online certification course<sup>15</sup> to meet the National Institute of Health (NIH) requirements on patient privacy issues. The investigators also attended seminars required by Howard University Hospital on the Health Insurance Portability and Accountability Act (HIPAA) of 1996.

### Digitization of the Mammography Films

#### *Film Collection*

Currently, mammography films from 260 patients from the Howard University Radiology Department have been digitized and entered into the database. All of these patients were diagnosed with breast cancer between 1994 and 2004 and were between the ages of 24 and 88. The patients' histology includes masses of different sizes with and without poorly defined borders, microcalcifications, clusters of calcifications, adenopathy, heterogeneous density, and solid nodules. Furthermore, the majority of these patients had undergone more than one mammography examination. For

these patients, the earlier exams typically were regular screening mammograms, which showed normal and benign images. Normal images were mammograms in which nothing suspicious was seen, and benign images were mammograms in which something suspicious was seen initially but with further examination found to be nonmalignant. The cancer appeared and was diagnosed in the later exam dates. Thus, we were able to obtain a wide variety of films showing normal, benign, and cancerous images. Table 1 gives an overview of the patient characteristics of the database.

Each examination date, on average, contained four films corresponding to the four typical views taken of the breasts during a mammogram. These views are: left mediolateral oblique view (LMLO), right mediolateral oblique view (RMLO), left craniocaudal view (LCC), and right craniocaudal view (RCC) (Fig. 1). The films generally came in two sizes:  $8 \times 10$  and  $10 \times 12$  in.

Majority of these mammograms had been done at Howard University Hospital using the MGX 2000 mammography machine from Instrumentarium Corporation, Imaging Division, Tuusula, Finland. The machine parameters include: a film focus distance of 26 in., AGFA Mamoray HDR-C high dynamic range film  $24 \text{ cm} \times 32 \text{ cm}$ , exposure of 75–130 mAs (depending on patient), tube voltage of 27–30 KeV, and a filter of 0.025 mm molybdenum, or 0.025 mm rhodium, or 0.5 mm aluminum. Some of the older mammograms had been done at the patient's previous hospital and the technical parameters of the machine used are unknown.

#### *Scanning and Technical Procedure*

The scanner used is the Kodak LS85 Laser Digitizer, specifically designed for high resolution teleradiology. Films can be converted into high resolution digital images of up to 5,120 pixels by 6,140 lines with 12 bits per pixel. Each pixel is assigned an optical digital value equal to  $1,000 \times$  optical density and has a spot size of  $50 \mu\text{m}$ . The digitizer has a scan rate of approximately 75 lines per second. It was purchased along with accompanying support software from RADinfo Systems, Dulles, Virginia. This accompanying software supports the digitization and burning of the images and includes: the Inter2000 Film Digitizer™

**Table 1. Representative Sample of the Patient Characteristics of the Database**

Patient	Age	Year Cancer Diagnosed	Histology	Digitization Date
MK833AI543	24	1999	Spiculated mass and speculated density in R. breast	6/10/2004
WM980RI062	26	2001	Abnormal, dilated ducts and microcalcifications	6/14/2004
BR815AA561	32	1999	Cluster of calcifications	1/22/2004
TN989IA352	39	2001	Malignant calcifications in L. breast, extensive ductal carcinoma in situ	6/2/2004
HS963AH074	45	1999	Large medial calcifications in L. breast	4/6/2004
BM869OI885	46	1998	Microcalcifications in L. Breast	6/19/2004
ME729OM197	55	2001	Malignant calcifications and solid mass	5/19/2004
AJ337DU655	56	1997	Solid mass with poorly defined borders in L. breast	7/7/2004, 7/8/2004
BJ567RA821	58	2001	Cluster of calcifications in L. Breast	1/30/2004
GI759HZ353	59	1998	Microcalcifications and lateral calcifications in L. breast	6/21/2004
DM795AA866	62	1999	Spiculated mass in R breast	3/25/2004
BM169AE858	62	1996	Density with obscured borders in L. breast	6/20/2004
MA935CN074	63	1999	Metastatic adenopathy in L axillary	6/10/2004
BD759AO805	65	2000	Breasts heterogeneously dense, highly suspicious mass with speculated borders and associated microcalcifications	2/24/2004, 3/1/2004
SS913TY027	66	2000	R. breast ductal carcinoma in situ	6/1/2004
DM710AA630	70	1998	Large mass and microcalcifications in R. breast	6/22/2004
GN216OO404	70	1997	Macro and micro calcifications in R breast	6/22/2004
KC717EL219	71	2000	R. breast carcinoma—irregular nodal density; Previous L. breast carcinoma (now irradiated)—spiculated mass with microcalcifications at the peripheral	5/28/2004
CG362AE888	71	1998	Large pulp mass solid with lobulated borders, small satellite lesions and large abnormal axillary node in L. breast	6/21/2004
BL316YO065	72	1999	Cluster of calcifications	1/23/2004
DS833AA858	73	1997	Mass and poorly defined post border in R. breast	6/21/2004
BM065RA569	74	1996	Malignant appearing calcifications in R. breast	6/19/2004
FD103LE602	76	1998	Irregular asymmetric density with associated microcalcifications in L breast	7/15/2004
JF393AR669	77	2001	Two spiculated masses, poorly defined	5/28/2004
MD782IE169	82	1998	Spiculated mass in L breast	6/24/2004
HK862AA996	83	2000	Solid and irregular polyp mass	5/17/2004

(I2000FD), RSVS Viewer <sup>TM</sup>, and CD Power-PACS <sup>TM</sup>.

The I2000FD<sup>TM</sup> is the interface for the film digitizer. This is where patient information is

entered, the digitizer is accessed for scanning, and where any necessary changes can be made to the film before the digital image is saved. Before scanning, patient information required by

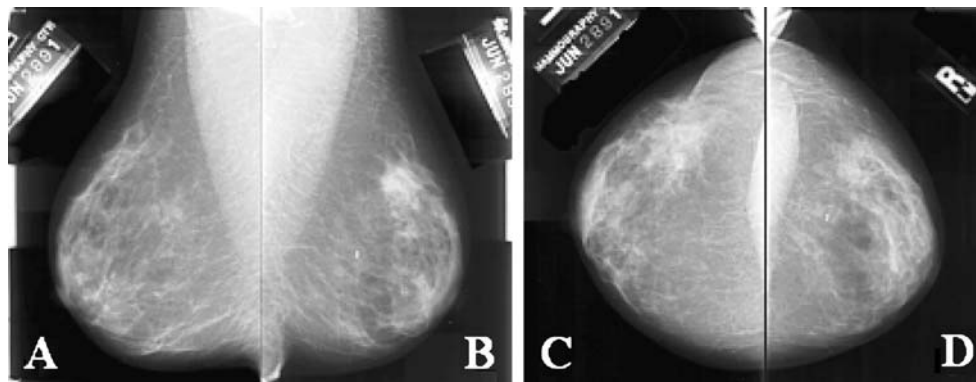


Fig 1. A typical mammography view: a LMLO, b RMLO, c LCC, and d RCC.<sup>13</sup>

I2000FD™ is entered. This information includes: the patient name written in a code to preserve patient's privacy rights, birth date, exam date, the ascension number used to keep track of each series, and the time and date of digitization of each film. This information is the essential information required by the program to stamp and classify each resulting digitized image. Next, the user specifies the resolution, bit depth, window level settings, and size of the film to be scanned. In this study, films are digitized at a resolution of 512 pixels/in. and a bit depth of 12, both of which are maximum values of the scanner, to give the highest image quality. The scan size chosen is either  $8 \times 10$  or  $10 \times 12$  in., depending on the size of the film to be scanned. Once the settings have been entered, the film is loaded into the Kodak scanner and digitized. Furthermore, the software allows us to cover the patient's name and other identifying information so that this is not seen in the digitized image in the software. The images are then saved and copies of them are transferred to the viewing software (RSVS™) and burning software (CD PowerPACS™). The sizes of these saved images are generally 40 MB for the  $8 \times 10$  films and 60 MB for the  $10 \times 12$  films. The RSVS™ is a viewing software for DICOM-formatted images, which allow us to further view and verify the digitized images. The CD PowerPACS™ software allows us to save and transfer the images to CD-R storage media. This program also saves a copy of the RSVS viewer on each CD.

#### Development of the Database

The Howard University Mammography Database<sup>16</sup> was developed using PHP and MySQL. MySQL is a simple relational database management system that allows users to add, access, and process data stored in a database.<sup>17</sup> The database contains relevant information such as encrypted patient name, patient ID, date of birth, type of scanner used, number of series in a case, exam date, total image count in a case, malignancy, and available image views (RMLO, LCC, etc.). New information can also be added when necessary. Our database is linked to a web-based search engine powered by PHP-recursive acronym for "PHP: Hypertext Preprocessor,"<sup>18</sup> which is a general-purpose open source scripting language that can be embedded in hypertext markup

language (HTML) for web-page development and which can run directly on the server, unlike other languages such as java script. Queries on the database are carried out using PHP. In addition, digitized images and patient information are stored in the database using PHP. Information in the database is first entered into Microsoft EXCEL, and then from there, is imported into the MySQL tables via PHP. This process makes entering new information into the database less tedious than directly entering it into MySQL from the Microsoft Windows command line. Furthermore, a login web page for the web-based search engine is also developed using PHP to limit use of this system to authorized users only. After being logged on to the system, a user can then specify search criteria via the web page. The query is then searched through the MySQL database, and the search results are displayed on the web page. The results are displayed as a list of case names with links to the actual images.

#### Development of the D-Viewer

The D-viewer is a viewing system developed for visualizing the digitized mammograms. By using this system, radiologists would not only be able to perform various image manipulations, such as circling the area of the cancer and making notes on the image, but could also save these markings as needed. The view system uses graphical user interface (GUI) for easy use and is to be DICOM compliant. The D-viewer system is developed with Microsoft Visual C#, an object-oriented programming language from Microsoft that is easy for manipulating graphics and creating window forms. Currently, the system accepts the following image formats: Windows bitmap (bmp), joint photographic experts group (jpg), tagged image file format (tif/tiff), graphics interchange format (gif), and portable network graphics (png).

#### RESULTS

Mammography films from 260 patients, each having approximately 20 to 40 images, have been digitized using the Kodak LS85 Laser Scanner. This has resulted in over 5,000 digitized images that have been stored into our database. Many patients had typically 20 to 40 images because they did several

regular screening mammograms before the mammography exam in which the cancer was diagnosed. Hence, on average for each patient, one could be looking at 4–10 different exam dates each of which would contain the four films representing the four typical views (LMLO, RMLO, LCC, RCC). Sometimes, for a particular examination, extra images were taken, depending on if the radiologist was interested in a particular region. All these patients are African-American women from Howard University Hospital who have been diagnosed with cancer between the years 1994 and 2004. In addition, we can compare normal images and images of benign and malignant lesions of the same patient. The image quality is excellent, as the films were digitized at the highest resolution possible by the Digitizer, which was at 512 pixels per inch at a bit depth of 12. Furthermore, there were no observable distortions or artifacts due to the digitization process, although there is some concern that some noise may have been picked up due to possible dirt spots on the films. These images were also approved by the radiologist consultant associated with this study. The digitized image size is either 40 or 60 MB, depending on the size of the mammogram film (8 × 10 or 10 × 12 in., respectively).

A database and a web-based search engine have been developed using MySQL and PHP. Patient information and the corresponding images can be retrieved when queries are made by selecting various criteria. A user is first required to login to access the database (Fig. 2). User accounts will be set up for general users just wanting to learn more about breast cancer and to peruse the database and for users requesting more functionality from the database, such as being able to download the images.

After a user logs in, he or she is directed to the web-search page where he or she can select his or her search criteria (Fig. 3). Currently, the search criteria available include whether the image is normal, benign, or cancer, the year the patient was born, the year the exam was done, total number of examinations for a patient, total number of images for a patient, and the mammography view. For example, a user may want to see all the cancer images of patients who were diagnosed with cancer during 1999–2000 and were born during 1961–1970. There is also a reset button on this page that clears all the search fields. After the search criteria has been selected and submitted, the database returns a list of all patient cases corresponding to that search. The list of cases contains the code name associated with that patient, each series and corresponding exam date of that series, the digitization date for each series, the total number of images in each series, and all available image views done. Figure 4 shows a sample results page of a search.

Finally, Figure 5 shows a snapshot of the D-viewer system with the LCC and RCC views of one of our digitized mammograms. The system can accept bitmap, tiff, jpg, gif, and png image formats. The D-viewer is currently under development.

## DISCUSSION

Our research attempts to provide the first major breast cancer database for African-American women. This would allow radiologists and other applicable parties to study various types of African-American women breast cancer cases. Howard University Hospital was chosen not only



Fig 2. Login page of the web-based search engine linked to the breast cancer database.



Fig 3. Web-based search page.

for its accessibility, but more importantly, because it services a large African-American community in the Washington DC, Maryland, and Virginia area, thus, providing a large number of African-American women mammography cases. This

research is also significant in an effort to close the gap of diversity in breast cancer mortality.

However, this research is not just about digitizing a large number of mammograms. The database is also being developed as an online

Fig 4. Results page of search.

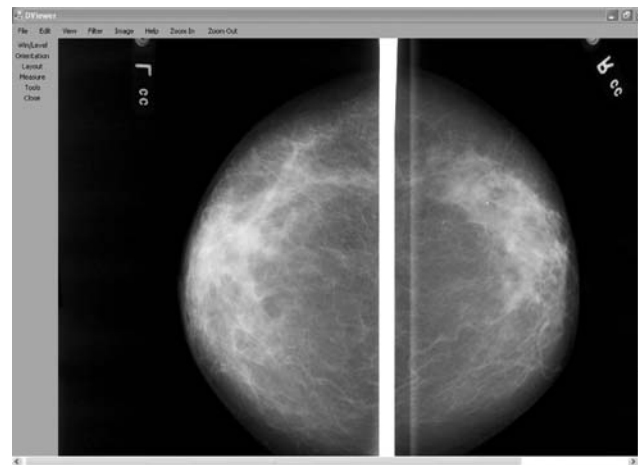


Fig 5. D-viewer user interface.

interactive teaching/training tool geared towards both the radiology students and others interested in learning more about breast cancer. For example, the site would contain general information on breast cancer and more detailed information. Medical students could be asked to perform tasks such as determining, from the image alone, the search criteria required to produce that particular image. This would require the students to be able to accurately identify specific characteristics of that image. Radiologists could also use this database to help their diagnosis process of difficult new cases by searching for similar cases or images.

Our database differs from current major databases such as the one developed by the University of South Florida<sup>14</sup> in that our patient data set consists of African-American women only. Furthermore, we intend our database to be an interactive training tool where the users can look at images and guess the search criteria that they would have had to put in to obtain that image. We also plan to extend the functionality of the database by making it an image-based retrieval system in which features in the image can be used to define the search criteria.

## CONCLUSIONS

We have digitized more than 5,000 mammography images of 260 African-American women patients and developed a database and viewing

system for these images. All patients in this study have already been diagnosed with breast cancer. The digitized images include normal, benign, and malignant mammograms, which were taken between the years 1994 and 2004. The normal and benign mammograms of a patient were from routine screenings done before breast cancer was diagnosed. All the mammography images are searchable in the database system via a web-based search engine. They can be viewed in the viewing system and easily manipulated during the viewing process.

Further research will be performed to improve the database and the viewing system. First of all, we will seek input from radiologists when they test our database and viewing system. They will be asked to identify key information from the images such as the presence or absence of malignant cancer, location of cancer, type of cancer (mass or calcification), assessment, subtlety, and density of the breast. Locations of the cancers, if present, on the digitized mammograms, will be marked and saved. The database will also be updated with these added data.

New mammograms will also be collected and digitized to increase the size of our database. The D-viewer system will be further enhanced to improve its functionalities based upon input from the radiologists after testing the system. We will also develop an interactive web-based learning/training/testing system, which can provide detailed information on breast cancer, training sessions for breast cancer diagnosis, and test platforms. To

improve the quality and versatility of our database, we plan to develop an image-based retrieval database, whereby, we can use images instead of words to determine our search criteria. For example, if we circle a region of interest on an image such as a mass, we could query the database to return all images and corresponding information that have a similar region of interest.

This database will be made accessible to radiologists and students via announcements on the Howard Medical School website and on the Howard University Electrical and Computer Engineering Department website. No fees will be charged for basic database access, but fees will be charged for any advanced functions such as image processing or content-based retrieval operations.

## ACKNOWLEDGEMENTS

We would like to thank the radiologists and other medical professionals in the Department of Radiology at Howard University Hospital who made significant contributions to this research. This research was supported by the US Army MPMC Breast Cancer Research Partnership Program (No. DAMD17-01-1-0267). Paul Wang was also supported by the following grants: NIH NCCR No. 2G12RR003048, NIH No. 5U54CA091431, US Army MPMC No. W81XWH-05-1-0291 and No. DAMA17-00-1-0291.

## REFERENCES

1. American Cancer Society: Breast Cancer Facts and Figures 2005–2006. Atlanta, GA: American Cancer Society, Inc., 2005
2. American Cancer Society: Cancer Facts and Figures 2006. Atlanta, GA: American Cancer Society, Inc., 2006
3. Abeloff MD, Wolff AC, Wood WC, McCormick B, Weber BL: Cancer of the Breast. In: Clinical Oncology, Philadelphia, PA: Elsevier, 2004
4. Young Jr, JL, Roffers SD, Ries LAG, Fritz AG, Hurlbut A, Eds.: SEER Summary Staging Manual—2001: Codes and Coding Instructions, Bethesda, MD: National Cancer Institute, 2001
5. Rovak-Schaler R, Rose DP: Mammography screening and breast cancer biology in African American women—a review. *Cancer Detect Prev* 26:180–191, 2002
6. SEER Cancer Statistics Review, 1975–2002, National Cancer Institute. Available at [http://seer.cancer.gov/csr/1975\\_2002/](http://seer.cancer.gov/csr/1975_2002/). Accessed 31 May 2006
7. Elledge RM, Clark GM, Chamness GC, Osborne CK: Tumor biologic factors and breast cancer prognosis among white, hispanic, and black women in the United States. *J Natl Cancer Inst* 86:705–712, 1994
8. Bach PB, Schrag D, Brawley OW, Galaznik A, Yakren S, Begg C: Survival of blacks and whites after a cancer diagnosis. *JAMA* 287:2106–2113, 2002
9. Joslyn SA: Racial differences in treatment and survival from early stage breast carcinoma. *Cancer* 95:1759–1766, 2002
10. Shavers VI, Brown ML: Racial and ethnic disparities in the receipt of cancer treatment. *J Natl Cancer Inst* 95:334–357, 2002
11. Chlebowski RT, Chen Z, Anderson GL, Rohan T, Aragaki A, Lane D, Dolan N, Paskett E, McTiernan A, Hubbell FA, Adams-Campbell LL, Prentice R: Ethnicity and breast cancer factors influencing difference in incidence and outcome. *J Natl Cancer Inst* 97:439–448, 2005
12. Porter PL, Lund MJ, Lin MG, Yuan X, Liff JM, Flag EW, Coates RJ, Eley JW: Racial differences in the expression of cell cycle-regulatory proteins in breast carcinoma: study of young African American and white women in Atlanta, Georgia. *Cancer* 100:2533–2542
13. Digital Database for Screening Mammography. Available at [http://figment.csee.usf.edu/Mammography/DDSMTumbnails/normals/normal\\_01/case0130/A-0130-1.html](http://figment.csee.usf.edu/Mammography/DDSMTumbnails/normals/normal_01/case0130/A-0130-1.html). Accessed 31 May 2006
14. University of South Florida Digital Mammography Home Page. Available at <http://figment.csee.usf.edu/Mammography/Database.html>. Accessed 31 May 2006
15. Human Participant Protections Education for Research Teams, National Cancer Institute. Available at <http://cme.cancer.gov/clinicaltrials/learning/humanparticipant-protections.asp>. Accessed 31 May 2006
16. Ross S, Ejofodomi O, Jendoubi A, Chouikha M, Lo B, Wang P, Zeng J: A mammography database and view system for the African American patients. In: Emerging Technologies and Applications for Imagery Pattern Recognition, Los Alamitos, CA: IEEE Computer Society, 2005
17. MySQL Reference Manual. Available at <http://dev.mysql.com/doc/refman/5.0/en/>. Accessed 31 May 2006
18. PHP: PHP Manual - Manual. Available at <http://www.phpbuilder.com/manual/>. Accessed 31 May 2006



# Alexa Fluor 680-labeled transferrin-cationic (NBD-labeled DOPE-DOTAP) liposome-encapsulated gadopentetate dimeglumine complex

## Tf<sup>NIR</sup>-Lip<sup>NBD</sup>-CA complex

Kenneth T. Cheng, Paul C. Wang, and Liang Shan

National Center for Biotechnology Information, NLM, NIH, Bethesda, MD  
E-mail: Chengke@mail.nih.gov

Department of Radiology, Howard University, Washington, DC, Corresponding Author  
E-mail: pwang@howard.edu

Department of Radiology, Howard University, Washington, DC  
E-mail: lshan@howard.edu

Created: October 18, 2007  
Updated: December 17, 2007

---

**Chemical name:** Alexa Fluor 680-labeled  
transferrin- cationic (NBD-  
labeled DOPE-DOTAP)  
liposome-encapsulated  
gadopentetate dimeglumine  
complex

**Abbreviated name:** Tf<sup>NIR</sup>-Lip<sup>NBD</sup>-CA complex

**Synonym:** Alexa Fluor 680-Tf-Lip-CA

**Backbone:** Liposome

**Target:** Transferrin receptor (TfR)

**Mechanism:**

**Method of detection:** Optical (Near-infrared (NIR)  
fluorescent) imaging,  
magnetic resonance imaging  
(MRI)

**Source of signal/ contrast:** Alexa Fluor 680, gadolinium

**Activation:** No

**Studies:** ☒ *In vitro*  
☒ Rodents

Click on protein [<http://www.ncbi.nlm.nih.gov/entrez/viewer.fcgi?db=protein&id=4507457>], nucleotide (RefSeq), [<http://www.ncbi.nlm.nih.gov/entrez/viewer.fcgi?db=nucleotide&id=123999041>] and gene [[http://www.ncbi.nlm.nih.gov/sites/entrez?Db=gene&Cmd=ShowDetailView&TermToSearch=7037&ordinalpos=1&itool=EntrezSystem2.PEntrez.Gene.Gene\\_ResultsPanel.Gene\\_RVDocSum](http://www.ncbi.nlm.nih.gov/sites/entrez?Db=gene&Cmd=ShowDetailView&TermToSearch=7037&ordinalpos=1&itool=EntrezSystem2.PEntrez.Gene.Gene_ResultsPanel.Gene_RVDocSum)] for more information about transferrin receptors.

---

## Background

---

[PubMed [[\]](http://www.ncbi.nlm.nih.gov/sites/entrez?Db=pubmed&Cmd=DetailsSearch&Term=(liposome)+AND+(Fluorescent)+AND+(Magnetic))

Alexa Fluor 680-labeled transferrin-cationic (NBD-labeled DOPE-DOTAP) liposome-encapsulated gadopentetate dimeglumine complex (Tf<sup>NIR</sup>-Lip<sup>NBD</sup>-CA complex) is a dual (multimodality) molecular imaging probe with fluorescent and magnetic properties that can be used for imaging tumors with overexpressed transferrin (Tf) receptors (1). Alexa Fluor 680 is a near-infrared (NIR) fluorescence dye with an absorption maximum of 679 nm, an emission maximum of 720 nm, and an extinction coefficient of 180,000 cm<sup>-1</sup>M<sup>-1</sup> (2). Gadopentetate dimeglumine (Gd-DTPA) is a water-soluble paramagnetic contrast agent approved by the United States Food and Drug Administration for contrast enhancement in magnetic resonance imaging (MRI) (3).

Tf is part of a family of proteins that includes serum Tf, ovotransferrin, and lactoferrin (4). Serum Tf is a monomeric glycoprotein (molecular mass, 80 kDa) that binds Fe<sup>3+</sup> for delivery to vertebrate cells through receptor-mediated endocytosis (1). The Tf receptor (TfR) mediates the internalization of iron-loaded Tf into cells (4, 5). The TfR (CD71) is a type II transmembrane glycoprotein and is found primarily as a homodimer (molecular mass, 180 kDa). It also contains other growth regulatory properties in certain normal and malignant cells. The elevated levels of TfR in some malignancies (e.g., 74% breast carcinomas, 76% lung adenocarcinomas, and 93% lung squamous cell carcinomas) and the extracellular accessibility of this molecule make TfR a potential molecular target for cancer imaging or therapy.

Liposomes (Lips) are small nontoxic vesicles composed of lipid bilayers enclosing aqueous volume, and they are versatile carriers of both therapeutic drugs and imaging agents (5-7). Although Lips are naturally taken up by the reticuloendothelial system, the size, charge, and surface of Lips can be modified for targeting purposes. Because of the intrinsically low sensitivity of MRI and the low penetration of light, optical and MRI multifunctional probes have been developed as one of the possible approaches to enhance the clinical and research applications of both imaging modalities (1, 8, 9). Shan et al. (1) reported the preparation of a dual probe with fluorescent and magnetic properties based on Lips targeting to TfR-overexpressed tumors. In this Tf<sup>NIR</sup>-Lip<sup>NBD</sup>-CA complex, Alexa Fluor 680-labeled Tf was linked on the surface of cationic Lips with Gd-DTPA encapsulated inside the vesicles.

## Synthesis

---

[PubMed [[\]](http://www.ncbi.nlm.nih.gov/sites/entrez?Db=pubmed&Cmd=DetailsSearch&Term=((liposome)+AND+(Fluorescent)+AND+(Magnetic))+)

The Tf<sup>NIR</sup>-Lip<sup>NBD</sup>-CA complex was synthesized with the Alexa Fluor 680 conjugate of human Tf (Tf<sup>NIR</sup>), cationic Lips (Lip<sup>NBD</sup>) and commercially available Gd-DTPA (CA) (1). The cationic Lip<sup>NIB</sup> used the green fluorescent formula of 1,2-dioleoyl-3-trimethylammonium-propane (DOTAP): 1,2-dioleoyl-sn-glycero-3-phosphoethanolamine (DOPE) in a ratio of 1:1 (w/w) plus 0.1% DOPE-N-(7-nitro-2-1,3-benzoxadiazole-4-yl) (NBD-DOPE). Briefly, the lipids were mixed in chloroform and then dried under a nitrogen stream. The Lip<sup>NBD</sup>-CA was formed by reconstituting the dried lipid

mixture with 50  $\mu$ l water containing 12  $\mu$ l of Gd-DTPA (commercial formulation of 469.01  $\mu$ g/ $\mu$ l). The Lip<sup>NBD</sup>-CA was homogenized and incubated for 10 min. The Lip volume was adjusted to 175  $\mu$ l with water and then sequentially downsized by sonication (80–90 W, 10 min) and filtration with decreasing pore diameter from 0.2 to 0.1  $\mu$ m. Finally, Tf<sup>NIR</sup> (5 mg/ml) was added and incubated for at least 10 min. Unencapsulated CA and free Tf<sup>NIR</sup> were removed by gel filtration chromatography. The final Lip:Tf:Gd-DTPA ratio was 10:12.50:0.56 (nmol: $\mu$ g:mg).

## ***In Vitro Studies: Testing in Cells and Tissues***

---

[PubMed [[http://www.ncbi.nlm.nih.gov/sites/entrez?Db=pubmed&Cmd=DetailsSearch&Term=\(\(liposome\)+AND+\(Fluorescent\)+AND+\(Magnetic\)\)+AND+in+vitro](http://www.ncbi.nlm.nih.gov/sites/entrez?Db=pubmed&Cmd=DetailsSearch&Term=((liposome)+AND+(Fluorescent)+AND+(Magnetic))+AND+in+vitro)]]

Shan et al. (1) conducted cellular uptake tests of Tf-Lip<sup>NBD</sup>-NIR dye with TfR-overexpressed MDA-MB-231-luc human breast cancer cells. In this study, Tf was not labeled with Alexa Fluor 680. Instead, Alexa Fluor 680 (red dye) was encapsulated by Lip<sup>NBD</sup> (green fluorescent) so that the encapsulated reagent (the red dye in place of CA) and the Lip could be observed by confocal microscopy. After incubation with the cells, both the green Lip<sup>NBD</sup> and the encapsulated red dye were observed in the cell cytoplasm as early as 5 min. The fluorescent intensity (FI) within the cytoplasm increased gradually and reached a maximum at ~1 h. The Lip<sup>NBD</sup> and red dye then accumulated again to form multiple endosomes at the peripheral area of the cytoplasm. The authors suggested that this might represent the release or degradation of the probe through the action of lysosomal enzymes. In comparison, when the red dye alone was incubated with the cells, no cellular uptake was observed. The efficiency of the uptake was quantified on cell pellets after 1 h of incubation. The red dye FI values ( $\text{p/s/cm}^2/\text{steradian (sr)} \times 10^9$ ;  $n = 3$ ) were  $6.88 \pm 0.59$ ,  $4.99 \pm 0.51$ , and  $0.23 \pm 0.006$  for Tf-Lip<sup>NBD</sup> dye, Lip<sup>NBD</sup> -dye, and dye alone, respectively. The green dye FI values ( $\text{p/s/cm}^2/\text{sr} \times 10^7$ ;  $n = 3$ ) were  $2.03 \pm 0.14$ ,  $1.64 \pm 0.09$ , and  $1.10 \pm 0.13$  for Tf-Lip<sup>NBD</sup>-dye, Lip<sup>NBD</sup>-dye, and dye alone, respectively. In the blocking study in which the cells were pretreated with unlabeled Tf (three-fold higher amount) before incubation with Tf-Lip<sup>NBD</sup> dye, the red dye FI value decreased from  $3.42 \times 10^9$  p/s/cm<sup>2</sup>/sr to  $2.45 \times 10^9$  p/s/cm<sup>2</sup>/sr with a 65.6% blockage of dye uptake. The green dye FI value for Lip<sup>NBD</sup> dye decreased from  $3.45 \times 10^7$  p/s/cm<sup>2</sup>/sr to  $2.57 \times 10^7$  p/s/cm<sup>2</sup>/sr with a 71.0% blockage of Lip<sup>NBD</sup> uptake.

In another study, where Tf<sup>NIR</sup>-Lip<sup>NBD</sup>-CA was incubated with the cells, optical imaging and confocal microscopy confirmed that both Tf<sup>NIR</sup> and Lip<sup>NBD</sup> were colocalized within cell cytoplasm after 5 min of incubation (1). To measure the presence of CA within the cells, MRI (400-MHz NMR spectrometer) was also performed on cell pellets obtained from cells incubated with Tf<sup>NIR</sup>-Lip<sup>NBD</sup>-CA. The T<sub>1</sub> relaxation times ( $n = 3$ ) were  $408.1 \pm 13.8$  ms,  $374 \pm 17.3$  ms, and  $366 \pm 17.1$  ms for cells incubated with CA, Lip<sup>NBD</sup>-CA, and Tf<sup>NIR</sup>-Lip<sup>NBD</sup>-CA, respectively.

## Animal Studies

---

### Rodents

[PubMed [http://www.ncbi.nlm.nih.gov/sites/entrez?Db=pubmed&Cmd=DetailsSearch&Term=((liposome)+AND+(Fluorescent)+AND+(Magnetic))+AND+mice]]

Shan et al. (1) evaluated the tumor signal enhancement in nude mice ( $n = 10$ ) bearing the subcutaneous MDA-MB-231-luc human breast cancer (0.4–1.2 cm diameter). Each mouse received 200  $\mu$ l of Tf<sup>NIR</sup>-Lip<sup>NBD</sup>-CA (containing 12  $\mu$ l Gd-DTPA) by i.v. injection. MRI imaging using a 400-MHz NMR spectrometer and a T<sub>1</sub>-weighted spin-echo sequence (repetition time = 800 ms, echo time = 11.4 ms) showed significant tumor contrast enhancement as early as 10 min and reached a maximum at 90–120 min. The enhancement appeared to be more heterogeneous in larger tumors but more uniform in smaller tumors. Pathology results showed that the highly enhanced regions represented the more actively proliferating tumor cells. The weakly enhanced areas contained dying cells and the necrotized regions. Giving the CA alone enhanced the tumor contrast only slightly. The CA enhancement started from the peripheral area to the center and reached the maximum in 30–60 min. CA containing Lip without linkage to Tf showed an even weaker signal enhancement. No blocking study was performed.

Optical imaging of Tf<sup>NIR</sup>-Lip<sup>NBD</sup>-CA based on Tf<sup>NIR</sup> showed clear tumor signal as early as 10 min and reached a maximum at 90–120 min (1). The FI was related to the tumor sizes and showed detectable FI in larger tumors (>0.8 cm diameter) after 2 days. The FI of Lip<sup>NBD</sup> was too weak to be detected. The probe was rapidly distributed throughout the body. It was taken up by well-perfused organs and then rapidly washed out. The probe activity remained in the tumor and was not washed out. The tumor/contralateral muscle ratios varied from 1.3 to 3.4 within 10 min to 48 h. This ratio appeared to be dependent on tumor sizes. Small tumors (<3 mm diameter) showed less FI than the bigger tumors. In comparison, administration of the red dye containing Lip without linkage to Tf showed no tumor signal enhancement.

### Other Non-Primate Mammals

[PubMed [http://www.ncbi.nlm.nih.gov/sites/entrez?Db=pubmed&Cmd=DetailsSearch&Term=((liposome)+AND+(Fluorescent)+AND+(Magnetic))+AND+(dog+OR+rabbit+OR+pig+OR+sheep)]]

No publication is currently available.

### Non-Human Primates

[PubMed [http://www.ncbi.nlm.nih.gov/sites/entrez?Db=pubmed&Cmd=DetailsSearch&Term=((liposome)+AND+(Fluorescent)+AND+(Magnetic))+AND+(primate+NOT+human)]]

No publication is currently available.

## Human Studies

---

[PubMed [[http://www.ncbi.nlm.nih.gov/sites/entrez?Db=pubmed&Cmd=DetailsSearch&Term=\(\(liposome\)+AND+\(Fluorescent\)+AND+\(Magnetic\)\)+AND+human](http://www.ncbi.nlm.nih.gov/sites/entrez?Db=pubmed&Cmd=DetailsSearch&Term=((liposome)+AND+(Fluorescent)+AND+(Magnetic))+AND+human)]]

No publication is currently available.

## NIH Support

---

NCRR 2G12RR003048, NIH 5U54CA091431.

## References

---

1. Shan L., Wang S., Sridhar R., Bhujwala Z.M., Wang P.C.. *Dual probe with fluorescent and magnetic properties for imaging solid tumor xenografts*. Mol Imaging **6**(2):85–95; 2007. (PubMed)
2. Berlier J.E., Rothe A., Buller G., Bradford J., Gray D.R., Filanoski B.J., Telford W.G., Yue S., Liu J., Cheung C.Y., et al. *Quantitative comparison of long-wavelength Alexa Fluor dyes to Cy dyes: fluorescence of the dyes and their bioconjugates*. J Histochem Cytochem **51**(12):1699–1712; 2003. (PubMed)
3. Runge V.M.. *Safety of approved MR contrast media for intravenous injection*. J Magn Reson Imaging **12**(2):205–213; 2000. (PubMed)
4. Daniels T.R., Delgado T., Rodriguez J.A., Helguera G., Penichet M.L.. *The transferrin receptor part I: Biology and targeting with cytotoxic antibodies for the treatment of cancer*. Clin Immunol **121**(2):144–158; 2006. (PubMed)
5. Daniels T.R., Delgado T., Helguera G., Penichet M.L.. *The transferrin receptor part II: targeted delivery of therapeutic agents into cancer cells*. Clin Immunol **121**(2):159–176; 2006. (PubMed)
6. Cheng K.T., Seltzer S.E., Adams D.F., Blau M.. *The production and evaluation of contrast-carrying liposomes made with an automatic high-pressure system*. Invest Radiol **22**(1):47–55; 1987. (PubMed)
7. Hatakeyama H., Akita H., Maruyama K., Suhara T., Harashima H.. *Factors governing the in vivo tissue uptake of transferrin-coupled polyethylene glycol liposomes in vivo*. Int J Pharm **281**(1-2):25–33; 2004. (PubMed)
8. Veisheh O., Sun C., Gunn J., Kohler N., Gabikian P., Lee D., Bhattarai N., Ellenbogen R., Sze R., Hallahan A., et al. *Optical and MRI multifunctional nanoprobe for targeting gliomas*. Nano Lett **5**(6):1003–1008; 2005. (PubMed)
9. Kircher M.F., Mahmood U., King R.S., Weissleder R., Josephson L.. *A multimodal nanoparticle for preoperative magnetic resonance imaging and intraoperative optical brain tumor delineation*. Cancer Res **63**(23):8122–8125; 2003. (PubMed)

# Dual Probe with Fluorescent and Magnetic Properties for Imaging Solid Tumor Xenografts

Liang Shan, Songping Wang, Rajagopalan Sridhar, Zaver M. Bhujwalla, and Paul C. Wang

## Abstract

A dual probe with fluorescent and magnetic reporter groups was constructed by linkage of the near-infrared (NIR) fluorescent transferrin conjugate (Tf<sup>NIR</sup>) on the surface of contrast agent-encapsulated cationic liposome (Lip-CA). This probe was used for magnetic resonance imaging (MRI) and optical imaging of MDA-MB-231-luc breast cancer cells grown as a monolayer *in vitro* and as solid tumor xenografts in nude mice. Confocal microscopy, optical imaging, and MRI showed a dramatic increase of *in vitro* cellular uptake of the fluorescent and magnetic reporter groups from the probe compared with the uptake of contrast agent or Lip-CA alone. Pretreatment with transferrin (Tf) blocked uptake of the probe reporters, indicating the importance and specificity of the Tf moiety for targeting. Intravenous administration of the dual probe to nude mice significantly enhanced the tumor contrast in MRI, and preferential accumulation of the fluorescent signal was clearly seen in NIR-based optical images. More interestingly, the contrast enhancement in MRI showed a heterogeneous pattern within tumors, which reflected the tumor's morphologic heterogeneity. These results indicate that the newly developed dual probe enhances the tumor image contrast and is superior to contrast agent alone for identifying the tumor pathologic features on the basis of MRI but also is suitable for NIR-based optical imaging.

**T**UMOR IMAGING exploits the differences in physical properties between malignant and normal tissues. These differences are often insufficient for good contrast resolution.<sup>1–3</sup> Contrast-enhanced magnetic resonance imaging (MRI) is one of the best noninvasive methodologies available today in clinical medicine for assessing the anatomy and function of tissues.<sup>4</sup> High spatial resolution and high soft tissue contrast are desirable features of noninvasive MRI. However, owing to intrinsically low sensitivity, high local concentration of contrast agents (CAs) is required to generate detectable magnetic resonance contrast. A large amount of CA has to be used owing to the nonspecific uptake by tumors and other

tissues *in vivo*. In recent years, targeted CA delivery systems have been developing based on the concept that molecular imaging can increase the signal to noise ratio by detecting differences in ‘molecular properties’ between cancer and normal tissues.<sup>5–7</sup> This should, in theory, allow for detection of smaller tumors. As one strategy, monoclonal antibodies or antibody fragments have been coupled with CA directly or linked with CA through liposome (Lip) carrier. However, insufficient direct linkage of gadolinium (Gd) with antibody or the relatively large molecular size of antibody-Lip-Gd particles may limit its use as a CA for imaging cell surface receptors in solid tumors because of inefficient extravasation and very slow diffusion in the interstitial compartment.<sup>2,8,9</sup> Furthermore, antibody immunogenicity, poor stability of the conjugates, and potential change of the antibody binding ability owing to changes in surface antigens are still problematic for *in vivo* application. A ligand with less toxic, high binding specificity for tumors and relatively small size and without immunogenicity is required to target the CA to tumors.

Optical imaging offers several advantages over other imaging techniques. Among these are the simplicity of the technique, high sensitivity, and absence of ionizing radiation. There is increasing interest in the development of techniques for *in vivo* evaluation of gene expression, monitoring of gene delivery, and real-time intraoperative

From the Departments of Radiology and Radiation Oncology, Howard University, Washington, DC; and Department of Radiology, Johns Hopkins University School of Medicine, Baltimore, MD.

This study was made possible by grant number 2G12RR003048 from the National Center for Research Resources, a component of the National Institutes of Health (NIH). It was also supported by the following grants: USAMRMC W81XWH-05-1-0291, DAMD17-00-1-0291, DAMD17-03-1-0759, and NIH 5U54CA091431.

Address reprint requests to: Paul C. Wang, PhD, Department of Radiology, Howard University, 2041 Georgia Avenue, NW, Washington, DC 20060; e-mail: pwang@howard.edu.

DOI 10.2310/7290.2007.00006

© 2007 BC Decker Inc



visualization of tumor margins and metastatic lesions to improve surgical outcome.<sup>10–12</sup> Limited depth of light penetration and a lack of tomographic information prevent in vivo efficiency of optical imaging. To overcome the limitations of various imaging modalities, multimodal probes have been developed for detection using multiple imaging devices.<sup>13–15</sup>

Transferrin receptor (TfR) is a cell surface internalizing receptor that is responsible for almost all iron sequestration in mammalian cells. TfR is overexpressed in 74% of breast carcinomas, 76% of lung adenocarcinomas, and 93% of lung squamous cell carcinomas. The expression level of TfR receptor is of great value in grading tumors and determining prognosis.<sup>16,17</sup> TfR has been successfully applied as a molecular target to direct therapeutic agents to tumor cells.<sup>17</sup> Transferrin (Tf), the TfR ligand, is a monomeric glycoprotein that binds  $\text{Fe}^{3+}$  for delivery to vertebrate cells through receptor-mediated endocytosis. Fluorescently labeled Tf has greatly aided the investigation of endocytosis in vitro. Tf has also been successfully used in targeted gene therapy in vivo.<sup>18,19</sup> We hypothesized that near-infrared (NIR) dye-labeled Tf ( $\text{Tf}^{\text{NIR}}$ ) would be an ideal ligand for targeting MRI and optical reporters to solid tumors, enabling better contrast-enhanced MRI and NIR-based optical detection. We developed a Tf- and Lip-mediated dual molecular probe with both fluorescent and magnetic reporter groups. The  $\text{Tf}^{\text{NIR}}$  was linked on the surface of Lip particles, whereas the MRI CA (Magnevist, obtained from Berlex Laboratories, Wayne, NJ) was encapsulated within the Lip. These components conjugated together and formed small uniform vesicles (less than 100 nm in diameter). In vitro analysis demonstrated that the probe dramatically improved the uptake of CA and NIR dye in monolayer cultures of MDA-MB-231-luc human breast cancer cells through both receptor- and Lip-mediated endocytosis. In vivo, the probe significantly enhanced the magnetic resonance signals from the MDA-MB-231-luc cells grown as solid tumor xenografts in nude mice and was superior to the CA alone for identifying the tumor morphology and infrastructure. Simultaneously, a significant preferential accumulation of fluorescent signal by the tumors was clearly detectable in  $\text{Tf}^{\text{NIR}}$ -based optical imaging.

## Materials and Methods

### Materials

Cationic lipids including 1,2-dioleoyl-sn-glycero-3-phosphoethanolamine (DOPE), 1,2-dioleoyl-3-trimethylammo-

nium-propane (DOTAP), and fluorescent lipid DOPE-N-(7-nitro-2-1,3-benzoxadiazole-4-yl) (NBD-DOPE) were purchased from Avanti Polar Lipids (Alabaster, AL). They were premixed and dissolved in chloroform in a formula of DOTAP:DOPE (1:1 w/w) (Lip) or in a fluorescent formula of DOTAP:DOPE + 0.1% NBD-DOPE ( $\text{Lip}^{\text{NBD}}$ ). Fluorescent Alexa fluor 680 conjugate of human Tf ( $\text{Tf}^{\text{NIR}}$ ), a SelectFX nuclear labeling kit, Alexa fluor 680 fluorophore, and enzyme-free phosphate-buffered saline (PBS)-based cell dissociation solution were purchased from Invitrogen (Carlsbad, CA). Holo-transferrin without fluorescent conjugate and MicroSpin G-50 columns were obtained from Sigma (St. Louis, MO) and Amersham Biosciences (Piscataway, NJ), respectively. The SPI-Pore polycarbonate membrane filter and filter holder were from Structure Probe Inc (West Chester, PA).

### Preparation of the Molecular Dual Probe: $\text{Tf}^{\text{NIR}}$ - $\text{Lip}^{\text{NBD}}$ -CA Complex

The  $\text{Tf}^{\text{NIR}}$ - $\text{Lip}^{\text{NBD}}$ -CA complex was constructed using  $\text{Tf}^{\text{NIR}}$ , cationic  $\text{Lip}^{\text{NBD}}$ , and Magnevist. Premixed  $\text{Lip}^{\text{NBD}}$  in chloroform (3.607  $\mu\text{L}$ ) was dried under a nitrogen stream and hydrated by adding 50  $\mu\text{L}$  of water containing 12  $\mu\text{L}$  of Magnevist. Each microliter of Magnevist contains 469.01  $\mu\text{g}$  of gadopentatate dimeglumine. The hydrated  $\text{Lip}^{\text{NBD}}$ -CA mixture was homogenized using a vortex generator and incubated for 10 minutes. The volume of the mixture was adjusted to 175  $\mu\text{L}$  with water. The mixture was then sequentially downsized by sonication (80–90 W, 10 minutes) in a water bath and by repeatedly passing through polycarbonate filters with decreasing pore diameter 0.2/0.1  $\mu\text{m}$ . Following that, 25  $\mu\text{L}$  of  $\text{Tf}^{\text{NIR}}$  (5 mg/mL) was mixed and incubated for at least 10 minutes. Gel filtration through a Sephadex G-50 column was used to remove unencapsulated CA and free  $\text{Tf}^{\text{NIR}}$ . A freshly prepared probe was used in all analysis. The final volume was 200  $\mu\text{L}$ , and Lip:  $\text{Tf}$ :Magnevist composition was 10:12.5:0.56 (nmol/ $\mu\text{g}$ /mg). To monitor different components of the probe, nonfluorescent Tf and Lip were used instead of fluorescent  $\text{Tf}^{\text{NIR}}$  and  $\text{Lip}^{\text{NBD}}$  in some experiments.

### Cell Culture and Animal Model

The MDA-MB-231-luc human breast cancer cell line (Xenogen, Alameda, CA) was used to test the efficiency of the probe in vitro and in vivo. This cell line is well documented for constitutional overexpression of TfR and has been transfected with the luciferase gene for luciferase-



based optical imaging. (In this study, we did not use luciferase-based imaging.) Cells were routinely maintained in Dulbecco's Modified Eagle's Medium/F-12 medium supplemented with 10% heat-inactivated fetal bovine serum (FBS) and 50 µg/mL each of penicillin, streptomycin, and neomycin (Invitrogen). The solid tumor xenograft model was developed by subcutaneous injection of  $1 \times 10^7$  subconfluent cells in 100 µL Dulbecco's phosphate-buffered saline (DPBS) in the lower back of female athymic nude mice (8–10 weeks old; Harlan, Indianapolis, IN). The probe was evaluated in a total of 10 nude mice bearing tumors from 0.4 to 1.2 cm in diameter.

### Confocal Microscopy

Tumor cells were grown on eight-chamber glass slides. Twenty-four hours later, the cells at 40 to 50% confluence were incubated with 25 µL of one of the following probes in 150 µL of medium without FBS and antibiotics. The probes included Tf<sup>NIR</sup>-Lip<sup>NBD</sup>-CA, Tf-Lip<sup>NBD</sup>-dye, and dye alone. To visualize the cellular uptake of probe reporters, an NIR dye Alexa fluor 680 fluorophore was used to replace the CA in the preparation of Tf-Lip<sup>NBD</sup>-dye probe at a concentration of 2 µL in a 200 µL total probe. Incubation was carried out for 5, 30, 60, and 120 minutes, separately. After PBS washing (three times), cells were fixed using 10% neutralized formalin for 10 minutes and cell nuclei were counterstained using 4',6-diamidino-2-phenylindole dihydrochloride (DAPI) blue-fluorescence dye. Confocal images were acquired with a Zeiss LSM 510 Confocal Microscopy System (Carl Zeiss Inc, Thornwood, NY) using a 633 nm excitation line and emission LP 650 filter for Tf<sup>NIR</sup> and Alexa fluor 680 fluorophore (red), 488 nm excitation line and emission BP 505 – 550 filter for Lip<sup>NBD</sup> (green), and 364 nm excitation line and emission BP 385 – 470 filter for DAPI (blue). Following sequential excitation, red, green, and blue fluorescent images of the same cells were merged using the Zeiss AIM software for colocalization of the probe different reporters within cells.

### In Vitro MRI and Optical Imaging

To quantify the cellular uptake of probe reporters, optical imaging and MRI of the cell pellets were performed. Similar numbers of tumor cells were seeded on 10 cm culture dishes for optical imaging and in 150 cm flasks for MRI. Cells grown to subconfluence were incubated with a 200 µL probe (in 3 mL medium) for 10 cm dishes and a 600 µL probe (in 10 mL medium) for 150 cm flasks.

Differently labeled probes, such as Tf<sup>NIR</sup>-Lip<sup>NBD</sup>-CA, Tf-Lip<sup>NBD</sup>-dye, Lip<sup>NBD</sup>-dye, CA alone, and dye alone, were used. Incubation was carried out for 60 minutes. After PBS washing (three times), cells were collected using enzyme-free cell dissociation solution and adjusted to the same number. Cells were pelleted in microcentrifuge tubes by centrifugation. The cell pellets were quantified with respect to fluorescent intensity (FI) using the Xenogen IVIS 200 imaging system with excitation/emission filters at 679/702 nm for Tf<sup>NIR</sup> and the Alexa fluor 680 fluorophore and at 464/531 nm for Lip<sup>NBD</sup> measurement. Statistical analysis (Student's two-tailed *t*-test) of the FI for cells with different treatments was performed using Microsoft Excel. To obtain enough cells for MRI, cell pellets were pooled from five replicates. MRI was acquired using a Bruker 400 MHz NMR machine (Bruker-Biospin, Billerica, MA). A spin-echo (SE) imaging sequence was used to obtain T<sub>1</sub>-weighted images. The imaging parameters were as follows: echo time (TE) = 11.416 milliseconds, repetition time (TR) = 500 milliseconds, number of averages = 4, field of view = 20 × 20 mm, matrix size = 256 × 128, and slice thickness = 2 mm. A fast imaging with steady-state precession sequence was used for T<sub>1</sub> measurement. The T<sub>1</sub> measurement parameters were as follows: TE = 1.5 milliseconds, TR = 3 milliseconds, number of averages = 8, number of frames = 16, number of segments = 32, inversion delay = 49.2 milliseconds, and inversion repetition = 2572.3 milliseconds. The MRIs were taken in the cross-sectional view of the microcentrifuge tubes. The central slice image, which was not influenced by the image distortion owing to the susceptibility effect from the air-pellet boundary, was used for signal intensity measurement. All analyses were performed using the Bruker image sequence analysis tools. All experiments were repeated at least three times. The representative data are presented.

### In Vivo MRI and Optical Imaging

The animal was anesthetized using 2% isoflurane and positioned with the tumor at the center of the coil. The physiologic condition of the animals was monitored using a respiratory gating device during the scanning. The tumor was scanned in the perpendicular direction of the tumor and animal skin interface using a Bruker 400 MHz, 89 mm NMR spectrometer. After a search for overall image quality, imaging time, and probe- and CA-mediated contrast enhancement using different imaging sequences and parameters, a multislice multiecho T<sub>1</sub>-weighted SE sequence was used for imaging studies, with a TR of 800 milliseconds, a TE of 11.4 milliseconds, and a slice

thickness of 1 mm. For each animal, a baseline image was first obtained; the tumors were then sequentially imaged at an interval of 10 minutes until 3 hours following intravenous injection of 200  $\mu\text{L}$  of  $\text{Tf}^{\text{NIR}}$ - $\text{Lip}^{\text{NBD}}$ -CA probe (containing 12  $\mu\text{L}$  of Magnevist) through the tail vein. This was equivalent to two times the Magnevist dosage used in the clinic. For comparative study, the same animals were also imaged following intravenous administration of the same dosage of Lip-CA and CA alone (12  $\mu\text{L}$  of Magnevist in 200  $\mu\text{L}$  of pure water). The interval period between the two MRI studies was at least 3 days to avoid any influence of CA from the previous imaging study. The direction of the tumor was marked each time with water-filled small balls and marker pens before imaging. For optical imaging, the FI of tumors was monitored from 10 minutes after administration of the probe to 3 to 5 days using a Xenogen IVIS 200 imaging system.

### Pathologic Analysis

After imaging, the mice were autopsied and the tumors were sampled, fixed in 10% neutral buffered formalin, and embedded in paraffin. Tumors were sectioned in the same direction as MRIs based on the markers of the tumor border made before MRI. Hematoxylin-eosin staining was used for pathologic examination. A comparison was performed between the tumor pathology and the image enhancement pattern in MRI.

## Results

### Visualization of Tf- and Lip-Mediated Cellular Uptake

For confocal microscopic observation of the cellular uptake of the probe reporters, cells were incubated with the probe  $\text{Tf-Lip}^{\text{NBD}}$ -dye or dye alone from 5 minutes to 2 hours. Here the probe was constructed using unlabeled Tf and NIR fluorescent dye instead of CA to visualize the uptake of encapsulated reagents within Lip. Figure 1 shows representative microscopic images. Both  $\text{Lip}^{\text{NBD}}$  (green) and fluorescent dye (red) were observed to be present in the cell cytoplasm as early as 5 minutes after incubation with the probe, and their FI within the cytoplasm increased gradually, reaching a maximum at about 1 hour of incubation (see Figure 1, A–C). Interestingly, the  $\text{Lip}^{\text{NBD}}$  and dye accumulated again, forming multiple endosomes. These endosomes were mainly located at the peripheral area of the cytoplasm and became more evident at 2 hours of incubation (see Figure 1, D–F), suggesting receptor-

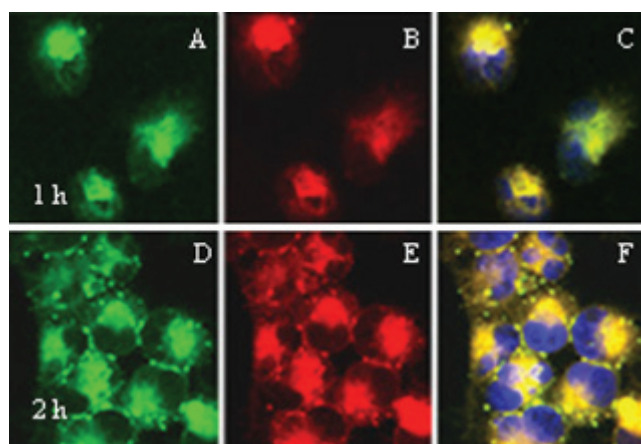


**Figure 1.** Confocal microscopic observation of cellular uptake of probe reporters. Cells were incubated with the probe transferrin-liposome-nitrobenzoxadiazole ( $\text{Tf-Lip}^{\text{NBD}}$ )-dye for 5 minutes to 2 hours. A to C are representative images acquired at the 1 hour of incubation time point showing distribution and colocalization of  $\text{Lip}^{\text{NBD}}$  (A) and near-infrared (NIR) dye (B) in the cytoplasm. D to F are representative images acquired at the 2 hours of incubation time point showing multiple endosomes formed by Lip (D) and NIR dye (E) and colocalized in the peripheral area of the cytoplasm (F). Nuclei were counterstained using 4',6-diamidino-2-phenylindole dihydrochloride (DAPI). Cells were imaged with a  $63 \times 1.4$  NA Plan-Apochromat oil-immersion objective.

mediated endocytosis and release or degradation of the probe reporters through the action of lysosomal enzymes. Cellular uptake of the dye was not evident in the cells incubated with dye alone.

To visualize whether the Tf and Lip were co-internalized, confocal microscopy and optical imaging were performed for cells incubated with  $\text{Tf}^{\text{NIR}}$ - $\text{Lip}^{\text{NBD}}$ -CA,  $\text{Lip}^{\text{NBD}}$ -CA, or CA alone. Similarly, from 5 minutes of incubation, the  $\text{Tf}^{\text{NIR}}$  (Figure 2A) and  $\text{Lip}^{\text{NBD}}$  (Figure 2B) were already colocalized within cell cytoplasm (Figure 2C). Optical imaging of the cell pellets further confirmed the uptake of the probe in tumor cells. To avoid membrane damage and probe leakage from cells, enzyme-free PBS-based cell dissociation solution was used instead of trypsin for cell dissociation from culture dishes. As shown in Figure 2D, only cells incubated with  $\text{Tf}^{\text{NIR}}$ - $\text{Lip}^{\text{NBD}}$ -CA showed a strong fluorescent signal of  $\text{Tf}^{\text{NIR}}$ . Both cells incubated with  $\text{Tf}^{\text{NIR}}$ - $\text{Lip}^{\text{NBD}}$ -CA and cells incubated with  $\text{Lip}^{\text{NBD}}$ -CA showed strong fluorescent signal of  $\text{Lip}^{\text{NBD}}$  (Figure 2E). Neither  $\text{Tf}^{\text{NIR}}$  nor  $\text{Lip}^{\text{NBD}}$  signal was detectable in cells incubated with CA alone.

We further evaluated whether the CA encapsulated within the probe was internalized into tumor cells using MRI of the cell pellets. A representative MRI of the cell pellets obtained from cells incubated with  $\text{Tf}^{\text{NIR}}$ - $\text{Lip}^{\text{NBD}}$ -

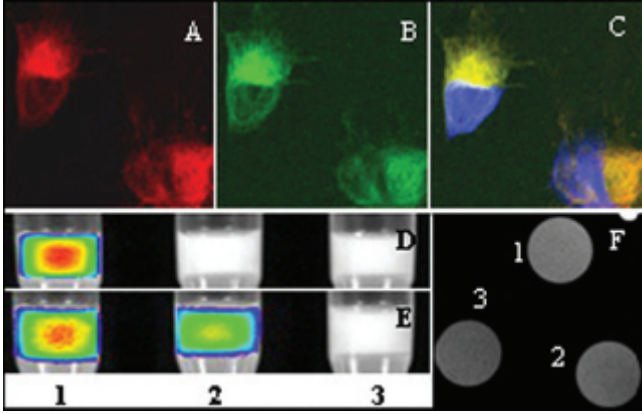


**Figure 2.** Confocal, optical, and magnetic resonance imaging (MRI) detection of the reporters in cells incubated with the probe near-infrared transferrin-liposome-nitrobenzoxadiazole-contrast agent ( $\text{Tf}^{\text{NIR}}\text{-Lip}^{\text{NBD}}\text{-CA}$ ) for 1 hour. A to C are representative confocal microscopic images showing distribution and colocalization of  $\text{Tf}^{\text{NIR}}$  (A) and  $\text{Lip}^{\text{NBD}}$  (B) in cytoplasm. D to E are optical images of the cell pellets. A strong fluorescent signal of Tf is detected in cells incubated with  $\text{Tf}^{\text{NIR}}\text{-Lip}^{\text{NBD}}\text{-CA}$  (D, lane 1) but not in cells incubated with  $\text{Lip}^{\text{NBD}}\text{-CA}$  or with CA alone (D, lanes 2 and 3). Similarly, the strongest signal of  $\text{Lip}^{\text{NBD}}$  is detected in cells incubated with  $\text{Tf}^{\text{NIR}}\text{-Lip}^{\text{NBD}}\text{-CA}$  (E, lane 1) and less in cells incubated with  $\text{Lip}^{\text{NBD}}\text{-CA}$  (E, lane 2) but not in cells incubated with CA alone (E, lane 3). F shows the MRIs of the cell pellets. A stronger signal enhancement and  $T_1$  shortening are obtained in cells incubated with  $\text{Tf}^{\text{NIR}}\text{-Lip}^{\text{NBD}}\text{-CA}$  and in cells incubated with  $\text{Lip}^{\text{NBD}}\text{-CA}$  (1 and 2) than in cells incubated with CA alone (3). The MRI parameters are as follows: echo time = 11.416 milliseconds, repetition time = 500 milliseconds, number of averages = 4, field of view =  $20 \times 20$  mm, matrix size =  $256 \times 128$ , and slice thickness = 2 mm.

CA,  $\text{Lip}^{\text{NBD}}\text{-CA}$ , or CA alone is shown in Figure 2F. The corresponding signal intensity and  $T_1$  relaxation time are shown in Table 1. Cells incubated with the probe  $\text{Tf}^{\text{NIR}}\text{-Lip}^{\text{NBD}}\text{-CA}$  or  $\text{Lip}^{\text{NBD}}\text{-CA}$  showed a much greater positive

contrast and  $T_1$  shortening than the cells incubated with CA alone. The  $T_1$  relaxation time shortened from 408 milliseconds for CA alone to 374 milliseconds for  $\text{Lip}^{\text{NBD}}\text{-CA}$  and 366 milliseconds for  $\text{Tf}^{\text{NIR}}\text{-Lip}^{\text{NBD}}\text{-CA}$  ( $p < .05$ ). The cells incubated with  $\text{Tf}^{\text{NIR}}\text{-Lip}^{\text{NBD}}\text{-CA}$  also showed higher signal intensity than the cells incubated with  $\text{Lip}^{\text{NBD}}\text{-CA}$ . These results highly indicate the importance and specificity of Tf moiety for targeting the probe internalization into tumor cells in vitro. The difference in signal intensity and  $T_1$  relaxation time mediated by  $\text{Lip}^{\text{NBD}}\text{-CA}$  and by CA alone might reflect the effective fusion of Lip with tumor cell membrane.

### Quantification of Tf- and Lip-Mediated Cellular Uptake

To evaluate the efficiency of Tf- and Lip-mediated cellular uptake, the FI of the  $\text{Lip}^{\text{NBD}}$  and NIR dye within the tumor cells was quantified following 1 hour's incubation of the cells with probes. The FI of NIR dye in the cells incubated with  $\text{Tf-Lip}^{\text{NBD}}\text{-dye}$  and with  $\text{Lip}^{\text{NBD}}\text{-dye}$  was more than 200-fold higher than that in the cells with dye alone (Table 2). Cells incubated with dye alone showed a similar level of FI to cells without probe and dye exposure (autofluorescence background). Approximately 1.5-fold higher FI of the intracellular NIR dye was observed in cells incubated with  $\text{Tf-Lip}^{\text{NBD}}\text{-dye}$  than in cells incubated with  $\text{Lip}^{\text{NBD}}\text{-dye}$ . Similarly, 2-fold higher FI of  $\text{Lip}^{\text{NBD}}$  was detected in cells incubated with  $\text{Tf-Lip}^{\text{NBD}}\text{-dye}$  or  $\text{Lip}^{\text{NBD}}\text{-dye}$  than in cells incubated with NIR dye alone (autofluorescent background) (see Table 2). The FI of  $\text{Lip}^{\text{NBD}}$  was 1.3-fold higher in cells incubated with  $\text{Tf-Lip}^{\text{NBD}}\text{-dye}$  than in cells incubated with  $\text{Lip}^{\text{NBD}}\text{-dye}$ . Student's  $t$ -tests (two-tailed)

**Table 1.** Comparison between Probe- and Contrast Agent-Mediated Signal Enhancement

MRI Measurement	$\text{Tf}^{\text{NIR}}\text{-Lip}^{\text{NBD}}\text{-CA}$	$\text{Lip}^{\text{NBD}}\text{-CA}$	CA Alone
Relative intensity ( $10^5$ )	$17.7 \pm 0.86$	$15.33 \pm 0.86$	$13.25 \pm 0.78$
$T_1$ relaxation time (ms)	$366.7 \pm 17.1$	$374.3 \pm 17.3$	$408.1 \pm 13.8$

CA = contrast agent; Lip = liposome; NBD = nitrobenzoxadiazole; NIR = near-infrared; Tf = transferrin.  $p < .05$  between probe and CA alone for both relative intensity and  $T_1$ .

**Table 2.** Optical Quantitation of Probe-Mediated Cellular Uptake of Reporters

Reporters	$\text{Tf-Lip}^{\text{NBD}}\text{-Dye}$	$\text{Lip}^{\text{NBD}}\text{-Dye}$	Dye Alone
NIR dye ( $\times 10^9$ )	$6.88 \pm 0.59$	$4.99 \pm 0.51$	$0.23 \pm 0.006$
$\text{Lip}^{\text{NBD}}$ ( $\times 10^7$ )	$2.03 \pm 0.14$	$1.64 \pm 0.09$	$1.10 \pm 0.13$

Lip = liposome; NBD = nitrobenzoxadiazole; NIR = near-infrared; Tf = transferrin.  $p < .05$  between probe and dye alone and also between  $\text{Tf-Lip}^{\text{NBD}}$  dye and  $\text{Lip}^{\text{NBD}}$  dye for both dye and  $\text{Lip}^{\text{NBD}}$  uptake. Quantitation is based on the fluorescence intensity (p/s/cm<sup>2</sup>/sr) of cell pellets.

between cells incubated with probe and with dye alone for both intracellular Lip<sup>NBD</sup> and NIR dye intensity were both significantly different ( $p < .05$ ). The FI in cells incubated with Tf-Lip<sup>NBD</sup>-dye and in cells incubated with Lip<sup>NBD</sup>-dye was also significantly different ( $p < .05$ ) for both intracellular Lip<sup>NBD</sup> and NIR dye uptake.

To further test the specificity of Tf-mediated cellular uptake, cells were first pretreated for 1 hour with unlabeled Tf before incubation with the probes. The amount of Tf was threefold (375  $\mu\text{g}/\text{dish}$ ) higher than that used in the probe (125  $\mu\text{g}/\text{dish}$ ). Following incubation with the probe Tf-Lip<sup>NBD</sup>-dye, the FI of the NIR dye in cells with and without Tf pretreatment was  $2.45 \times 10^9$  and  $3.42 \times 10^9$  p/s/cm<sup>2</sup>/sr, respectively (Table 3). The FI of the Lip<sup>NBD</sup> in cells with and without Tf pretreatment was  $2.57 \times 10^7$  and  $3.45 \times 10^7$  p/s/cm<sup>2</sup>/sr, respectively. Calculation based on the control cells incubated with Lip<sup>NBD</sup>-dye revealed a blockage of 65.6% of the dye uptake and 70.97% of the Lip<sup>NBD</sup> uptake by Tf pretreatment. These results indicate that the probe reporter uptake in vitro was mediated by both Tf and cationic Lip. Tf and Lip have an apparent synergistic effect on the cellular uptake of the probe reporters.

### Probe-Mediated Signal Enhancement of the Tumors In Vivo

Signal enhancement was evaluated in 10 athymic nude mice with solid tumor xenografts. The tumor size ranged from 0.4 to 1.2 cm in diameter. To compare the signal enhancement mediated by the probe and mediated by the CA alone, the same mice were used for the probe and CA-alone studies sequentially with an interval of at least 3 days. Intravenous administration of the probe Tf<sup>NIR</sup>-Lip<sup>NBD</sup>-CA significantly enhanced the tumor image contrast (Figure 3). The enhancement was observed as early as 10 minutes after administration and increased gradually, reaching the maximum at 90 minutes to 2 hours. After that, a gradual decrease in the signal enhancement was observed. Interestingly, the enhancement was greatly heterogeneous within the tumors (see Figure 3). The enhancement

pattern became relatively consistent from 1 to 3 hours. Some areas of the tumors were strongly enhanced initially, whereas other areas were weakly enhanced. The signals from the strongly enhanced region decreased much more slowly than the signals from the region with weak enhancement. For small tumors, the enhancement was relatively uniform and the enhancement was usually observed starting from the peripheral area. Magnevist alone slightly enhanced the image contrast of tumors compared with the baseline images (Figure 4). The maximum enhancement was usually observed at 30 to 60 minutes after injection. The image contrast enhancement started from the peripheral area to the center of the tumors and was relatively uniform within tumors irrespective of the sizes studied here. The signal enhancement decreased rapidly and returned to baseline within 3 hours. The pharmacokinetics of pure Magnevist was different from that of Tf-labeled Magnevist containing Lip. Magnevist containing Lip without linkage to Tf showed a much weaker signal enhancement than either CA alone or Tf<sup>NIR</sup>-Lip<sup>NBD</sup>-CA.

### Detection and Dynamic Change of the Fluorescent Signal in Tumors In Vivo

To understand whether the probe was preferentially accumulated in tumors and whether the fluorescent signal was optically detectable in vivo, tumors were monitored using Tf<sup>NIR</sup>-based optical imaging. The fluorescent signal was clearly detectable as early as 10 minutes and reached the maximum intensity at about 90 minutes to 2 hours after intravenous injection of the probe Tf<sup>NIR</sup>-Lip<sup>NBD</sup>-CA (Figure 5). The FI was related to the tumor sizes, and significant FI was still detectable after 2 days for larger tumors (usually  $> 0.8$  cm in diameter). The FI of smaller tumors became very weak at 24 hours. The FI of Lip<sup>NBD</sup> was too weak to be detectable by optical imaging in vivo, although it was clearly detected ex vivo. High background fluorescence was another reason for the failure to detect Lip<sup>NBD</sup> in tumors. Following intravenous injection, the probe was rapidly distributed throughout the body and

**Table 3.** Blockage of Transferrin-Mediated Uptake of Reporters by Transferrin Pretreatment

Reporters	Tf-Lip <sup>NBD</sup> -Dye	Tf-Lip <sup>NBD</sup> -Dye	Lip <sup>NBD</sup> -Dye
NIR dye ( $\times 10^9$ )	$3.42 \pm 0.17$	$2.45 \pm 0.21$	$1.94 \pm 0.20$
Lip <sup>NBD</sup> ( $\times 10^7$ )	$3.45 \pm 0.29$	$2.57 \pm 0.21$	$2.21 \pm 0.16$

Lip = liposome; NBD = nitrobenzoxadiazole; NIR = near-infrared; Tf = transferrin.

$p < .05$  between pretreated and untreated cells for both dye and Lip<sup>NBD</sup> uptake. Quantitation is based on the fluorescence intensity (p/s/cm<sup>2</sup>/sr) of cell pellets.



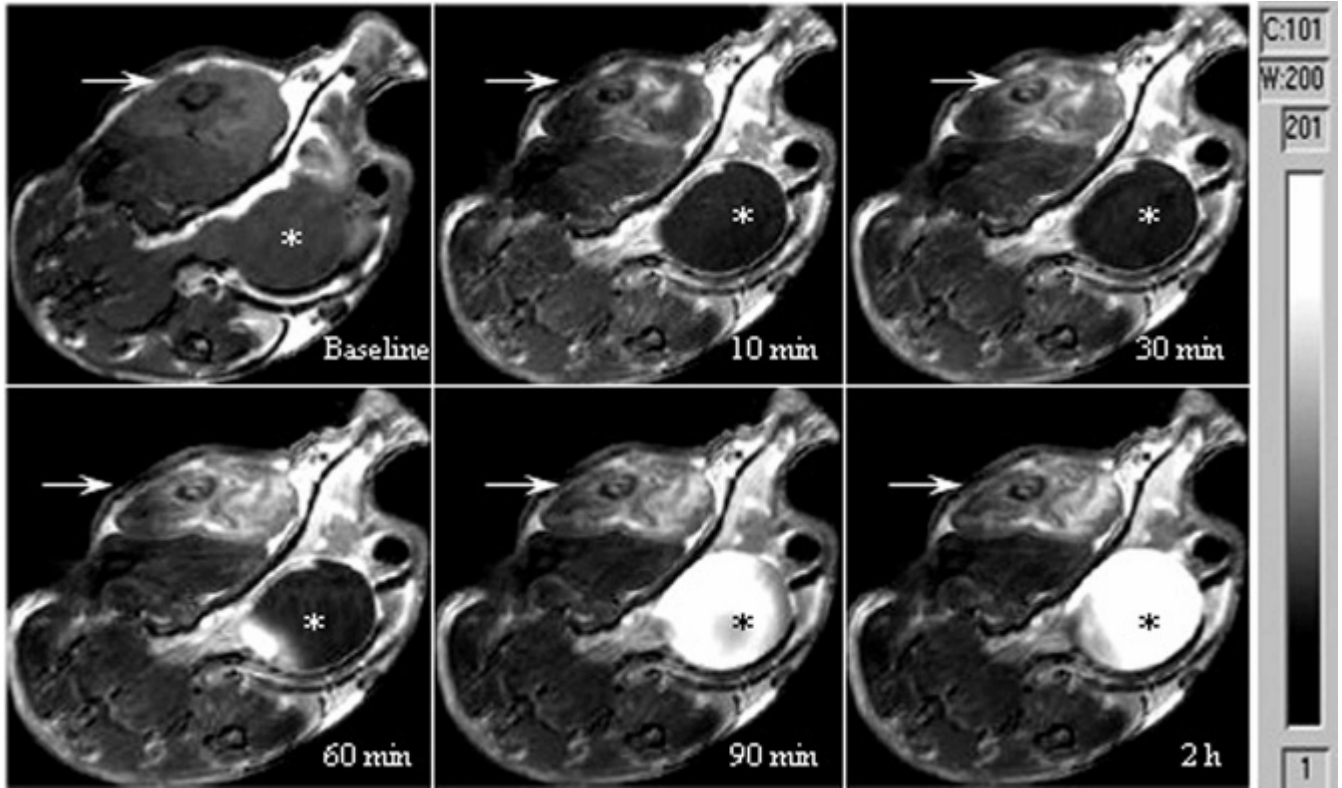


**Figure 3.** In vivo time course of tumor magnetic resonance imaging (MRI) after intravenous administration of the probe transferrin-liposome-nitrobenzoxadiazole-contrast agent ( $\text{Tf}^{\text{NIR}}\text{-Lip}^{\text{NBD}}\text{-CA}$ ) showing gradually increased enhancement of the tumor signal (arrow) and a heterogeneous enhancement pattern. Gradual accumulation of contrast agent in the urinary bladder is evident (\*). The MRI parameters are as follows: echo time = 11.416 milliseconds, repetition time = 800 milliseconds, number of averages = 4, field of view =  $28 \times 30$  mm, matrix size =  $256 \times 192$ , and slice thickness = 1.0 mm.

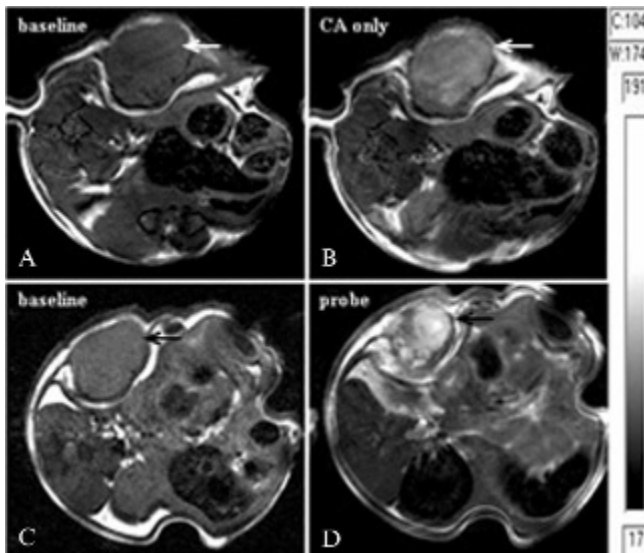


**Figure 4.** Comparison of the signal enhancement by contrast agent (CA) alone (A–B) and by the probe transferrin-liposome-nitrobenzoxadiazole-contrast agent ( $\text{Tf}^{\text{NIR}}\text{-Lip}^{\text{NBD}}\text{-CA}$ ) (C–D). The magnetic resonance images (MRIs) are from the same tumor, with an interval of 72 hours between studies with the probe and with CA alone. A stronger, heterogeneous signal enhancement is achieved with  $\text{Tf}^{\text{NIR}}\text{-Lip}^{\text{NBD}}\text{-CA}$  over CA alone. The MRI parameters are the same as for Figure 3.

was first taken up by the well-perfused organs, such as the liver, spleen, lung, and bone marrow. However, the probe was rapidly washed out from these organs but not from solid tumors. The uptake of the probe in tumors was enhanced because of binding to TfR in the tumor. After the initial rapid increase in the background fluorescence following injection of the probe, the background fluorescence decreased rapidly, as shown in Figure 5H. The tumor to normal (contralateral muscle) ratio varied from 1.3 to 3.4 at the different time points following injection (from 10 minutes to 48 hours), which was related to the tumor sizes. Small tumors (less than 3 mm in diameter) showed less fluorescent signal, perhaps owing to differences in vasculature. Similar to the MRI finding, fluorescent dye containing Lip without Tf linkage failed to induce a preferential increase in fluorescent signal in tumors.

#### Comparison between MRI Signal Enhancement and Pathologic Findings

To understand the underlying mechanism of heterogeneous contrast enhancement within the tumors by the

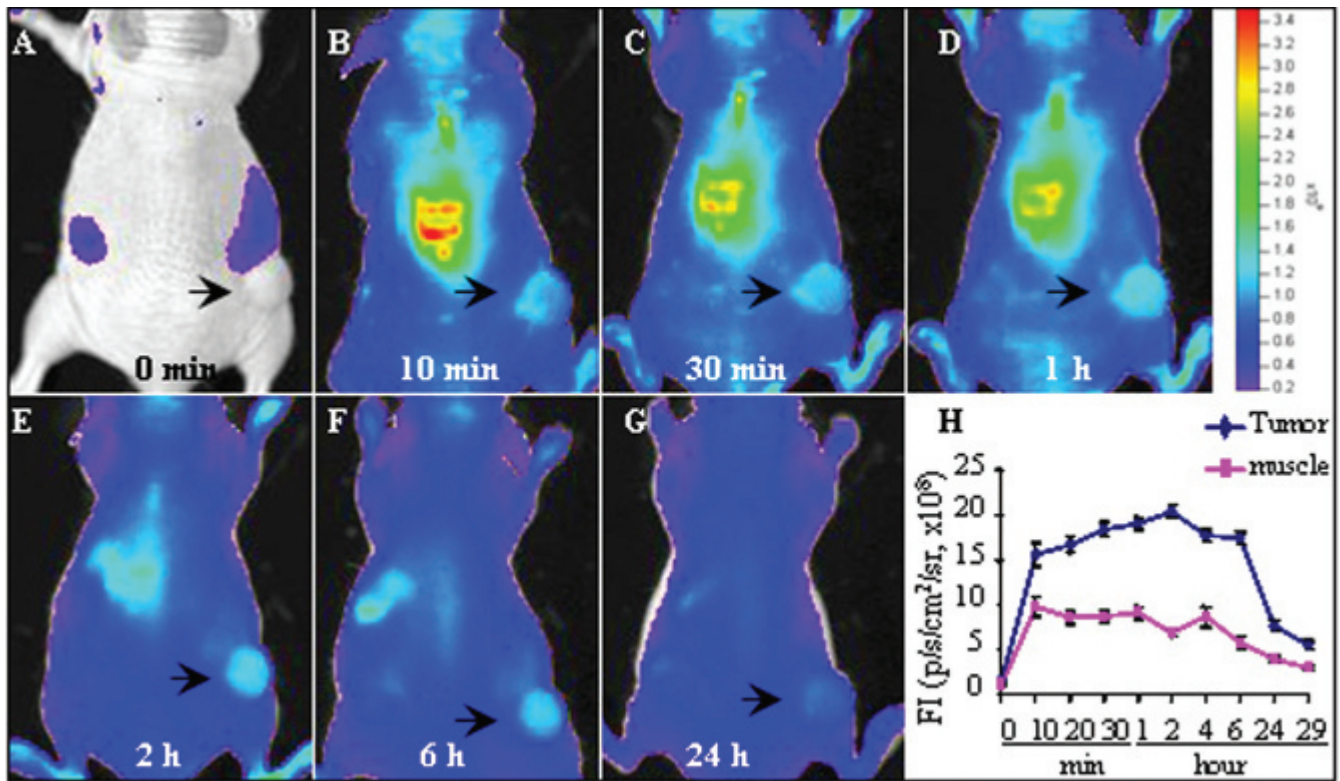


**Figure 5.** Optical imaging of the tumor after intravenous administration of transferrin-liposome-nitrobenzoxadiazole-contrast agent ( $\text{Tf}^{\text{NIR}}\text{-Lip}^{\text{NBD}}\text{-CA}$ ) showing preferential accumulation of fluorescent signal in tumors (A–G). The fluorescence signal was detectable as early as 10 minutes and reached a maximum at about 2 hours and then deceased gradually. H shows the plot of time versus signal intensity obtained from the tumor and the contralateral muscle. The signal intensity is expressed as  $\text{p/s/cm}^2/\text{sr}$ .

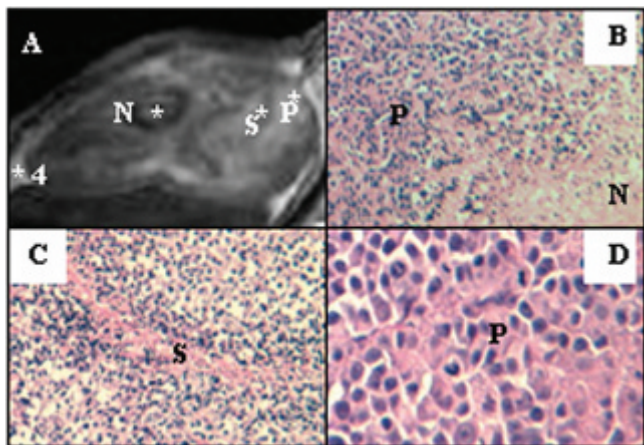


**Figure 6.** Correlation of magnetic resonance imaging (MRI) with pathologic findings showing high consistency between the probe-mediated enhancement pattern in MRI and pathologic findings (hematoxylin-eosin stain). A is a representative MRI (same as Figure 3) showing a heterogeneous enhancement pattern. B shows a region with high proliferation and necrosis ( $\times 250$  original magnification). C shows the stromal tissue ( $\times 250$  original magnification), and D shows the proliferating tumor cells with high mitotic activity ( $\times 400$  original magnification). N = necrosis; P = proliferating cells; S = stromal tissue.

probe, a comparative analysis was performed between MRI signal enhancement and pathologic findings (Figure 6). Pathologically, the tumor cells in large tumors with heterogeneous enhancement usually presented various stages of growth and necrosis. In some areas, the tumor cells were completely necrotized and became amorphous and liquefied. In some other regions, the tumor cells showed dying features such as condensed or broken nuclei or only shadow cells remaining. The highly enhanced regions of the tumors in MRIs represented the more actively proliferating tumor cells, whereas the weakly enhanced areas contained less active or dying cells. The completely necrotized region showed the least enhancement. The heterogeneous signal enhancement by the probe was well correlated with the in vivo morphologic features of the tumors.

**Discussion**

The human Tf-targeted cationic Lip–deoxyribonucleic acid (DNA) complex has been used for efficient gene

transfer in animal models recently. The formulation for optimal transfection of cancer cells has been optimized as a DNA:lipid:Tf ratio of 1  $\mu$ g:10 nmol:12.5  $\mu$ g with Lip composition of DOTAP:DOPE (1:1, w/w). This complex of Tf-Lip-DNA demonstrates a highly compact structure that resembles a virus particle with a dense core enveloped by a membrane coated with Tf molecules spiking the surface.<sup>20,21</sup> Successful gene delivery using Tf-targeted cationic Lip is based on the fact that TfR is overexpressed in various malignant tumors and Tf-TfR-mediated endocytosis is highly efficient. Furthermore, cationic Lip has many advantages, such as high encapsulation capacity, much less immunogenicity and toxicity, and dramatically increased transfection efficiency through linkage with ligands.<sup>22</sup> These characteristics of this system also fulfill the criteria for an ideal system for molecular imaging in vivo. Using the advantages of this system, we developed the probe with both NIR fluorescence and MRI reporters, which is suitable for both optical and nuclear MRI.

Use of the NIR fluorescence molecule minimizes the autofluorescence interference from healthy tissue and allows the visualization of tissues millimeters in depth because of efficient penetration of photons in the NIR range.<sup>11,12</sup> To encapsulate the CA, we directly hydrated the dried Lip films with concentrated CA solution and downsized the Lip-CA complex by sonication and repeated passing through the membrane before linkage with Tf. The Lip:Tf ratio (10:12.5) used in the probe was optimized as reported previously.<sup>20–24</sup> The dosage of Magnevist was 0.2 mmol/kg, corresponding to two times the recommended dose for the patient. For this amount of Magnevist (even threefold more), almost all of the Magnevist was found to be encapsulated within the Lip, as estimated by gel filtration and fluorescence study. Our previous study also confirmed Magnevist encapsulation within Lip using scanning electron microscopy and scanning probe microscopy.<sup>25</sup> The Tf, cationic Lip, and Gd complex was coupled through charge interaction, which makes the preparation of the probe simple enough to be freshly prepared before use. A concern for Lip carrier, as in the gene delivery, is its size. It has been reported that linkage with Tf condenses the Lip-DNA complex with a uniform size of 50 to 90 nm.<sup>20,23</sup> After sonication of the probe, we found that repeated passing through 200 and 100 nm polycarbonate membranes resulted only in a loss of less than 10% of the probe and the majority of the probe particles were within 100 nm in size based on the fluorescence measurement of the probe. Transportation of the probe across tumor vessels occurs via open gaps, vesicular vacuoles, and/or fenestrations. A characteristic pore cutoff size is measured

ranging from 200 nm to 1.2  $\mu$ m in tumors.<sup>26</sup> Another analysis points out that the pore cutoff size is around 400 nm based on in vivo fluorescence microscopy studies of the transportation of sterically stabilized Lip into solid tumors.<sup>27</sup> Therefore, the size of our probe should not be a limitation to transport from tumor vasculature into tumor cells.

We first evaluated the probe-mediated uptake efficiency of the reporters in vitro. To visualize and quantify the efficiency, the components of the probe were differentially labeled. On confocal microscopy, Tf<sup>NIR</sup>, Lip<sup>NBD</sup>, and the encapsulated NIR dye were clearly codistributed within the cytoplasm of tumor cells. They accumulated and formed endosomes again in the peripheral area of the cytoplasm. In Tf-Lip-mediated plasmid DNA transfection, similar endosome formation has been reported by Lee and Kim.<sup>28</sup> They also found nuclear localization of the Tf-Lip. In our system, no nuclear signal of the probe was observed. Quantitative analysis using optical imaging further confirmed the finding of confocal microscopy. The cellular uptake was mediated by both Tf and Lip. Blockage of the TfR with Tf led to significantly decreased uptake. The possibility of nonspecific binding to free NIR dye was excluded because no fluorescent signal of the dye was detected in cells incubated with dye alone. Higher cellular uptake of the Lip and dye in cells incubated with Lip<sup>NBD</sup>-dye without Tf linkage than in cells incubated with dye alone is not surprising. The probe reporters are taken up in vitro by two different pathways. One is due to Lip-mediated endocytosis and membrane fusion process because Lip is an effective transfection reagent.<sup>22</sup> The other is due to binding to TfR. The pretreatment with Tf is not expected to prevent endocytosis of the probe reporters owing to Lip fusion with the cell membrane. Importantly, Tf and Lip showed a synergistic effect on the probe uptake by cells based on our quantitative and blocking analysis. MRI of the cell pellets revealed a similar finding that CA is internalized and the internalization is mediated by both Tf and Lip. The apparent synergistic effect may be explained by a three-step mechanism. The important first step is the specific binding of Tf with TfR on the cell surface followed by the interaction of cationic Lip with anionic cell membrane and finally the receptor- and Lip-membrane fusion-mediated endocytosis.<sup>29</sup>

For MRI study, a T<sub>1</sub>-weighted imaging technique was used to evaluate the positive contrast enhancement mediated by our probe. The actual T<sub>1</sub> shortening in vivo depends on the accumulation of the probe in time, which, in turn, depends on tumor physiology. We have searched the best imaging strategy by using different imaging



sequences and by varying the imaging parameters. The choice of SE sequence with TR = 800 milliseconds and TE = 11.4 milliseconds was based on the consideration of overall image quality, imaging time, and the differences of contrast enhancement between the probe and CA-alone studies. Consistent with our *in vitro* findings, specific targeting of the probe *in vivo* was demonstrated by both optical imaging and MRI. A preferential accumulation of the fluorescent signal in tumors and a significant signal enhancement are clearly achieved with the dual probe but not with CA alone. Time course study revealed a high consistency among confocal images, optical fluorescence, and MRI contrast enhancement. The maximum signal enhancement and FI in tumors are seen at  $\approx 90$  minutes, and both reach a plateau (which includes the maximum) between 1 and 3 hours after intravenous injection, whereas the maximal magnetic resonance contrast enhancement is achieved at about 45 minutes following administration of CA alone and the enhancement reduces to baseline within 3 hours. The magnetic resonance signal enhancement achieved by the dual probe is much stronger than that achieved by the CA alone. These results are consistent with the finding in gene therapy using a Tf-mediated Lip system that high gene transfection efficiency is observed within tumors.<sup>23,24</sup> More interestingly, heterogeneous enhancement in MRIs is evident in large tumors, which correlates well with the histologic findings. Within the range of tumor sizes in the present study, CA alone could enhance the image contrast, but the enhancement was weak and relatively uniform. Heterogeneous enhancement that could be correlated with histology may be potentially valuable. It makes it possible to interpret the pathologic features based on specifically enhanced MRI. More information could be provided to the clinician without further invasive procedure of biopsy.<sup>3,30</sup> *In vivo*, significant uptake of the probe reporters was not observed in the case of Magnevist or fluorescent dye containing Lip without linkage to Tf. This may be explained by the fact that the majority of the Lip accumulated within well-perfused organs, such as the liver, spleen, bone marrow, and lung. The uptake and retention of Magnevist or fluorescent dye containing Lip were very low in tumors. This is in contrast to the uptake of Lip bound to Tf. Positive CA may be superior to the negative CA, such as an iron oxide probe. A decrease in the image intensity by negative CA will complicate interpretation of tumor necrosis and poor expression of target receptors. The advantages of using a superparamagnetic Tf-labeled iron oxide probe are the small size and long-range  $T_2$  effect. Because of the long-range  $T_2$  effect, it requires less compound for a greater image intensity change. Our probe

can be used for optical detection of tumors and is potentially useful for imaging the expression level of TfR and tumor cell growth. These parameters are of great value in predicting the prognosis and treatment selection. This goal can be achieved by measuring the intensity of fluorescence in optical images. However, limited penetration of fluorescence is still a problem, particularly for deep organ tumors. Clearly, use of multimodality reporter constructs can overcome many of the shortcomings of each modality alone.<sup>14,15</sup>

In conclusion, we have described a novel nano-sized molecular probe with both optical and MRI reporters. *In vitro* and *in vivo* analysis confirmed the probe specificity, internalizing efficiency, and sufficiency for multimodality detection. In MRI, the probe significantly enhances the tumor contrast so that it can increase the sensitivity to detect small tumors. The tumor enhancement pattern could help evaluate the pathologic features of tumors *in vivo*, which provides more information for the clinician. Preferential accumulation of the probe NIR fluorescence makes the tumor detectable using NIR-based optical imaging. Furthermore, it provides the possibility of quantifying the specific biomarkers expressed in tumors, which will be helpful to determine the patient's prognosis and response to treatment.

## Acknowledgments

We thank Dr. Elizabeth G. Snyderwine and Dr. Minshu Yu (Laboratory of Experimental Carcinogenesis, National Cancer Institute [NCI], NIH) for their scientific advice. We are grateful to Stephen M. Wincovitch and Susan H. Garfield (CCR Confocal Microscopy Core Facility, NCI, NIH) for help and consultation with confocal microscopy.

## References

1. Pautler RG. Mouse MRI: concepts and applications in physiology. *Physiology* 2004;19:168–75.
2. Artemov D. Molecular magnetic resonance imaging with targeted contrast agent. *J Cell Biochem* 2003;90:518–24.
3. Massoud TF, Gambhir SS. Molecular imaging in living subjects: seeing fundamental biological processes in a new light. *Gene Dev* 2003;17:545–80.
4. Persigehl T, Heindel W, Bremer C. MR and optical approaches to molecular imaging. *Abdom Imaging* 2005;30:342–54.
5. Blasberg RG. Molecular imaging and cancer. *Mol Cancer Ther* 2003;2:335–45.
6. Funovics MA, Kapeller B, Hoeller C, et al. MR imaging of the her2/neu and 9.2.27 tumor antigens using immunospecific contrast agents. *Magn Reson Imaging* 2004;22:843–50.

7. Basilion JP. Current and future technologies for breast cancer imaging. *Breast Cancer Res* 2001;3:14–6.
8. Artemov D, Mori N, Okollie B, Bhujwalla ZM. MR molecular imaging of HER-2/neu receptor in breast cancer cells using targeted iron oxide nanoparticles. *Magn Reson Med* 2003;49:403–8.
9. Mulder WJM, Strijkers GJ, Griffioen AW, et al. A liposomal system for contrast-enhanced magnetic resonance imaging of molecular targets. *Bioconjugate Chem* 2004;15:799–806.
10. Graves EE, Weissleder R, Ntziachristos V. Fluorescence molecular imaging of small animal tumor models. *Curr Mol Med* 2004;4: 419–30.
11. Ntziachristos V, Bremer C, Weissleder R. Fluorescence imaging with near-infrared light: new technological advances that enable in vivo molecular imaging. *Eur Radiol* 2003;13:195–208.
12. Hoffman RM. The multiple uses of fluorescent proteins to visualize cancer in vivo. *Nature* 2005;5:796–806.
13. Schellenberger EA, Sosnovik D, Weissleder R, Josephson L. Magneto/optical annexin V, a multimodal protein. *Bioconjugate Chem* 2004;15:1062–7.
14. Blasberg RG. In vivo molecular-genetic imaging: multi-modality nuclear and optical combinations. *Nucl Med Biol* 2003;30:879–88.
15. Veisheh O, Sun C, Gunn J, et al. Optical and MRI multifunctional nanoprobe for targeting gliomas. *Nano Lett* 2005;5:1003–8.
16. Jones DT, Trowbridge IS, Harris AL. Effects of transferrin receptor blockade on cancer cell proliferation and hypoxia-inducible factor function and their differential regulation by ascorbate. *Cancer Res* 2006;66:2749–56.
17. Hogemann-Savellano D, Bos E, Blondet C, et al. The transferrin receptor: a potential molecular imaging marker for human cancer. *Neoplasia* 2003;5:495–506.
18. Xu L, Pirollo KF, Tang WH, et al. Transferrin-liposome-mediated systemic p53 gene therapy in combination with radiation results in regression of human head and neck cancer xenographs. *Hum Gene Ther* 1999;10:2941–52.
19. Bellocq NC, Pun SH, Jensen GS, Davis ME. Transferrin-containing, cyclodextrin polymer-based particles for tumor-targeted gene delivery. *Bioconjugate Chem* 2003;14:1122–32.
20. Xu L, Frederik P, Pirollo KF, et al. Self-assembly of a virus-mimicking nanostructure system for efficient tumor-targeted gene delivery. *Hum Gene Ther* 2002;13:469–81.
21. Kursu M, Walker GF, Roessler V, et al. Novel shielded transferring-polyethylene glycol-polyethylenimine/DNA complexes for systemic tumor-targeted gene transfer. *Bioconjugate Chem* 2003;14:222–31.
22. Simoes S, Pires P, Duzgunes N, Pedrosa de Lima M. Cationic liposomes as gene transfer vectors: barriers to successful application in gene therapy. *Curr Opin Mol Theory* 1999;1:147–57.
23. Nakase M, Inui M, Okumura K, et al. p53 gene therapy of human osteosarcoma using a transferring-modified cationic liposome. *Mol Cancer Ther* 2005;4:625–31.
24. Pirollo KF, Xu L, Chang EH. Non-viral gene delivery for p53. *Curr Opin Mol Ther* 2002;2:168–75.
25. Pirollo K, Dagata J, Wang P, et al. A tumor-targeted nanodelivery system to improve early MRI detection of cancer. *Mol Imaging* 2006;5:41–52.
26. Hobbs SK, Monsky WL, Yuan F, et al. Regulation of transport pathways in tumor vessels: role of tumor type and microenvironment. *Proc Natl Acad Sci U S A* 1998;95:4607–12.
27. Umezaki S, Maruyama K, Hosoda JI, et al. Direct measurement of extravasation of poly-ethyleneglycol-coated liposomes into solid tumor tissue by in vivo fluorescence microscopy. *Int J Pharm* 1996; 144:11–7.
28. Lee SM, Kim JS. Intracellular trafficking of transferring-conjugated liposome/DNA complexes by confocal microscopy. *Arch Pharm Res* 2005;28:93–9.
29. Yin J, Lin AJ, Buckett PD, et al. Single-cell FRET imaging of transferrin receptor trafficking dynamics by sf-p-catalyzed, site-specific protein labeling. *Chem Biol* 2005;12:999–1006.
30. Mankoff D. Imaging in breast cancer—breast cancer imaging revisited. *Breast Cancer Res* 2005;7:276–8.

## Noninvasive Methodology for Wellness Baseline Profiling

Danny Wen-Yaw Chung<sup>1</sup>, Yuh-Show Tsai<sup>1</sup>; Shaou-Gang Miaou<sup>1</sup>, Walter H. Chang<sup>1</sup>, Yaw-Jen Chang<sup>1</sup>,  
Shia-Chung Chen<sup>1</sup>, Y.Y. Hong<sup>1</sup>, C.S. Chyang<sup>1</sup>,  
Quan-Shong Chang<sup>2</sup>, Hon-Yen Hsu<sup>2</sup>, James Hsu<sup>2</sup>, Wei-Cheng Yao<sup>2</sup>, Ming-Sin Hsu<sup>2</sup>;  
Ming-Chung Chen<sup>3</sup> and Shi-Chen Lee<sup>3</sup>,  
Charles Hsu<sup>4</sup>, Lidan Miao<sup>4</sup>, Kenny Byrd<sup>4</sup>, Mohamed F. Chouikha<sup>4</sup>, Xin-Bin Gu<sup>4</sup>, Paul C. Wang<sup>4</sup>, and  
Harold Szu<sup>4,5</sup>

<sup>1</sup>Chung Yuan Christian University, Dept. ECIS & Dept. BME, Chung-Li, Taiwan,

<sup>2</sup>Ming-Shen Hospitals at Long Tan, Chung-Li, Taiwan,

<sup>3</sup>Institute of Bio-Medical Engineering, National Taiwan University Hospital, NTU, Taipei, Taiwan

<sup>4</sup>School of Dentistry and Radiology Dept. of Medical School Hospital, Howard University, Wash. DC;

<sup>5</sup>Office of Naval Research & Q23 of NSWCDD, VA

### ABSTRACT

We develop an accumulatively effective and affordable set of smart pair devices to save the exuberant expenditure for the healthcare of aging population, which will not be sustainable when all the post-war baby boomers retire (78 millions will cost 1/5~1/4 GDP in US alone). To design an accessible test-bed for distributed points of homecare, we choose two exemplars of the set to demonstrate the possibility of translation of modern military and clinical know-how, because two exemplars share identically the noninvasive algorithm adapted to the Smart Sensor-pairs for the real world persistent surveillance. Currently, the standard diagnoses for malignant tumors and diabetes disorders are blood serum tests, X-ray CAT scan, and biopsy used sometime in the physical checkup by physicians as cohort-average wellness baselines. The loss of the quality of life in making second careers productive may be caused by the missing of timeliness for correct diagnoses and easier treatments, which contributes to the one quarter of human errors generating the lawsuits against physicians and hospitals, which further escalates the insurance cost and wasteful healthcare expenditure. Such a vicious cycle should be entirely eliminated by building an “individual diagnostic aids (IDA),” similar to the trend of personalized drug, developed from daily noninvasive intelligent databases of the “wellness baseline profiling (WBP)”. Since our physiology state undulates diurnally, the Nyquist anti-aliasing theory dictates a minimum twice-a-day sampling of the WBP for the IDA, which must be made affordable by means of noninvasive, unsupervised and unbiased methodology at the convenience of homes. Thus, a pair of military infrared (IR) spectral cameras has been demonstrated for the noninvasive spectrogram ratio test of the spontaneously emitted thermal radiation from a normal human body at 37°C temperature. This invisible self-emission spreads from 3 microns to 12 microns of the radiation wavelengths. This pair of cameras are used in the military satellite surveillance imaging operated at 3~5 mid IR band and 8~12 long IR band accompanied by several other UV and visible bands cameras. We can thereby measure accurately both the thermal emission bands at the mid IR and the long IR ( $X_1$   $X_2$ ). The spectral ratio will be independent of the depth and imaging environment. Similarly, we will take six times per pair saliva samples ( $X_1$   $X_2$ ) inside the upper jaw for three meals daily, of which the dynamics is shown as a delayed mirror image of “blood glucose level”. And for which we must design a portable lab “system on chip (SOC),” and the micro-fluidity of pair channels per chemical reactions. According to the same biochemical principle of spontaneity, we apply the identical algorithm to determine both the ratio of hidden malignant and benign heat sources ( $s_1$ ,  $s_2$ ) and the blood glucose & other sources ( $s_1$ ,  $s_2$ ) leaking into the saliva. This is possible because of the Gibbs isothermal spontaneous process, in which the Helmholtz free energy must be minimized for the spontaneous thermal radiation from unknown mixing of malign and benign sources or the diffusion mixing of glucose  $s_1^*$  and other sources  $s_2^*$ . We have derived a general formula relating two equilibrium values, before and after, in order to design our devices. Daily tracking the spectrogram ratio and saliva glucose levels are, nevertheless, needed for a reliable prediction of individual malignant angiogenesis and blood glucose level in real time.

**Keywords:** Diabetes, Blood Glucose Level, Saliva Glucose Level, Angiogenesis, Malign Tumor Detection, Point of Care, Blind Sources Separation, Free Energy, Unsupervised Learning.

## 1. WELLNESS BASELINE PROFILE EXAMPLARS

Why do we explore, despite of available hospitals paid by the insurance, those military high-tech instruments and clinical know-how for homecare? When we visit hospitals, we are either seriously ill or other is or we are taking annul physical check. We know we become what we eat, we need daily exercise, and both our minds and bodies related intimately to our wellness. Yet, we are less familiar with the Nyquist aliasing fact of tracking diurnal physiology change requires a minimum of twice per day sampling rate of our vital signs to help determine the complex transition from multiple healthy states to binary sickness, of which only the final consequence is familiar when it happens, but not before it does. Usually for ourselves we are often too late than early for we have nothing to help us, other than those pre-moon landing antiquity tools available at households to help maintaining a better quality of retirement life. We need developing new affordable homeowner security surveillance system, which can not only save the escalating healthcare expenditure and avoid those unnecessary litigation wastes against physicians, hospitals and health agencies [1]. To minimize human errors, we need to practice “a stitch in time saves nine” by applying advanced defense surveillance methodology against home-front infectious microorganism, where the wellness is deteriorating and the disease occurring. We need affordable and convenient household devices for protecting one of the most insidious diseases---malign tumors and diabetics, among cardiovascular, and dementia disorders attacking one-quarter of aging population of US alone. When compared to a yearly baseline physical checkup alone, this military smart sensor web can measure by noninvasive means the wellness baseline profile (WBP) for individual diagnostic aids (IDA), which promises the timeliness in early diagnosis with much less human errors.

The anatomic architecture of human brains and endocrine glands define the physiology enzymatic constraints of macroscopic variables. The central nervous system (CNS) and endocrine glands may be found in EU Neuroscience Site and Am. Acad. Otolaryngology for ENT MD. We shall refrain from complex CNS anatomy, rather call out the simpler salivary glands the parotid, submandibular, and sublingual glands depicted in Fig. 1 (lower part of endocrine thyroidal, pancreatic, kidney’s and etc. are not shown). Since our report for diabetes follows the same thesis of translating military know-how of the power of pair sensors for invariant feature extraction by the same underlying unsupervised learning principle, we will further explain the details as follows:

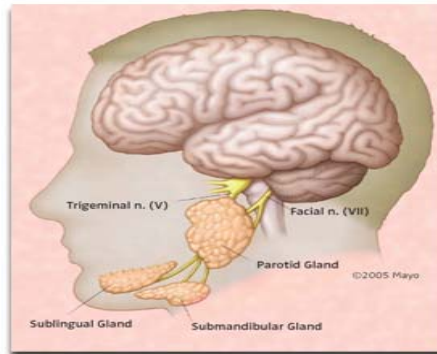


**Fig. 1 Anatomy of CNS and ENT Saliva glands**

To demonstrate such feasibility of the translation of military real world know-how, we focus on two exemplars for a noninvasive surveillance: early breast tumors detection and diabetic glucose level profile. The lesson learned reported in this paper may be useful for other common syndromes for aging population such as Alzheimer dementia and cardiovascular disorders. We have demonstrated early warning automatic target recognition (ATR) capability by using two infrared spectral bands satellite cameras tracking woman soldiers’ breast tumors over the time that is several months ahead of the confirmation by X-ray mammograms [2].

Historically, a single infrared imaging using spectral-integrated CCD camera for temperature map was called the thermograms (as opposed to our ratio of spectrograms), which was unfortunately disapproved by

physicians. This denial for quantitative analyses is because of the procedure of measuring temperature map suffering too many variables giving different answers to an identical patient by taking two snapshots at two different times (one at the moment of disrobe, the other minutes later after hands being cooled down by ice water whereas malign tumor persist hot temperature). This new military approach should be sharply in contrast to that of single night-vision camera. The night-vision camera, of which its CCD sensory material can spectrally integrated over the full infrared spectrum, has enough SNR without the need of cumbersome liquid Nitrogen cryogenic cooling of imaging plan. On the other hand, such a CCD camera can only produce a local temperature distribution of breasts, or faces, before and after artificial cooling of the subject, known as the infrared “thermograms” plagued with both heat source depth variation and environmental uncertainty. Perhaps, this inadequacy experience was not unlike those passive SARS test by one-time and one-infrared-camera at the airport where the suspects took the Aspirin suppressing SARS fever and passed the quarantine checkpoints.

The most important of all is that our spectrogram ratio is invariant towards variable attenuations due to different breast tissues, sizes and imaging environments whose effects are cancelled naturally by the division for computing the ratio. Although both spectral components suffer individually a similar attenuation factor at arbitrary depth of malign tumors (or in the propagation through an identical turbulent atmosphere) and the same condition of imaging environment, the spectral ratio of the same hot tumor source, a tank engine, or military supply lines can cancel out the same attenuation factor, and becomes invariant to both the depth of malign tumor hot sources and the imaging environmental variation. Thus, new noninvasive IR spectral ratio over time provides credible warning signs at a much earlier stage than the invasive X-ray mammogram at the metastasis stage. It is at the Angiogenesis stage (Greek: vessel generate) promoted by the Vascular Endothelial Growth Factor (VEGF) protein generating inflammation and new capillary vessels, before the tumor extravasations and metastasis stages (behaving not unlike military buildup of supply-line before war declaration which is likewise detectable passively by multispectral satellite images).

In our patent [2] we have computed the percentage of malign versus benign tumor cells per pixel. Given only two infrared spectral data ( $x_1$ ,  $x_2$ ) per pixel ( $x_1$  at 3~5 micron wavelength and  $x_2$  at 8~12 micron wavelength), we can predict the spontaneous thermal radiation from hot infrared sources ( $s_1$ ,  $s_2$ ) ( $s_1$  stands for the number of malign tumor cells at local inflammation elevated temperature localized at a specific depth, where  $s_2$  for the number of normal body cells or benign tumor at the healthy temperature), without knowing individual breast tissue medium impulse response matrix [A] mixing those infrared heat sources ( $s_1$ ,  $s_2$ ). The missing conditions causing an ill-posed matrix inversion are identified correctly to be the Gibb’s biochemistry spontaneity principle of minimization of isothermal Helmholtz free energy. Since Gibb’s principle of spontaneity will be also useful for us to estimate a saliva glucose source and the other non-glucose source in Sect.2, we explain the passive spectrograms imaging for the early screening of malign tumors. The gold standard diagnosis of well-developed breast cancers remains to be the X-ray mammograms and in situ biopsies, which has helped to discover 250 thousands women and 2 thousands men annually in US alone, and documented the trend of breast cancer risk due to modern child less syndrome [3]. According to Sweden epidemiology studies over last few decades, women with breast cancers whether taking the mammograms or not, their average life expectancy is the same about five years [4]. In other words, the discovery of breast cancers happens at the final metastasis stage too late and too dangerous in a region filled with lymph nodes for spreading. The metastasis left behind micro-calcification deposits due to the apoptosis of cells, which could not keep up the rapid growth rate. These calcium deposits became opaque to the X-ray mammogram imaging and showed a dark morphology recognizable to the oncology radiologists. There are several stages of cancers. They are the primary tumors stage; invasion blood vessel stage; blood intra-vasation stage Fig.2; extravasations transport stage; and the metastasis stage.

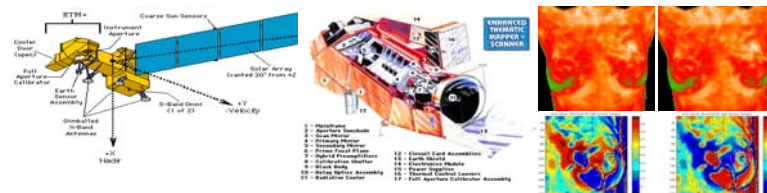


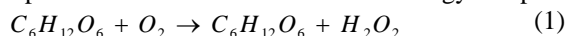
Fig. 2 Transition of military persistent surveillance to the wellness of woman soldiers for breast cancer warning at early angiogenesis stage by tracking the dual color infrared spectral ratio per pixels.

Although the diagnoses by means of two infrared spectrograms ratio over time are nonspecific, they provide noninvasive and convenient warning sign for households. This important invariant feature is derived from the signal and noise ratio (SNR) pre-conditioning allowing the blind sources separation (BSS) by the power of two cameras. While Phase II Receiver Operation Characteristics efficacy studies is going on according to FDA standard of double-blind with independent control and referee system, another hardware team works for affordable ODM/OEM of dual IR-spectral camera [5]. For affordability about \$1K, we merge two cameras into one camera. We adopt one compound lens following the main optical beam interrupted by a beam splitter which focuses the Mid IR portion of the incoming light towards a mini-cryogenic Mid IR image plan located below the main camera and is orthogonally to the main beam where the CCD night vision digital camera locates. In this report for diabetes, we translate military know-how of the power of pairs and the same underlying unsupervised learning, but a new teaming following Sony lesson of “parallel market design of sequential product line.” We choose the semiconductor ODM/OEM Taiwan and the policy-center, Washington DC, responsible for one-fifth GDP expenditure for the healthcare of 78 millions aging baby boomers.

## 2. SALIVA

The parotid through tubes that drain saliva, called salivary ducts, near our upper teeth, submandibular under our tongue, and the sublingual through many ducts in the floor of our mouth, and they all secrete saliva into our mouth. Besides these glands, there are many tiny glands called minor salivary glands located in our lips, inner cheek area (buccal mucosa), and extensively in other linings of our mouth and throat. Salivary glands produce the saliva used to moisten our mouth, initiate digestion, and help protect our teeth from decay. As a good health measure, it is important to drink lots of liquids daily. Dehydration is a risk factor for salivary gland disease. Obstruction to the flow of saliva most commonly occurs in the parotid and submandibular glands, usually because stones have formed. A dental x-rays may show where the calcified stones are located. The most common salivary gland infection in children is mumps (not caused by stone constriction) which involves the infectious parotid glands. In fact, many of these lymph nodes are actually located on, within, and deep in the substance of the parotid gland or near the submandibular glands. Thus, saliva is rich with IGG. Diabetes may cause enlargement of the salivary glands, especially the parotid glands. Alcoholics may have salivary gland swelling, usually on both sides. Saliva digests starch or other carbohydrate through glycerin into single monomer e.g, glucose etc easily entering intestine blood stream.

Then, the pancreatic insulin endocrine helps it enter into living cells where an oxygenated denaturalization of glucose can produce 4.3 calories of stored free energy and peroxide Eq.(1).



Equation (1) is the main chemistry reaction for the measurement of glucose by measuring the electrical charge property of the peroxide [9,10]. Optical florescence spectrum has been also used [10] for molecular tagged imaging for real time hospital kidney dialyses.

We now digress to introduce pancreas insulin and blood sugar glucose. Insulin is a long peptide chain secreted naturally by  $\beta$ -islets of pancreas Schwamm cell, artificially synthesized by Nobel Laureate Bruce Merrifield of Rockefeller (attached one end of peptide to a solid suspension and efficiently work on the other side chain as invented independently by a Shanghai biologist published in Chinese journal). Insulin can unlock gateways of our body's cells and help blood sugar penetrate cell membrane as energy to perform daily activities. The blood sugar is the simplest digested carbohydrate:  $C_6H_{12}O_6$ , as if 6 carbons C were merged with 6 waters  $H_2O$ . However, the glucose needs to store more free energy than fat and protein in 3D morphology. Unlike 6-carbon forming a flat hexagon benzene ring, the glucose has only 5 carbons, pluses 1 oxygen displacing the sixth carbon into a zigzag backbone plane in either 3 segments over the plane like a chair formation, or 2 segments like a bow-tie symmetry. All 6 carbons, including the displaced one, are further connecting to the hydrophilic hydroxide OH, which to taste sweet must be attached along the z-axis perpendicular to the backbone (otherwise along the x-y orbital plane is not sweet glucose). Evolutionally over billion years, the oxygen entering cellular metabolism provides large free energy storage, much more metabolic reactions and rich variety of trans-membrane communications for Cambrian



explosion era circa 543 MY of eukaryotic complex cellular organisms [Nature V. 455, p. 35, 2007; p.47, 2007]. Now, we return to define 3 types of diabetic disorders. In type 1 diabetes, the insulin deficiency is due to pancreatic lymph nodes, mediated by the death of pancreatic  $\beta$  cells, produce immunological T-cells targeting Peri-islet Schwann cell, called the “autoimmunity.” The pancreatic sensory neurons have defective capsaicin TRPV1 (Transient Receptor Potential Vanilloid-1) receptors of insulin causing pancreas islet inflammation, due to imbalance of neuron response of neuro-peptide substance p & insulin [6]. Type 2 diabetes is caused by “insulin resistance,” namely our body does not use insulin properly. As a result, glucose entry into cells is impaired as if the cells were insulin-resistive. A hybrid of “autoimmunity” and “insulin resistance” is called diabetes type 1-1/2. Recently, NICHD explored the Saliva IGG for the accurate timing for the effectively administrating the second booster shot for the vaccination of new born infant in Vietnam with their patented conjugated vaccines. Pasteur Institute of France with the inscription motto: “chances favors a prepared mind” has discovered from the saliva a new substance called Opiorphine which is about 3~6 times stronger than morphine and easily metabolized over time.

A non-invasive prototype device, monitoring the blood glucose levels, will be implemented according to the indirect measurements of pair of saliva glucose levels using the micro-fluidity-intake dual channels with a system on chip computation as a pocket lab on chips. Twenty millions’ diabetes exists in US alone, of which one out of three does not even know that they have the disease until damage is done. Diabetic symptoms are frequent urination, increase fatigue, excess thirty, irritability, extreme hunger, blurry vision, and unusual weight loss, compared to ones own past data presumably in a healthy initial state. Those seniors who are not obese and those who have weight challenge have different risk of diabetes, but increased with deteriorate physique. The excessive blood sugar, glucose, helps lipids and fatty cholesterol streaks enter the artery lining forming plagues (called atherosclerosis, due to excessive triglyceride converted from glucose by liver). The plague in veins and arteries can severely reduce blood flow, and diminish the nutrient and the oxygen supply (attached to the red blood cell via iron of hemoglobin) to the vital organs, the brain and the heart, resulting respectively in stroke and heart attack. While blood test-kits and pressure guns for insulin injection are available, the stress of intrusive measurement and the inconvenience with potential contamination are not so desirable on daily basis for both junior diabetes and aging baby boomers. In this paper, we design a noninvasive pocket saliva test kit for minutia saliva intakes, based on our exact equilibrium solution of a time-averaged model of spontaneous biochemistry diffusion of glucose substance from excessive “blood glucose level (BGL)” seeping through saliva glands mechanism. Such a dynamics profile “saliva glucose level (SGL)” is delayed and much reduced in the magnitude about few percentages. If we could measure for each individual both dynamics in a time-average sense about 30 minutes, we might deduce a correct prediction formula for the peak quantity of BGL and the time for the individual and thus reduce the unwanted frequency of real-time blood tests. This prediction aspect will report in the future studies after we finish and can apply the SOC prototype model I. We will concentrate on the development of an analytical modeling for the purpose of designing dual intake channels SOC, together with some numerical values obtained from few hospital sick patients.

However, such a hope between the correlation between “saliva and diabetics” has a mixed opinion in the last four decades, according to the archival 78 articles of NIH/National Library of Medicine. Braun et al. of Hungarian reported the first observation in 1966; Mehrotra et al. of Indian reported in 1968 of a village of diabetic seniors having serious periodontal disease. Recently in 2006, Siudikiene et al. of Lithuania studied diabetes-type 1 inferring from saliva [6,7]. Carda et al. of Espana investigated diabetes-type 2 using saliva [8]. Recent works [9] revealed large individual variation between blood and saliva glucose levels (BGL & SGL), the universal correlation between BGL and SGL has not yet been fully established [10]. We notice that most of the correlation experiments were based only on the second order statistics of selected sparse sampling, e.g. during the office hours after fasting the night before. Although the saliva kit is less accurate per se than blood tests in general; the unsupervised blind sources separation (BSS) of pair saliva sampling might produce invariant features, which over time development might relate better with arbitrary delay to those permeable blood constituents through the gland-blood barrier membrane.

### 3. UNSUPERVISED ALGORITHM FOR HOMEOSTASIS RESOURCE SHARING

Microscopic molecular kinetics model is currently beyond our ability to understand how exactly the unknown sources  $S = (s_1, s_2) = (s_{\text{malign}}, s_{\text{benign}}) = (s_{\text{glucose}}, s_{\text{other}})$  are diffusively emissive and permeate matrix



[A?] through breast tissue and saliva glands ducts respectively. Currently, advanced in vivo studies with molecular-tagged imaging may illuminate the complete pictures of underlying signaling pathways and molecular mechanisms for physiological modeling and treatments. In this treaty, we concentrate on the equilibrium biochemistry principle to develop macroscopic model.

Following the Gibb's spontaneity principle governing biochemistry processing, we introduce a resource sharing homeostatic learning theory deriving the unsupervised learning Hebb rule and sigmoid logic for effortless sensory processing since 1999[14-16]. Accordingly, the (isothermal) Helmholtz free energy defined in thermodynamics as  $H = E - T_o S$ , where  $E$  is information processing synaptic energy and  $T_o$  is the local temperature of the brain at an averaged value 37°C for most healthy humans; and Shannon-Boltzmann-Clausius Entropy is  $S = -s_I \log s_I - (1-s_I) \log (1-s_I)$  for two normalized component sources. Several interesting remarks are in order:

(i) Why do intelligent animals involve pair inputs and isothermal brains?

(a) Fact 1: constant temperature of their brains per species (37°C for humans; 40°C for chicken) and

(b) Fact 2: paired input sensory organs (e.g. binaural hearing, binary vision, zonal tasting, & tactile, etc) while in contrast the output sensory organ is always singular (e.g. one mouth to speak, one exit going for bathroom, etc.). An efficient fusion must happen at the points of correspondence of two sensors, based on the Gibb's principle of the aforementioned minimization of the isothermal Helmholtz free energy  $H$ . This is called the power of pairs: "agreement, the signal; disagreement, the noise" requiring no delay of outside teacher supervision. Imagine the clarity power would be if adopted for coincidence-accounted binaural hearing aids. In order to save the processor energy,  $H$  must be vanishingly small for any isothermal spontaneous processing.

(ii) About the conscience of all hot blooded animals. Nobel Laureate Francis Crick has led a frontier research for decades with the help of Dr. Cristof Koch at Neuroscience of Salt Institute who seek for the anatomical structure supporting the consciousness. In the last publication [Philos. Trans. Royal Soc. of London, 2005], he stated that the architecture must infer the functionality and vice versa. Koch and he had tentatively identified the consciousness architecture is a thin sheet of grey matter resides in parallel two way connections to and below the cortex computing feelings, seeing, hearing, language and decide what to do, known as the "Clastrum, the conductor of an orchestra binding all".

In early theory they measured an ubiquitous firing rates binding at 30Hz as the wakening of consciousness. Our free energy theory might estimate a bound on the size of neurons involved in the Clastrum. In other words, such a spontaneous firing rate must be satisfied a minimum isothermal free energy. The firing rate involves the phase transition from the un-consciousness randomness to the consciousness ground state. Gibbs theory of the biochemical spontaneity support the Crick-Koch ubiquitous firing rates, for which the minimum Helmholtz free energy associated at the 37°C Celsius temperature, should effortlessly support all neurons. Owing to the linearity of the Einstein-Boltzmann energy formula the uncertainty of our brain size can be estimated

$$E = Nhf = K_B T_o,$$

ranging between 20 billions and 10 billions neurons corresponding to the range between 30Hz and 60 Hz firing rates respectively for the ground state of mindlessness for which it must be less than the consciousness decision at a synaptic junction as measured experimentally by Nobel Laureates Hodgkin and Huxley about 100Hz firing rates. The computation follows from a physics units table issued by NIST as follows:

$$\begin{aligned}
E &= N hf = N \times 6.67 \times 10^{-34} \text{ Joule} \cdot \text{sec} \times 30 \text{ sec}^{-1} = N \times 200.1 \times 10^{-34} \text{ Joule} \\
&= K_B T_o = K_B (273 + 37) = 310 \times 1.38 \times 10^{-23} \text{ J} = 427.8 \times 10^{-23} \text{ Joule} \\
\text{Thus, the number of neurons of a human brain is } N &\cong 2 \times 10^{11} \text{ about 2 times 10 billions} \\
\text{The body thermal energy} &= \frac{310}{300} \left( \frac{1}{40} \text{ eV} \right) = 0.025825 \text{ eV} = 2.6 \% \text{ eV} \\
\text{which emits a Planck spectrum peaked at the long IR at } \lambda &\cong 8 \sim 12 \text{ micron} \\
\text{where the Planck } h &= 6.67 \times 10^{-34} \text{ J} \cdot \text{sec} = 6.67 \times 10^{-34} \text{ J} \cdot \text{sec} \frac{1 \text{ eV}}{1.6 \times 10^{-19} \text{ J}} = 4.17 \times 10^{-15} \text{ eV} \cdot \text{sec} \\
\text{Boltzmann } K_B &= 1.38 \times 10^{-23} \text{ J} \cdot \text{K}^{-1} = 1.38 \times 10^{-23} \text{ J} \cdot \text{K}^{-1} \frac{1 \text{ eV}}{1.6 \times 10^{-19} \text{ J}} = 0.86 \times 10^{-4} \text{ eV} \cdot \text{K}^{-1} \leq 0.01 \% \text{ eV} \cdot \text{K}^{-1}
\end{aligned}$$

In summary, if we take seriously Crick and Koch model of ubiquitous binding of firing rates for the wakening of consciousness, we can estimate our brain beginning at the binding of 30Hz firing rates which might effortlessly support up to all 20 billions' neurons per an isothermal brains kept at 37°C.

(iii) We assert that the sharing of (neural transmitting) resources at isothermal equilibrium value may be responsible for Gibb's phenomena and lateral inhibition at ganglion neurons level (for computational proof, see Frank McFadden & Szu [17]). The Gibb's overshooting & undershooting phenomena could be understood as resource sharing at the isothermal equilibrium. In other words, a limited constant resource of neuro-transmitting must be shared by neighborhood neurons. For example, a ideal step-function light illumination is shown in Figure 3 a), in which (beneath layers of 150 millions of rods & 6.2 millions of cons) the sensory bipolar and ganglion neurons on the bright side at a light-dark edge boundary can utilize locally shared resources that are underutilized by the neurons on the dark side; therefore, they are relatively overexcited compared with other neurons on the bright side. This over-utilization of un-used resource by dark side neurons, in turn, leads to depletion of resources in the isothermal equilibrium available to the neurons on the dark side near the boundary. A similar phenomenon occurs with a rectangular light illumination in Fig 3 b) with the phenomena of lateral inhibition (as seen in the Mexican hat shaped response curve at the ganglion level) –over-utilization of local resources by neurons closer to the peak depletes resources that would otherwise be available to nearby neurons. Fig. 3c shows the limited resource due to the isothermal free energy minimization.

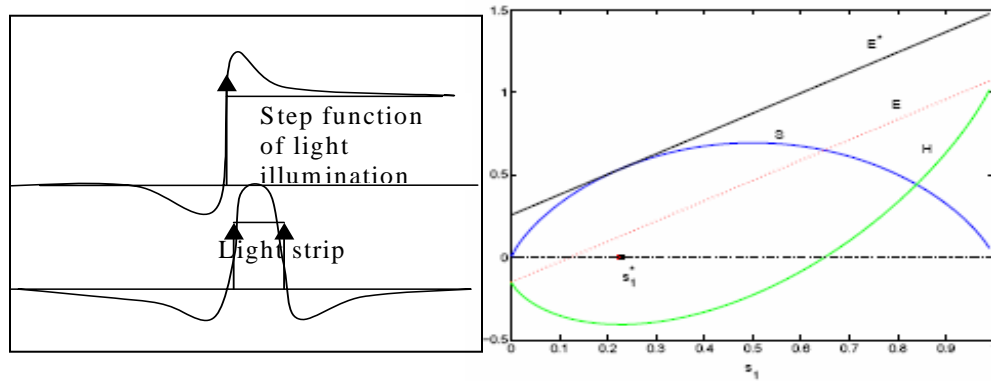


**Figure 3. Over-utilization of shared resources among neurons of those light-stimulated receptors in the neighborhood of non-stimulated receptors responsible for the a) Gibb's overshooting & undershooting; in case of a lighted stripe we obtain by the symmetry of two opposite step functions b) Lateral inhibition in the Mexican hat shape, and c) Gibbs spontaneity principle for effortless fusion of early vision mediated by local sharing of neuro-transmission resources: namely the equilibrium predicted by Szu<sup>36</sup> occurs at  $s_1^*$ , where minimum isothermal free energy  $H$  is minimized. [17]**

A difficulty of this explanation in terms of equilibrium model is associated with the long replenish time needed neuro-transmitting vesicle substance associated slow thermal diffusion process. However, this phenomenon is overcome by eyeballs jittering with different focal points, called saccades at hundred Hertz frequency, in order to rapidly utilize those under-used neighborhood receptors and firing neurons, so long that internally the brain keeps track of eye motion with respect to the inertial frame (as the neural circuitry to accomplish this detail balance reported in Nature 2007). As a result, we stabilize the jittering and mosaic images (Hsu et al. on UAV videos, loc. Cit.).

(iv) Szu assumed further that  $E$  is analytic in the input sensory pair vector  $X$  and the output feature vector  $S$ , such that a piecewise linear model is  $X \cong [A]S$  where matrix  $[A]$  is an unknown impulse response matrix. The information fusion energy can be analytically expanded near the unexcited equilibrium state  $E_o$  as Taylor series  $E = E_o + \text{linear} + \text{higher order terms}$ . In fact, the Hebbian learning rule for unsupervised learning of data  $X_j$  drops out from the analyticity of information fusion energy

$$E = E_o + \mu ([W]X - S) + \text{second order} \quad (2a)$$

$$\frac{\partial W_{ij}}{\partial t} = -\frac{\partial H}{\partial W_{ij}} \Rightarrow \Delta W_{ij} \approx \mu_i X_j \quad \text{Unsupervised Hebb learning rule} \quad (2b)$$

The sigmoid logic follows from rigorously from the minimization of free energy [15,16] yields the components of feature vector  $S$ .

$$\frac{\partial H}{\partial s_i} = 0 \Rightarrow \sigma(\mu_i) = s_i \quad \text{McCullough \& Pitts neuronal sigmoid logic rule} \quad (2c)$$

This basic theorem has established biological observations by Hebb, for synaptic efficacy Eq.(2a), McCullough and Pitts neuron threshold logic Eq.(2b) from the Gibbs principle of biochemistry—spontaneity according to which the isothermal free energy Eq(4a) must be at the minimum. An exact solution for simple two component case is recently derived by Szu, Miao and Qi [11] as  $s^*_i = 1 - \exp(-E_o/K_B T_o)$ .

(v) We remark on the biomedical relevance of the biological natural intelligence (NI) model as follows: Szu conjectured (in his space-variant breast tumor research by means of a single-pixel blind source separation (BSS) [1,11,15,16] that the Lagrange multiplier vector  $\mu$  must be measured in the units of Amperes (of which a single ion contributing to dendrite ion current has been measured in pico-Amperes first by Nobel Laureates Neher and Zsigmond) behaving like a house-keeping glial cells. This is because of its physics unit nature of Lagrange multiplier with the synaptic weight  $[W]$  in Volts (of which a millivoltage was measured first by Nobel Laureates Hodgkin and Huxley). Thus, we can obtain the internal energy  $E$  at homeostasis temperature  $T_o$ .

#### 4. APPLICATION TO SOLVE ILL-POSED INVERSE SOURCE PROBLEM

We follow the minimum thermodynamic free energy methodology introduced first by Gibbs and recently for passive breast two color infrared spectrum imaging by Szu [1,11,16,17] for earliest tumor detection at a single pixel in question. Szu took two (3~5  $\mu$ , & 8~12  $\mu$ ) infrared (IR) spectrum measurements  $X = (x_{\text{long IR}}, x_{\text{mid IR}})$  per pixel [1]. Likewise, in saliva case, sources are glucose and other none-glucose at one sample point after meal together few neighborhood distant time points pre-meal as individual baseline. Given single-time-point two components' vector measurements of the saliva quantity for left and right upper jaws (taken after brush cleaning etc. standardization only for establish correlation with blood test, not needed for household practice):

$$X = (x_{\text{left}}, x_{\text{right}})^T \quad (3)$$

Where the superscript T denotes the matrix transpose without knowing how the diffusively mixing of the sipping of excessive blood glucose level with other liquids sources  $S = (s_1, s_2)^T$  as represented by the mixing matrix  $[A?]$ . We wish to invert the 2x2 matrix  $X = [A?] S$  in case of an unknown mixing matrix  $[A?]$ . This is called Blind Sources Separation (BSS). We develop a unique single-time-point BSS formula for senior saliva test kit. All other direct measurements, based on glucose chemical reaction Eq.(1), must be bounded by two equilibrium values pre-meal and after-meal to be given in the following:

The first *principle of biochemistry* is the "*spontaneity*" principle, according to which the thermodynamic isothermal free energy of cellular reaction process---namely the glucose leakage through blood-gland membrane into saliva for isothermal diffusion at mouth temperature  $T_o = 37^\circ\text{C}$ . According to the biochemical minimum free energy principle of the spontaneity, the isothermal free energy Helmholtz is reduced to zero for an equilibrium spontaneous diffusion of the glucose through the saliva glands at the fixed point  $s^*_i$  where all slopes vanish.

H(isothermal free energy) = (diffusion energy)E - (mouth temperature)T<sub>o</sub> (Shannon entropy)S

$$H \equiv E - T_o S; \quad (4a,b,c)$$

$$H = 0;$$

$$\frac{dH}{ds_1} = 0$$

We define a time-integrated average results of saliva vector  $\mathbf{X}$ , mixing impulses response matrix  $[\mathbf{A}]$ , and glucose & other sources vector  $\mathbf{S}$  in terms of slow macroscopic time scales minutes  $t$ , while the fast time scale of dynamics is denoted by the time-integrated microscopic variable  $\tau$ .

$$X(t) = \frac{1}{t} \int_{\tau_o}^{\tau_o+t} d\tau X(\tau) \quad (4d)$$

After the time average, we assume a linear model valid usually in the averaged limit of weak signals. Then, a single macroscopic time point data model is:

$$X(t) = a_o[A(t)?]S_o(t) \quad (4e)$$

Equation (3) has introduced two independent measurements of saliva quantity vector  $\mathbf{X}$ , and we need to invert the unknown saliva-gland-blood-glucose mixing matrix to determine three unknowns (two unit de-mixing vectors of matrix  $[\mathbf{A}]$  and one percentage sources  $\mathbf{S}$ ), other than a damping scaling factor  $a_o$  to be determined by experimental measurement of blood glucose level. Such an ill-posed inverse problem is common in physics inverse problem, which is usually consistently determined by applying the physics conservation and symmetry laws. In our case, we apply the biochemistry spontaneity reaction Gibbs principle Eq(4a-e) of minimum isothermal free energy of Helmholtz, Eqs(4a,b,c). First, we demonstrate that the isothermal free energy for an equilibrium spontaneous diffusion of the glucose through the saliva glands is indeed a linear function of source  $s_1$  and the baseline energy interception  $E_o$  is associated with the so-called fasting saliva level. The diffusion energy  $E$  must be macroscopically determined [4] within measurement accuracy as an analytic, or differentiable, function of input and output data

$$E = E_o + \sum_{i=1,2} \frac{\partial E}{\partial s_i^{(o)}} (s_i - s_i^{(o)}) = E_o + \sum_{i=1,2} \mu_i \left( \sum_{j=1,2} [W_{ij}] X_j - S_i \right) \quad (5)$$

where  $\mu_i$  is called Lagrange vector parameter to be consistently determined by unsupervised learning of Artificial Neural Network (ANN)[1,4]. While the entropy is a concave function as illustrated in Fig. 1, it peaks at 50-50% minimum information. The informative diffusion energy  $E$  is linear. Free energy diagram in it the simple complex curve is the entropy, and internal energy is a linear line their intersection defines the Helmholtz isothermal free energy

$$E = E_o + [\mu_1 \ \mu_2] \begin{bmatrix} (W_1^T, X) - s_1 \\ (W_2^T, X) - s_2 \end{bmatrix} = E_o + \mu_1 (W_1^T, X) + \mu_2 (W_2^T, X) - \mu_2 + (\mu_2 - \mu_1) s_1 \quad (6)$$

Secondly, we derive the linear energy expression, according to the biochemical principle of spontaneity, i.e. the minimum Helmholtz free energy Eq(4a) summarized in the following theorem.

**Theorem 1 Minimum Helmholtz free Energy determines a linear & stationary function of saliva glucose level of saliva measurements:** *Given isothermal equilibrium system at the minimum Helmholtz free energy defined by Eqs.(4,5), the departure from an individual baseline level satisfies a canonical ensemble average behavior, in terms of analytic input & output data  $\mathbf{X}$  and  $\mathbf{S}$ . Then, the departure of the baseline according to minimum thermodynamics free energy one obtains*

$$s_{\text{glucose}}(t_+) = 1 - \exp(-E_o^*(t_-)/K_B T_o) \quad (7)$$

**Proof:**

In order to determine the correct zero-order formulation for the baseline  $E_o$ , one need to derive the relationship between the true solution  $E_o^*$  (indicated by the superscript \*) and the true unknown source  $s^*_1$ . Shannon using the unit-sum-rule entropy formulae:

$$S = -s_1 \log s_1 - (1 - s_1) \log (1 - s_1) \quad (8)$$

The first order slope of energy tangent line at each point is obtained by calculating the derivative of the entropy  $S$  with respect to  $s_1$

$$\frac{dS}{ds_1} = -\log s_1 - \frac{s_1}{s_1} + \frac{1-s_1}{1-s_1} + \log(1-s_1) = \log(1-s_1) - \log s_1 \quad (9)$$

Since at equilibrium  $H=E-T_oS=0$ , then  $E=T_oS$ , and the slope of the energy line equals to the slope of the entropy line. If we know the intercept  $E_o^*$  from the immediately previous baseline measurement, the energy line can be uniquely determined

$$E/K_B = \text{slope } s_1 + \text{intercept} = T_o \frac{dS}{ds_1} s_1 + E_o^* = T_o \{\log(1-s_1) - \log s_1\} s_1 + E_o^* / K_B \quad (10)$$

Then, substituting the aforementioned entropy formula  $S$  Eq(8) and equaling it to the derived energy  $E$  formulae Eq(10) (because Eq(2a)  $H=0$  implying  $E=T_oS$ ), we have obtained

$$S = -s_1 \log s_1 - (1-s_1) \log(1-s_1) = \{\log(1-s_1) - \log s_1\} s_1 + E_o^* / K_B T_o = E / K_B T_o \quad (11)$$

which is simplified as follows

$$E_o^* / K_B T_o = -\log(1-s_1^*), \text{ or,} \quad (12)$$

$$s_1^* = 1 - \exp\left(-\frac{E_o^*}{K_B T_o}\right) \quad (13) \quad \text{Q.E.D.}$$

Note that there is a one-to-one mapping between the informative diffusion baseline energy at the immediately previous time point  $t$ , say after the fasting saliva test with blood test. We determine the unknown glucose source  $s_1^*$  at time  $t_+$ . Moreover, the mapping is exponentially nonlinear as typical solution of the statistical-mechanical canonical ensemble under local mouth temperature  $T_o$ . If we can get the true information energy from data, the abundance fraction can be directly according to Canonical ensemble calculated without a learning process. Let  $X = (X_1, X_2, X_3, \dots, X_n)$  denote the data within a time neighborhood, where each column vector represents a data point and  $n$  is the size of neighborhood. The center pixel is represented by  $X_c$ . The informative diffusion energy  $E_o^*$  is calculated by the summation of the angles between the center pixel and its neighbors expressed as

$$E_o^* = \sum_{i=1}^n \arccos\left(\frac{X_i^T X_c}{\|X_c\| \|X_i\|}\right) \quad (14)$$

After calculating the baseline  $E_o^*$ , the source solution can be tabulated through aforementioned equilibrium solution.

#### 4. HOSPITAL TRAINING DATA GATHERING

The Phase II clinical investigation of noninvasive dual color IR imaging tracking early breast cancer detection has been going on at both Vatican of Rome, and Taiwan National University Hospital [5,11]. We will have results to share in the near future. Meanwhile, we concentrate on the Phase I study of saliva glucose level experiments. The blood droplet data are likewise collected with left and right fingertips capillary blood draw. Different informative diffusion energy is estimated to lead by the Theorem 1 the desired glucose content. We augment our Institute Review Board & Patient Consent Form under Ming-Shen Hospital IRB & PCF led by Physician of Endocrinology and Metabolism, Dr. Chang, who understood a pair of independent saliva measurements, and concurrently another pair of blood droplet measurements. Extraction of both glucose levels shall be processed according to MS hospital protocol in conformity with the experiments of Tokyo Agriculture & Technology University.

We integrate personnel saliva over time through three pairs of micro-fluidity channels front ends for measuring pH, glucose and IGG, respectively, and a smart System on Chip (SOC) back-end. The intelligent part of SOC will be embedded with unsupervised learning Automatic Target Recognition (ATR) algorithm in handling unpredictable environmental variability for hourly noninvasive measurements and unbiased feature extraction of useful personnel baseline profile. Then, a higher order statistics, or ICA,

could extract his feature vectors to compare with temporal field tests for better assurance of authentication. Such an interface philosophy tracks hundreds points temporal heavier to reveal the stable higher order feature statistics (HOS) for better predict the tide of blood glucose level, so that an appropriate quantity of insulin may be administrated at proper lead time for maximum control of physiology. Toward a more timely response of continuously deteriorating aging baby boomers, a yearly baseline check-up is not sufficient and proves often the missing of the timeliness of critical treatment period. Thus, preferably daily checkups at the convenience of home may produce continuous profile of health dynamics in a so-called “baseline profile” trend, which may help medical doctors (MD) conduct hospital check-up with less errors in critical diagnosis judgment call. Therefore, we suggest that an idea situation for early diagnosis should include the first line defense at households (beyond traditional hospitals, insurance agencies, social service and governing body).

1. Two groups of volunteers, one cohort with diabetes and another cohort without it (but may need to stay hospital for different reasons).
2. Carry out their routine daily life at the hospital, so that nurse can take their hourly droplet-blood for lab tests together with lab saliva hourly tests. Every sample should be pairs (e.g. left & right side of fingers, left & right deep inside of mouth).
3. We need enough sample size to measure the Glucose, & the others, e.g. amylase, IGG, etc.
4. One-day 24 hours including fast baseline at early morning wake up before and after a breakfast.
5. Although a commercial saliva test could be used for the soaking sponge at inner gum area, in hospital setup, we can design our own way so long as it is consistent.

The device frequency is to be determined by doctor in the future, but in this training data for our to-be-design device we would like to have over sampling--- for example hourly two blood-droplets (left & right), and half-hour two saliva samples at exact time marked.

Without yet using the test kit, we intend to have your Hospital at Long Tan co-worked on a test bed training data gathering for the necessary benchmark of our pocket test kit.

## **5. SYSTEM ON CHIP & MICROFLUIDITY**

The use of saliva for disease diagnostics and normal health surveillance will bridge the oral health research into systemic diseases through the biofluid that filters and processes itself from the vasculature that nourishes the salivary glands (Fig.1). Due to the recently developed technologies, the barriers to widespread implementation of salivary diagnostics have been largely overcome. Techniques are emerging from a combination of miniaturization technologies and discoveries in many different fields including biology, chemistry, physics, and engineering that are leading to high throughput (the ability to process and analyze a large number of samples in the real time), automated, portable, low cost, compact, more efficient, and rapid biochemical analyses. Miniaturized diagnostic technologies will be able to yield patient information reflecting health and disease status with minute amounts of body fluids. The advent of digital microfluidic MEMS/NEMS (Micro/Nano Electro-Mechanical Systems) technology offers such a detection system due to the advantages in portability, reduction of the volumes of the sample and reagents, faster analysis times, increased automation, low power consumption, compatibility with mass manufacturing, and high throughput. Fig.4.a shows a demonstration of the electrowetting MEMS integrated with optical detection. MEMS/NEMS are integrating systems consisting of mechanical elements, sensors, actuators, and electronics on a common silicon substrate (a substance upon which an enzyme acts) developed through microfabrication technology. These systems use a small sample and a reagent volume (a substance used to produce a chemical reaction, so as to detect, measure, or produce other substances), coupled with integrated detection methods to perform analyses. While the economic outlook seems grim for many sectors, Nanoelectronic technology is thriving. Built with nanotubes and various self-assembling molecular structures, scientists can anticipate a switch from lithographed silicon chips to nanoelectronics. The switch

is attributed to the physical limitations of silicon-based circuits. These constraints will soon be met, so scientists have been searching for other options to conventional silicon electronics. Not without its share of problems, nanotechnology will still profoundly impact the electronics sector.

A new technology named System on a Chip (SoC) will be able to perform multiple operations in parallel in nonlaboratory settings such as the field, factory, hospital clinic, or home. Such technologies will allow the simultaneous assessment of multiple conditions of health and disease and provide clinicians with prevention and therapeutic strategies to meet patient needs. System on Chip (SoC or SOC) is an idea of integrating all components of a computer or other electronic system into a single integrated circuit (chip). It may contain digital, analog, mixed-signal, and often radio-frequency functions – all on one chip. A typical application is in the area of embedded systems. Our SoC design Fig. 4b) provides a compact, cost-effective, low-power, portable, solution, which consists of one microcontroller or DSP; memory blocks including a selection of ROM, RAM, EEPROM and Flash; timing sources including oscillators and phase-locked loops; peripherals including counter-timers; real-time timers and power-on reset generators; external interfaces including industry standards such as USB, FireWire, Ethernet, USART, SPI; analog interfaces including ADCs and DACs; voltage regulators and power management circuits. The bio-sensor IC implemented in another device is connected and digitized through the ADC of our SoC solution, and the detection and diagnosis program can be downloaded via the USB device into the local memory device. This configuration and infrastructure provide the most effective solution. The SoC structure with MEMS/NEMS technology is depicted as follows Fig. 4c):

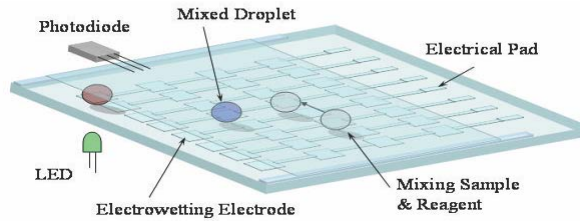


Fig.4.a) The schematic of the electrowetting MEMS integrated with optical detection

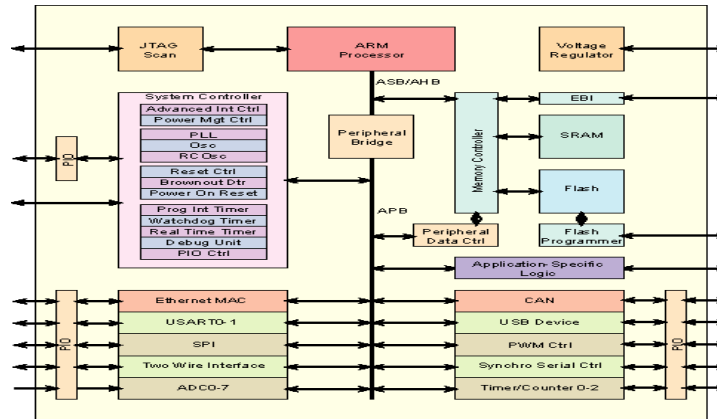


Fig.4.b) Functional Block Diagram of the SoC System.

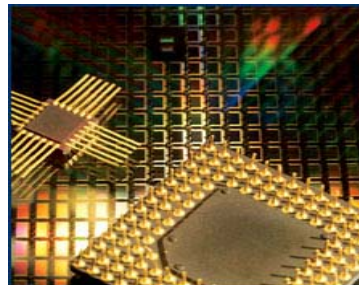




Fig.4.c) An SOC Fabrication Example

Once we have made a prototype model I, we will conduct large scale phase I & IIa studies in order to prove it do no harm, since the controversy remains about the utility of measuring saliva glucose levels. Tokyo team concluded significant differences were observed in individuals between the time-course changes of SGL and BGL. Furthermore, they observed the shape of the flow cell was an important factor in measurement accuracy. The shape of the flow cell (made of acrylic resin) in the saliva analyzing system was designed so that low-level glucose concentrations, in the order of 0.1 mg/dl, could be measured. Since the volume of saliva sample was limited to 200:1, the flow cell volume was set as 147:1, nearly two thirds of the sample volume. The shape of inflow port was designed so that the sample solution could be poured vertically onto the measuring plane of the enzyme sensor. The sensor current was first measured using 200:1 of the sample solution, with flow rate in the range of 0.3 to 0.5 ml/min, the same conditions as used for the saliva sample. Then, the OGIT was carried out on a subject. The time-course changes of BGL and SGL were simultaneously measured with the blood glucose auto-analyzer and the saliva analyzing system, respectively.

- (i) In hardware design, we take geriatrics into account the saliva quantity requiring the micro-fluidity channels, which match well with the micron electrical-mechanical system (MEMS) together with a smart System on Chip (SOC).
- (ii) In software design, we follow the principle of binaural hearing based on the “power of two measurements per time-sampling” useful for signal pre-conditioning: “coincidence, the signal; otherwise, noise”. We can further apply channel equalization with sensible normalization.
- (iii) Our methodology adopt for each individual the unsupervised learning methodology based on single-time multiple-point Blind Sources Separation beyond the second order of statistics.
- (iv) In logistics operation, we accept no universality correlation between blood & saliva, but treat personnel variation individually, and conduct a persistent surveillance individual blood and saliva data gathering for individual “baseline profiles.”
- (v) To commence the design, we took a hospital-lab data acquisition system to gather a few healthy & diabetic adult volunteers with complete BGL and SGL daily dynamics.
- (vi) To benchmark the performance, we conduct large-scale experiments at the Senior Wellness Centers (operated in association with Ming-Shen Hospitals, Howard University Hospital and Senior Wellness Centers of DC) in order to assure the utility in preserving quality of life.

## 6. TEST & EVALUATION METHODOLOGY

Sweden scientists Annika Borg Andersson, Döwen Birkhed, et. al. ([birkhed@odontologi.gu.se](mailto:birkhed@odontologi.gu.se), Eur J Oral Sci 1998; 106: 931–937) had found significant correlation after 2 hours after intake for tenth diabetes patients of type 2 & 1, divided into insulin treatment or not, compared with healthy control groups. All the teeth which were sampled were located in upper jaw. Cotton rolls were placed in the *vestibulum* region 13–23 and easy air blow was performed to dry the teeth before sampling. The extract was frozen at –20°C until it was analyzed for glucose. An *enzymatic method* was used (Cat. No 139041, Boehringer Mannheim, Germany) (cf. Secretion of glucose in human parotid. Borg et al., Scand J Dent Res 1988; 96: 551–556.). In Study A, samples Study B. were analyzed using a *hexokinase method* (A colorimetric serum glucose determination using hexokinase and glucose-6-phosphate dehydrogenase. cf. Carroll et al., Biochem Med 1970; 4: 171–180.) and in Study B using the *Exatech system* (Medisense Sverige, Sollentuna, Sweden). Glycosylated hemoglobin (HbA1c) was determined using a *liquid chromatographic assay* (Measurement of hemoglobin A1c by new liquid chromatographic assay: methodology, clinical utility and relation to glucose tolerance evaluated. Jeppsson et al. Clin Chem 1986; 32: 1867–1872).

The concentration of glucose in parotid saliva was measured after glucose/food intake in two separate studies (A and B). In Study A, 10 subjects with impaired glucose tolerance (IGT), 10 subjects with newly diagnosed Type 2 diabetes and 12 healthy controls were included. Study B comprised 15 subjects with Type 1 or Type 2 diabetes on insulin treatment, nine subjects with Type 2 diabetes on treatment with oral antidiabetic drugs and 12 healthy controls. After a 10-h overnight fast, the participants in Study A were given a 75 g oral glucose load, while those in Study B received a standardized breakfast. Citric acid-stimulated parotid saliva was collected up to two hours after the intake. Capillary blood and gingival exudate samples were also taken. On the basis of AUC values (area under the curve over baseline), the glucose concentration in parotid saliva increased significantly in individuals with IGT and Type 2 diabetes

compared with controls in Study A and in diabetic patients on treatment with insulin and oral antidiabetic drugs compared with controls in Study B. No effect by the glucose/food intake on the glucose concentration in gingival exudate could be demonstrated in any of the studies. The correlation coefficient between the AUC values of glucose in saliva and blood, when all three groups were combined, was 0.38 in Study A and 0.52 in Study B. It is concluded that the concentration of glucose in parotid saliva is elevated at least 2 h after glucose/food intake in individuals with both IGT and manifest diabetes mellitus.

Unfortunately, we also mention that Hashemipour et al. (Iran. J.Endocrinol Metab 2001, V.2 ,No.4) found an insignificant relationship between blood and saliva glucose levels in 10 healthy men. This was a cross sectional study. 130 blood and 130 saliva samples were obtained from 10 healthy men 13 times in 5 days. Each day samples were taken in 3 times, fasting, postprandial and evening. Samples were analyzed with glucose oxidase method. Value of blood glucose level ranged from 58mg/dl to 118 mg/dl. Mean of fasting blood glucose level was  $84.9 \pm 3.13$  mg/dl. Value of saliva glucose level ranged from 0.322mg/dl to 4.941 mg/dl. Mean of saliva glucose level was  $1.22 \pm 0.81$  mg/dl. Correlation coefficient between BGC and SGL from the 5 days of measurement was 0.23. Correlation coefficient for each day was 0.38 (first day), 0.21 (second day), 0.01 (third day) 0.37 (fourth day). Correlation coefficient for each person was 0.31 (case A), 0.07 (case B), 0.07 (case C), 0.07 (case D), 0.45 (case E), 0.10 (case F), -0.05 (case G), 0.32 (case H), 0.87 (case I), 0.87 (case J). Unfortunately, considering the values of correlation coefficients and the limited range of SGL, we cannot use saliva for detecting BGL.

Experiments led by Masaki Yamaguchi et al. Fig. 5 of Tokyo Agriculture & technology University in 1998 [9] took six young adults of ages  $24 \pm 4.6$  with fast BGL at  $93.1 \pm 7.9$  mg/dl to produce second order statistics as follows. Alternatively to photometric methods, biological screening using body fluids that are obtained non-invasively, such as urine, sweat, lacrima, etc., have long been considered. K. S. Arai et al. of Japan 1991 [11] have attempted to establish a non-invasive saliva enzyme method for measurement of BGL. Their study consisted of administration of the 75 g oral glucose tolerance test (OGTT) to determine the time-course changes in BGL and SGL. In addition, a new system for saliva analysis using an enzyme sensor was developed. The measurement transducer used was an enzyme Amperometric glucose sensor (7820L, DKK Co., Tokyo), with electrodes of silver (anode) and gold (cathode), and a potassium chloride electrolyte solution. The voltage applied across the electrodes was 0.7 volts. The electrodes were covered with a Teflon membrane, over which an immobilized enzyme membrane was placed. As a test solution, a phosphate-buffer (pH 7.3) with temperature held at 37°C was passed through the flow cell by a rotary pump (U4-XV, ALITEA, Sweden). The enzyme sensor generated a current that was proportional to the concentration of dissolved oxygen in the buffer. Using a micro-syringe, a sample solution was then injected, and the following reaction took place at the enzyme sensor.

The concentration of dissolved oxygen to reach the sensor is reduced as the above reaction progresses, resulting in a decrease in the output current from the sensor. When the amount of oxygen consumed on the enzyme membrane equilibrates with the amount released from the sensor, a constant current is generated. The magnitude of this current is proportional to the glucose concentration of the sample solution. This current was detected by an ion meter (IOL-50, DKK Co., Tokyo). SGL was determined by the enzymatic Glucose CII-Testwako, GOD-POD method (Wako Pure Chemical Industries, Ltd., Tokyo). Three ml of the enzymatic reagent was added to 200  $\mu$ l of saliva and incubated at 37°C for 5 mins after mixing. The optical density (OD) at 505 nm was measured with a spectrophotometer (U-2000A, Hitachi Ltd., Tokyo).

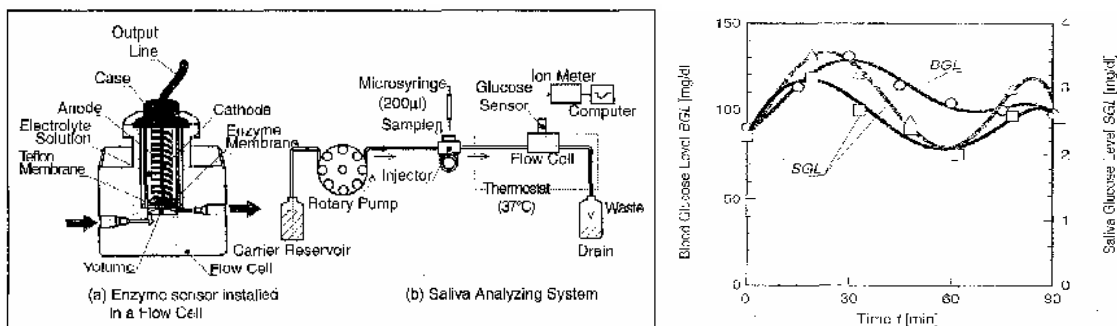


Fig. 5 Cross-section of enzyme sensor installed in a flow cell (a), and schematic diagram of a flow-injection-type saliva analyzing system (b). (c) Results of oral glucose tolerance test (OGTT) in normal subjects using the saliva analyzing system. (O: BGL, U: SGL measured by saliva analyzing system,  $\Delta$ : SGL Measured by spectrophotometer (Courtesy of [9])

## 7. CONCLUSION

We have assumed that the saliva glands in the mouth jaw produce saliva samples ( $X_1$   $X_2$ ) through a linearly, instantaneous, and time-independent mixing of pre-gland glucose  $s_1^*$  with other liquid  $s_2^*$  during the slow time scale of minute sampling. In this paper, we have proved a macroscopic permeable equilibrium theorem to determine the inverse sources by a single-time Blind Sources Separation (BSS). In reality, this might be only the zero-th order equilibrium approximation of a general time-dependent nonlinear convolution-mixing problem. Our equilibrium solution could be considered as a useful time average over minute's saliva sampling. It could serve as the first term for perturbation correction terms, e.g. a time-dependent linear convolution equation solved by Fourier transforms methodology. In other words, we have theoretically derived a local equilibrium glucose  $s_1^*$  content, whose time integration average over minutes shall equal to the experimental glucose quantity present in the saliva. However, we argue that the equilibrium average saliva glucose level should be sufficient for monitoring a relatively slow-time variation of blood glucose level over hours. Hopefully, with a slow variation function of time after a meal, our equilibrium model of saliva test kit can serve as a useful predictor for each individual his or her blood glucose level when & how much, after the saliva glucose level is benchmarked with his or her own equilibrium dynamics of blood glucose levels. Then, appropriate amount of insulin could be administrated to help glucose entering cells for needed energy conversion metabolism without damaging the delicate balance of blood glucose and insulin levels in the long run. We can help achieve better quality of life for aging population worldwide.

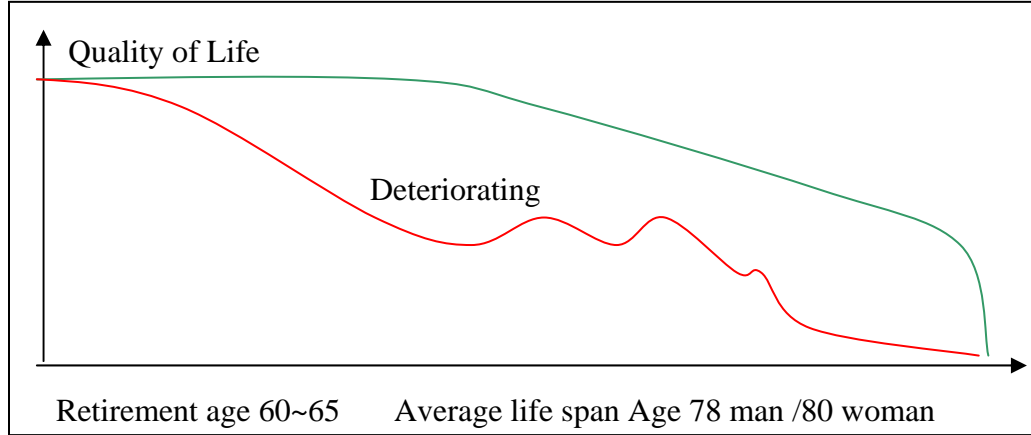


Fig. 6. The gain over an individual Quality of Life insures a productive second & third career in value-added production as opposed to a normal red deficit burden to the society.

The root cause is identified in this and other related paper that is waiting for nothing can be done in the current healthcare payment policy until missing the timeliness and early diagnosis getting seriously sick at hospital retreat. Affordable point of care smart sensors system, which implements two new concepts of Wellness Baseline Profile (WBP) for physician Individual Diagnostic Aids (IDA), must comprise biological power of pair concept translated from military real world experience on the persistent surveillance, together with military know-how of authenticated privacy communication Next Gen Network. Saliva test kit is merely one of four type's surveillance tools for WBP and IDA. The others and this one will be further developed and tested by concerned citizen and numerous collaborators worldwide.

In the near future, we will describe experimental findings and SOC results. We seek worldwide collaboration to predict blood glucose level as a function of time near hours after meal by measuring a time point of saliva glucose level. This will be a challenging application. Our initial approach is applying Neural Control Methodology to construct both a plant model and a feedback control loop, based on lot of past

history data to extract the invariant feature by means of the stationary Kurtosis analysis. Artificial Neural Network model similar to Narandra of Yale University in Trans IEEE NN V.1 might be useful.

### ACKNOWLEDGEMENT:

The project described was supported by Ming-Shen Hospitals for Ubiquitous Health Care Project, partially by the Excellency Grant of Chung Yun Christian University, and partially by the grants to Dr. Chung and Dr. Tsai from National Science Council. Dr. Wang of the Radiology Department of Howard University Hospital wishes to thank NIH/NCI/NCRR Grant 2G12RR00304816A1, USAMRA Grant W81XWH-05-1-0291, and NIH Grant 2U54 CA091431-06A1. Dr. Gu of the School of Dentistry of Howard University wishes to acknowledge a partial support from NIH grant: NIH/NCI P20CA118770-01. Institute of Biomedical Engineering of National Taiwan University wishes to acknowledge the Excellence Grant of NTU, and the Grant by Taiwan National Science Council. Ming-Shen Hospital wishes to acknowledge the U-Care partial supported by Taiwan Ministry of Economic Yuan.

### REFERENCES:

- [1]. General Account Office (GAO) Report 2002 on 78 Million aging baby boomers costs ranging from 1/5 GDP toward ¼ GDP in decades; Federal Reserve Chair Mr. Alan Greenspan thanked China 2006 Sept. for low cost quality product to keep US inflation in check, his successor Mr. Ben Benanke warned 2006 Oct. the financial un-sustainability of social entitlement due to the retirement of aging baby boomers.
- [2] Szu, Harold, ONR Press Release "From Tanks to Tumors," 2002; Szu et al., Publication of US Patent Trade Office **2004/0181375**.
- [3] Seow, S.W. Duffy, M. A. McGeem, J. Lee, and H. P. Lee, "Breast Cancer in Singapore trends in incidence 1968-1992," *Int'l J. of Epidemiology*, V. **25**, pp. **40-45**, **1996**;
- [4] Kelsey J. L. and Gammon, M. D. "the epidemiology of breast cancer," *Cancer J. for clinicians*, V. **41**, pp. **146-165**, **1991**;
- [5] While Prof. Basti of Lateran Pontific University is leading a team using passive infrared imaging at Lateran Hospital near Vatican of Rome for Phase Ib studies under EU/Italy funding, Prof. Ming-Chung Chen is leading a team of Biomedical Institute and Hospital of National Taiwan University under NTU Excellence Grant for Phase II efficacy studies. President Shi-Chen Lee of NTU leads a third team to design single co-axial lens camera for double infrared spectral band under National Science Council grant.
- [6] Bour-Jordan H., Bluestone J. A., "Sensory neurons link the nervous system and autoimmune diabetes," *Cell* **127**, pp. **1097-1099**, Dec 15 2006; R. Razavi, Y. Chan, F.N. Afifyan, X. J. Liu, X. Wan, J. Yantha, H. Tsui, L. Tang, S. Tsai, P. Santamaria, J.P. Driver, D. Serreze, M. W. Salter, and H.-M. Dosch, "TRPV1<sup>+</sup> Sensory neurons control b cell stree and islet inflammation in autoimmune diabetes," *Cell* **127**, pp. **1123-1137**, Dec 15 2006.
- [7] Siudikiene Jolanta, Machiulskiene Vita, Nyvad Bente Tenovuo, Jorma, Nedzeiskienu Irena, "Dental caries and salivary status in children with type 1 diabetes mellitus, related to the metabolic control of the disease, *Eur. J. Oral Sci.* V. **114**, pp. **8-14**, **2006**.
- [8] Carda Carmen, Mosquera-Lloreda Nezly, Salom Lucas, Gomez de Ferraris Maria Elsa, Peydro Amando, "Strutural and functional salivary disorders in type 2 diabetic patients, *Med. Oral ptol Oral Bucal* V. **11**, pp. **E309-314**, **2006**.
- [9] Masaki Yamaguchi, Masayuki Mitsumori, and Yoshio Kano, "Noninvasive Measuring Blood Glucose Using Saliva," *IEEE Trans on Biomedical Eng.* V. **45**, pp. **59-63**, May/June 1998.
- [10] Kayashima S, Arai T, Kikuchi M, Sato N, and Nagata N, et al.: New noninvasive transcutaneous approach to blood glucose monitoring: Successful glucose monitoring on human 75g OGTT with novel sampling chamber, *IEEE Trans on Biomed. Eng.* V. **38**, pp. **752-757**, **1991**.
- [11] Szu, Harold. Miao, Lidan, Qi, Hairong, "Thermodynamic Free-energy Minimization for Unsupervised Fusion of Dual-color Infrared Breast Images," *Proc. SPIE* V. **6247**, "ICA Wavelets etc. (editor Szu)" pp. (Orlando, FL 2005)
- [12] Chung, Wen-Yaw, Yang, Chung-Huang, Wang, Yaw-Feng, Chan, Yi-Je, Torbicz W., Pijanowski Dorota G., "A signal processing ASIC for ISFET-based chemical sensors," *Microelectronics Journal* V. **35** (2004) pp. **667-675**

- [13] Chang Y.J., Chang Y.P., and Cheng K.Y. (2005), "Operation Principle And Simulation of Loop-Type Microfluidic Biochips", Proceedings of ICAM 2005 .
- [14] Szu Harold & Mehmood Amir, "RFID/SC Hybrid Solutions for Authentication, Privacy & Security Applications," Proc. SPIE V. **6247** "ICA Wavelets etc. (edited Szu)", pp. (Orlando FL, 2005)
- [15] Szu H., "Unsupervised learning Artificial Neural Networks," IN: "*Computational Intelligence, the experts speak*," (ed. Fogel & Robinson) Wiley Interscience and IEEE Press, **2003, Ch. 16, pp.219-245**.
- [16] Szu H., "Thermodynamics Energy for both supervised and unsupervised learning neural nets at a constant temperature," *Int'l J. Neural Sys.* **9, 175-186, June 1999**.
- [17] McFadden F., Szu, H. "Implicit differential analysis for cortical models," loc. cit. SPIE Proceeding V. **6576 (2007)**

# Nicotine Decreases the Cytotoxicity of Doxorubicin towards MCF-7 and KB-3.1 Human Cancer Cells in Culture

Yanfei Zhou, PhD; Xinbin Gu, MD, PhD; Ebrahim Ashayeri, MD; Renshu Zhang, MD; and Rajagopalan Sridhar, PhD

Financial support: This research was partially supported by grant DAMD17-03-1-0123, DAMD17-03-1-0759, DAMD 17-98-1-8109 from U.S. Army Medical Research Materiel Command, and grant 2G12 RR003048 from RCMI program, NCRR/National Institutes of Health.

The harmful effects of tobacco use and nicotine are well known. There is strong epidemiological evidence for smoking as a risk factor for cancer of the lung and oral cavity. The evidence for second-hand smoke as a risk factor for breast cancer is rapidly accumulating. The anthracycline doxorubicin is used in the treatment of many types of malignancies, including breast cancer. The effect of nicotine on doxorubicin toxicity was evaluated in MCF-7 and KB-3.1 cancer cell cultures. Nicotine partially inhibited doxorubicin toxicity towards MCF-7 and KB-3.1 cells, as judged by clonogenicity and flow cytometry assays. Flow cytometric analysis showed that <10% of cells treated with doxorubicin underwent apoptosis, while necrosis was the major mode of cell death. Inhibition of apoptosis and necrosis in cancer cells by nicotine can diminish the effectiveness of doxorubicin in cancer therapy.

Key words: nicotine ■ doxorubicin ■ cancer ■ chemotherapy

© 2007. From the Department of Radiation Oncology (Zhou, Ashayeri, Zhang, Sridhar); Cancer Center, College of Medicine (Zhou, cancer biology; Gu; Zhang; Sridhar); Department of Oral Diagnosis, College of Dentistry (Gu); and Department of Genetics and Human Genetics (Sridhar), Howard University, Washington, DC. Send correspondence and reprint requests for *J Natl Med Assoc.* 2007;99:xxx-xxx to: Dr. Rajagopalan Sridhar, Department of Radiation Oncology, Howard University Hospital, 2041 Georgia Ave. NW, Washington, DC 20060; phone: (202) 865-4968; fax: (202) 667-1686; e-mail: raj.sridhar@gmail.com

## INTRODUCTION

The deleterious effects of smoking and tobacco use have been well documented.<sup>1-9</sup> About 30% of cancer deaths in the United States are associated with the use of tobacco products.<sup>2</sup> Tobacco use is well recog-

nized as the major cause of lung, and head and neck cancers.<sup>2,3</sup> Evidence for breast cancer risk from active and passive smoking is accumulating.<sup>4-7</sup> There is increasing evidence that the use of tobacco can decrease the efficacy of cancer treatment and increase the risk of recurrence.<sup>8-10</sup> Recent studies have shown that nicotine inhibits apoptosis of cancer cells treated with a variety of chemotherapeutic drugs. Blunting of anticancer efficacy of chemotherapeutic drugs has been associated with inhibition of drug-induced apoptosis of cancer cells by nicotine.<sup>10</sup> However, it is important to recognize that apoptosis is not a major mode of cell death in solid tumors.<sup>11,12</sup> Necrosis rather than apoptosis is the major mode of cell death in some solid tumors. Clonogenicity assays are preferable to apoptosis assays for evaluating therapeutic potential of drugs and ionizing radiation against solid tumors.<sup>11,12</sup> Doxorubicin is a versatile anticancer drug that is used for treating a variety of malignancies, including breast cancer. This provides a strong rationale for investigating the influence of nicotine, a tobacco alkaloid, on the cytotoxicity of doxorubicin towards human breast cancer cells. Clonogenicity and apoptosis assays showed that nicotine partially protected MCF-7 human breast cancer cells against cytotoxicity of doxorubicin. The mechanisms by which nicotine may inhibit the cytotoxic effects of doxorubicin are discussed briefly.

## MATERIALS AND METHODS

### Reagents

Chemicals were of the highest available grade from commercial sources. (-)-Nicotine, doxorubicin, ethidium bromide, 3-[4,5-dimethylthiazol-2-yl]-2,5-diphenyltetrazolium bromide (MTT) and methylene blue were purchased from Sigma Chemical Co. (St. Louis, MO). Tissue culture reagents such as glutamine, sodium pyruvate, trypsin and fetal bovine serum were obtained from GIBCO, Grand Island, NY.

## Cell Culture

MCF-7 human breast cancer cells and KB-3.1 human nasopharyngeal cells were grown in RPMI 1640 medium supplemented with 10% fetal bovine serum, glutamine (2  $\mu$ M), sodium pyruvate (1 mM), 100 U penicillin/ml and 100  $\mu$ g streptomycin/ml. Cells were subcultured twice weekly and maintained as exponentially growing monolayers in a humidified 5% carbon dioxide air atmosphere at 37°C.

## Clonogenicity Assay

Cells were seeded at densities of 300 and 1,500 cells per 100-mm diameter tissue culture dish. The cells were allowed to attach overnight. The cultures were treated with nicotine (10 or 20  $\mu$ M) for two hours. Control cultures were treated with same volume of medium without nicotine. After the two-hour exposure to nicotine, the cultures were treated with different concentrations of doxorubicin for 90 minutes. Appropriate controls without doxorubicin were also included. The medium was removed from each dish and the cells were washed with Dulbecco's phosphate buffered saline (PBS), and fresh drug-free culture medium (10 ml) was added; the cultures returned to the incubator for colony formation to

progress for 10 days. Any colony containing >50 cells was considered to represent a viable clonogenic cell. The colonies in the dishes were counted after staining with 0.1% methylene blue in 50% ethanol.<sup>13</sup> Cell survival was calculated relative to a 100% value for untreated controls. The experiment was performed four times for each treatment.

## MTT Assay for Cell Viability

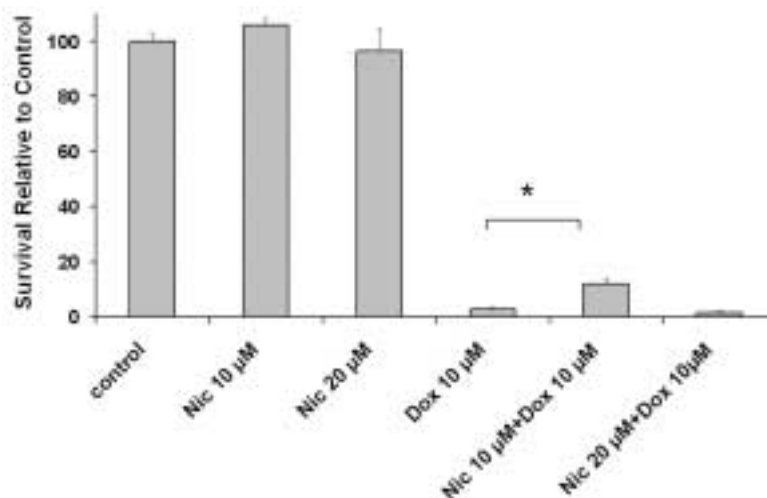
Exponentially growing cells were harvested and plated in 96 well flat-bottom plates at 10,000 cells per well containing 200  $\mu$ l of complete culture medium, and the cells were allowed to attach overnight. The cells were then pretreated with nicotine (1–10  $\mu$ M) for two hours, followed by exposure to doxorubicin (0.1–1.0  $\mu$ M) with or without nicotine (1–10  $\mu$ M) for 72 hours at 37°C. Mitochondrial dehydrogenase levels, which are correlated to cell viability, were determined by the enzyme-mediated cleaving of the tetrazolium salt ring of 3-[4,5-dimethylthiazol-2-yl]-2,5-diphenyltetrazolium bromide to yield purple formazan crystals. These crystals were dissolved in isopropanol, and the absorption at 560 nm was determined spectrophotometrically. Appropriate control experiments were run to determine spec-

Table 1. Effect of nicotine in combination with doxorubicin on MCF-7 cell proliferation

	Control	Dox 0.1 mM	Dox 0.5 mM	Dox 1.0 mM
Nic 0 $\mu$ M	100 $\pm$ 5 *	91 $\pm$ 5*	26 $\pm$ 1*	21 $\pm$ 2*
Nic 1 $\mu$ M	87 $\pm$ 8	97 $\pm$ 5	30 $\pm$ 1	20 $\pm$ 3
Nic 5 $\mu$ M	105 $\pm$ 7	117 $\pm$ 3*	38 $\pm$ 4*	25 $\pm$ 2
Nic 10 $\mu$ M	126 $\pm$ 5 *	123 $\pm$ 6*	40 $\pm$ 3*	28 $\pm$ 3*

Cell viability was determined using the MTT assay for cell proliferation as described under methods. Data are presented as mean  $\pm$  STD; \* p<0.05 (Student's t test)

Figure 1. Effect of nicotine on doxorubicin cytotoxicity towards MCF-7 cells determined using clonogenicity assays



For combination treatment, cells were pretreated with nicotine (10 or 20  $\mu$ M) for two hours followed by a 90-minute treatment with dox (10  $\mu$ M) as described under methods. Data represent the mean  $\pm$  S.D of four experiments; \* p<0.05 (Student's t test)



trophotometric background and absorption due to reagent blanks.

## Apoptosis Assays

The levels of apoptosis after treatment of MCF-7 cells with nicotine (10 and 20  $\mu$ M) or doxorubicin alone and in combination with each other were measured using Annexin V-EGFP (enhanced green fluorescent protein) apoptosis detection kit (MBL, Nagoya, Japan). For these experiments, a two-hour pretreatment with nicotine was followed by 90 or 120 minutes of treatment with doxorubicin (10  $\mu$ M). After treatment with or with-

out drug(s), the cells were harvested by trypsinization followed by centrifugation. The cell pellet was resuspended to obtain  $5 \times 10^5$  cells in 500  $\mu$ l of binding buffer and followed by addition of 5  $\mu$ l of Annexin V-EGFP and 5  $\mu$ l of propidium iodide solution. The resulting mixture was incubated at room temperature for 5 minutes in the dark. Annexin binding and propidium iodide staining were analyzed using a flow cytometer (FAC-SCalibur; BD Biosciences, San Jose, CA).

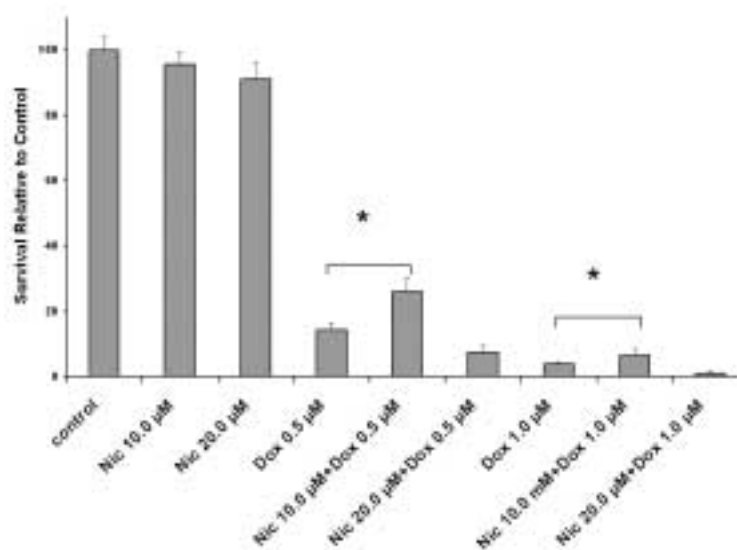
Apoptosis was also estimated in the case of MCF-7 cells, by measuring caspase-3 and caspase-8 activities using a caspase-3/CPP32 fluorometric protease assay kit

Table 2. Combined effect of nicotine and doxorubicin on apoptosis and necrosis

	Apoptosis (Early Stage) (Lower Right Quadrant)	Necrosis and Late-Stage Apoptosis (Upper Left and Right Quadrant)	Mixture of Late-Stage Apoptosis and Necrosis (Upper Right Quadrant)
MCF-7 Cells			
Control	1.18	10.61	5.51
Nic 10 $\mu$ M	2.38	11.36	7.12
Dox 10 $\mu$ M 90 min	1.96	63.26	6.68
Nic 10 $\mu$ M + dox 10 $\mu$ M 90 min	1.71	47.60	6.84
KB-3.1 Cells			
Control	2.48	2.91	2.11
Nic 10 $\mu$ M	3.28	4.69	3.24
Dox 1.0 $\mu$ M 90 min	1.13	63.42	5.38
Nic 10 $\mu$ M + dox 1.0 $\mu$ M	1.82	49.27	5.77
Control for 120-min treatment	2.77	2.03	1.33
Nic 10 $\mu$ M	4.80	8.79	5.98
Dox 1.0 $\mu$ M 120 min	0.79	68.46	4.30
Nic 10 $\mu$ M + dox 1.0 $\mu$ M 120 min	1.64	60.14	7.48

Nic: nicotine; Dox: doxorubicin; Data are percentages of apoptosis and necrosis, as determined by counting cells in each of the four quadrants of the flow cytometer dot plots obtained using the annexin V-EGFP apoptosis kit (Figure 4).

Figure 2. Influence of nicotine on clonogenic potential of KB-3.1 cells treated with doxorubicin



For combination treatment, cells were pretreated with nicotine (10 or 20  $\mu$ M) for two hours followed by a 90-minute treatment with dox (0.5 and 1.0  $\mu$ M) as described under methods. Data represent the mean  $\pm$  S.D of four experiments; \*  $p < 0.05$  (Student's  $t$  test)

and a caspase-8/Fluorimetric protease assay kit (MBL, Nagoya, Japan).<sup>14,15</sup> About  $2 \times 10^6$  cells were seeded per 75-cm<sup>2</sup> tissue culture flask and allowed to grow overnight and then cultures were subjected to different treatments. After treatment with or without drug(s), the cells were harvested by trypsinization followed by centrifugation to obtain cell pellets. The pellet was resuspended in 50  $\mu$ l of chilled cell lysis buffer and kept on ice for 10 minutes. This was followed by addition of 50  $\mu$ l of 2x reaction buffer containing 10  $\mu$ M DTT and 5  $\mu$ l of 1

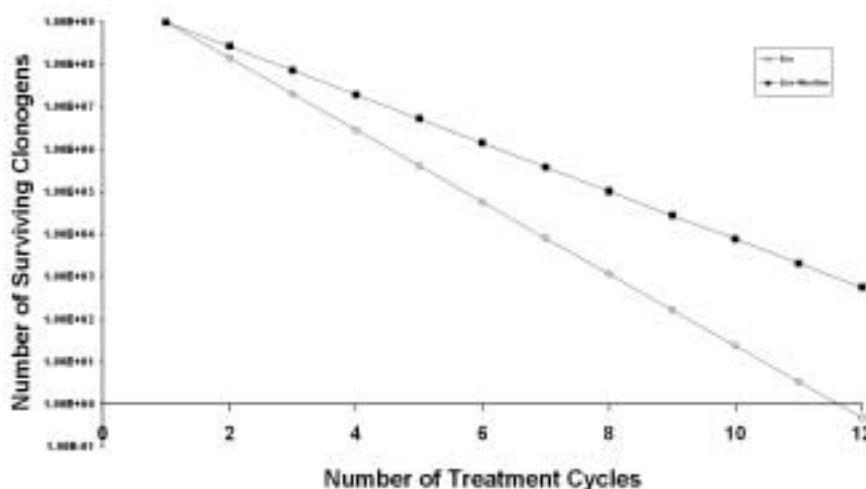
mM DEVD-AFC substrate for caspase-3 (50  $\mu$ M final concentration) and the mixture incubated at 37°C for 1–2 hours. Fluorescence intensity was measured in a fluorometer equipped with a 400-nm excitation filter and 505-nm emission filter. Caspase-3 activity was normalized to the protein content of the samples, and the protein concentration was determined using Biorad protein assay kit. Similarly, caspase-8 activity was estimated using 5  $\mu$ l of 1 mM IETD-AFC substrate for caspase-8.

Apoptosis was also detected on the basis of DNA

Table 3. Diverse mechanisms involved in the pharmacological action of doxorubicin

Mechanism Involved	Reactive Intermediates and Targets Involved	Comments
Formation of deleterious free-radical metabolites	Doxorubicin metabolism by microsomal and mitochondrial enzymes	Doxorubicin semiquinone radicals and reactive oxygen species are produced as documented by electron spin resonance studies. <sup>22-26</sup>
Non enzymic production of free radicals from doxorubicin interaction with iron	Iron-mediated reaction with $\alpha$ -hydroxyketone side chain of doxorubicin is a source of hydroxyl radicals.	Spin trapping with 5,5-dimethylpyrroline 1-oxide (DMPO) proved the formation of free radicals. <sup>27-30</sup>
Inhibition of topoisomerase	Cytotoxic effects of doxorubicin are attributed to inhibition of topoisomerase.	Cleavable complex of DNA, topoisomerase and doxorubicin causes DNA strand breaks leading to cell death. <sup>31</sup>
Formation of doxorubicinol by reduction of the side chain	This reduction can be due to the action of carbonyl reductase.	Doxorubicinol has been implicated as the cardiotoxic metabolite of doxorubicin. <sup>32,33</sup>

Figure 3. Simulation of the effect of multiple cycles of doxorubicin treatment with and without nicotine



The graph shows the number of clonogens remaining in a hypothetical one gram tumor after multiple cycles of treatment with doxorubicin in the presence and absence of nicotine. The hypothetical one gram tumor has been assumed to contain  $10^9$  clonogens at the start of therapy. It is assumed that the tumor is homogeneous and that the effectiveness is the same for each cycle of therapy. The level of cytotoxicity for a single treatment cycle is arbitrarily taken from the cell survival data for 90 minute treatment of KB-3.1 cells to doxorubicin (0.5  $\mu$ M) with or without prior exposure to nicotine (10  $\mu$ M). Cell proliferation occurring between cycles has been ignored and the duration of action of each dose of doxorubicin has been assumed not exceed 90 minutes. Open circles represent data for doxorubicin alone and closed squares represent doxorubicin treatment following nicotine pretreatment. It is clear that less than one clonogen is expected to survive after 12 cycles of doxorubicin alone, 555 clonogens would survive after 12 cycles of doxorubicin following nicotine pretreatment.

fragmentation analysis after gel electrophoresis (1.5% agarose gel) and ethidium bromide staining.<sup>16,17</sup>

## RESULTS

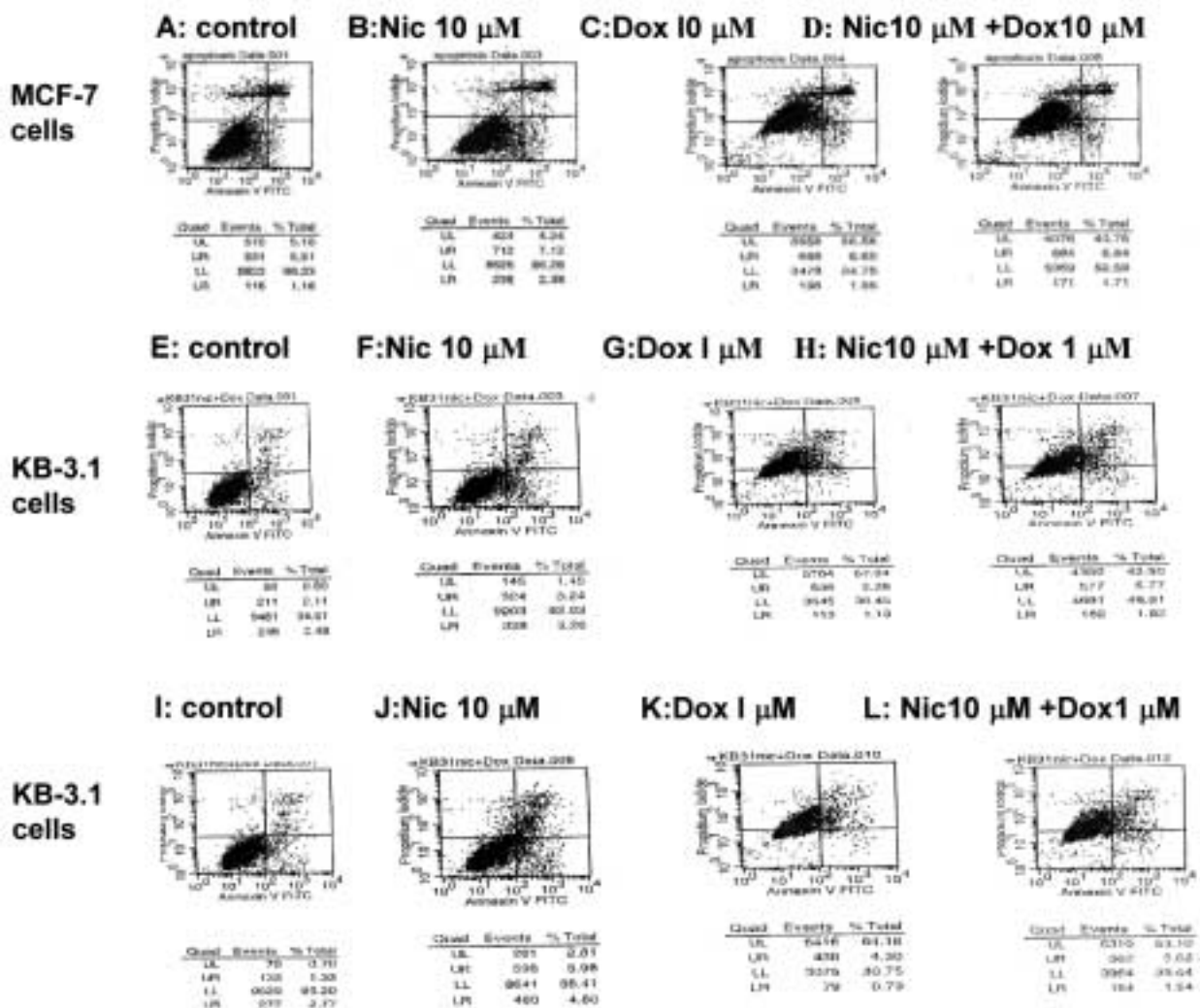
### Partial Inhibition of Doxorubicin Toxicity towards Cells Pretreated with Nicotine

Exposure of MCF-7 monolayers to doxorubicin decreased cell survival as determined on the basis of clonogenicity assays. A 90-minute treatment of MCF-7 cells with

doxorubicin (10  $\mu$ M) alone killed >97% cells. However, pretreatment with 10  $\mu$ M but not 20  $\mu$ M of nicotine afforded significant protection to MCF-7 cells treated with doxorubicin (10  $\mu$ M) (Figure 1). Similar results were obtained with KB-3.1 nasopharyngeal carcinoma cells pretreated with nicotine (10  $\mu$ M and 20  $\mu$ M), followed by exposure to doxorubicin (0.5 and 1.0  $\mu$ M) (Figure 2). Significant protection against doxorubicin cytotoxicity was observed in cells pretreated with nicotine (10  $\mu$ M but not 20  $\mu$ M).

The effect of nicotine on doxorubicin cytotoxicity towards MCF-7 cells was also examined using MTT assay

Figure 4. Flow cytometric measurement of apoptosis in MCF-7 and KB-3.1 cells treated with nicotine in combination with doxorubicin



Data are presented as dot plots in which the vertical axis represents fluorescence due to PI staining and the horizontal axis represents the fluorescence associated with annexin V. The upper left quadrant contains necrotic (PI positive) cells, the upper right region contains late stage apoptotic and necrotic (mixture of PI and annexin V positive) cells. The lower left region contains viable non-apoptotic (PI and annexin V negative) cells, and the lower right region contains early apoptotic (PI negative and annexin V positive) cells.

A, B, C and D are the results for MCF-7 cells pretreated with nicotine followed by 90 minutes of doxorubicin (10  $\mu$ M) treatment. A: Control; B: Nicotine (10  $\mu$ M); C: Doxorubicin (10  $\mu$ M); D: Doxorubicin (10  $\mu$ M) + Nicotine (10  $\mu$ M).

E, F, G and H are the results for KB-3.1 cells pretreated with nicotine followed by 90 minutes of doxorubicin (1  $\mu$ M) treatment. E: Control; F: Nicotine (10  $\mu$ M); G: Doxorubicin (1  $\mu$ M); H: Doxorubicin (1  $\mu$ M) + Nicotine (10  $\mu$ M).

I, J, K and L are the results for KB-3.1 cells pretreated with nicotine followed by 120 minutes of doxorubicin (1  $\mu$ M) treatment. I: Control; J: Nicotine (10  $\mu$ M); K: Doxorubicin (1  $\mu$ M); L: Doxorubicin (1  $\mu$ M) + Nicotine (10  $\mu$ M).

for cell viability. A dose-dependent protection by nicotine was seen after 72 hours exposure to graded doses of doxorubicin (Table 1). Interestingly, nicotine appeared to increase the number of viable cells over a 72-hour period and consistently protected against doxorubicin toxicity.

In clonogenicity experiments with KB-3.1 cultures, the survival was 14.19% after a 90-minute treatment with 0.5  $\mu$ M doxorubicin alone, but the survival increased to 27.16 (average of four experiments, range 22.22–34.57%) when a two-hour treatment with 10- $\mu$ M nicotine preceded doxorubicin (0.5  $\mu$ M) treatment. Such inhibition of doxorubicin cytotoxicity by nicotine will have a profound effect on tumor control. This is illustrated by simulating the effect of multiple treatments with doxorubicin alone and in the presence of nicotine. The graph (Figure 3) depicts the number of clonogens remaining after multiple courses of treatment of a hypothetical 1-g tumor containing  $10^9$  clonogenic cells at the start of therapy. It is assumed that the tumor is homogeneous and that the effectiveness of treatment is the same for each cycle of therapy. Effects of tumor cell proliferation between treatment cycles have been ignored in this simulation based on this equation for (N), the number of surviving clonogens that remain at the end of n cycles of therapy:

$N = I (SF)^n$  where (I) is the number of clonogens in the tumor at the start of (n) cycles of therapy and SF is the surviving fraction after one cycle of treatment.<sup>18,19</sup>

### Pretreatment of Cells with Nicotine Decreases Doxorubicin Induced Necrosis and Apoptosis

Two-color flow cytometry with annexin V and propidium iodide labeling showed necrosis to be the predominant mode of cell death in MCF-7 cells treated with doxorubicin (10  $\mu$ M) for 90 minutes, while early apoptosis accounted for <5% cell death. Pretreatment with nicotine (10  $\mu$ M) decreased necrosis and late apoptosis due to doxorubicin (10  $\mu$ M) treatment of MCF-7 cells (Figure 4 and Table 2). Similar results were obtained using KB-3.1 human nasopharyngeal cells treated with nicotine and doxorubicin (0.5 and 1.0  $\mu$ M), (Figure 4 and Table 2).

### Effect of Nicotine on DNA Fragmentation and Caspase-3 and Caspase-8 Levels in MCF-7 Cells Treated with Doxorubicin

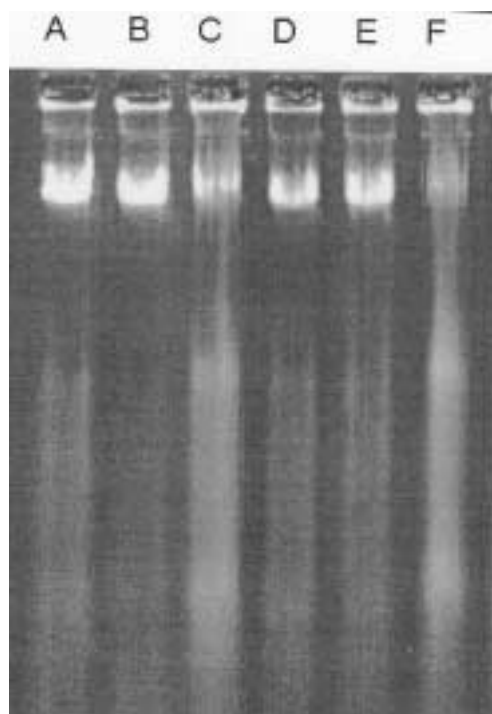
The results of DNA fragmentation assays (Figure 5) showed that treatment of MCF-7 cells with doxorubicin alone (lane F) induced most DNA fragments compared to untreated control (lane E) and other treatment groups, including treatment with nicotine alone (lanes A, B) or in combination with doxorubicin (lanes C, D). Nicotine (10 and 20  $\mu$ M) pretreatment for 120 minutes followed by doxorubicin treatment for 90 minutes caused less DNA fragmentation (lanes C, D) compared to treatment with doxorubicin alone (lane F) (Figure 5). Nicotine at 20  $\mu$ M was more effective than nicotine (10  $\mu$ M) in preventing doxorubicin-mediated DNA fragmentation. Treatment with nicotine alone did not have any appreciable effect (lanes A, B). This was further examined on the basis of caspase-3 and caspase-8 assays for apoptosis (Figure 6).

Treatment of MCF-7 cells with 10  $\mu$ M of doxorubicin alone for 90 minutes increased caspase-3 activity to 142% and caspase-8 activity to 126% relative to 100% activity for each enzyme in untreated control cultures. However, a two-hour pretreatment with 20  $\mu$ M of nicotine followed by doxorubicin treatment for 90 minutes resulted in caspase-3 activity of 114% and caspase-8 activity of 101% relative to control (Figure 6). This corresponds to a 20% inhibition of doxorubicin-induced apoptosis by 20  $\mu$ M of nicotine in these cells. A two-hour pretreatment with 10  $\mu$ M of nicotine did not have a significant effect on doxorubicin induced caspase-3 and caspase-8 activities.

## DISCUSSION

Nicotine at 10  $\mu$ M but not 20  $\mu$ M protected against doxorubicin mediated loss of clonogenic potential of MCF-7 and KB-3.1 cells. This is probably due to differences in the

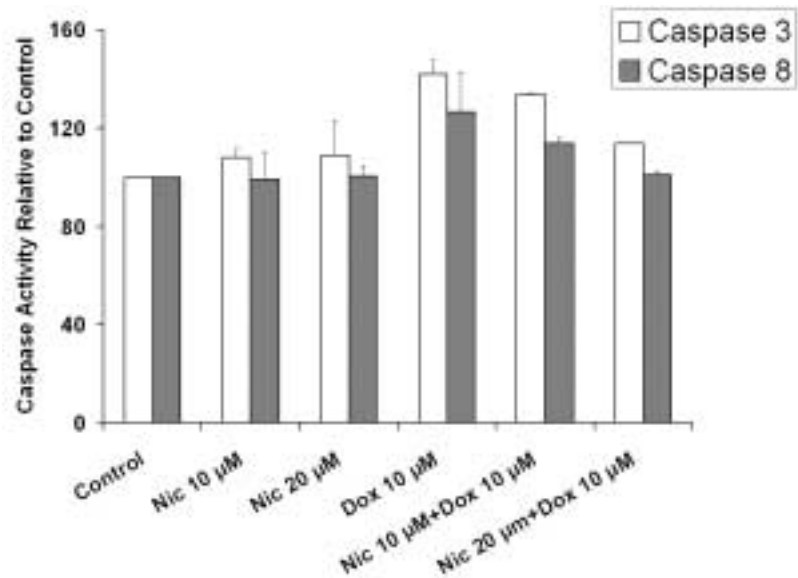
Figure 5. Effect of nicotine on DNA fragmentation induced by doxorubicin in MCF-7 cells



The agarose gel patterns for DNA fragmentation are shown for the different treatment groups. The different treatment groups in lanes A-F are: Lane A: nicotine 10  $\mu$ M; Lane B: nicotine 20  $\mu$ M; Lane C: nicotine 10  $\mu$ M + doxorubicin 10  $\mu$ M; Lane D: nicotine 20  $\mu$ M + doxorubicin 10  $\mu$ M; Lane E: control; Lane F: doxorubicin 10  $\mu$ M.

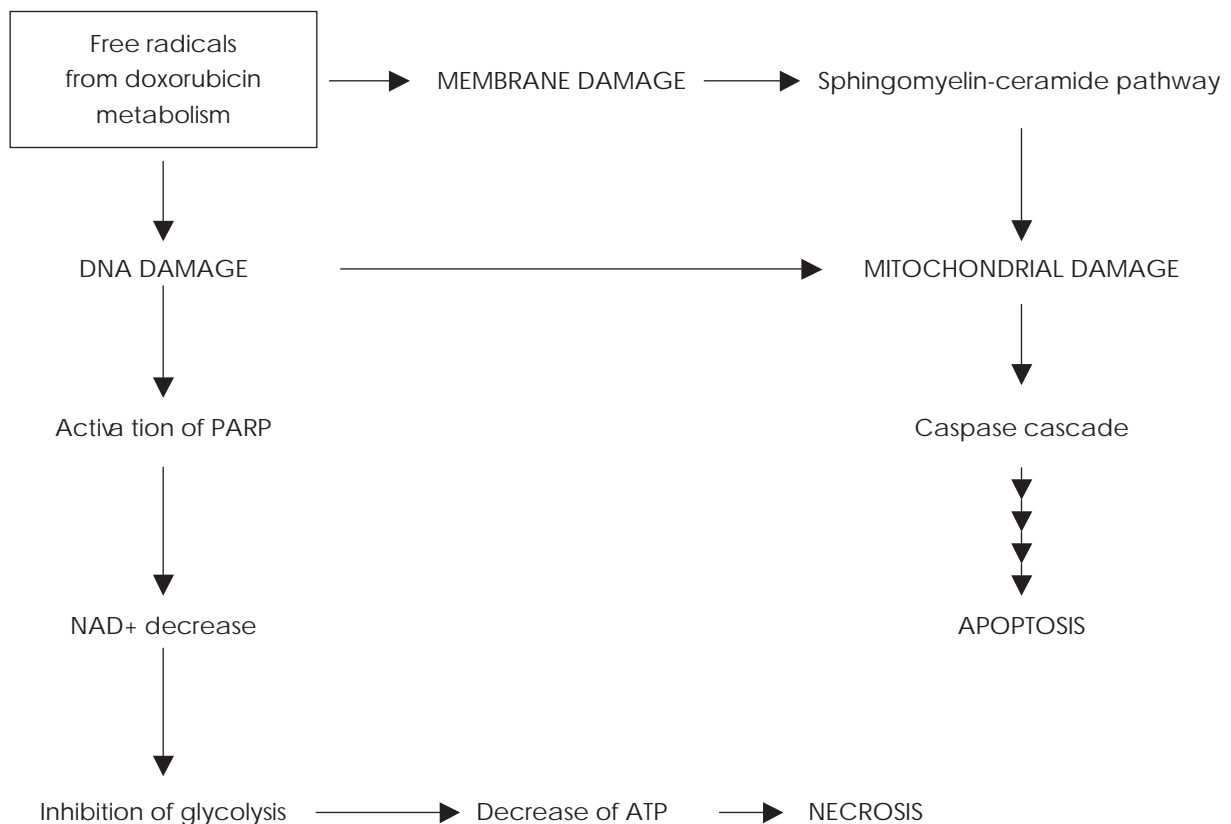
effect of nicotine on cell signaling at these two concentrations.<sup>20</sup> The aim of cancer therapy is to eliminate clonogenic cells in a tumor since tumor recurrence depends on continued growth of surviving clonogens. Programmed cell death or apoptosis occurs in both normal tissues and tumors. There is concern that apoptosis assays may be inadequate for predicting the response of tumors to drug and radiation treatment.<sup>11,12</sup> The treatment outcome depends on several decades of cell killing (multilog cell kill), which is related to clonogenic cell survival. Loss of colony formation from surviving clonogens is the main event in treated tumor cells, and apoptosis assays do not reflect the clonogenic potential of tumor cells. Moreover, studies com-

Figure 6. Caspase assays for apoptosis in MCF-7 cells



Inhibition of doxorubicin-mediated apoptosis of MCF-7 cells was also demonstrated on the basis of caspase-3 (clear bars) and caspase-8 (stippled bars) assays as described under methods. Data represent the mean  $\pm$  S.D of three experiments.

Figure 7. Scheme illustrating the pathways leading to apoptosis and necrosis in cells subjected to free radicals derived from doxorubicin<sup>29</sup>





paring apoptosis and cell survival responses in tumor cells usually fail to demonstrate a causal effect.<sup>11,21,22</sup> Inhibition of apoptosis of damaged normal cells may be important in carcinogenesis, while inhibition of apoptotic response may be associated with tumor resistance to therapy. It is known that apoptosis is not the main mechanism for death of cells in nonhematogenous solid tumors.<sup>11,12</sup> This leads to the conclusion that other modes of cell death are also important in the response to therapy. Doxorubicin is a cell cycle-independent cytotoxic agent that is quite effective in decreasing the clonogenic potential of cells. This drug owes its cytotoxic properties to several mechanisms including, but not restricted to, the formation of an array of free radicals through diverse mechanisms. (Table 3 and Figure 7). Free radicals formed during doxorubicin metabolism can initiate DNA damage that can lead to cell death via apoptosis or necrosis depending on the cellular levels of ATP (Figure 6).<sup>34</sup>

The inhibition of doxorubicin cytotoxicity by nicotine is in accord with accumulating evidence that nicotine can affect the cytotoxic effects of anticancer drugs.<sup>8-10</sup> The exact mechanisms by which nicotine affects cell viability is a matter of speculation, and several mechanisms have been proposed. Different possibilities are discussed below. There is convincing evidence that nicotine upregulates antiapoptotic proteins such as XIAP and survivin to give a survival advantage to certain lung cancer cells.<sup>10</sup> Nicotine was shown to induce multisite phosphorylation of proapoptotic proteins Bad and Bax in lung cancer cells and suppress drug-induced apoptosis.<sup>20,24</sup> Inactivation of proapoptotic function of Bad and Bax via phosphorylation also involves nicotine-mediated activation of PI3K/AKT, which acts as a kinase for Bax and Bad phosphorylation. It is noteworthy that treatment of A549 human lung cancer cells for 60 minutes with nicotine (10  $\mu$ M but not 20  $\mu$ M) induced phosphorylation of AKT.<sup>20</sup> Therefore, nicotine (10  $\mu$ M but not 20  $\mu$ M) activates AKT, leading to suppression of apoptosis because of Bad and Bax phosphorylation.<sup>20</sup> In this context, it is interesting that nicotine (10  $\mu$ M rather than 20  $\mu$ M) protected against cell killing by doxorubicin in our experiments.

Nicotine itself has been reported to possess some antioxidant as well as prooxidant properties. As an antioxidant, nicotine can decrease cell killing mediated by reactive oxygen species.<sup>36</sup> Nicotine can affect mitochondria and decrease cellular ATP production<sup>37,38</sup> and modulate doxorubicin-mediated apoptosis and necrosis. Nicotine inhibits glycolysis and enhances oxygen uptake in isolated perfused rat liver.<sup>39</sup> Programmed cell death (apoptosis) requires an adequate supply of ATP.<sup>34</sup> Perhaps decreased levels of ATP in nicotine-treated cells may explain the slight inhibition of doxorubicin-mediated apoptosis by nicotine pretreatment.

Nicotine inhibits iron uptake and iron transport in certain biological systems without actually affecting the levels of transferrin. Nicotine at a high nonphysiological

concentration of 15 mM inhibits iron uptake by about 60%.<sup>40</sup> Nicotine is a weak base, which inhibits release of iron from transferrin. Such perturbation of iron uptake by nicotine may affect the availability of iron for interaction with doxorubicin. Nicotine may interfere with free-radical generation resulting from the interaction of doxorubicin with iron. This may alter free-radical yield and decrease the cytotoxic effect of doxorubicin.

Nicotine may affect membrane permeability<sup>41</sup> and consequently affect the cytotoxicity of doxorubicin. This effect due to lysosomotropic effect of nicotine, if any, would be modest.

Nicotine induces oxidative stress and initiates cell signaling pathways involving transcription factor NF  $\kappa$ B.<sup>42-44</sup> Interventions that decrease free-radical flux would decrease apoptosis. The influence of nicotine on apoptosis has been described in terms of its effect on the antiapoptotic protein Bcl2 and proapoptotic proteins Bad and Bax.<sup>20,45</sup> There are conflicting reports on the influence of nicotine on apoptosis. There are several references to proapoptotic<sup>42,44,46,47</sup> as well as antiapoptotic<sup>10,20,35,45,48-50</sup> effects of nicotine.

The concentration of nicotine used in our experiments is slightly higher than the physiological concentration of 1  $\mu$ g per gram (about 6  $\mu$ M) found in the tissue of smokers.<sup>50</sup> The plasma half-life of nicotine is approximately 2 hours.<sup>51</sup> Exposure to nicotine in our experiments was for 2 hours, whereas smokers will likely be subjected to more prolonged exposure.

## CONCLUSION

Nicotine decreases the cytotoxicity of doxorubicin as indicated by assays for apoptosis, necrosis and clonogenicity. Necrosis, but not apoptosis, is the major cause of cell death in MCF-7 cells and KB-3.1 cells treated with doxorubicin under the conditions of our experiments. MCF-7 cells and KB-3.1 cells showed only a weak apoptotic response to doxorubicin treatment. Inhibition of apoptosis and reproductive cell death can affect tumor control. This statement must further be tempered by the fact that tumor response to therapy depends on tumor cell killing, cell proliferation and cell loss factor. The use of a transdermal nicotine patch during doxorubicin therapy may decrease overall efficacy.

## REFERENCES

1. U.S. Department of Health and Human Services, Office on Smoking and Health. The health consequences of smoking: Cancer: a report of the Surgeon General. Washington, DC: DHHS (P(1-47)HS) publication, no 82-50179; 1982:322.
2. Gritz ER, Dresler C, Sarna L. Smoking, the missing drug interaction in clinical trials: ignoring the obvious. *Cancer Epidemiol Biomarkers Prev*. 2005;14:2287-2293.
3. Nair U, Bartsch H. Metabolic polymorphisms as susceptibility markers for lung and oral cavity cancer. *IARC Sci Publ*. 2001;154:271-290.
4. Johnson KC. Accumulating evidence on passive and active smoking and breast cancer risk. *Int J Cancer*. 2005;117:619-628.
5. Lash TL, Aschengrau A. Active and passive cigarette smoking and the occurrence of breast cancer. *Am J Epidemiol*. 1999;149:5-12.
6. Kropp S, Chang-Claude J. Active and passive smoking and risk of breast



- cancer by age 50 years among German women. *Am J Epidemiol*. 2002;156:616-626.
7. Lee HY, Oh SH, Woo JK, et al. Chemopreventive effects of deguelin, a novel Akt inhibitor, on tobacco-induced lung tumorigenesis. *J Natl Cancer Inst*. 2005;97:1695-1699.
  8. Berger MR, Zeller WJ. Interaction of nicotine with anticancer treatment. *Klin Wochenschr*. 1988;66(suppl 11):127-133.
  9. Onoda N, Nehmi A, Weiner D, et al. Nicotine affects the signaling of the death pathway, reducing the response of head and neck cancer cell lines to DNA damaging agents. *Head Neck*. 2001;23:860-870.
  10. Dasgupta P, Kinkade R, DeCook, et al. Nicotine inhibits apoptosis induced by chemotherapeutic drugs by up-regulating XIAP and survivin. *Proc Natl Acad Sci U S A*. 2006;103:6332-6337.
  11. Brown JM, Attardi LD. The role of apoptosis in cancer development and treatment response. *Nat Rev Cancer*. 2005;5:231-237.
  12. Steel GG. The case against apoptosis. *Acta Oncol*. 2001;40:968-975.
  13. Desai PB, Bhardwaj R, Damle B. Effect of tamoxifen on mitoxantrone cytotoxicity in drug-sensitive and multidrug-resistant MCF-7 cells. *Cancer Chemother Pharmacol*. 1995;36:368-372.
  14. Connor CE, Burrows J, Hearps AC, et al. Cell cycle arrest of hematopoietic cell lines after treatment with ceramide is commonly associated with retinoblastoma activation. *Cytometry*. 2001;43:164-169.
  15. Soeda J, Miyagawa S, Sano K, et al. Cytochrome c release into cytosol with subsequent caspase activation during warm ischemia in rat liver. *Am J Physiol Gastrointest Liver Physiol*. 2001;281:G1115-1123.
  16. Mu YM, Yanase T, Nishi Y, et al. Saturated FFAs, palmitic acid and stearic acid induce apoptosis in human granulosa cells. *Endocrinology*. 2001;142:3590-3597.
  17. Alles K, Alley JC, Barrett R et al. Apoptosis: a general comment. *FASEB J*. 1991;5:2127-2128.
  18. Hall EJ. Radiobiology for the Radiologist. Philadelphia, PA: Lippincott Williams & Wilkins; 2000.
  19. Scott SL, Gumerlock PH, Beckett L, et al. Survival and cell cycle kinetics of human prostate cancer cell lines after single- and multifraction exposures to ionizing radiation. *Int J Radiat Oncol Biol Phys*. 2004;59:219-227.
  20. Xin M, Deng X. Nicotine inactivation of the proapoptotic function of Bax through phosphorylation. *J Biol Chem*. 2005;280:10781-10789.
  21. Yanagihara K, Nii M, Numoto M, et al. Radiation-induced apoptotic death in human gastric epithelial tumor cells: correlation between mitotic death and apoptosis. *Int J Radiat Biol*. 1995;67:677-685.
  22. Mimnaugh EG, Gram TE, Trush MA. Stimulation of mouse heart and liver microsomal lipid peroxidation by anthracycline anticancer drugs: characterization and effects of reactive oxygen scavengers. *J Pharmacol Exp Ther*. 1983;226:806-816.
  23. Engineer FN, Sridhar R. Attenuation of daunorubicin-augmented microsomal lipid peroxidation and oxygen consumption by calcium channel antagonists. *Biochem Biophys Res Commun*. 1991;179:1101-1106.
  24. Sridhar R, Dwivedi C, Anderson J, et al. Effects of verapamil on the acute toxicity of doxorubicin in vivo. *J Natl Cancer Inst*. 1992;84:1653-1660.
  25. Mimnaugh EG, Trush MA, Gram TE. Enhancement of rat heart microsomal lipid peroxidation following doxorubicin treatment in vivo. *Cancer Treat Rep*. 1983;67:731-733.
  26. Sinha BK, Trush MA, Kennedy KA, et al. Enzymatic activation and binding of adriamycin to nuclear DNA. *Cancer Res*. 1984;44:2892-2896.
  27. Kotamraju S, Kalivendi SV, Konorev E, et al. Oxidant-induced iron signaling in doxorubicin-mediated apoptosis. *Methods Enzymol*. 2004;378:362-382.
  28. Minotti G, Recalcati S, Menna P, et al. Doxorubicin cardiotoxicity and the control of iron metabolism: quinone-dependent and independent mechanisms. *Methods Enzymol*. 2004;378:340-361.
  29. Zweier JL. Iron-mediated formation of an oxidized adriamycin free radical. *Biochim Biophys Acta*. 1985;839:209-213.
  30. Xu X, Persson HL, Richardson DR. Molecular pharmacology of the interaction of anthracyclines with iron. *Mol Pharmacol*. 2005;68:261-271.
  31. Bodley A, Liu LF, Israel M, et al. DNA topoisomerase II-mediated interaction of doxorubicin and daunorubicin congeners with DNA. *Cancer Res*. 1989;49:5969-5978.
  32. Olson LE, Bedja D, Alvey SJ, et al. Protection from doxorubicin-induced cardiac toxicity in mice with a null allele of carbonyl reductase 1. *Cancer Res*. 2003;63:6602-6606.
  33. Forrest GL, Gonzalez B, Tseng W, et al. Human carbonyl reductase over-expression in the heart advances the development of doxorubicin-induced cardiotoxicity in transgenic mice. *Cancer Res*. 2000;60:5158-5164.
  34. Martin DS, Bertino JR, Koutcher JA. ATP depletion + pyrimidine depletion can markedly enhance cancer therapy: fresh insight for a new approach. *Cancer Res*. 2000;60:6776-6783.
  35. Jin Z, Gao F, Flagg T, et al. Nicotine induces multi-site phosphorylation of Bad in association with suppression of apoptosis. *J Biol Chem*. 2004;279:23837-23844.
  36. Sugano N, Ito K. Nicotine switches the form of H(2)O(2)-induced cell death from apoptosis to necrosis in U937 cells. *Immunol Lett*. 2000;72:163-166.
  37. Newman MB, Arendash GW, Shytle RD, et al. Nicotine's oxidative and antioxidant properties in CNS. *Life Sci*. 2002;71:2807-2820.
  38. Guan ZZ, Yu WF, Nordberg A. Dual effects of nicotine on oxidative stress and neuroprotection in PC12 cells. *Neurochem Int*. 2003;43:243-249.
  39. Dewar BJ, Bradford BU, Thurman RG. Nicotine increases hepatic oxygen uptake in the isolated perfused rat liver by inhibiting glycolysis. *J Pharmacol Exp Ther*. 2002;301:930-937.
  40. McArdle HJ, Tysoe J. Effect of nicotine on transferrin binding and iron uptake by cultured rat placenta. *J Cell Physiol*. 1988;134:509-513.
  41. Klugmann FB, Decorti G, Crivellato E, et al. Effect of lysosomotropic and membrane active substances on adriamycin uptake and histamine release. *Anticancer Res*. 1990;10:1571-1577.
  42. Crowley-Weber CL, Dvorakova K, Crowley C, et al. Nicotine increases oxidative stress, activates NF-kappaB and GRP78, induces apoptosis and sensitizes cells to genotoxic/xenobiotic stresses by a multiple stress inducer, deoxycholate: relevance to colon carcinogenesis. *Chem Biol Interact*. 2003;145:53-66.
  43. Tsurutani J, Castillo SS, Brognard J, et al. Tobacco components stimulate Akt-dependent proliferation and Nf-kappaB-dependent survival in lung cancer cells. *Carcinogenesis*. 2005;26:1182-1195.
  44. Ravikumar R, Flora G, Geddes JW, et al. Nicotine attenuates oxidative stress, activation of redox-regulated transcription factors and induction of proinflammatory genes in compressive spinal cord trauma. *Brain Res Mol Brain Res*. 2004;124:188-198.
  45. Mai H, May WS, Gao F, et al. A functional role for nicotine in Bcl2 phosphorylation and suppression of apoptosis. *J Biol Chem*. 2003;278:1886-1891.
  46. Wu YP, Kita K, Suzuki N. Involvement of human heat shock protein 90 alpha in nicotine-induced apoptosis. *Int J Cancer*. 2002;100:37-42.
  47. Jang MH, Shin MC, Jung SB, et al. Alcohol and nicotine reduce cell proliferation and enhance apoptosis in dentate gyrus. *Neuroreport*. 2002;13:1509-1513.
  48. Garrido R, Mattson MP, Hennig B, et al. Nicotine protects against arachidonic-acid-induced caspase activation, cytochrome c release and apoptosis of cultured spinal cord neurons. *J Neurochem*. 2001;76:1395-1403.
  49. Hakki A, Pennypacker K, Eidzadeh S, et al. Nicotine inhibition of apoptosis in murine immune cells. *Exp Biol Med (Maywood)*. 2001;226:947-953.
  50. Hakki A, Friedman H, Pross S. Nicotine modulation of apoptosis in human coronary artery endothelial cells. *Int Immunopharmacol*. 2002;2: 1403-1409.
  51. Benowitz NL, Jacob P III, Denaro C, Jenkins R. Stable isotope studies of nicotine kinetics and bioavailability. *Clin Pharmacol Ther*. 1991;49:270-277. ■

## Vitamin E Succinate Induces Ceramide-Mediated Apoptosis in Head and Neck Squamous Cell Carcinoma *In vitro* and *In vivo*

Xinbin Gu,<sup>1,4</sup> Xiaodong Song,<sup>5,6</sup> Yongheng Dong,<sup>7</sup> Hui Cai,<sup>1</sup> Eric Walters,<sup>2</sup> Renshu Zhang,<sup>3,4</sup> Xiaowu Pang,<sup>1</sup> Tianpei Xie,<sup>5</sup> Yinhan Guo,<sup>7</sup> Rajagopalan Sridhar,<sup>3,4</sup> and Joseph A. Califano<sup>8</sup>

**Abstract Purpose:** Vitamin E succinate ( $\alpha$ -TOS) inhibits the growth of cancer cells without unacceptable side effects. Therefore, the mechanisms associated with the anticancer action of  $\alpha$ -TOS, including ceramide-mediated apoptosis, were investigated using head and neck squamous cell carcinoma (HNSCC) *in vitro* and *in vivo*.

**Experimental Design:** Five different human HNSCC cell lines (JHU-011, JHU-013, JHU-019, JHU-022, and JHU-029) were treated with  $\alpha$ -TOS, and its effects on cell proliferation, cell cycle progression, ceramide-mediated apoptosis, and ceramide metabolism were evaluated. The anticancer effect of  $\alpha$ -TOS was also examined on JHU-022 solid tumor xenograft growth in immunodeficient mice.

**Results:**  $\alpha$ -TOS inhibited the growth of all the HNSCC cell lines *in vitro* in a dose- and time-dependent manner. Thus, JHU-013 and JHU-022 cell lines were more sensitive to  $\alpha$ -TOS than the other cell lines. Cellular levels of ceramide, sphingomyelinase activity, caspase-3, and p53 were elevated with increasing time of exposure to  $\alpha$ -TOS. The degradation of poly(ADP-ribose) polymerase protein in JHU-022 cells treated with  $\alpha$ -TOS provided evidence for apoptosis. The amounts of nuclear factor  $\kappa$ B, Bcl-2, and Bcl-X<sub>L</sub> proteins were reduced in the cells treated with  $\alpha$ -TOS for 6 hours. The levels of caspase-9, murine double minute-2, and I $\kappa$ B- $\alpha$  proteins were unchanged after  $\alpha$ -TOS treatment. I.p. administration of  $\alpha$ -TOS slowed tumor growth in immunodeficient mice.

**Conclusions:**  $\alpha$ -TOS showed promising anticancer effects to inhibit HNSCC growth and viability *in vivo* and *in vitro*. The induction of enzymes involved in ceramide metabolism by  $\alpha$ -TOS suggests that ceramide-mediated apoptosis may expand therapeutic strategies in the treatment of carcinoma.

Each year, ~31,000 Americans are diagnosed with head and neck cancer and ~7,400 die from the disease (1). Overall survival rates of head and neck cancers have only marginally improved over the last three decades (2). In addition, the incidence of oral cancer in African American men has been approximately twice higher than in Caucasian men, and the 5-year relative survival is lower for African Americans (1).

Therefore, novel therapeutic and preventive approaches are warranted.

Accumulating evidence suggested that an esterified derivative of RRR- $\alpha$ -tocopherol ( $\alpha$ -TOH), RRR- $\alpha$ -tocopheryl succinate ( $\alpha$ -TOS), is a vitamin E analogue, which inhibits tumor growth (3–7). It induces apoptosis, inhibits tumor cell proliferation and differentiation, arrests DNA synthesis, and blocks cell cycle progression in various cancer cell lines and animal models of breast, colon, head and neck, prostate, and lung cancers (8–18). In addition,  $\alpha$ -TOS selectively kills tumor cells without toxic effects on normal cells and tissues (4, 7, 18). The parent compound of vitamin E,  $\alpha$ -TOH, is a free radical-scavenging antioxidant, which protects polyunsaturated fats from peroxidation in human body but does not induce cancer cell apoptosis (19). In contrast to  $\alpha$ -TOH,  $\alpha$ -TOS is a redox-inactive molecule, which has a charged side group when it exists at physiologic pH.  $\alpha$ -TOS can be converted to  $\alpha$ -TOH by cellular esterase (20). All the reports thus far indicate that  $\alpha$ -TOS causes an increase in cancer cell apoptosis (3–7), but the mechanism(s) of  $\alpha$ -TOS-induced cancer cell apoptosis and inhibition of cancer cell growth are not fully understood.

In previous studies, we found that  $\alpha$ -TOS induced apoptosis in a hamster cheek pouch carcinoma cell line (HPCPC-1) and altered sphingolipid metabolism (11). Moreover, cell viability was significantly reduced in cultures treated with  $\alpha$ -TOS. A critical finding in our study was that  $\alpha$ -TOS interacts with cell membrane to shift phospholipids and sphingolipid in the lipid

**Authors' Affiliations:** Departments of <sup>1</sup>Oral Diagnostic Service, <sup>2</sup>Biochemistry and Molecular Biology, and <sup>3</sup>Radiation Oncology, and <sup>4</sup>Cancer Center, Howard University, Washington, District of Columbia; <sup>5</sup>Shanghai TenGen Biomedical Co. Ltd., Shanghai, China; <sup>6</sup>Experiment Center, Binzhou Medical College, Shandong, China; <sup>7</sup>Oriental TenGen Tech Development Co. Ltd., Beijing, China; and <sup>8</sup>Department of Otolaryngology-Head and Neck Surgery, Johns Hopkins University, Baltimore, Maryland

Received 7/24/07; revised 10/23/07; accepted 1/11/08.

**Grant support:** NIH grants CA118770 and CA91409 and the Tianjue Gu Foundation.

The costs of publication of this article were defrayed in part by the payment of page charges. This article must therefore be hereby marked *advertisement* in accordance with 18 U.S.C. Section 1734 solely to indicate this fact.

**Requests for reprints:** Xinbin Gu, Department of Oral Diagnostic Service, College of Dentistry, Howard University, 600 W Street, NW, Washington, DC 20059. Phone: 202-806-0345; Fax: 202-806-0446. E-mail: xgu@howard.edu.

©2008 American Association for Cancer Research.

doi:10.1158/1078-0432.CCR-07-1811

bilayer of the abnormal plasma membrane. This makes sphingolipids more accessible to hydrolases and then to generate ceramide. Ceramide is a central molecule in sphingolipid metabolism, having a significant role in the apoptotic response of various cancer cells (21–27). For example, androgen ablation in LNCaP prostate cancer cells results in selective accumulation of *de novo* generated C<sub>16</sub>-ceramide. This accumulation of ceramide leads to G<sub>0</sub>-G<sub>1</sub> arrest followed by apoptosis (24). Mice deficient in acid sphingomyelinase lose the ability to accumulate ceramide and acquire resistance to radiation-induced apoptosis (25). Interruption of sphingomyelin synthesis or hydrolysis of sphingomyelin by sphingomyelinase can increase cellular levels of ceramide. Increased levels of ceramide can damage mitochondria and induce apoptosis (27, 28). Experiments designed to reveal the relationship between  $\alpha$ -TOS and ceramide-mediated apoptosis in cancer cells, especially in head and neck cancer cells, are warranted.

We hypothesized that  $\alpha$ -TOS may activate the accumulation of ceramide in the cancer cells of head and neck squamous cell carcinoma (HNSCC), and that ceramide buildup triggers apoptotic events. In this report, we tested this hypothesis in five different human HNSCC cell lines, including JHU-011, JHU-013, JHU-019, JHU-022, and JHU-029 cell lines, using *in vitro* and *in vivo* systems.

## Materials and Methods

**Chemical reagents.** Chemicals were of the highest available grade. Ceramide (N-octadecanoyl-D-erythro-sphingosine),  $\alpha$ -TOS, and phosphatidylcholine were obtained from Sigma Chemical Company. *Escherichia coli* sn-1,2-diacylglycerol kinase (specific activity >2 units/mg protein) and octyl- $\beta$ -D-glucopyranoside were obtained from Calbiochem, and [ $\gamma$ -<sup>32</sup>P]ATP (3,000 Ci/mmol) was obtained from Amersham.

**$\alpha$ -TOS-liposome preparation.** Two types of small unilamellar vesicles (SUV), vehicle-SUV and  $\alpha$ -TOS encapsulated SUV, were made for *in vitro* experiments based on the previously reported method (11). The vehicle-SUV was a suspension of phosphatidylcholine liposomes in PBS, and  $\alpha$ -TOS-SUV consisted of phosphatidylcholine liposomes encapsulating 1 mmol/L  $\alpha$ -TOS. In brief, 0.2 g/mL phosphatidylcholine lipid stock solution in 1:1 mixture of chloroform/methanol was dried under nitrogen and then mixed with an isotonic solution of physiologic saline (0.9% NaCl) along with the anionic detergent sodium cholate. The resulting mixed micellar solution was then dialyzed in a Mini Lipoprep dialyzer (5,000 MW cutoff; Amika Corporation) for 4 h against an 8-liter reservoir of 0.9% NaCl solution. To encapsulate  $\alpha$ -TOS into the SUV,  $\alpha$ -TOS was dissolved along with phosphatidylcholine using the mixture of chloroform and methanol (1:1). This was then processed as described above for the preparation of SUV.

**Cell lines and culture.** HNSCC cell lines including JHU-011 (larynx, p53 mutated), JHU-013 (neck node metastasis, p53 mutated), JHU-019 (tongue), JHU-022 (larynx, wild type of p53), and JHU-029 (wild type of p53) were established by Johns Hopkins University. The HNSCC cells were grown in RPMI 1640 supplemented with 10% fetal bovine serum (Life Technologies, Inc.) and antibiotic-antimycotic mixture (100 IU/mL penicillin and 100  $\mu$ g/mL streptomycin; Cellgro). Cells were grown in 5% CO<sub>2</sub> at 37°C and were subcultured at an initial density of  $1 \times 10^5$ /mL every 3 to 4 d. Cell density was determined with a hemocytometer and a phase-contrast microscope. Trypan blue dye exclusion assay (Sigma-Aldrich) detected 0.1% of dead cells in the untreated culture. All experiments were done with cells in logarithmic phase of growth.

**3-(4,5-Dimethylthiazol-2-yl)-2,5-diphenyltetrazolium bromide assays.** HNSCC cells were seeded in flat-bottomed 96-well cell culture

plate (Costar) at a density of 5,000 per well and allowed to attach overnight. The cells were then treated with  $\alpha$ -TOS-SUV at various concentrations (5–80  $\mu$ mol/L) for 12 h. Twenty microliters of 3-(4,5-dimethylthiazol-2-yl)-2,5-diphenyltetrazolium bromide solution (Sigma) were added to each well and then the plate was incubated in a humidified CO<sub>2</sub> incubator at 37°C for 5 h. After removing the media, 200  $\mu$ L of DMSO were added to each well and mixed for 30 min at room temperature to dissolve crystals. The plate was placed inside a 37°C incubator for 5 min. Finally, the plate was transferred to a microplate reader (Bio-Rad) and absorbance at 550 nm was measured.

**Colony formation assay.** HNSCC cells were seeded at a density of 200 per well in BD Falcon six-well tissue culture plate. The cells were allowed to attach overnight. The cultures were treated with  $\alpha$ -TOS-SUV (20  $\mu$ mol/L) for 3 to 24 h. Control cultures were treated with the same volume of medium with vehicle (SUV). The medium was removed from each well and the cells were washed with PBS. Fresh drug-free culture medium (5 mL) was added to the cultures, which were then placed back into the incubator to form colonies in 10 d. Any colony containing >50 cells was considered to represent a viable clonogenic cell. The colonies in the wells were counted after staining with 0.1% methylene blue in 50% ethanol. The experiment was done thrice for each treatment.

**Flow cytometry assay.** HNSCC cells ( $5 \times 10^4$ ) were seeded in six-well, flat-bottomed plates and were exposed to 20  $\mu$ mol/L  $\alpha$ -TOS-SUV for 6, 12, and 24 h. The cells were collected, washed, and suspended in cold PBS. The cells were fixed in chilled 75% methanol and then incubated in the dark for 15 min at room temperature in a solution containing Annexin V-FITC (Clontech Laboratories, Inc.) and propidium iodide (5  $\mu$ g/mL). The expression of Annexin V and cell cycle status were analyzed by FACStar flow cytometer (Becton Dickinson & Co.). Ten thousand cells per sample were analyzed.

**Human tumor xenograft in mice.** Four-week-old, female, athymic nude mice (Nu/Nu) were obtained from Harlan Sprague-Dawley, Inc. They were given Harlan Teklad #2018 Global 18% Protein Rodent Diet containing 101 mg/kg  $\alpha$ -tocopherol and water *ad libitum* in the animal facility for 3 wk before use. Mice were housed in temperature-controlled rooms (74  $\pm$  2°F) with a 12-h alternating light-dark cycle. The mice were separated into three groups (three to five per group):  $\alpha$ -TOS treatment group, DMSO vehicle control group, and untreated control group. The body weight and food/water intake were measured twice a week. The mice in the  $\alpha$ -TOS group received a 3-wk pretreatment with  $\alpha$ -TOS (1.0 mg dissolved in 0.1-mL DMSO/mouse by i.p. injection) every other day before injecting JHU-022 cells. The mice in the DMSO group received 0.1-mL DMSO by i.p. injection. JHU-022 cancer cells ( $2 \times 10^6$ /100  $\mu$ L/mouse) were injected s.c. into the lower back of the mice using a 25-gauge needle on day 21. I.p. injections of  $\alpha$ -TOS were continued on alternate days till day 55. Thus, each mouse in the  $\alpha$ -TOS group received a total of 25 mg of  $\alpha$ -TOS via i.p. injection for the 55-d treatment period. Tumor volume was determined from either caliper measurements ( $T_{vol} = \text{length} \times \text{width} \times \text{depth} \times 0.5236$ ) or directly by weighing the tumor. Guidelines for the humane treatment of animals were followed as approved by the Howard University Animal Care and Use Committee.

**Immunohistochemistry.** Tumor tissues were fixed in 10% formalin, embedded in paraffin, and cut into 5- $\mu$ m-thick sections. The immunostaining was done using the Universal DAKO LSAB2 system (DAKO Corporation). Briefly, the tissue sections were deparaffinized in xylene and rehydrated in a graded series of ethanol/water rinses. Antigen retrieval was done by heating the slides in a steamer to 95°C to 99°C in Target Retrieval Solution (DAKO) for 20 min. At room temperature, the slides were then treated with 3% hydrogen peroxide for 10 min, followed by primary antibody, monoclonal ceramide antibody (Alexis USA), used at a 1:100 dilution, for 1 h. Visualization with streptavidin-horseradish peroxidase (Biogenex) and 3-amino-9-ethylcarbazole was followed by a hematoxylin counterstain (Biomed).

**$\alpha$ -TOS analysis.** Blood was collected from the mouse before the termination of the experiment on day 55.  $\alpha$ -TOS was measured by using

reverse-phase high-performance liquid chromatography. Each plasma sample (100  $\mu$ L) was extracted thrice in hexane/ethanol 3:1 with SDS. The lipid fraction was evaporated to dryness under a nitrogen stream. The samples were then resuspended in methanol and injected into Agilent 1100 high-performance liquid chromatography. The mobile phase consisted of 99.4% methanol and 0.6% glacial acetic acid. Samples were separated on an Elite hypersil ODS2 5  $\mu$ m (250  $\times$  4.6 mm) column (Elite). HPLC detector was set at 284 nm for all detection. Quantitation of the separated compounds was done based on  $\alpha$ -TOS standard pattern and Agilent software for data analyses.

**Diacylglycerol kinase assay.** Ceramide levels were determined with the diacylglycerol kinase assay as described in the previous study (11). In brief, monolayer cultures of HNSCC cells ( $10^6$ ) were treated with  $\alpha$ -TOS-SUV (20  $\mu$ M/L) or SUV for 30 min to 9 h. Cellular lipids were extracted from the treated cells using a mixture of chloroform/methanol/1 N HCl at a ratio of 100:100:1 (v/v), and then hydrolyzed with 0.1 N methanolic KOH for 1 h at 37  $^{\circ}$ C to remove glycerophospholipids. Ceramide containing samples were resuspended in 100  $\mu$ L of reaction mixture containing 150  $\mu$ g cardiolipin, 280  $\mu$ M/L diethylenetriaminepentaacetic acid, 51  $\mu$ M/L octyl- $\beta$ -D-glucopyranoside (Calbiochem), 1 mmol/L ATP, 10  $\mu$ Ci [ $\gamma$ - $^{32}$ P]ATP (DuPont New England Nuclear), and 35  $\mu$ g/mL *E. coli* diacylglycerol kinase, pH 6.5 (Calbiochem). After 60 min at room temperature, the reaction was stopped by extraction of lipids with 1 mL of solvent mixture of chloroform/methanol/1 N HCl (100:100:1, v/v). Ceramide 1-phosphate was separated on TLC plate using a solvent system of chloroform/methanol/acetic acid (65:15:5, v/v) and detected by autoradiography. The incorporated  $^{32}$ P was quantified by liquid scintillation counting. Ceramide was determined by comparison with standard samples containing known amounts of ceramide.

**In vivo sphingomyelinase assay.** Sphingomyelinase assay was modified based on Cifone's method (29). In brief, the monolayer culture of HNSCC cells with 5% serum was labeled for 48 h with [*N*-methyl- $^{14}$ C]-choline (NEN Life Science Products, Inc.). The cells were washed thrice with Ca- and Mg-free PBS and then treated with  $\alpha$ -TOS-SUV (20  $\mu$ M/L) or SUV for 30 min to 6 h. The cells were harvested from cultures by trypsinization and kept at 4 $^{\circ}$ C to avoid protein degradation. Cellular lipids were extracted with a mixture of ice-cold methanol/chloroform/water at a ratio of 250:125:100 (v/v), and the samples corresponding to equal amounts of proteins were loaded onto individual lanes on the TLC plate. The lipids were separated by developing the thin layer chromatogram using a mixed solvent system composed of chloroform/methanol/acetic acid/water at a ratio of 100:60:20:5 (v/v). The radioactive spots were visualized by autoradiography and scraped along with silica gel from the plate and transferred to a scintillation vial containing 1 mL of scintillation cocktail of water and aquasol for determination of radioactivity.

**Apoptain assay.** Caspase-3 activity measurement was done with FluorAce Apoptain Kit (Bio-Rad Laboratories) according to the manufacturer's instructions. In brief, the  $\alpha$ -TOS-SUV-treated (20  $\mu$ M/L) or SUV-treated cells ( $1 \times 10^6$ ) were lysed with apoptain cell lysis buffer and the supernatant was incubated with fluorogenic peptide substrate Ac-DEVD-AFC, 55  $\mu$ M/L, and reaction buffer at 37 $^{\circ}$ C. At the same time, to distinguish caspase-3 activity from nonspecific protease activity, the sample reactions were carried out after adding relatively nonselective caspase inhibitor z-VAD-fmk (50  $\mu$ M/L) or caspase-3 inhibitor z-DEVD-fmk (50  $\mu$ M/L; Clontech). The fluorescence readings were recorded after 30 and 60 min of incubation using a VersaFluor fluorometer (Bio-Rad), with excitation and emission wavelengths of 390 and 520 nm, respectively. Results were expressed as units of Apoptain per 0.1 milligram of protein, according to the formula provided with the FluorAce Apoptain Assay Kit. Protein concentration was measured using a DC Protein Assay kit (Bio-Rad Laboratories).

**Western immunoblotting.** The treated and untreated HNSCC cells were harvested and washed twice in PBS and then suspended in lysis

buffer [50 mmol/L Tris (pH 8.0), 150 mmol/L NaCl, 0.1% SDS, 0.5% sodium deoxycholate, 1% NP40, phenylmethylsulfonyl fluoride at 100  $\mu$ g/mL, aprotinin at 2  $\mu$ g/mL, pepstatin at 1  $\mu$ g/mL, and leupeptin at 10  $\mu$ g/mL]. This mixture was placed on ice for 30 min. After centrifugation at 15,000  $\times$  g for 15 min at 4 $^{\circ}$ C, the supernatant was collected. Protein concentrations were quantitated by using the Bio-Rad protein assay (Bio-Rad Laboratories). Whole-cell lysates (30  $\mu$ g) were separated by 8% SDS-PAGE gel, transferred onto a polyvinylidene difluoride membrane (Immobilon; Amersham Corp.), and then probed sequentially with antibodies against the following proteins: caspase-3, caspase-9, poly(ADP-ribose) polymerase (PARP), Bcl-2, Bcl-xL, p53, murine double minute-2, nuclear factor  $\kappa$ B, I $\kappa$ B- $\alpha$ , and  $\beta$ -actin (Sigma). Blots were washed thrice for 10 min with PBS + 0.1% Tween 20 and incubated with horseradish peroxidase-conjugated antirabbit, antimouse, or antigoat antibody (Santa Cruz Biotechnology) for 1 h at room temperature. Blots were developed by a peroxidase reaction using the enhanced chemiluminescence detection system (Bio-Rad).

**Statistical analyses.** Results are presented relative to untreated controls. Values represent mean  $\pm$  SD of three or more replicate tests.

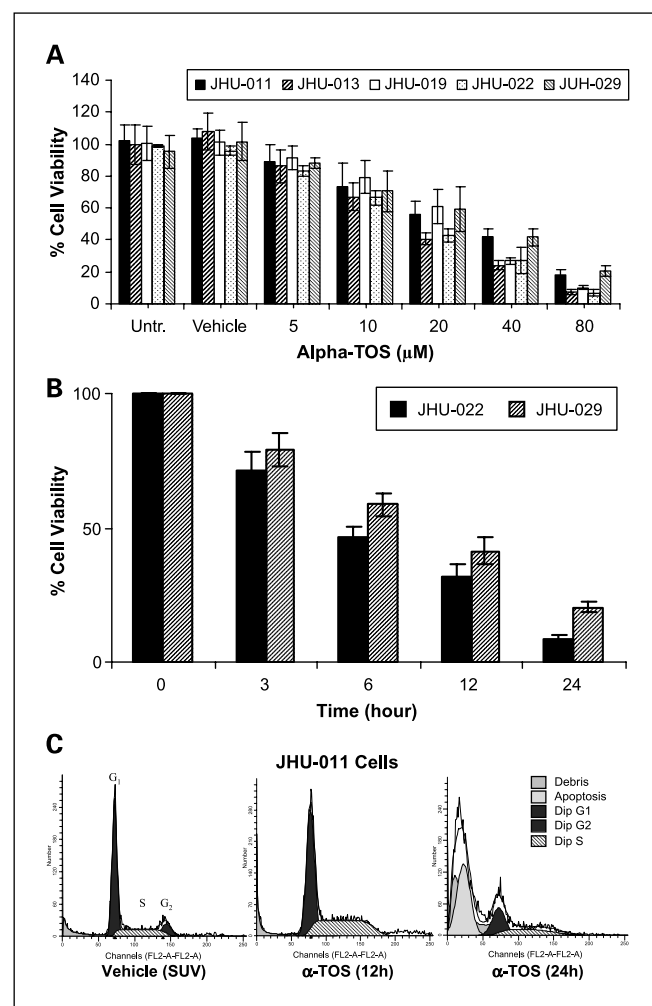


**Fig. 1.** Cytotoxicity of  $\alpha$ -TOS toward HNSCC cell lines. **A**, 3-(4,5-dimethylthiazol-2-yl)-2,5-diphenyltetrazolium bromide assay was used to determine the viability of cells in five different HNSCC cell lines treated with graded doses (0–80  $\mu$ M/L) of  $\alpha$ -TOS-SUV for 12 h. **B**, cell survival was determined on the basis of colony formation assays after incubation of JHU-022 and JHU-029 cells with  $\alpha$ -TOS-SUV (20  $\mu$ M/L) for 0 to 24 h. **C**, flow cytometry profiles of JHU-011 cells treated with SUV (vehicle alone) or  $\alpha$ -TOS-SUV (20  $\mu$ M/L) for 12 and 24 h. Columns, mean cell viability of two independent experiments with triplicate dishes; bars, SD.



Data were analyzed by Duncan test following the ANOVA procedure when multiple comparisons were made.  $P < 0.05$  was considered significant.

## Results

**Effect of  $\alpha$ -TOS on the proliferation and viability of HNSCC cell lines *in vitro*.** We first confirmed the inhibitory effects of  $\alpha$ -TOS on cell proliferation and viability in five different human HNSCC cell lines (JHU-011, JHU-013, JHU-019, JHU-022, and JHU-029) *in vitro* by using 3-(4,5-dimethylthiazol-2-yl)-2,5-diphenyltetrazolium bromide and colony formation assays.  $\alpha$ -TOS inhibited cell proliferation in all five cell lines in a dose-dependent manner when the cells were exposed to graded doses (5–80  $\mu$ mol/L) for 12 hours. This inhibition was most pronounced in JHU-013 and JHU-022 cell lines (Fig. 1A). Because 20  $\mu$ mol/L  $\alpha$ -TOS-SUV was the half maximal inhibitory concentration ( $IC_{50}$ ) in JHU-013 and JHU-022 cell lines, this dose of  $\alpha$ -TOS-SUV was used for further *in vitro* studies. The potency of  $\alpha$ -TOS was determined by using colony formation assay to measure the reproductive integrity of JHU-022 and JHU-029 cells treated with 20  $\mu$ mol/L  $\alpha$ -TOS-SUV from 0 to 24 hours (Fig. 1B). As expected, clonogenic capacities of JHU-022 and JHU-029 cell lines decreased with increasing exposure time to 20  $\mu$ mol/L  $\alpha$ -TOS-SUV (Fig. 1B). As compared with untreated cancer cells, the relative survival of JHU-022 cells decreased to 31.9% and 8.7%, whereas survival of JHU-029 cells decreased to 43.3% and 20.4% after treatment with  $\alpha$ -TOS-SUV for 12 and 24 hours, respectively (Fig. 1B). The effects of  $\alpha$ -TOS-SUV treatment of the different cell lines were explored further by flow cytometry analysis for cell cycle distribution and estimation of apoptosis. As summarized in Table 1, flow cytometry data indicated that a 24-hour exposure to  $\alpha$ -TOS induced S-phase arrest and reduced the proportion of cells in  $G_1$  phase in all five HNSCC cell lines after treatment. Moreover,  $\alpha$ -TOS induced a significant proportion of apoptosis in JHU-011 (57.87%), JHU-013 (58.02%), JHU-019 (54.87%), JHU-022 (49.39%), and JHU-029 (48.23%) cell lines after a 24-hour exposure (Table 1). However, there was <1% apoptotic cells in JHU-011 cells treated for 12 hours with  $\alpha$ -TOS-SUV, vehicle (SUV), and untreated control cells

**Table 1.** Comparison of cell cycle in  $\alpha$ -TOS–treated cell lines

Cell line	$G_1$ (%)	$G_2$ (%)	S (%)	Apoptosis (%)
JHU-011 untreated	61.04	12.18	26.78	0.12
JHU-011 vehicle	62.33	11.62	26.05	0.16
JHU-011 $\alpha$ -TOS	51.83	8.97	39.19	57.87
JHU-013 untreated	62.09	11.15	26.76	0.08
JHU-013 vehicle	63.31	12.15	24.54	0.10
JHU-013 $\alpha$ -TOS	54.26	9.09	36.65	58.02
JHU-019 untreated	63.03	12.63	24.34	0.15
JHU-019 vehicle	61.07	13.56	25.37	0.07
JHU-019 $\alpha$ -TOS	57.5	13.17	29.33	54.87
JHU-022 untreated	61.27	11.08	27.65	0.16
JHU-022 vehicle	60.68	15.56	23.76	0.08
JHU-022 $\alpha$ -TOS	54.68	8.06	37.26	49.39
JHU-029 untreated	60.02	10.98	29	0.09
JHU-029 vehicle	58.34	10.61	31.05	0.06
JHU-029 $\alpha$ -TOS	52.79	11.11	36.10	48.23

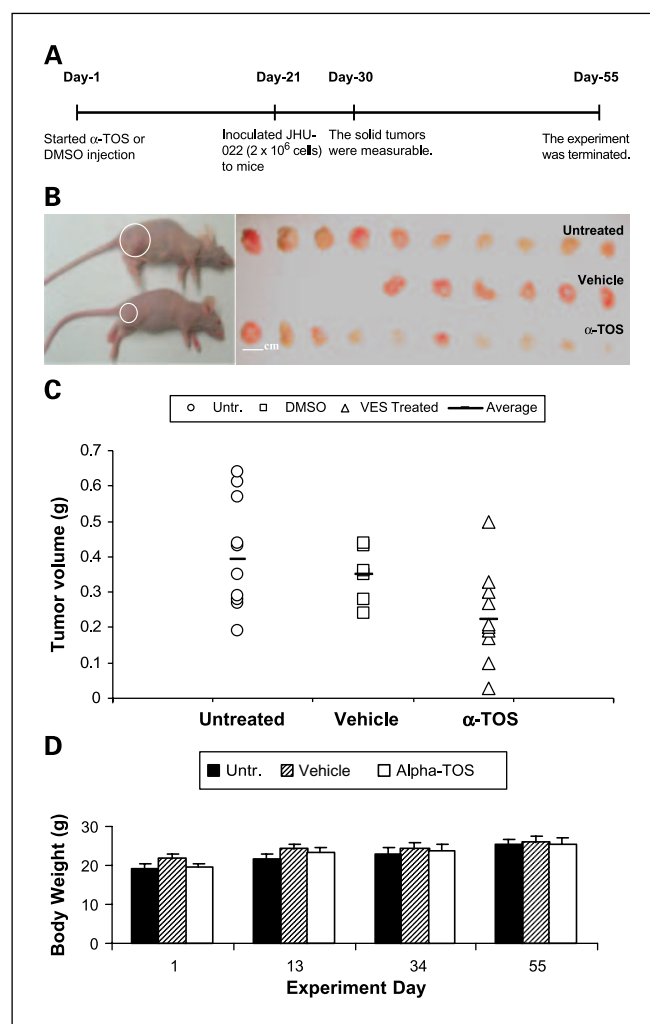


**Fig. 2.** Inhibition of JHU-022 tumor xenograft growth in mice by  $\alpha$ -TOS. **A**, schematic representation of the *in vivo* animal study. There were three groups of mice that included untreated control group,  $\alpha$ -TOS–treated group, and DMSO vehicle control group. The experiment start date is indicated as day 1, when  $\alpha$ -TOS and DMSO (vehicle) treatment was initiated. JHU-022 cells were injected s.c. on day 21, and the mice were sacrificed 34 d later on day 55. **B**, left, picture of mice with tumor. The circled region represents the location of tumor. Right, dissected tumors from the untreated group (top), DMSO group (middle), and  $\alpha$ -TOS group (bottom). **C**, scatter plot of tumor weights from the different groups. The average tumor mass is indicated as a bold bar in each scatter group;  $P < 0.001$ . **D**, the mouse body weight was measured periodically at different days during the 55-d experimental period.

(Fig. 1C). There were no significant differences in the cell cycle distribution patterns of untreated cultures and control cultures treated with SUV alone.

**Antitumor effect of  $\alpha$ -TOS against JHU-022 human and head neck cancer cells *in vivo*.** We further examined the antitumor effects of  $\alpha$ -TOS on JHU-022 cell growth as solid tumor xenografts in immunodeficient mice. The experiment is outlined in Fig. 2A. Tumor growth occurred in all JHU-022 inoculated mice. All mice were euthanized on day 55 and tumors were dissected and weighed. The mice in the  $\alpha$ -TOS–treated group showed suppression of tumor growth as compared with untreated and DMSO control groups (Fig. 2B and C). Average tumor weight was significantly lower in the  $\alpha$ -TOS–treated group (0.24 g) than in the untreated (0.39 g) and DMSO–treated (0.36 g) groups (Fig. 2C). The body weight increased

slightly in all mice during the 55-day experiment, with no significant differences among  $\alpha$ -TOS-treated group and the two control groups (Fig. 2D). In addition, there were no differences in food and water intake among the groups. The blood samples were also collected on the last day of the experiment and the plasma  $\alpha$ -TOS levels were determined by high-performance liquid chromatography. Plasma  $\alpha$ -TOS was only detected in the  $\alpha$ -TOS-treated group and was not detectable in the control and DMSO-treated groups. The plasma  $\alpha$ -TOS level in the  $\alpha$ -TOS-treated group was in an average range of 5  $\mu$ g  $\alpha$ -TOS/100  $\mu$ L plasma ( $P < 0.001$ ).

**Effect of  $\alpha$ -TOS on ceramide metabolism in JHU-022 cancer cells.** The effects of  $\alpha$ -TOS on the ceramide expression and sphingomyelinase activity in JHU-022 cells were studied. The amount of ceramide product gradually increased with time in JHU-022 cell cultures treated with 20  $\mu$ mol/L  $\alpha$ -TOS-SUV for up to 6 hours. The levels of ceramide were maintained nearly at this elevated level in cultures treated with  $\alpha$ -TOS-SUV for 6 and 9 hours (Fig. 3A). There was an  $\sim 2.5$ -fold increase in the ceramide level of cells treated with  $\alpha$ -TOS-SUV for 6 hours compared with control cells treated with vehicle (SUV) alone (Fig. 3A). The level of sphingomyelinase activity was significantly increased in the first hour of treatment of cells with  $\alpha$ -TOS-SUV. There was a 3.3-fold and a 3.7-fold increase

of the sphingomyelinase activity in cells after treatment with  $\alpha$ -TOS-SUV for 30 minutes and 1 hour, respectively. After that, the enzyme activity gradually diminished to  $\sim 2.5$ -fold higher level relative to DMSO-treated cells and remained at this level throughout the treatment period (Fig. 3B). The ceramide level in tumor specimens was examined by immunohistologic methods. Tumors from mice treated with  $\alpha$ -TOS exhibited a significant degree of immune staining of ceramide within the cellular membranous regions, whereas the untreated group or DMSO-vehicle control group displayed little staining with ceramide antibody (Fig. 3C).

**Effects of  $\alpha$ -TOS on caspase-3, caspase-9, and PARP proteins.** Caspase-3 activities were nearly 8-fold higher in JHU-022 cells treated with  $\alpha$ -TOS for 12 hours and JHU-029 treated similarly for 6 hours, compared with control cells treated with the vehicle (DMSO) alone (Fig. 4A). Caspase-3 activities were lower in cultures treated with  $\alpha$ -TOS for longer periods. Coadministration of the selective caspase-3 inhibitor z-DEVD-fmk or nonselective caspase inhibitor z-VAD-fmk significantly reduced  $\alpha$ -TOS induced caspase-3 activities with a range of 70% to 84% inhibition in both JHU-022 (Fig. 4A) and JHU-029 (Fig. 4B) cell lines. In addition, both caspase inhibitors showed an ability to partially protect against  $\alpha$ -TOS-induced cell death in JHU-22 cell cultures (Fig. 4C). The expression

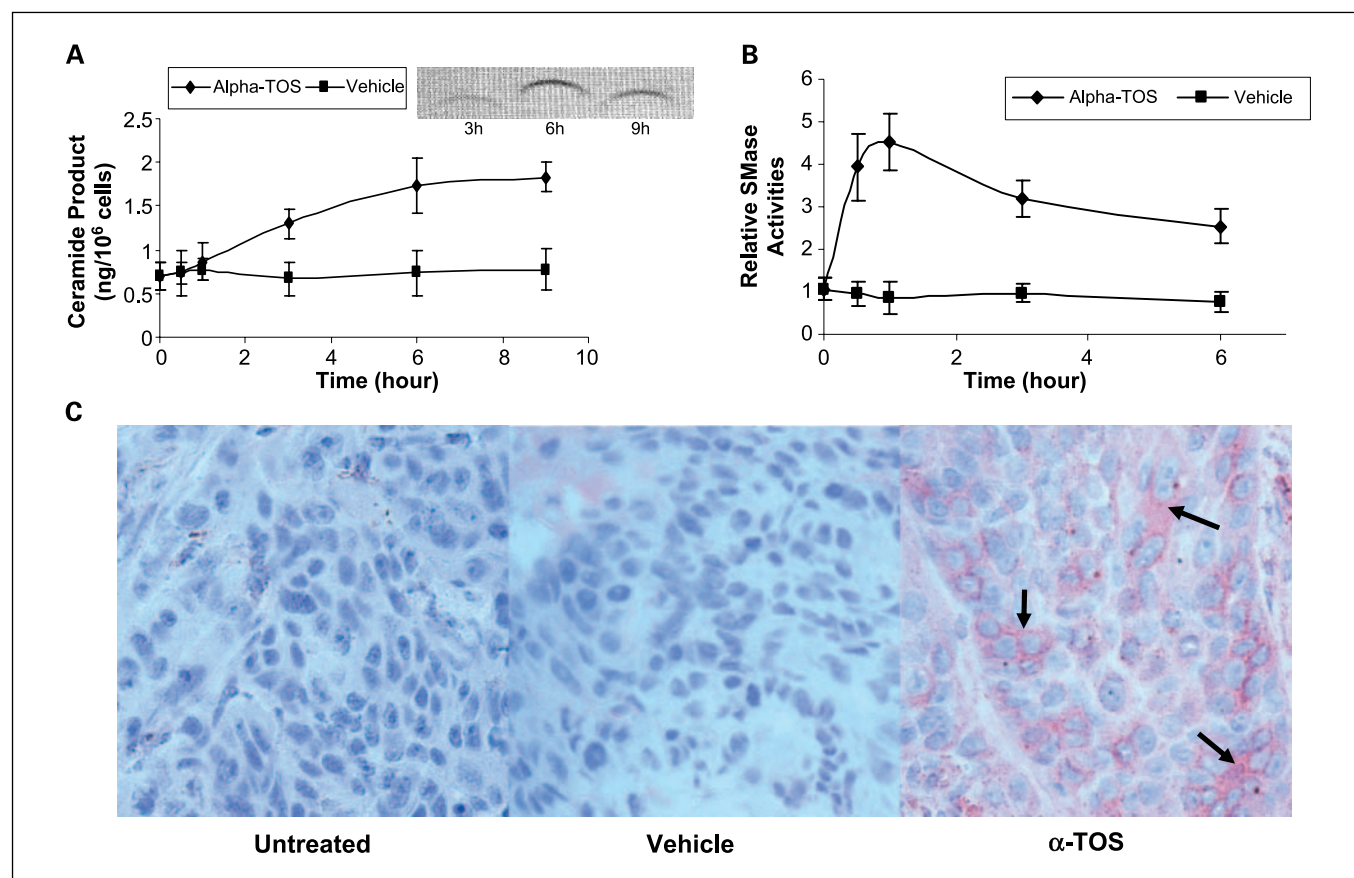


**Fig. 3.** Increased levels of ceramide in JHU-022 cells treated with  $\alpha$ -TOS. **A**, ceramide levels in JHU-022 cells treated with  $\alpha$ -TOS-SUV (20  $\mu$ mol/L) for 0 to 9 h. Top right inset, TLC bands of ceramide from cells treated with  $\alpha$ -TOS-SUV (20  $\mu$ mol/L) for 3, 6, and 9 h. **B**, acid-sphingomyelinase (SMase) activity relative to untreated control in JHU-022 cells treated with  $\alpha$ -TOS-SUV (20  $\mu$ mol/L) or vehicle (SUV) for various exposure times from 0 to 6 h. Points, mean ceramide levels and relative sphingomyelinase activity of two independent experiments with triplicate dishes; bars, SD. **C**, immunohistochemical staining of ceramide in JHU-022 tumor specimens from mice, which were untreated or treated with DMSO (vehicle) or  $\alpha$ -TOS as described in Materials and Methods. At the end of the experiment, JHU-022 tumors were removed, fixed in formalin, and stained with H&E and ceramide monoclonal antibody. Arrows, ceramide specific staining. Magnification,  $\times 400$ .



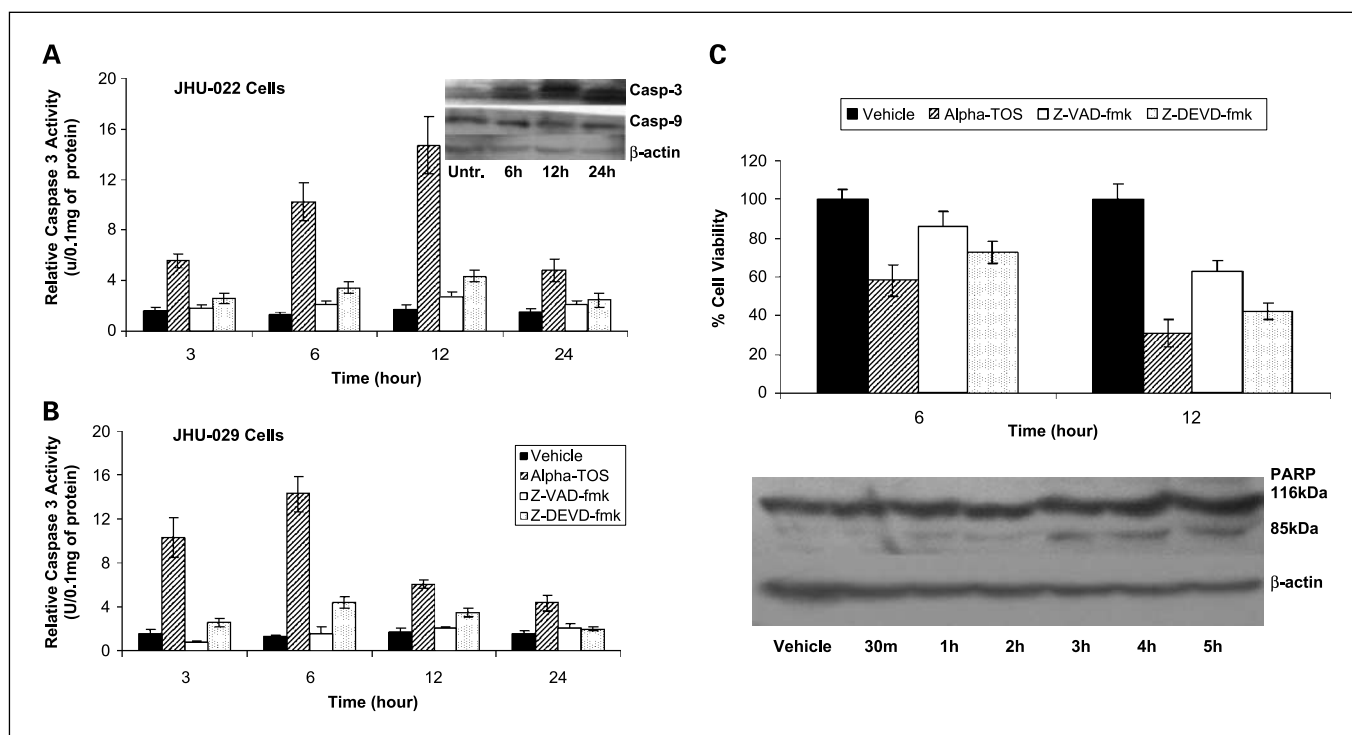


**Fig. 4.** Effect of  $\alpha$ -TOS on activity of caspase-3 and related markers in JHU-022 cells. **A**, caspase-3 activities (apopain levels) were measured in JHU-022 or JHU-029 cells treated with  $\alpha$ -TOS-SUV (20  $\mu$ mol/L) for 0, 3, 6, 12, and 24 h. The caspase-3 inhibitors such as z-DEVD-fmk and z-VAD-fmk were used as enzyme-specific controls. Columns, mean enzyme activity of two independent experiments with triplicate dishes; bars, SD. The protein levels of caspase-3 and caspase-9 in  $\alpha$ -TOS-SUV-treated JHU-022 cells were also analyzed by Western blot (*top right*). The cell lysates were harvested after 6, 12, and 24 h for Western blot, which was probed sequentially for expression of caspase-3, caspase-9, and  $\beta$ -actin. Control cells were treated with vehicle alone. **B**, JHU-022 cells were pretreated with z-VAD-fmk and z-DEVD-fmk for 30 min, followed by treatment with  $\alpha$ -TOS-SUV (20  $\mu$ mol/L) for 6 or 12 h. Cell viability was measured by 3-(4,5-dimethylthiazol-2-yl)-2,5-diphenyltetrazolium bromide assay. **C**, the JHU-022 cells were treated with  $\alpha$ -TOS-SUV (20  $\mu$ mol/L) for 30 min and 1, 2, 3, 4, and 5 h. PARP expression and degradation were analyzed by Western blotting with antibodies directed against PARP protein. The intact form of PARP is 116 kDa and the cleaved form is 85 kDa. The amount of protein was normalized to  $\beta$ -actin content.

levels of caspase-3 protein and related molecules such as caspase-9 and PARP proteins were also analyzed by Western blot (Fig. 4A and C). A qualitative assessment of apoptotic markers in JHU-022 cell cultures treated with  $\alpha$ -TOS for 3 to 24 hours showed an increase in caspase-3, but not caspase-9, protein (Fig. 4A). Treatment of JHU-022 cells with  $\alpha$ -TOS for  $\geq 3$  hours resulted in apoptosis as indicated by PARP cleavage to produce 85-kDa fragments (4 D).

**Effects of  $\alpha$ -TOS on the expression of ceramide-related apoptotic markers.** The role of ceramide-mediated apoptosis was examined in  $\alpha$ -TOS-treated JHU-022 and JHU-029 cells. First, Annexin V-FITC antibody was applied to track the cells through apoptosis when exposed to  $\alpha$ -TOS (Fig. 5A). The cells were labeled with Annexin V-FITC antibody and propidium iodide and analyzed by flow cytometry. The data indicated that 41.30%, 44.39%, and 64.82% of the JHU-022 cells underwent early apoptosis after exposure to  $\alpha$ -TOS-SUV for 6, 12, and 24 hours, respectively. Thirty-eight percent of JHU-022 cells were no longer viable (late apoptosis) after 12-hour exposure to  $\alpha$ -TOS. Higher proportion (24.24%) of late apoptosis was found in JHU-029 cell cultures treated with  $\alpha$ -TOS for 12 hours. An increase in the proportion (16.23 to 34.18%) of early apoptosis was seen in JHU-029 cells when  $\alpha$ -TOS treatment was increased from 6 to 24 hours (Fig. 5A).

We also examined the expression levels of apoptosis associated proteins such as Bcl-2, Bcl-X<sub>L</sub>, p53, murine double minute-2, nuclear factor  $\kappa$ B, and I $\kappa$ B- $\alpha$  by Western blot analysis

(Fig. 5B and C). The expression levels of Bcl-2 and Bcl-X<sub>L</sub> were dramatically decreased in JHU-022 cells treated with  $\alpha$ -TOS for 6 and 12 hours as compared with control groups (Fig. 5B). A slight recovery of expression of Bcl-2 and Bcl-X<sub>L</sub> proteins was seen in cultures treated for 24 hours with  $\alpha$ -TOS (Fig. 5B). The level of p53 increased with prolonged exposure of JHU-022 cells to  $\alpha$ -TOS. In contrast, the level of nuclear factor  $\kappa$ B was lower in JHU-022 cells treated with  $\alpha$ -TOS for 12 hours. There was a very slight change in murine double minute-2 protein level of cells treated with  $\alpha$ -TOS. There was no change in the level of I $\kappa$ B- $\alpha$  in the  $\alpha$ -TOS-treated and control groups (Fig. 5C).

## Discussion

The key findings from the present study are that  $\alpha$ -TOS inhibits the growth and viability of human HNSCC, and that this effect may be a consequence of ceramide-mediated apoptosis. *In vitro* studies showed dose- and time-dependent cytotoxicity of  $\alpha$ -TOS. *In vivo* studies showed that i.p. injection of low-dose  $\alpha$ -TOS on alternating days significantly decreased primary tumor burden. Regarding the safety of  $\alpha$ -TOS, our limited studies in mice suggest that it is relatively nontoxic for up to 55 experimental days. The  $\alpha$ -TOS treatment did not produce any overt signs of toxicity such as weight loss or observable changes in behavior. Clearly, more studies are needed for establishing the safety of  $\alpha$ -TOS for potential use in cancer chemoprevention or treatment.

Our data showed that  $\alpha$ -TOS induced sphingomyelinase activity and enhanced ceramide levels in cultured cells and tumor specimens. The importance of ceramide lies in its ability to modulate the biochemical and cellular processes that lead to apoptosis (30, 31). The accumulation of ceramide in cells could be influenced through one or more routes of ceramide generation and/or clearance. Sphingomyelinase catalyzes the hydrolysis of sphingomyelin to ceramide and phosphocholine. Mechanism for generation of ceramide may also involve the activation of acid sphingomyelinase, which participates in regulating apoptotic responses. Neutral sphingomyelinase is also implicated in the regulation of apoptosis in response to a range of stimuli, including tumor necrosis factor  $\alpha$  in breast cancer cells, ethanol in HepG2 hepatoma cells, and the Alzheimer proapoptotic amyloid- $\beta$  peptide in neuronal cells

(24, 32, 33). Our analysis of sphingomyelinase activity included neutral and acidic contributions toward ceramide formation.

The results also show that ceramide-mediated apoptotic signaling seems to affect activation of caspase and Bcl-2 family proteins. One effect of  $\alpha$ -TOS is the activation of caspase-3 activity and expression. Caspase-3 is a member of the caspase family of aspartate-specific cysteine proteases that play a central role in the execution of the apoptotic program, and is primarily responsible for the cleavage of PARP during cell death. The sequence at which caspase-3 cleaves PARP is very well conserved in the PARP protein, indicating the potential importance of PARP cleavage in apoptosis (34–36). In  $\alpha$ -TOS-treated JHU-022 cells, caspase-3-like activity, measured with a specific apopain enzymatic assay *in vitro*, peaks at 12 hours after exposure to  $\alpha$ -TOS, concomitant with the onset

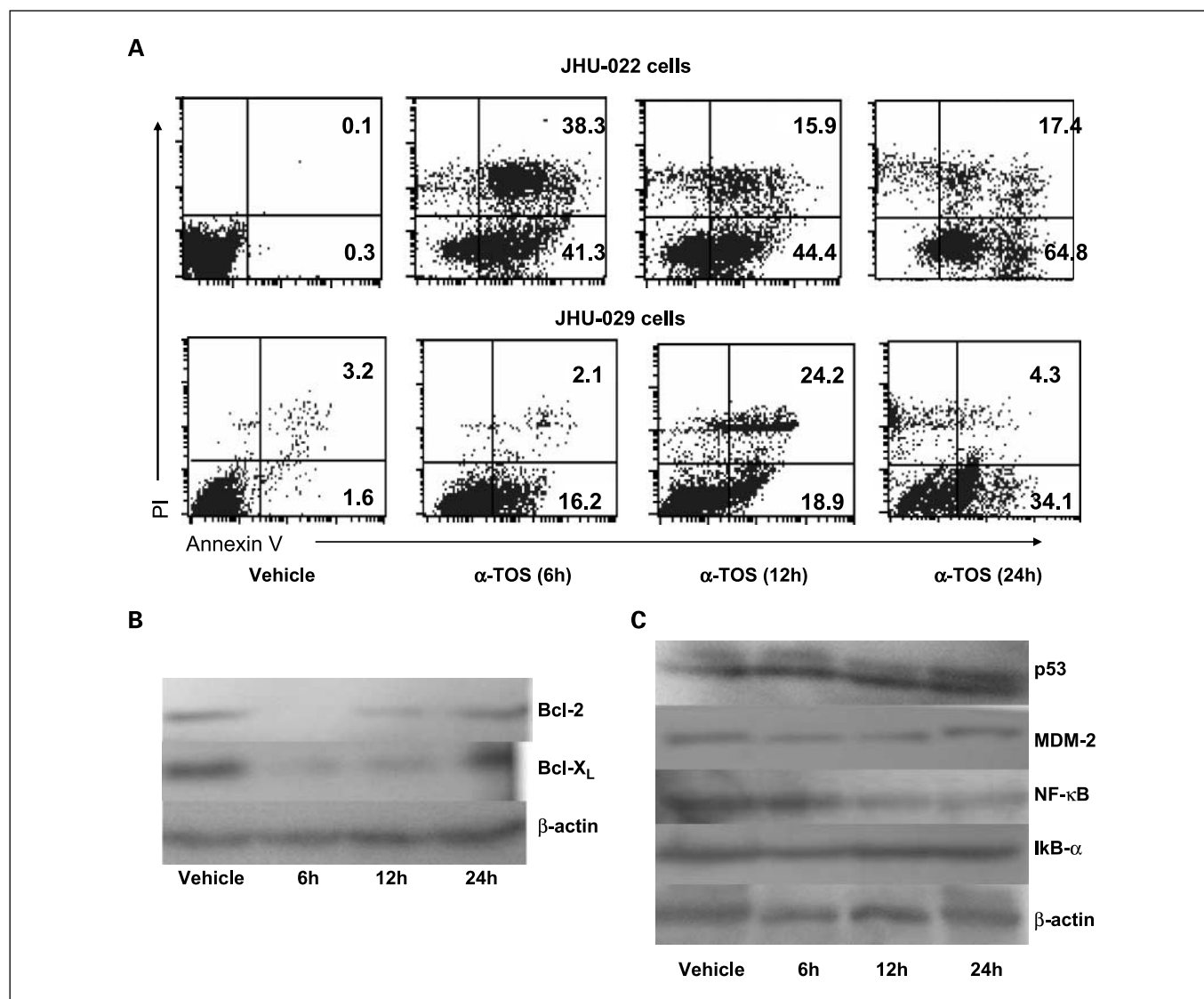


**Fig. 5.** Effect of  $\alpha$ -TOS on the induction of apoptosis in JHU-022 cells. **A**, JHU-022 and JHU-029 cells were cultured either with  $\alpha$ -TOS-SUV (20  $\mu$ mol/L) or vehicle for 0, 3, 6, 12, and 24 h, followed by measurement of Annexin V protein in the cell membrane by flow cytometry using FITC-conjugated Annexin V antibody. The cells were also stained with propidium iodide. Vehicle-treated cells served as controls. The pixels in the bottom right quadrant of each panel display V-FITC-positive and propidium iodide (PI) – negative cells, indicating that the cells were in an early stage of apoptosis. Pixels in the top right quadrant represent cells stained with both propidium iodide and Annexin V, indicating that the cells were in late apoptosis or no longer viable. **B**, JHU-022 cells were treated with  $\alpha$ -TOS-SUV (20  $\mu$ mol/L) for 0, 3, 6, 12, and 24 h, and the expression levels of apoptotic markers such as Bcl-2, Bcl-X<sub>L</sub>, p53, murine double minute-2 (MDM-2), nuclear factor  $\kappa$ B (NF- $\kappa$ B; p65), and I $\kappa$ B- $\alpha$  were evaluated by Western blot with appropriate antibody probes. The amount of protein was normalized to  $\beta$ -actin.

of apoptosis. The expression level of caspase-3 was significantly increased after exposure to  $\alpha$ -TOS, whereas the amount of caspase-9 remained constant. In addition, pretreatment with caspase-3 inhibitor or nonselective caspase inhibitor blocks  $\alpha$ -TOS-mediated cell death, suggesting that caspase-3 activity is involved in ceramide-mediated apoptosis in HNSCC cells. We have also examined the time course of PARP protein cleavage during apoptosis in these cells by Western blot analysis. PARP cleavage occurred at an early stage of induced apoptosis in JHU-022 cells. Further work will be required to discern whether  $\alpha$ -TOS-induced ceramide-mediated apoptosis is truly caspase-9 independent or involves other regulation such as phosphorylation of caspase-9 protein. We should note that the immunoblotting experiments reflect a limited assessment of relative differences of apoptotic markers within and between samples, and more detailed quantitation of the apoptotic profiles under  $\alpha$ -TOS treatment is warranted. Furthermore, the variability observed when using specific and nonspecific caspase inhibitors may be a consequence of using a single concentration of inhibitor, culture conditions, or the degree of sensitivity of the cell lines. Caspase-9 has been linked to ceramide-induced neuronal death (37). The regulation of alternative processing of pre-mRNA of both caspase-9 and Bcl-X<sub>L</sub> was reported in response to the proapoptotic action of ceramide (38). A collective interpretation of our data suggests that the rapid response of sphingomyelinase activity and ceramide accumulation in cells exposed to  $\alpha$ -TOS (Fig. 3A and B) precede the maximal caspase expression profiles and earliest detection of PARP cleavage (Fig. 4A and C). This is consistent with the hypothesis that caspase-mediated apoptosis is a consequence of ceramide accumulation within HNSCC treated with  $\alpha$ -TOS.

This study also provides evidence that inhibition of Bcl-X<sub>L</sub>/Bcl-2 function represents a major pathway whereby  $\alpha$ -TOS induces ceramide-mediated apoptosis in head and neck cancer cells. The data indicate that  $\alpha$ -TOS can markedly decrease the levels of Bcl-X<sub>L</sub> and Bcl-2 in the first 12 hours of treatment. The tendency of Bcl-2 and Bcl-X<sub>L</sub> to recover during later time points could reflect metabolic degradation of  $\alpha$ -TOS on prolonged incubation with cells. Bcl-2 and Bcl-X<sub>L</sub> are antiapoptotic paralogues that inhibit apoptosis elicited by a wide variety of stimuli, and play critical roles in cancer development and resistance to treatment. Many clinical studies have indicated that expression of these antiapoptotic proteins in tumors is associated with poor prognosis (39). In addition, the nuclear factor- $\kappa$ B expression level seemed to decrease after the exposure of cells to  $\alpha$ -TOS. Nuclear factor  $\kappa$ B is an important molecular target that has a role in carcinogenesis and cancer progression (40).

In summary, our data show that the vitamin E analogue  $\alpha$ -TOS decreases primary tumor burden in a human tumor xenograft model. The findings presented here strongly suggest that antitumor activity of  $\alpha$ -TOS is initiated through a ceramide-mediated apoptotic pathway without any overt toxic effects *in vivo*.

## Acknowledgments

We thank Dan Zhang for her excellent technical assistance in the animal experiments, Dr. Liang Shan for pathologic analysis, Dr. Yanfei Zhou for statistical analysis, and Hongli Zhu for high-performance liquid chromatography analysis of  $\alpha$ -TOS in plasma.

## References

- Jemal A, Siegel R, Ward E, et al. Cancer statistics, 2006. *CA Cancer J Clin* 2006;56:106–30.
- Kelloff G, Lippman SM, Dannenberg AJ, et al. Progress in chemoprevention drug development: the promise of molecular biomarkers for prevention of intraepithelial neoplasia and cancer—a plan to move forward. *Clin Cancer Res* 2006;12:3661–97.
- Hampton T. Vitamin E derivative packs anticancer punch. *JAMA* 2006;296:32.
- Weber T, Lu M, Andera L, et al. Vitamin E succinate is a potent novel antineoplastic agent with high selectivity and cooperativity with tumor necrosis factor-related apoptosis-inducing ligand (Apo2 ligand) *in vivo*. *Clin Cancer Res* 2002;8:863–9.
- Wang XF, Dong L, Zhao Y, Tomasetti M, Wu K, Neuzil J. Vitamin E analogues as anticancer agents: lessons from studies with  $\alpha$ -tocopheryl succinate. *Mol Nutr Food Res* 2006;50:675–85.
- Basu A, Imrhan V. Vitamin E and prostate cancer: is vitamin E succinate a superior chemopreventive agent? *Nutr Rev* 2005;63:247–51.
- Prasad KN, Kumar B, Yan XD, Hanson AJ, Cole WC.  $\alpha$ -tocopheryl succinate, the most effective form of vitamin E for adjuvant cancer treatment. *J Am Coll Nutr* 2003;22:108–17.
- Kline K, Yu W, Sanders BG. Vitamin E and breast cancer. *J Nutr* 2004;134:3458–62S.
- Wang XF, Birringer M, Dong LF, et al. A peptide conjugate of vitamin E succinate targets breast cancer cells with high ErbB2 expression. *Cancer Res* 2007;67:3337–44.
- Ramanathapuram LV, Hahn T, Dial SM, Akporiaye ET. Chemo-immunotherapy of breast cancer using vesiculated  $\alpha$ -tocopheryl succinate in combination with dendritic cell vaccination. *Nutr Cancer* 2005;53:177–93.
- Gu X, Schwartz J, Pang X, Zhou Y, Sirois D, Sridhar R. Cytotoxicity of liposomal  $\alpha$ -tocopheryl succinate towards hamster cheek pouch carcinoma (HCPC-1) cells in culture. *Cancer Lett* 2006;239:281–91.
- Schwartz JL, Gu X, Kittles RA, Shklar G. Experimental oral carcinoma of the tongue and buccal mucosa: possible biologic markers linked to cancer at two anatomic sites. *Eur J Oral Oncol* 2000;36:225–35.
- Shiau CW, Huang JW, Wang DS, et al.  $\alpha$ -tocopheryl succinate induces apoptosis in prostate cancer cells in part through inhibition of Bcl-X<sub>L</sub>/Bcl-2 function. *J Biol Chem* 2006;281:11819–25.
- Ni J, Chen M, Zhang Y, Li R, Huang J, Yeh S. Vitamin E succinate inhibits human prostate cancer cell growth via modulating cell cycle regulatory machinery. *Biochem Biophys Res Commun* 2003;300:357–63.
- Stapelberg M, Gellert N, Swettenham E, et al.  $\alpha$ -tocopheryl succinate inhibits malignant mesothelioma by disrupting the fibroblast growth factor autocrine loop: mechanism and the role of oxidative stress. *J Biol Chem* 2005;280:25369–76.
- Lee E, Choi MK, Lee YJ, et al.  $\alpha$ -tocopheryl succinate, in contrast to  $\alpha$ -tocopherol and  $\alpha$ -tocopheryl acetate, inhibits prostaglandin E2 production in human lung epithelial cells. *Carcinogenesis* 2006;27:2308–15.
- Zhang Y, Ni J, Messing EM, Chang E, Yang CR, Yeh S. Vitamin E succinate inhibits the function of androgen receptor and the expression of prostate-specific antigen in prostate cancer cells. *Proc Natl Acad Sci U S A* 2002;99:7048–13.
- Neuzil J, Weber T, Gellert N, Weber C. Selective cancer cell killing by  $\alpha$ -tocopheryl succinate. *Br J Cancer* 2001;84:87–9.
- Barroso MP, Gomez-Diaz C, Lopez-Lluch G, Malagon MM, Crane FL, Navas P. Ascorbate and  $\alpha$ -tocopherol prevent apoptosis induced by serum removal independent of Bcl-2. *Arch Biochem Biophys* 1997;343:243–8.
- Neuzil J.  $\alpha$ -tocopheryl succinate epitomizes a compound with a shift in biological activity due to pro-vitamin-to-vitamin conversion. *Biochem Biophys Res Commun* 2002;293:1309–13.
- Gutierrez G, Mendoza C, Montano LF, Lopez-Marure R. Ceramide induces early and late apoptosis in human papilloma virus+ cervical cancer cells by inhibiting reactive oxygen species decay, diminishing the intracellular concentration of glutathione and increasing nuclear factor- $\kappa$ B translocation. *Anticancer Drugs* 2007;18:149–59.
- Ogretmen B, Hannun YA. Biologically active sphingolipids in cancer pathogenesis and treatment. *Nat Rev Cancer* 2004;4:604–16.
- Pettus BJ, Chalfant CE, Hannun YA. Ceramide in apoptosis: an overview and current perspectives. *Biochim Biophys Acta* 2002;1585:114–25.
- Eto M, Bennouna J, Hunter OC, Lotze MT, Amoscato AA. Importance of C16 ceramide accumulation during apoptosis in prostate cancer cells. *Int J Urol* 2006;13:148–56.
- Santana P, Pena LA, Haimovitz-Friedman A, et al. Acid sphingomyelinase-deficient human lymphoblasts and mice are defective in radiation-induced apoptosis. *Cell* 1996;86:189–99.
- Luberto C, Hassler DF, Signorelli P, et al. Inhibition of tumor-necrosis factor-induced cell death in MCF7 by a novel inhibitor of neutral sphingomyelinase. *J Biol Chem* 2002;277:41128–39.
- Weber T, Dalen H, Andera L, et al. Mitochondria play

- a central role in apoptosis induced by  $\alpha$ -tocopheryl succinate, an agent with antineoplastic activity: comparison with receptor-mediated pro-apoptotic signaling. *Biochemistry* 2003;42:4277–91.
28. Jiang Q, Wong J, Fyrst H, Saba JD, Ames BN.  $\gamma$ -Tocopherol or combinations of vitamin E forms induce cell death in human prostate cancer cells by interrupting sphingolipid synthesis. *Proc Natl Acad Sci U S A* 2004;101:17825–30.
  29. Cifone MG, Roncaioli P, De Maria R, et al. Multiple pathways originate at the Fas/APO-1 (CD95) receptor: sequential involvement of phosphatidylcholine-specific phospholipase C and acidic sphingomyelinase in the propagation of the apoptotic signal. *EMBO J* 1995;14:5859–68.
  30. Lin CF, Chen CL, Lin YS. Ceramide in apoptotic signaling and anticancer therapy. *Curr Med Chem* 2006;13:1609–16.
  31. Hail N, Jr., Carter BZ, Konopleva M, Andreeff M. Apoptosis effector mechanisms: a requiem performed in different keys. *Apoptosis* 2006;11:889–904.
  32. Lee JT, Xu J, Lee JM, et al. Amyloid- $\beta$ -peptide induces oligodendrocyte death by activating the neutral sphingomyelinase-ceramide pathway. *J Cell Biol* 2004;164:123–31.
  33. Liu JJ, Wang JY, Hertervig E, et al. Activation of neutral sphingomyelinase participates in ethanol-induced apoptosis in HepG2 cells. *Alcohol* 2000;35:569–73.
  34. Ratnam K, Low J. Current development of clinical inhibitors of poly(ADP-Ribose) polymerase in oncology. *Clin Cancer Res* 2007;13:1384–8.
  35. Deep G, Oberlies NH, Kroll DJ, Agarwal R. Isosilybin B and isosilybin A inhibit growth, induce G<sub>1</sub> arrest and cause apoptosis in human prostate cancer LNCaP and 22Rv1 cells. *Carcinogenesis* 2007;28:1533–42.
  36. Israel K, Yu W, Sanders BG, Kline K. Vitamin E succinate induces apoptosis in human prostate cancer cells: role for Fas in vitamin E succinate-triggered apoptosis. *Nutr Cancer* 2000;36:90–100.
  37. Movsesyan VA, Yakovlev AG, Dabaghyan EA, Stoica BA, Faden AI. Ceramide induces neuronal apoptosis through the caspase-9/caspase-3 pathway. *Biochem Biophys Res Commun* 2002;299:201–7.
  38. Chalfant CE, Rathmen K, Pinkerman RL, et al. *De novo* ceramide regulates the alternative splicing of caspase 9 and Bcl-x in A549 lung adenocarcinoma cells. Dependence on protein phosphatase-1. *J Biol Chem* 2002;277:12587–95.
  39. Thomadaki H, Scorilas A. BCL2 family of apoptosis-related genes: functions and clinical implications in cancer. *Crit Rev Clin Lab Sci* 2006;43:1–67.
  40. Aggarwal BB. Nuclear factor- $\kappa$ B: the enemy within. *Cancer Cell* 2004;6:203–8.

## Original Research

# Detection of Cerebral Metabolites by Single-Voxel-Based PRESS and COSY Techniques at 3T

S. Sendhil Velan, PhD,<sup>1\*</sup> Susan K. Lemieux, PhD,<sup>1</sup> Raymond R. Raylman, PhD,<sup>1</sup> Warren Boling, MD,<sup>2</sup> Gerald R. Hobbs, PhD,<sup>3</sup> Richard G. Spencer, MD, PhD,<sup>4</sup> Rajagopalan Sridhar, PhD,<sup>5–8</sup> Periannan Kuppusamy, PhD,<sup>9,10</sup> and M. Albert Thomas, PhD<sup>11</sup>

**Purpose:** To compare point-resolved spectroscopy (PRESS) and localized two-dimensional (2D) correlated spectroscopy (L-COSY) in the detection of cerebral metabolites in humans on a clinical scanner at 3T and to estimate their respective inter- and intrasubject variances.

**Materials and Methods:** Measurements were made on nine healthy subjects to assess intersubject variance, and daily on a single subject over a period of seven days to assess intrasubject variance. All L-COSY measurements were performed with a voxel size of 27 mL ( $3 \times 3 \times 3$  cm<sup>3</sup>) and a measurement time of ~34 minutes in the occipitoparietal lobe of the brain. Relative metabolite concentrations were estimated with respect to N-methyl creatine.

**Results:** While the sensitivity of PRESS is twice that of L-COSY, the greater spectral resolution offered by L-COSY resulted in greater consistency in estimates of the concentrations of several cerebral metabolites, as indicated by a superior intraclass correlation and a significantly lower standard deviation (SD) in a matched pair intrasubject analysis.

**Conclusion:** Our pilot results demonstrate that L-COSY is an effective approach for resolving cerebral metabolites, and demonstrates a lower coefficient of variance (CV) than the conventional 1D localized spectroscopic approach using LC Model for quantification.

**Key Words:** brain; 2D MRS; 1D MRS; intraclass correlations; 3 Tesla

**J. Magn. Reson. Imaging 2007;26:405–409.**

© 2007 Wiley-Liss, Inc.

<sup>1</sup>Center for Advanced Imaging and Radiology, West Virginia University, Morgantown, West Virginia, USA.

<sup>2</sup>Department of Neurosurgery, West Virginia University, Morgantown, West Virginia, USA.

<sup>3</sup>Department of Statistics, West Virginia University, Morgantown, West Virginia, USA.

<sup>4</sup>NMR Unit, National Institute on Aging, National Institutes of Health, Baltimore, Maryland, USA.

<sup>5</sup>Department of Radiation Oncology, Howard University, Washington, DC, USA.

<sup>6</sup>Department of Genetics, Howard University, Washington, DC, USA.

<sup>7</sup>Department of Human Genetics, Howard University, Washington, DC, USA.

<sup>8</sup>Cancer Center, Howard University, Washington, DC, USA.

<sup>9</sup>Department of Internal Medicine, Ohio State University Medical Center, Ohio, USA.

<sup>10</sup>Department of Biomedical Engineering, Ohio State University Medical Center, Ohio, USA.

<sup>11</sup>Department of Radiology, University of California, Los Angeles, California, USA.

Contract grant sponsor: National Center for Research Resources, National Institutes of Health (NIH); Contract grant number: 2G12 RR003048-16A1; Contract grant sponsor: Department of Defense; Contract grant numbers: DAMD 17 03-1-0759; DAMD 17 03-1-0123; Contract grant sponsor: NIH; Contract grant number: 1R01MH065695; Contract grant sponsors: National Institute on Aging, NIH; Internal Health Sciences Center, West Virginia University.

\*Address correspondence to: S.S.V., Center for Advanced Imaging and Radiology, West Virginia University, Morgantown, WV 26506. E-mail: svelan@hsc.wvu.edu

Received June 13, 2006; Accepted January 24, 2007.

DOI 10.1002/jmri.20968

Published online in Wiley InterScience (www.interscience.wiley.com).

LOCALIZED 1D magnetic resonance spectroscopy (MRS) permits the detection and quantification of metabolites within a selected volume in vivo (1,2). At typical clinical field strengths of 1.5T and 3T, cerebral metabolite resonances exhibit substantial overlap, so that sophisticated fitting procedures (3,4) are required to extract quantitative information.

In an effort to overcome this problem, localized 2D correlated spectroscopic (2D L-COSY) sequences have recently been implemented on clinical MRI scanners (5–10). Metabolites that do not exhibit *J*-coupling appear only in the diagonal, with their chemical shifts represented equivalently on the two axes. In contrast, spins that interact through *J*-coupling exhibit off-diagonal cross peaks in addition to their representations on the diagonal of the 2D spectrum. One of the main advantages of 2D L-COSY over localized 1D MRS is that connectivity between distinct individual spins is delineated, and *J*-coupled multiplets are spread over two spectral dimensions. This leads, in effect, to a substantial improvement in spectral resolution and hence a more definitive identification of the resonance frequencies corresponding to individual metabolites. In addition, the baseline distortions characteristic of crowded 1D spectra are greatly reduced in 2D spectroscopy.



The 1D analog of 2D L-COSY exhibits a factor of 2 sensitivity loss as compared to direct 1D methods, such as point-resolved spectroscopy (PRESS). The superior sensitivity of 1D methods can be traded off to improve resolution, so the question remains as to whether 1D or 2D methods ultimately yield greater accuracy. Accordingly, the objective of this work was to record both 1D PRESS and 2D L-COSY MR spectra from healthy human brains *in vivo* and to assess and compare the reproducibility of the measurements.

## MATERIALS AND METHODS

### Brain Phantom

A brain phantom was created by mixing 17 brain-relevant metabolites at physiological concentrations in a spherical glass container. The concentration of each chemical was matched to reported values (11) for the human brain:  $\gamma$ -aminobutyric acid (GABA) 1 mM, L-aspartate (Asp) 1 mM, choline (Ch) 0.9 mM, creatine (Cr) 5.4 mM, ethanolamine (Et) 3.3 mM, glucose (Glc) 1 mM, glutamate (Glu) 8.1 mM, glutamine (Gln) 1.6 mM, glutathione (GSH) 2 mM, glycerophosphorylcholine (GPC) 1 mM, myo-inositol (ml) 3.5 mM, lactate (Lac) 0.4 mM, phosphocreatine (PCr) 1.6 mM, phosphorylcholine (PCh) 0.6 mM, taurine (Tau) 0.9 mM, N-acetyl aspartate (NAA) 7.6 mM, and threonine (Thr) 0.3 mM. The metabolites were prepared in a buffer containing 1 mM 2,2-Dimethyl-2-silapentane-5-sulfonate sodium salt (DSS), 72 mM  $K_2HPO_4$ , 28 mM  $KH_2PO_4$ , 200 mM Na formate, and 1 g/L  $NaN_3$ . The pH of the mixture was adjusted to be 7.2. The L-COSY spectrum from this phantom was used to assign cross peaks and diagonal peaks to specific metabolites *in vivo*.

### Subjects

*In vivo* experimental data were acquired from the brain of nine healthy subjects (age range: 21–30 years) who gave informed consent to this study, which was conducted according to procedures approved by the local institutional review board. The subjects were positioned supine inside the magnet with the coil adjacent to the occipital lobe. An axial slice showing the medial part of the parietooccipital lobe was chosen as the reference image in which the MRS voxel was localized. A final  $3 \times 3 \times 3$  cm<sup>3</sup> voxel within the gray matter of the occipitoparietal lobe was established using anatomic landmarks.

### Pulse Sequences

All experiments were performed using a 3T MRI/MRS scanner (GE Healthcare Technologies, Waukesha, WI, USA) running on the VH3 platform equipped with self-shielded gradients (40 mT/m). An extended quadrature visual coil tuned at 127.7 MHz was used for both excitation and signal reception. Gradient-echo images were acquired in the axial, coronal, and sagittal planes with 5-mm-thick slices and in-plane spatial resolution =  $976 \mu\text{m} \times 976 \mu\text{m}$ , repetition time (TR) = 14.7 msec, number of excitations (NEX) = 1, and echo time (TE) = 2.25 msec. These images were used to localize the vol-

ume of interest (VOI) for both *in vitro* and *in vivo* experiments. All spectroscopic measurements were performed using a  $3 \times 3 \times 3$  cm<sup>3</sup> (27 mL) volume. High-order shimming was performed to reduce magnetic field inhomogeneity.

After chemical shift-selective (CHESS) water suppression and outer volume saturation, localized 1D MR spectral data were recorded using a PRESS (1) sequence consisting of three slice-selective RF pulses ( $90^\circ - 180^\circ - 180^\circ$ ) designed according to the Shinnar-LeRoux algorithm (12), defining a volume of interest (VOI). The duration and bandwidth of the  $90^\circ$  pulse were 3.6 msec and 2367 Hz, and corresponding values for the  $180^\circ$  pulse were 5.2 msec and 1.4 kHz, respectively. The second half of the second spin echo was acquired from protons within the VOI. Data from all subjects were acquired using a TE of 30 msec and a TR of 2 seconds, with 64 averages. Additional data obtained from a single subject (seven measurements) for intrasubject variability analysis were acquired with 1024 averages. All experiments were performed with 2048 complex points for acquisition and a spectral width of 5 kHz. Unsuppressed water spectra from the VOI were acquired with 16 averages for all experiments. The spectra were fitted in the frequency domain and quantified using LC Model software (version 6.1-4) and LCMgui (version 2.1-4) (3).

A localized 2D L-COSY sequence (8) employing a  $180^\circ$  spin echo and a  $90^\circ$  coherence transfer echo was used to acquire 2D MRS data following the PRESS MRS experiments. The same VOI was used for both pulse sequences. Water suppression and outer volume saturation were identical to those employed for the PRESS sequence. The L-COSY sequence was designed using RF pulses similar to those employed for PRESS. The VOI was localized in one shot by a combination of three slice-selective RF pulses ( $90^\circ - 180^\circ - 90^\circ$ ) in combination with appropriate  $B_0$  crusher gradient pulses. The last  $90^\circ$  RF pulse performed both slice selection and coherence transfer. An incremental period for the second dimension was inserted immediately after the formation of the spin echo.  $B_0$  crusher gradients were employed around the  $180^\circ$  and final  $90^\circ$  pulses. The minimum TE for the two echoes was 30 msec with an incremental period of 0.8 msec, resulting in a spectral bandwidth of 1250 Hz. A total of 64  $t_1$  increments were performed for all 2D experiments, with 16 averages taken for each experiment, for a total acquisition time of 34 minutes. The second-half of the coherence transfer echo was sampled using 2048 complex points in the acquisition ( $t_2$ ) dimension, with a bandwidth of 5000 Hz. The bandwidth along the indirectly detected ( $t_1$ ) dimension was 1250 Hz. Processing of all 2D data sets was performed using FELIX software (Accelrys Inc., San Diego, CA, USA).

### Spectral Processing

PRESS data were processed using the LC Model software (3), in which metabolite concentrations are determined using an optimal linear combination of individual *in vitro* metabolite basis spectra that comprise a



basis set. A basis set consisting of Ala, Asp, Cr, GABA, Glc, Gln, Glu, GPC, PCh, Lac, ml, NAA, Tau, GSH, Thr, Et, scyllo inositol, lipids, and macromolecules was used for the analysis. Relative metabolite concentrations were obtained by normalizing to the Cr resonance amplitude.

Localized 2D L-COSY data were processed using FELIX software. The residual water signal was removed by a convolution-based approach. Prior to Fourier transformation, the time domain data matrix was multiplied with a phase-shifted sine squared filter in both  $t_1$  and  $t_2$  dimensions. The length of the window functions was adjusted for the sine bell filters to reach zero at the last experimental data point in both dimensions. The diagonal and cross peaks of the metabolites were assigned and quantified by volume integrals as described previously (13). Normalized peak ratios were computed by dividing each 2D peak volume by that of creatine resonance located at  $F_2 = F_1 = 3.03$  ppm. The full width at half maximum (FWHM) of the water signal ranged between 8–10 Hz.

### Statistical Analysis

Analysis of variance (ANOVA, mixed model) was used to partition the variability of measurements of each of the individual metabolites into the portions due to interday variability, intraday variability, and residuals. The mixed-model analysis used the restricted maximum likelihood (REML) and the Kenward-Rogers adjustment. Comparison of L-COSY and PRESS variability in metabolite measurements was done using a matched pair  $t$ -test. Intraclass correlations, ICC (14,15), which incorporate within-subject variance arising from measurement error, biological variation over time, and differences between subjects, were estimated by:  $ICC = \text{variance between subjects} / (\text{variance between subjects} + \text{variance within subjects across different days})$ . The particular methodology we used to partition the variability into its component parts forces negative estimates of variance compounds to zero, and thus adjustments in other factors are also made. All analysis was done with JMP software (SAS Institute, Cary, NC, USA).

### RESULTS

Figure 1 shows a PRESS spectrum recorded from the occipitoparietal gray matter region of a 25-year-old subject. The top trace shows the LC Model-fitted spectrum superimposed on the original data, and the second to fourth traces show the contribution of GABA, GSH, and Et to the fitted spectrum. The region around 1.00 ppm is dominated by lipids and macromolecules overlapping with metabolites such as Ala and Lac. The ICC estimated from the PRESS spectra of nine subjects and seven repeated measurements of one subject ranged between 90% to 100% for Glu, Gln, Glutamate+Glutamine (Glx), and ml; between 80% to 90% for NAA, Asp, and Glc; between 60% to 80% for PCh+GPC and GABA, and less than 60% for PCh, GPC, GSH, Tau, Thr, and Et/Phospho Ethanolamine (PEt). Lactate was not detected.

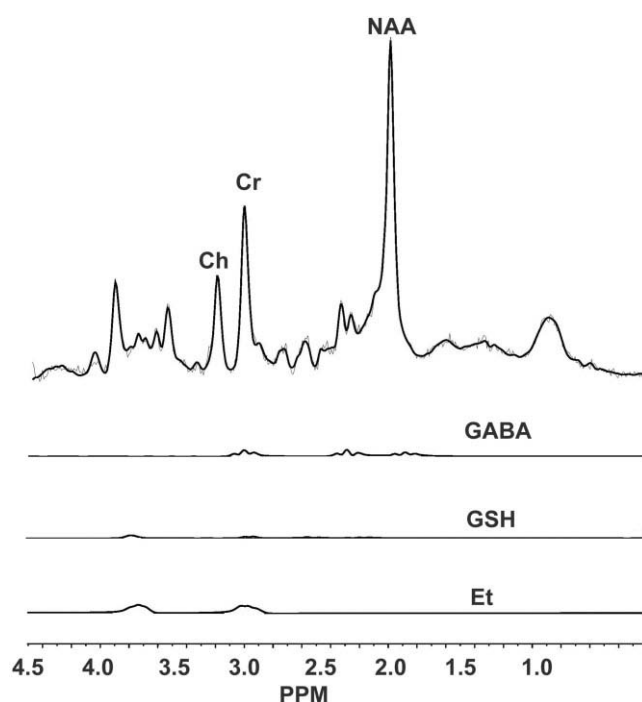


**Figure 1.** A PRESS spectrum recorded from the occipitoparietal lobe of a 25-year-old healthy subject with TR = 2 seconds, TE = 30 msec, NEX = 1024, and voxel size =  $3 \times 3 \times 3$  cm<sup>3</sup> (27 mL). In the top trace the dark line shows the LC Model fitted curve and the gray line shows the actual spectrum. The lower traces show the individual contributions of GABA, GSH, and Et to the fitted spectrum.

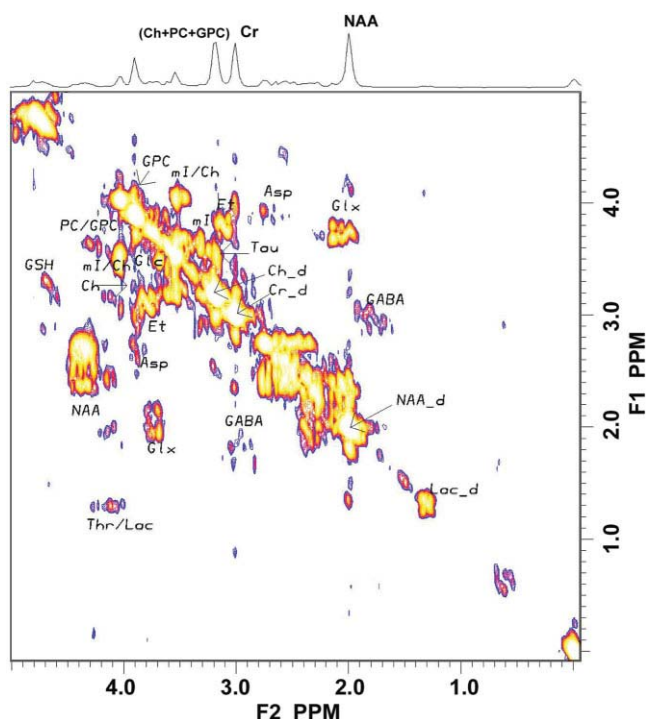
Figure 2 shows an L-COSY spectrum obtained from the brain phantom. Assignments obtained from this spectrum were used to identify metabolites in the in vivo spectra.

Figure 3 shows an L-COSY spectrum recorded from the same subject and the same VOI as employed for the PRESS experiment shown in Fig. 1. In addition to the other metabolites detected by PRESS, L-COSY permits detection of lactate, as shown. The ICC estimated from measurements of nine subjects and seven repeated measurements of one subject ranged between 90% to 100% for NAA, Glx, GSH, Asp, Lac+Thr, and Tau; between 80% to 90% for GABA and Glc; 60% to 80% for Ch+PCh+GPC, PCh+GPC, ml, ml+Ch, and Et+PEt, and was less than 60% for GPC.

Table 1 shows the results of the matched pair  $t$ -test analysis characterizing the relative variability of 1D and 2D metabolite ratios. Standard deviations (SDs) were significantly lower for L-COSY than for PRESS results for several metabolites.

### DISCUSSION

In this study we compared variations in relative metabolite levels using localized PRESS and L-COSY MRS techniques in vivo. The coefficient of variation (CV) and ICC were estimated for both approaches. ICC is the fraction of the total variance that can be attributed to true biological variation rather than measurement error. It is estimated from the variances of the measure-



**Figure 2.** A 2D L-COSY spectrum recorded from the brain phantom containing 17 metabolites with TR = 2 seconds, minimum TE = 30 msec, NEX = 16 for each  $t_1$ , 64  $t_1$  increments, and voxel size =  $3 \times 3 \times 3 \text{ cm}^3$  (27 mL).

ments made on separate subjects and repeatedly on a single subject. If the measurement error is small compared to the subject variance, the ICC will approach unity (15).

A localized PRESS spectrum exhibits twice the signal-to-noise ratio (SNR) of an equivalent 2D spectrum obtained by L-COSY from the same size voxel. However, in spite of the fact that the 2D approach requires a longer scan time (34 minutes) due to the indirectly detected spectral dimension, the improved spectral dispersion minimizes the variance in the measured metabolite signals. In contrast to the 1D analysis, COSY detected Et/PET and Thr due to their distinct representations at  $[F1, F2] = [3.8, 3.2 \text{ ppm}]$  and  $[4.3, 1.3 \text{ ppm}]$ , respectively, in the 2D spectra. In addition, it also improved the ICC for several severely overlapping metabolites, including GABA, GSH, Lac, Thr, Tau, Glx, Glc, and Et/PET.

Our in vivo results demonstrate certain advantages of L-COSY spectroscopy of the brain. The individual signals from PC/GPC, GPC, (Ch+PC+GPC) and Et/PET will be of interest for evaluating the response of brain tumors to therapy (16). In addition, the resonance overlap due to lipids and macromolecules in the high-field region from 0–2 ppm is minimized, allowing improved metabolite detection. Further, baseline distortions associated with 1D spectra can be avoided by the 2D approach, improving the overall dynamic range of the measurement.

In spite of the greater spectral resolution afforded by 2D spectroscopy, certain metabolites, such as Glu and Gln, cannot be separated at 3T. This may be remedied

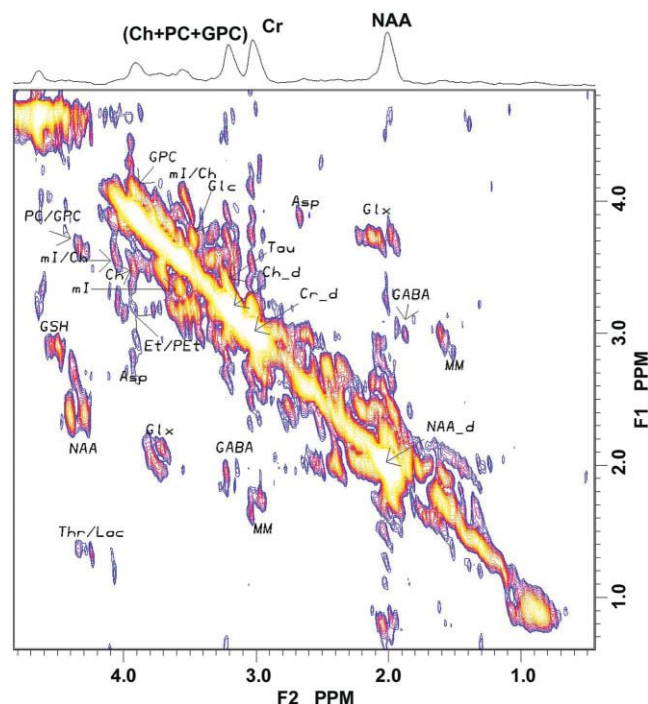


**Figure 3.** A 2D L-COSY spectrum recorded from the occipitoparietal lobe of a 25-year-old healthy subject with TR = 2 seconds, minimum TE = 30 msec, NEX = 16 for each  $t_1$  increment, 64  $t_1$  increments, and voxel size =  $3 \times 3 \times 3 \text{ cm}^3$  (27 mL).

by the development of more sophisticated fitting algorithms for deconvolving such metabolites. The reduced SNR of the COSY technique currently restricts its application to larger voxel sizes. However, this may be overcome with the development of optimal phased array RF coils and/or combining COSY with multi-voxel based MR spectroscopic imaging (MRSI) approaches. Finally, the development of a 2D fitting procedure analogous to the ProFit (17) method currently used to fit 2D

Table 1  
Matched Correlation Analysis of Metabolites Obtained From PRESS and L-COSY Data Recorded From the Occipitoparietal Lobe of One 30-Year-Old Subject\*

Metabolite ratios (/Cr)	1D PRESS		2D L-COSY	
	SD (%)	CV (%)	SD (%)	CV (%)
NAA	8.7	9.2	5.7	5.4
Glx	4.8	6.8	0.3	4.9
PCh+GPC	2.2	7.9	0.2	11.9
GPC	6.3	44.1	1.0	18.5
mI	4.8	10.1	0.8	15.1
Et/PET	17.1	77.1	0.4	17.5
GSH	4.2	34.7	0.2	9.2
Asp	2.9	13.1	0.5	18.4
GABA	5.2	27.7	0.3	24.9
Glc	8.5	142.3	1.5	17.2
Tau	5.1	42.8	0.7	13.0

\*Both 1D and 2D experiments were performed over a period of seven days.  $P$  value for 1D vs 2D:  $P < 0.001$ ;  $P$  value for CV,  $P < 0.07$ .

JPRESS (18) may permit absolute quantification with L-COSY.

## ACKNOWLEDGMENTS

We thank the staff of the Center for Advanced Imaging and Radiology for support of the 3T MRI/MRS system. In addition, we thank Drs. David Murray and William W. Wallace for helpful discussions. This research was supported in part by a Internal Health Sciences Center Grant from West Virginia University (WVU), NIH (1 RO1MH065695-01A1 to M.A.T), Department of Defense (DAMD 17 03-1-0759; DAMD 17 03-1-0123 to R.S), National Center for Research Resources, NIH (2G12 RR003048-16A1 to R.S) and by the National Institute on Aging, Intramural Research Program, of the NIH (R.G.S).

## REFERENCES

1. Bottomley PA. Spatial localization in NMR spectroscopy *in vivo*. Ann NY Acad Sci 1987;508:333–348.
2. Frahm J, Merboldt KD, Hanicke WJ. Localized proton spectroscopy using stimulated echoes. J Magn Reson 1987;72:502–508.
3. Provencher SW. Estimation of metabolite concentrations from localized *in vivo* proton NMR spectra. Magn Reson Med 1993;30:672–679.
4. Naressi A, Couturier C, Castang I, de Beer R, Graveron-Demilly D. Java-based graphical user interface for MRUI, a software package for quantitation of *in vivo*/medical magnetic resonance spectroscopy signals. Comput Biol Med 2001;31:269–286.
5. Brereton IM, Galloway GJ, Rose SE, Doddrell DM. Localized two-dimensional shift correlated spectroscopy in humans at 2 Tesla. Magn Reson Med 1994;32:251–257.
6. Kreis R, Boesch C. Spatially localized one- and two-dimensional NMR spectroscopy and *in vivo* application to human muscle. J Magn Reson B 1996;113:103–118.
7. Prescott AP, Dzik-Jurasz AS, Leach MO, et al. Localized COSY and DQF-COSY 1H MRS sequences for investigating human tibial bone marrow *in vivo* and initial application to patients with acute leukemia. J Magn Reson Imaging 2005;22:541–548.
8. Thomas MA, Yue K, Binesh N, Davanzo P, et al. Localized two-dimensional shift correlated MR spectroscopy of human brain. Magn Reson Med 2001;46:58–67.
9. Ziegler A, Gillet B, Beloeil JC, Macher JP, Dècorps M, Nèdelec JF. Localized 2D correlation spectroscopy in human brain at 3T. MAGMA 2002;14:45–49.
10. Thomas MA, Hattori N, Umeda M, Sawada T, Naruse S. Evaluation of two-dimensional L-COSY and JPRESS using a 3T MRI scanner: From phantoms to human brain *in vivo*. NMR Biomed 2003;16: 245–251.
11. Govindaraju V, Young K, Maudsley AA. Proton NMR chemical shifts and coupling constants for brain metabolites. NMR Biomed 2000; 13:129–153.
12. Ikonomidou VN, Sergiadis GD. Improved Shinnar-Le Roux algorithm. J Magn Reson 2000;143:30–34.
13. Binesh N, Yue K, Fairbanks L, Thomas MA. Reproducibility of localized 2D correlated MR spectroscopy. Magn Reson Med 2002; 48:942–948.
14. Fleiss J. The design and analysis of clinical experiments. New York: Wiley; 1986. 432 p.
15. Tofts P. Quantitative MRI of the brain. Measuring changes caused by disease. London: John Wiley & Sons Ltd.; 2003. 633 p.
16. Ackerstaff E, Glunde K, Bhujwala ZM. Choline phospholipid metabolism: a target in cancer cells. J Cell Biochem 2003;90:525–533.
17. Schulte RF, Boesiger P. ProFit: two-dimensional prior knowledge fitting of J-resolved spectra. NMR Biomed 2006;19:255–263.
18. Schulte RF, Lange T, Beck J, Meier D, Boesiger P. Improved two-dimensional J- resolved spectroscopy. NMR Biomed 2006;19:264–270.

## Original Research

# Investigation of Muscle Lipid Metabolism by Localized One- and Two-Dimensional MRS Techniques using a Clinical 3T MRI/MRS Scanner

S. Sendhil Velan, PhD,<sup>1\*</sup> Christopher Durst, BS,<sup>1</sup> Susan K. Lemieux, PhD,<sup>1</sup> Raymond R. Raylman, PhD,<sup>1</sup> Rajagopalan Sridhar, PhD,<sup>2,6,7</sup> Richard G. Spencer, MD, PhD,<sup>3</sup> Gerald R. Hobbs, PhD,<sup>4</sup> and M. Albert Thomas, PhD<sup>5</sup>

**Purpose:** To demonstrate the feasibility of estimating the relative intra- and extramyocellular lipid (IMCL and EMCL) pool magnitudes and calculating the degree of lipid unsaturation within soleus muscle using single-voxel localized one- and two-dimensional (1D and 2D) MR spectroscopy (MRS).

**Materials and Methods:** Localized 1D point resolved spectroscopy (PRESS) and 2D correlation spectroscopy (L-COSY) were performed in identical locations in the soleus muscle of 10 healthy subjects. A GE 3-T MRI/MRS scanner and a quadrature extremity transmit/receive coil was used.

**Results:** The 1D and 2D MR spectra were used to compute IMCL/creatine (Cr) and EMCL/Cr ratios. In addition to cross peaks between the methyl and methylene protons in the high-field region, the 2D spectra showed cross peaks due to *J*-coupling between allylic, diallylic methylene protons, and olefinic protons. The cross-peak volume ratios also provided a measure of double bonds, suggesting that

this ratio can be used to assess unsaturation within IMCL and EMCL lipid pools.

**Conclusion:** We have demonstrated the feasibility of detecting 2D cross peaks between different groups of IMCL and EMCL, including the unsaturated protons within these two lipids pools. This protocol may be easily extended to study the lipids present in other tissues.

**Key Words:** IMCL; EMCL; unsaturated fatty acids; MRS; muscle

**J. Magn. Reson. Imaging 2007;25:192–199.**  
© 2006 Wiley-Liss, Inc.

FATTY ACIDS are supplied to cells either by de novo fatty acid biosynthesis or by dietary uptake (1). Fatty acid desaturation is an oxygen-dependent process that can introduce a double bond located nine, six, five, or four carbon atoms from the carboxyl end of a fatty acyl-CoA thioester. These reactions are catalyzed by separate desaturase enzymes, termed the  $\Delta^9$ ,  $\Delta^6$ ,  $\Delta^5$ , and  $\Delta^4$  desaturases. Linoleic and linolenic acid are the two principal fatty acids supplied by dietary uptake and are called essential fatty acids. They are required for synthesis of polyunsaturated fatty acids (1).

Unsaturated fatty acids are essential for modulating the mechanical properties and functions of cell membranes. Several human diseases show abnormal patterns of unsaturated fatty acids attributable to abnormal metabolism, particularly diminished capabilities for desaturation or chain elongation. The analysis of lipid composition is also a major factor in understanding the biochemical changes associated with neoplasticity and the treatment of cancer (2).

Phospholipid alterations have been reported in sickle cell patients (3), mammary tumors (4), Alzheimer's disease (5), muscular dystrophy (6), cardiovascular disease (7), liver disease (8), lung disease (9), malaria (10), malignant renal cell carcinoma (11), and human immunodeficiency virus (HIV) (12). For example, the fatty acid composition in individuals with insulin resistance and metabolic syndrome is typically characterized by high levels of saturated fatty acids and low levels of polyunsaturated fatty acids (13,14). It has also been suggested

<sup>1</sup>Center for Advanced Imaging and Radiology, West Virginia University, Morgantown, West Virginia, USA.

<sup>2</sup>Department of Radiation Oncology, Howard University, Washington, DC, USA.

<sup>3</sup>NMR Unit, National Institute on Aging, National Institutes of Health, Baltimore, Maryland, USA.

<sup>4</sup>Department of Statistics, West Virginia University, Morgantown, West Virginia, USA.

<sup>5</sup>Department of Radiology, University of California, Los Angeles, California, USA.

<sup>6</sup>Department of Genetics and Human Genetics, Howard University, Washington, DC, USA.

<sup>7</sup>Cancer Center, Howard University, Washington, DC, USA.

Contract grant sponsor: National Institutes of Health (NIH) Intramural Research Program; Contract grant sponsor: National Institute on Aging; Contract grant sponsor: Internal Health Sciences Center Grant, West Virginia University (WVU), Research Centers in Minority Institutions (RCMI); Contract grant sponsor: National Institutes of Health (NIH), National Center for Research Resources (NCRR); Contract grant numbers: 2G12 RR003048-16A1; Contract grant sponsor: National Institutes of Health (NIH); Contract grant number: 1R01MH065695-01A1; Contract grant sponsor: Department of Defense; Contract grant numbers: DAMD 17 03-1-0759 and DAMD 17 03-01-0123.

\*Address Correspondence to: S.S.V., Assistant Professor, Center for Advanced Imaging and Radiology, West Virginia University, Morgantown, WV, 26506. E-mail: svelan@hsc.wvu.edu

Received May 4, 2006; Accepted August 30, 2006.

DOI 10.1002/jmri.20786

Published online 6 December 2006 in Wiley InterScience (www.interscience.wiley.com).



that  $\beta$ -cell apoptosis is predominantly determined by the content of unsaturated fatty acids in a mixed fatty acid pool (15). Therefore, the evaluation of lipid unsaturation in these and other disorders may provide prognostic information or a therapeutic target. Thus, techniques that can detect lipid components and estimate the degree of unsaturation within a clinical setting may be of immense value.

Localized MR spectroscopy (MRS) has been applied successfully to human skeletal muscle *in vivo* to detect the two lipid pools referred to as intramyocellular lipids (IMCL) and extramyocellular lipids (EMCL). The resonances from the lipids in the muscle spectra are split into two signals due to the geometrical arrangement of these lipid compartments. EMCL are nestled in long fatty septa along the muscle fiber bundles or fasciae, whereas IMCL are located within the cytoplasm of muscle cells as spherical droplets. This results in a chemical shift separation of 0.2 ppm between IMCL and EMCL resonances in the tibialis anterior and 0.15 ppm in the soleus compartment (16,17). The  $^1\text{H}$  spectrum of human skeletal muscle also displays an orientation-dependent dipolar splitting caused by incomplete motional averaging for several compounds, including creatine (Cr), phosphocreatine (PCr), taurine, lactate, and carnosine (17–23). In particular, the methylene and methyl groups of creatine appear as a dipolar doublet and triplet when the muscle fibers are oriented parallel to the external magnetic field (18,20). The resonances collapse to a singlet in muscle fibers aligned at the magic angle of  $54.7^\circ$  with respect to the main magnetic field. Quantification of IMCL by  $^1\text{H}$  MRS permits noninvasive detection of intracellular substrate storage and turnover in human muscle in the setting of, for example, disease states and activity. The relation between skeletal muscle triglycerides and insulin resistance, obesity and exercise has been investigated in humans (24) and in rodents (25). In this context composition of fat could also be important since the increase in saturated fatty acids has been associated with insulin resistance (26,27).

Aside from detection of IMCL and EMCL, localized 1D MRS techniques have been employed to estimate unsaturation in osteoporosis (28) and renal cell carcinoma (11). In bone marrow and the kidney, there is a single chemical environment for lipids and hence no chemical shift separation analogous to that between IMCL and EMCL in muscle. Therefore, it is possible to estimate unsaturation by detecting the olefinic protons in the lipid chains. To extend this capability, spatially resolved localized two-dimensional (2D) correlated spectroscopic approaches have been implemented recently to overcome the limitations of inadequate spectral dispersion in localized one-dimensional (1D) MRS (29,30). The main advantage of 2D over 1D MRS is that connectivity between distinct individual spins is delineated, so that  $J$ -coupled multiplet resonance peaks are dispersed over two spectral dimensions. This leads to a substantial improvement in peak discrimination. A recent study in tibial bone marrow (30) estimated the unsaturated lipid proton index using the cross peaks and diagonal peaks of the 2D spectrum which have different phase characteristics (31). Note that the diagonal peak of

$(\text{CH}_2)_n$  from lipids are generated from both saturated and unsaturated lipid components.

In the present study we investigate the metabolite composition of skeletal muscle tissue by localized 1D and 2D MRS techniques, and also describe a procedure to measure the degree of unsaturation within these two lipid pools. This procedure can readily be extended to localized 2D MRS studies of other organs, including breast, liver, kidney, and heart.

## MATERIALS AND METHODS

### Subjects

All experiments were performed in the soleus muscle of 10 healthy subjects (age range 20–30 years) who gave informed consent to this study, conducted according to procedures approved by the local institutional review board. The soleus muscle was selected for this study since its location permitted optimal  $B_0$  homogeneity in the volume of interest (VOI) and it has a substantially larger volume than the anterior tibialis muscle. The subjects were positioned supine feet first inside the magnet with their right calf placed inside the standard clinical quadrature transmit/receive extremity coil. In order to standardize the position and alignment of the subject's leg, the following procedure was implemented prior to each experiment. First, the distance from the medial condyle to the medial malleolus of the subject's right leg was measured, and the point one-third of the way from the medial condyle to the medial malleolus was marked. The subject was then positioned on the bed with his or her right lower leg placed in the coil such that the marked position was used for all the MRS experiments. Padding was added to minimize the amount of movement during the scan. One localized 2D correlation spectroscopy (L-COSY) experiment was performed in the trabecular bone marrow fat of a healthy subject to compare that lipid profile with that of the calf muscle.

### Pulse Sequences

All experiments were performed using a 3-T MRI/MRS scanner (GE Healthcare Technologies, Waukesha, WI, USA) running on the VH3 platform with self-shielded gradients (40 mT/m). Gradient echo-based magnetic resonance images (MRI) were acquired in the axial, coronal, and sagittal planes with 5-mm-thick slices, in-plane spatial resolution =  $976 \times 976 \mu\text{m}^2$ , repetition time (TR) = 14.7 msec, number of excitations (NEX) = 1, and echo time (TE) = 2.25 msec. These images were used to localize the target volume for both phantom and *in vivo* experiments. All spectroscopic measurements were performed using a  $3 \times 3 \times 3 \text{ cm}^3$  (27 mL) volume. In addition to use of linear gradient shims, higher-order shimming was performed to reduce magnetic field inhomogeneity.

Localized 1D MRS was performed using a point-resolved spectroscopy (PRESS) (32) sequence consisting of three selective pulses ( $90^\circ$ – $180^\circ$ – $180^\circ$ ), creating two spin echoes. The sequence employed Shinnar-Le Roux radiofrequency (RF) pulses (33), including a 3.6 msec long  $90^\circ$  pulse with an excitation bandwidth of 2367 Hz

and a 5.2 msec long refocusing  $180^\circ$  pulse with a bandwidth of 1.4 kHz. TR/TE of 2 second/24 msec and 64 averages (NEX) were employed. The acquisition incorporated 2048 complex points and a spectral width of 5 kHz. A total of 16 averages of unsuppressed water spectra from the same VOI were also acquired in order to correct for eddy currents and permit phasing of the metabolite spectra.

A 2D L-COSY sequence (29) employing two echoes, a spin echo and a coherence transfer echo, was implemented following collection of the 1D dataset. These spectra were recorded from the same VOI as examined in the 1D experiments. The chemical shift selective (CHESS) module for global water suppression and outer volume saturation module were combined with this sequence. The  $90^\circ$  and  $180^\circ$  RF pulses had similar duration and bandwidth as described for the PRESS sequence. The VOI was localized with a  $90^\circ$ – $180^\circ$ – $90^\circ$  pulse train in combination with appropriate  $B_0$  crusher gradient pulses. The last  $90^\circ$  RF pulse was used for both slice selection and coherence transfer. An incremental period for creation of the second dimension was inserted immediately after the formation of the spin echo.  $B_0$  crusher gradients were employed around the second  $180^\circ$  and third  $90^\circ$  pulses. The minimal duration for the two echoes was 30 msec, and 50 incremental time steps were performed with  $\Delta t_1 = 0.8$  msec, resulting in a spectral bandwidth of 1250 Hz along the second spectral dimension. The signals for each incremental period were averaged over eight scans and the total acquisition time for the experiment was approximately 13 minutes. More than 50% of the coherence transfer echo was sampled using 2048 complex points. The acquisition dimension ( $t_2$ ) had a bandwidth of 5000 Hz with 2048 complex points sampled. The postprocessing of all 2D data sets was performed using FELIX software (Accelrys Inc., San Diego, CA, USA).

### Phantom Experiments

The aim of the in vitro experiments was to measure unsaturation indices by the 2D L-COSY technique. Linoleic (18:2) and linolenic (18:3) acids in pure form were purchased from Sigma-Aldrich Inc. (St. Louis, MO, USA), and dissolved in deuterated chloroform. 2D L-COSY MRS experiments were performed using a 27-mL voxel.

### Spectral Processing

All the in vivo 1D MRS data were fitted and quantified using Java-based Magnetic Resonance User Interface (jMRUI) software based on the Advanced Method for Accurate, Robust, and Efficient Spectral fitting (AMARES) algorithm (34). For the AMARES fitting procedure six resonances, including the methyl ( $\text{CH}_3$ ), methylene protons ( $\text{CH}_2$ )<sub>n</sub>, creatine (Cr), and trimethylamines (TMA) from IMCL and EMCL, were described with the assumption of Gaussian line shapes. Prior knowledge was incorporated into the fitting algorithm by a previously described procedure (35). The ratios of IMCL and EMCL with respect to Cr were determined from the ( $\text{CH}_2$ )<sub>n</sub> signals of IMCL and EMCL and the

creatine signal at 3.00 ppm for both approaches. A correction was included for the creatine resonance saturation, since the  $T_1$  of creatine is 1 second (36) in the soleus muscle at 3 T.

Localized 2D L-COSY data were processed using the FELIX software. Prior to Fourier transformation, the time domain data matrix was apodized using shifted sine squared filters in both the  $t_1$  and  $t_2$  dimensions. The length of the window functions was adjusted for the sine bell filters to reach zero at the last experimental data point in both dimensions. All data sets were linear predicted from 50  $t_1$  points to 100  $t_1$  points along the  $F_1$  dimension and zero filled to 256 points. The diagonal and cross peaks were assigned and the volume integrals were quantified as described previously (37). The size of the volume for each cross and diagonal peak was adjusted to be uniform across all data sets. The diagonal peak volumes from ( $\text{CH}_2$ )<sub>n</sub> protons from the IMCL and EMCL (1.2 and 1.35 ppm), creatine signal at 3.00 ppm, and olefinic protons at 5.5 ppm were estimated. The cross peak volumes at (5.3, 2.0 ppm), (5.3, 2.7 ppm) of IMCL and (5.45, 2.15 ppm), (5.45, 2.85 ppm) of EMCL were obtained. The degree of unsaturation was estimated by employing these two sets of cross peaks from IMCL and EMCL.

### Statistical Analysis

Analysis of variance was used to assign the variability of IMCL and EMCL into inter- and intrasubject differences. Data from all 10 subjects were employed for intersubject analysis, while five measurements performed on one subject were utilized for intrasubject analysis. Comparison of the variability of the degree of unsaturation within the IMCL and EMCL lipid pools was performed with a paired *t*-test. Intraclass correlations (38) were used to assess the relative contributions to the variance between and within subjects for IMCL/Cr and EMCL/Cr. A two-tailed unpaired *t*-test was been used for the comparisons between the 1D and 2D data. All analysis was carried out using JMP software (SAS Institute, Cary, NC, USA). Data are presented as mean  $\pm$  SD, and statistical significance assigned at the  $P < 0.05$  level.

## RESULTS

The ratios IMCL/Cr and EMCL/Cr were computed using the 1D and 2D MR spectral data recorded from the soleus muscle. The signals from the *n*-methylene protons resonating at 1.2 ppm for IMCL, 1.35 ppm for EMCL, and the signal of the methyl group from the creatine at 3.00 ppm were used to derive these ratios from the 1D datasets. In the 2D spectra, the diagonal peaks at 1.2, 1.35, and 3.00 ppm were used.

Figure 1 shows a 1D spectrum fit with the AMARES algorithm. The resonances due to ( $\text{CH}_3$ ), ( $\text{CH}_2$ )<sub>n</sub> from IMCL and EMCL, Cr, and TMA were used for the fitting procedure. Traces in Fig. 1a and b show the actual acquired spectra whereas traces in Fig. 1c and d show the individual spectral components and residuals. Values for the ratios IMCL/Cr and EMCL/Cr were  $11.8 \pm 3.34$  and  $18.0 \pm 3.6$ , respectively. The corresponding ratios for



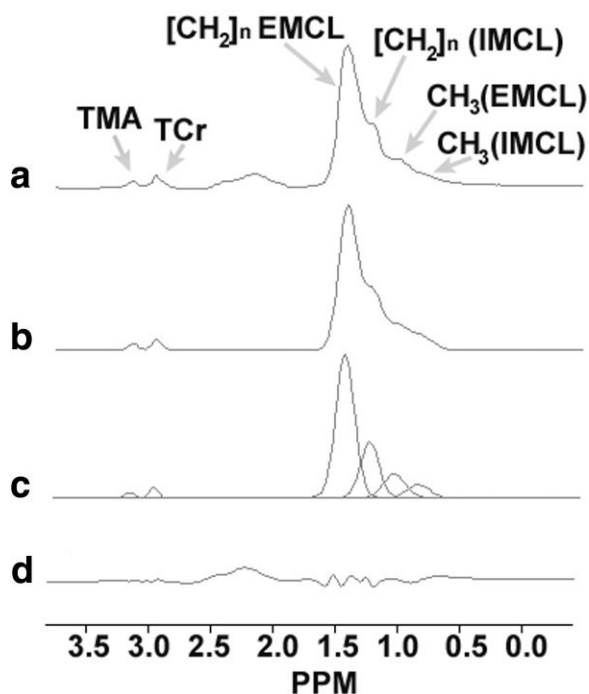


**Figure 1.** PRESS-localized 1D MR spectrum recorded from the soleus muscle of a 30-year-old healthy subject with TE = 24 msec, TR = 2 seconds, NEX = 64, and voxel size = 27 mL fitted by AMARES algorithm within jMRUI software. The resonances from methyl, n-methylene peaks from IMCL, EMCL, Cr, and TMA were used for the fitting procedure. Traces (a) and (b) show the actual acquired spectrum and fitted spectrum, whereas traces (c) and (d) show the individual components and residuals.

the intrasubject measurements were  $12.6 \pm 1.91$  and  $19.5 \pm 2.09$ , respectively. The intraclass correlation was 75% for both IMCL/Cr and EMCL/Cr.

Figure 2 shows a 2D L-COSY spectrum. The assignments of various resonances are given in Table 1. The average IMCL/Cr and EMCL/Cr ratios obtained from all subjects were  $10.2 \pm 1.9$  and  $15.4 \pm 2.9$ , respectively, while the corresponding values for the intrasubject measurements were  $11.23 \pm 1.24$  and  $17.5 \pm 1.67$ , respectively. The intraclass correlation was 70% for IMCL and 76% for EMCL.

In addition to the methyl and n-methylene groups of IMCL and EMCL, a 2D L-COSY spectrum (Fig. 2) provides information on cross peaks due to the scalar couplings within IMCL, EMCL and glycerol backbone protons. Cross peaks C1, C3, and C8 arise from spin-spin coupling between olefinic ( $-\text{CH}=\text{CH}-$ ) and allylic methylene protons  $\text{CH}_2\text{CH}=\text{CH}$  of IMCL and EMCL, respectively. The cross peaks C2, C4, and C7 arise from the indirect spin-spin coupling between olefinic ( $-\text{CH}=\text{CH}-$ ) and diallylic methylene protons ( $-\text{CH}=\text{CH}-\text{CH}_2-\text{CH}=\text{CH}-$ ) of IMCL and EMCL, respectively. Note that the cross peaks C7 and C8 are not resolved into IMCL and EMCL components due to the lower spectral resolution along the F1 dimension. The C5 cross peaks are due to the correlation between  $\text{CH}_2$  and CH groups of the glycerol backbone protons. The L-COSY spectrum also exhibits orientation dependent residual dipolar

couplings at the  $\text{CH}_2$  group of creatine with diagonal frequencies [3.9, 3.9 ppm] and carnosine. The C6 cross peaks are due to the residual dipolar coupling between CH groups from imidazole protons of carnosine at [7, 8 ppm] and [8, 7 ppm]. The frequency coordinates correspond to [F2, F1] dimensions in the 2D spectrum.

Figure 3a and b show the L-COSY spectra of pure linoleic and linolenic acids. The diagonal frequencies [F2, F1] for methyl [1.3, 1.3 ppm], n-methylene [1.4, 1.4 ppm], allylic methylene [2.1, 2.1 ppm], diallylic methylene [2.9, 2.9 ppm], and olefinic protons [5.5, 5.5 ppm] were identified for these lipids. The cross peaks C1 and C2 are due to correlation between olefinic protons and allylic and diallylic protons, respectively. The measure of unsaturation was obtained by computing the ratio of the cross peak C2 to cross peak C1. The degree of unsaturation for linoleic and linolenic were 2.1 and 3.2, respectively.

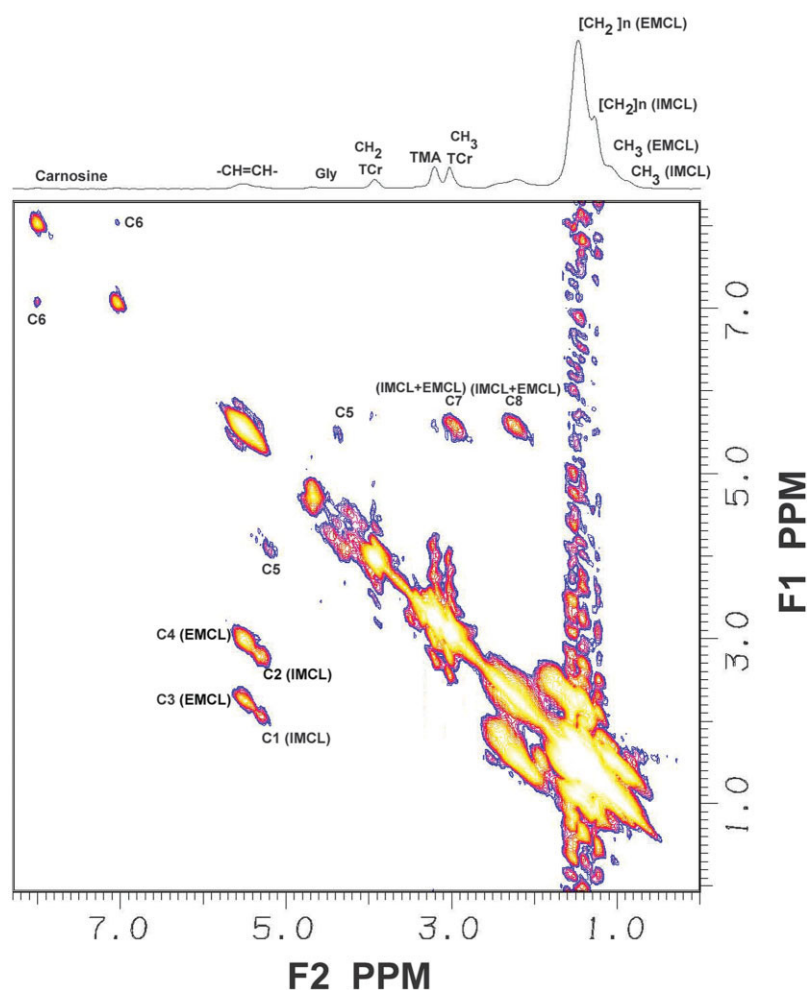
Similar ratios were computed for the IMCL and EMCL in the soleus muscle of the healthy subjects using the cross peaks C2/C1 for IMCL and C4/C3 for EMCL as shown in Fig. 2. The ratios of the cross peaks from C2/C1 and C4/C3 were  $1.1 \pm 0.11$  and  $0.87 \pm 0.12$  for IMCL and EMCL, respectively, for the intersubject measurements and  $1.27 \pm 0.16$  and  $1.03 \pm 0.11$  for intrasubject measurements. A paired *t*-test performed on the intersubject analysis showed that the degree of unsaturation is significantly different between IMCL and EMCL, with a *t* value of  $-5.56$  and *P* value of 0.0004. A paired *t*-test performed for the intrasubject measurements showed that the degree of unsaturation between IMCL and EMCL was significantly different, with a *t* value of  $-3.89$  and *P* value of 0.0176.

Figure 4 shows a spectrum recorded from the trabecular bone marrow fat of a healthy subject. This spectrum shows only one cross peak C1 at [5.5, 2.0] and C2 at [5.5, 2.9] ppm, indicating the presence of an unsaturated lipid component.

## DISCUSSION

Detection of IMCL and EMCL is of interest in characterizing diabetes, metabolic syndrome, exercise physiology, and other states involving lipid alterations. Current research is focused on understanding and differentiating the biochemical pathways for accumulation of IMCL in different muscle types (39). In addition to this, the degree of unsaturation within the IMCL and EMCL in vivo is likely to represent an important parameter in lipid metabolism. Localized 1D MRS provides information about the IMCL and EMCL in muscle tissue via, primarily, resonances from methyl and n-methylene protons; however, it is difficult to separate the contribution of olefinic protons from IMCL and EMCL due to the width of the relevant lines and the limited spectral resolution at clinical field strengths. Thus, localized 2D MR spectroscopic approaches provide increased spectral dispersion on clinical scanners.

In this investigation we measured IMCL/Cr and EMCL/Cr ratios in the soleus muscle using both 1D and 2D MRS techniques. In order to validate the results of the 2D approach, 1D MR spectra were processed by jMRUI software using the AMARES algorithm (34) (Fig.



**Figure 2.** A 2D L-COSY spectrum recorded from the soleus muscle of a 30-year-old healthy subject with TR = 2 seconds, minimal TE = 30 msec, NEX = 8 for each  $t_1$ , 50  $t_1$  increments, and voxel size = 27 mL. The assignments are shown in Table 1. Note that the spectral resolution along F2 and F1 is different, and the 2D data is presented in a square format for visualization purposes.

1). The L-COSY spectrum shown in Fig. 2 demonstrates detection and differentiation of several resonances from the saturated and unsaturated protons of IMCL and EMCL. The estimate of EMCL/Cr showed a trend to-

Table 1  
Assignment of Various Resonances in the 2D L-COSY Spectrum of Soleus Muscle

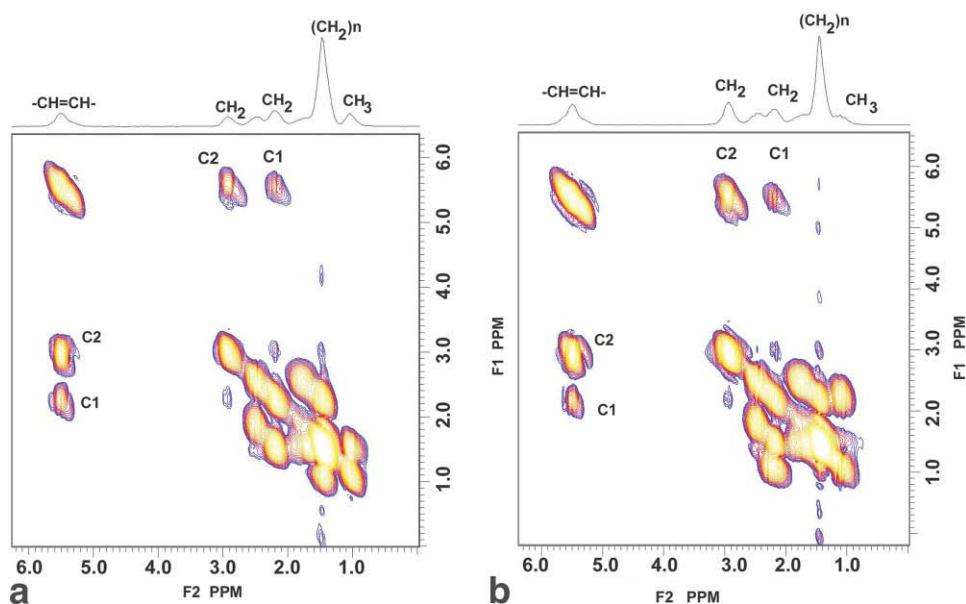
Resonance	Frequency coordinates (ppm)
CH <sub>3</sub> (IMCL)	[0.8/0.8]
CH <sub>3</sub> (EMCL)	[0.95/0.95]
(CH <sub>2</sub> ) <sub>n</sub> (IMCL)	[1.2/1.2]
(CH <sub>2</sub> ) <sub>n</sub> (EMCL)	[1.35/1.35]
CH <sub>2</sub> CH = CH (IMCL)	[2.0/2.0] Allylic methylene
CH <sub>2</sub> CH = CH (EMCL)	[2.15/2.15]
—CH = CHCH <sub>2</sub> CH = CH (IMCL)	[2.7/2.7] Diallylic methylene
—CH = CHCH <sub>2</sub> CH = CH (EMCL)	[2.85/2.85]
CH <sub>3</sub> (creatine)	[3.0/3.0]
TMA	[3.2/3.2]
CH <sub>2</sub> (creatine)	[3.9/3.9]
—CH = CH— (IMCL)	[5.3/5.3]
—CH = CH— (EMCL)	[5.45/5.45]
Carnosine	[7.0/7.0]
Carnosine	[8.0/8.0]
CH <sub>2</sub> OCOR (glycerol)	[4.3/4.3]
CHOCOR (glycerol)	[5.2/5.2]

ward a slightly lower value when calculated from the 2D dataset as compared to the 1D approach, although the difference did not reach statistical significance ( $P = 0.09$ ). This trend is likely due to the greater  $T_2$  losses in the L-COSY technique compared to the short echo time 1D PRESS experiments; the  $T_2$  values for the (CH<sub>2</sub>)<sub>n</sub> resonances of IMCL and EMCL at 3 T are 90 and 78 msec, respectively (36). In addition to the cross peaks of IMCL and EMCL it is also possible to detect cross peaks from glycerol backbone protons.

The L-COSY experiment also provides information on residual dipolar couplings from creatine and imidazole protons of carnosine. The residual dipolar coupling of the CH<sub>3</sub> group of creatine at [3.0, 3.0 ppm] is less prominent compared to the CH<sub>2</sub> group at [3.9, 3.9 ppm]. Note that the cross peaks from the imidazole protons of carnosine are due to residual dipolar couplings since the long range  $J$  coupling ( $\sim 1$  Hz) would be difficult to detect in in vivo experiments given the large degree of inhomogeneous broadening of the spectral lines. The carnosine resonances in the aromatic region can be used to estimate intracellular pH in the muscle (40).

The cross peaks C1 at [5.3, 2.0 ppm] and C2 at [5.3, 2.7 ppm] shown in Fig. 3 are due to the olefinic, allylic, and diallylic methylene protons of the IMCL lipid pool. The cross peaks C3 at [5.45, 2.15 ppm] and C4 at [5.45, 2.85 ppm] are due to the olefinic, allylic, and diallylic

**Figure 3.** a: 2D L-COSY spectrum recorded from the linoleic acid phantom with TR = 2 seconds, minimal TE = 30 msec, NEX = 16 for each  $t_1$  increment, 50  $t_1$  increments, and voxel size =  $3 \times 3 \times 3$  cm<sup>3</sup> (27 mL). b: 2D L-COSY spectrum recorded from the linolenic acid phantom with identical experimental parameters. Both compounds were dissolved in deuterated chloroform. The chemical shifts were assigned with reference to olefinic protons (5.5 ppm); there is a slight difference in chemical shifts compared to the in vivo spectra due to solvent effects.



methylene protons from the EMCL lipid pool. Thus, the two sets of cross peaks (C1, C2 from IMCL and C3, C4 from EMCL) present in the muscle spectra (Fig. 2) can be employed to determine the degree of unsaturation within the IMCL and EMCL lipid pools. The amplitude and volume of cross peaks will show a dependence on line-widths and on the number of points collected in the  $t_1$  dimension, defining the spectral resolution in the F1

dimension. The ratio of cross peak volumes provides a measure of mono-unsaturated site as compared to multiple unsaturated sites, but does not necessarily reflect actual concentrations. Nevertheless, this measure permits estimation of the degree of unsaturation within the IMCL and EMCL lipid pools. Note that the cross peaks at the upper diagonal labeled C7 and C8 are not resolved into IMCL and EMCL components due to the

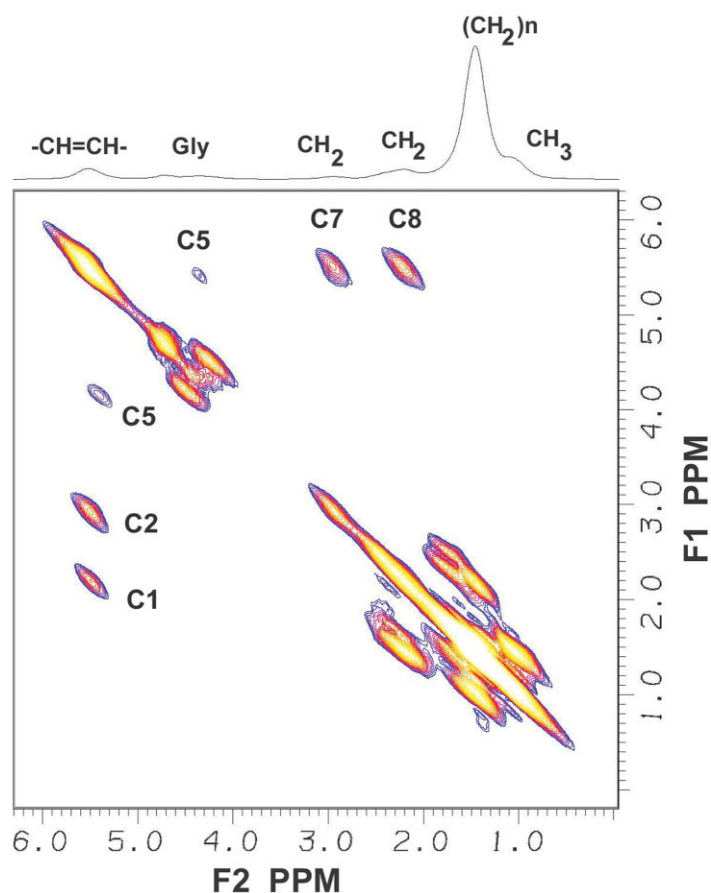


**Figure 4.** A 2D L-COSY spectrum recorded from the trabecular bone marrow fat of a 30-year-old healthy subject with TR = 2 seconds, minimal TE = 30 msec, NEX = 8 for each  $t_1$ , 50  $t_1$  increments, and voxel size = 27 mL.

limited spectral resolution (25 Hz/point) along the F1 dimension as compared to the F2 spectral resolution (2.4 Hz/point). To ensure that the cross peaks labeled C1–C4 are from IMCL and EMCL we also investigated trabecular bone marrow fat using identical experimental parameters as used for the muscle lipid measurements. Figure 4 shows the 2D L-COSY spectrum from trabecular bone marrow fat showing only one cross peak C1 at [5.5, 2.0] and C2 at [5.5, 2.9] ppm. This indicates the presence of only one type of lipid, including unsaturated and saturated components, confirming that the two types of lipids seen in muscle, IMCL and EMCL, can be distinguished only due to their geometrical arrangement.

To validate our procedure we employed pure linoleic and linolenic acids, which have 18 carbon chains and two or three double-bonded sites, respectively. The chemical shifts are slightly different from those observed in *in vivo* spectra since the pure acids were dissolved in deuterated chloroform. The cross peaks C1 and C2 seen in Fig. 3a and 3b of linoleic and linolenic acids are due to the correlation between the allylic methylene protons and the olefinic protons. Cross peak C1 arises due to the scalar coupling between olefinic ( $-\text{CH}=\text{CH}-$ ) and allylic methylene protons  $\text{CH}_2\text{CH}=\text{CH}$  and thus appears if the methylene protons are adjacent to only one unsaturated site proton. Cross peak C2 arises from the scalar coupling between olefinic ( $-\text{CH}=\text{CH}-$ ) and diallylic methylene protons ( $-\text{CH}=\text{CH}-\text{CH}_2-\text{CH}=\text{CH}-$ ). They occur if there are at least two unsaturated sites and the methylene protons are located between the unsaturated site protons. The ratio of cross peak volumes C2/C1 is thus a measure of the degree of unsaturation. An increase in the number of unsaturated site protons in a fatty acyl chain increases the number of methylene protons situated between two unsaturated site protons compared to the number of methylene protons bordered by only a single unsaturated proton. The ratio of cross peak volumes C2/C1 for linolenic and linoleic fatty acids clearly demonstrates the ratio of unsaturated sites; the spectra of linoleic (18:2) and linolenic (18:3) acids show an increase of the C2/C1 ratio as a function of the number of double bonds. Thus, this ratio is sensitive to double bonds, permitting estimation of the degree of muscle lipid unsaturation *in vivo*.

The evaluation of the cross peaks generated between the olefinic and allylic and diallylic methylene protons within the IMCL and EMCL lipid pools from 2D L-COSY spectra of the healthy subjects showed higher unsaturation for the IMCL compared to the EMCL, indicating the relative efficiency of double bond creation within the cell as compared to the lipid pool outside the cell. The desaturation (conversion of  $-\text{CH}_2\text{CH}_2-$  to  $-\text{CH}=\text{CH}-$ ) is carried out by the desaturase enzymes (1). Therefore, this approach has potential utility in the study of lipid disorders in which the function of desaturase enzymes is abnormal, including diabetes and metabolic syndrome.

To our knowledge, this study is the first to demonstrate the feasibility of detecting the degree of unsaturation within the IMCL and EMCL pools *in vivo*. Our results indicate higher unsaturation in IMCL as com-

pared to EMCL. Although the L-COSY technique provides information on the degree of unsaturation, the signal-to-noise ratio (SNR) per unit time is lower by a factor of two as compared to the PRESS sequence. However, with appropriate RF coils, such as use of a phased array, this limitation may be relaxed, permitting investigation of smaller voxels with reduced acquisition time. We conclude that the 2D L-COSY technique has the potential to become a useful tool in the investigation of lipid disorders in various settings, including breast and cardiovascular disease.

## ACKNOWLEDGMENTS

We thank the staff of the Center for Advanced Imaging and Radiology for support of the 3-T system. In addition, we thank Drs. Stephen Alway, Randy Bryner, Greg Doyle, Lisa Salati, William W. Wallace, David Murray, and Ad Bax for helpful discussions. This research was supported in part by an Internal Health Sciences Center Grant from West Virginia University (WVU), National Center for Research Resources, NIH (2G12 RR003048-16A1 to R.S.), the National Institutes of Health (1R01MH065695-01A1 to M.A.T.), and the National Institute on Aging (to R.G.S.).

## REFERENCES

- Longmuir KJ. Phospholipid biosynthesis. In: Cevc G, editor. *Phospholipids handbook*. New York: Marcel Dekker; 1993. p 65–95.
- Hietanen E, Punnonen K, Punnonen R, Auvinen O. Fatty acid composition of phospholipids and neutral lipids and lipid peroxidation in human breast cancer and lipoma tissue. *Carcinogenesis* 1986; 7:1965–1969.
- Akinyanju PA, Akinyanju CO. Plasma and red cell lipids in sickle cell disease. *Ann Clin Lab Sci* 1976;6:521–524.
- Tan WC, Chapman C, Takatori T, Privett OS. Studies of lipid class and fatty acid profiles of rat mammary tumors induced by 7, 12-dimethylbenz(a)anthracene. *Lipids* 1975;10:70–74.
- Kwee IL, Nakada T, Ellis WG. Elevation in relative levels of brain membrane unsaturated fatty acids in Alzheimer's disease: high resolution proton spectroscopic studies of membrane lipid extracts. *Magn Reson Med* 1991;21:49–54.
- Kwok CT, Austin L. Phospholipid composition and metabolism in mouse muscular dystrophy. *Biochem J* 1978;176:15–22.
- Szczepaniak LS, Dobbins RL, Metzger GJ, et al. Myocardial triglycerides and systolic function in humans: *in vivo* evaluation by localized proton spectroscopy and cardiac imaging. *Magn Reson Med* 2003;49:417–423.
- Thomas EL, Hamilton G, Patel N, et al. Hepatic triglyceride content and its relation to body adiposity: a magnetic resonance imaging and proton spectroscopic study. *Gut* 2005;54:122–127.
- Rutter A, Mackinnon WB, Huschtscha LI, Mountford CE. A proton magnetic resonance spectroscopy study of aging and transformed human fibroblasts. *Exp Gerontol* 1966;31:669–686.
- Beaumelle BD, Vial HJ. Modification of the fatty acid composition of individual phospholipids and neutral lipids after infection of the simian erythrocyte by *Plasmodium knowlesi*. *Biochim Biophys Acta* 1986;877:262–270.
- Katz-Brull R, Rofsky NM, Morrin MM, et al. Decreases in free cholesterol and fatty acid unsaturation in renal cell carcinoma demonstrated by breath-hold magnetic resonance spectroscopy. *Am J Physiol Renal Physiol* 2005;288:F637–F641.
- Torriani M, Thomas BJ, Barlow RB, Librizzi J, Dolan S, Grinspoon S. Increased intramyocellular lipid accumulation in HIV-infected women with fat redistribution. *J Appl Physiol* 2006;100:609–614.
- Vessby B, Gustafsson IB, Tengblad S, Boberg M, Andersson A. Desaturation and elongation of fatty acids and insulin action. *Ann NY Acad Sci* 2002;967:183–195.
- Warensjo E, Riserus U, Vessby B. Fatty acid composition of serum lipids predicts the development of the metabolic syndrome in men. *Diabetologia* 2005;48:1999–2005.



15. Eitel K, Staiger H, Brendel MD, et al. Different role of saturated and unsaturated fatty acids in  $\beta$ -cell apoptosis. *Biochem Biophys Res Commun* 2002;299:853–856.
16. Boesch C, Slotboom J, Hoppeler H, Kreis R. In vivo determination of intramyocellular lipids in human skeletal muscle by means of localized  $^1\text{H}$  MR-spectroscopy. *Magn Reson Med* 1997;37:484–493.
17. Steidle G, Machann J, Claussen CD, Schick F. Separation of intra- and extramyocellular lipid signals in proton MR spectra by determination of their magnetic field distribution. *J Magn Reson* 2002;154:228–235.
18. Kreis R, Boesch C. Liquid-crystal-like structures of human muscle demonstrated by in vivo observation of direct dipolar coupling in localized proton magnetic resonance spectroscopy. *J Magn Reson B* 1994;104:189–192.
19. Asllani I, Shankland E, Pratam T, Kushmerick M. Anisotropic orientation of lactate in skeletal muscle observed by dipolar coupling in  $^1\text{H}$  NMR spectroscopy. *J Magn Reson* 1999;139:213–224.
20. Hanstock CC, Thompson RB, Trump ME, Gheorghiu D, Hochachka PW, Allen PS. Residual dipolar coupling or the Cr/PCr methyl resonance in resting human medial gastrocnemius muscle. *Magn Reson Med* 1999;42:421–424.
21. Asllani I, Shankland E, Pratum T, Kushmerick M. Effects of pH and molecular charge on dipolar coupling interactions of solutes in skeletal muscle observed by DQF,  $^1\text{H}$  NMR spectroscopy. *J Magn Reson* 2003;163:124–132.
22. Kreis R, Boesch C. Orientation dependence is the rule, not the exception in  $^1\text{H}$ -MR spectra of skeletal muscle: the case of carnosine. *Proc Intl Soc Magn Reson Med* 2000;8:31.
23. Schroder L, Bachert P. Evidence for a dipolar-coupled AM system in carnosine in human calf muscle from in vivo  $^1\text{H}$  NMR spectroscopy. *J Magn Reson* 2003;164:256–269.
24. Machann J, Haring H, Schick F, Stumvoll M. Intramyocellular lipids and insulin resistance. *Diabetes Obes Metab* 2004;6:239–248.
25. Kuhlmann J, Neumann-Haefelin C, Belz U, et al. Intramyocellular lipid and insulin resistance. A longitudinal in vivo  $^1\text{H}$ -spectroscopic study in Zucker diabetic fatty rats. *Diabetes* 2003;52:138–144.
26. Montell E, Turini M, Marotta M, et al. DAG accumulation from saturated fatty acids desensitizes insulin stimulation of glucose uptake in muscle cells. *Am J Physiol Endocrinol Metab* 2001;280:E229–E237.
27. Decsi T, Minda H, Hermann R, et al. Polyunsaturated fatty acids in plasma and erythrocyte membrane lipids of diabetic children. *Prostaglandins Leukot Essent Fatty Acids* 2002;67:203–210.
28. Yeung DK, Griffith JF, Antonio GE, Lee FK, Woo J, Leung PC. Osteoporosis is associated with increased marrow fat content and decreased marrow fat unsaturation: a proton MR spectroscopy study. *J Magn Reson Imag* 2005;22:279–285.
29. Thomas MA, Yue K, Binesh N, et al. Localized two-dimensional shift correlated MR spectroscopy of human brain. *Magn Reson Med* 2001;46:58–67.
30. Prescott AP, Dzik-Jurasz AS, Leach MO, Sirohi B, Powles R, Collins DJ. Localized COSY and DQF-COSY  $^1\text{H}$ -MRS sequences for investigating human tibial bone marrow in vivo and initial application to patients with acute leukemia. *J Magn Reson Imaging* 2005;22:541–548.
31. Ernst RR, Bodenhausen G, Wokaun A. Principles of nuclear magnetic resonance in one and two dimensions. Oxford: Clarendon Press; 1987. 610 p.
32. Bottomley PA. Spatial localization in NMR spectroscopy in vivo. *Ann NY Acad Sci* 1987;508:333–348.
33. Pauly J, Le Roux P, Nishimura D, Macovski A. Parameter relations for the Shinnar-Le Roux selective excitation pulse design algorithm. *IEEE Trans Med Imaging* 1991;10:53–65.
34. Naressi A, Couturier C, Castang I, de Beer R, Graveron-Demilly D. Java-based graphical user interface for MRUI, a software package for quantitation of in vivo medical magnetic resonance spectroscopy signals. *Comput Biol Med* 2001;31:269–286.
35. Rico-Sanz J, Hajnal JV, Thomas EL, Mierisova S, Ala-Korpela M, Bell JD. Intracellular and extracellular skeletal muscle triglyceride metabolism during alternating intensity exercise in humans. *J Physiology* 1998;510:615–622.
36. Krssak M, Mlynarik V, Meyerspeer M, Moser E, Roden M.  $^1\text{H}$  NMR relaxation times of skeletal muscle metabolites at 3T. *MAGMA* 2004;6:155–159.
37. Binesh N, Yue K, Fairbanks L, Thomas MA. Reproducibility of localized 2D correlated MR spectroscopy. *Magn Reson Med* 2002;48:942–948.
38. Fleiss, J. The design and analysis of clinical experiments, New York: Wiley; 1986. 432 p.
39. Shulman GI. Cellular mechanisms of insulin resistance. *J Clin Invest* 2000;106:171–176.
40. Pan JW, Hamm JR, Rothman DL, Shulman RG. Intracellular pH in skeletal muscle by  $^1\text{H}$  NMR. *Proc Natl Acad Sci USA* 1988;85:7836–7839.



# Molecular Imaging of Solid Tumor in Small Animal Using a Dual Fluorescent and MRI Probe

Paul C. Wang, Liang Shan, Songping Wang, Alexandru Korotcov, Tongxin Wang

Department of Radiology, Howard University, Washington D.C.

## ABSTRACT

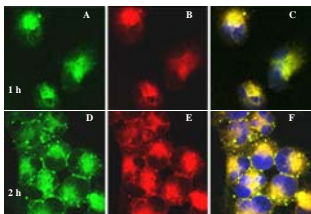
A dual molecular probe with fluorescent and magnetic reporter groups for MRI and optical imaging of tumors was developed by linkage of near-infrared (NIR) fluorescent transferrin conjugate ( $Tf^{NIR}$ ) on the surface of contrast agent (CA, Magnevist)-encapsulated cationic fluorescent liposome ( $Lip^{NBD}$ ). The efficiency of the probe was evaluated in MDA-MB-231-luc cells grown as monolayers *in vitro* and as solid tumor xenografts in nude mice. Confocal microscopy, optical imaging and MRI showed a 1.5-2 fold increase of the *in vitro* cellular uptake of both fluorescent and magnetic reporter groups from the complete probe  $Tf^{NIR}$ - $Lip^{NBD}$ -CA or  $Tf$ - $Lip^{NBD}$ -dye compared to the uptake of NIR dye,  $Lip$ -dye, CA or  $Lip$ -CA alone. The importance and specificity of the Tf moiety for targeting the probe to tumor cells was also shown by a 65% decrease in the cellular uptake of the probe reporters in cells which were pretreated with a 3-fold higher concentration of unlabeled Tf for 1 hour. Intravenous administration of the dual probe to nude mice significantly enhanced the tumor contrast in MRI and preferential accumulation of the fluorescent signal was clearly seen in optical images. The dynamic change of the probe-enhanced MRI intensity was consistent with that of the fluorescent signal accumulation in tumors and showed a left shift in signal-time curve (about 1 hour delay to achieve the maximum signal) compared to the intensity enhancement achieved by CA alone. More interestingly, the contrast enhancement in MRI showed a heterogeneous pattern within tumors, which was correlated with the tumor morphological heterogeneity. These results indicate that the newly developed dual probe enhances the tumor image contrast and is superior to CA alone for identifying the tumor pathological features on the basis of MRI, but also is suitable for NIR-based optical imaging.

## I. Preparation of the molecular dual probe: $Tf^{NIR}$ - $Lip^{NBD}$ -CA complex

The  $Tf^{NIR}$ - $Lip^{NBD}$ -CA complex was constructed using fluorescent alexa fluor® 680 conjugate of human transferrin ( $Tf^{NIR}$ ), cationic fluorescent liposome (DOTAP:DOPE+0.1% NBD-DOPE ( $Lip^{NBD}$ )) and Magnevist. The Magnevist was encapsulated within liposome particles and the  $Tf^{NIR}$  was then tagged on the particle surface. The particle sizes were controlled by sonication and repeatedly passing through polycarbonate filters. Gel-filtration through Sephadex G-50 column was used to remove un-encapsulated CA and free  $Tf^{NIR}$ . The  $Lip$ : $Tf$ :Magnevist composition was 10:12.5:0.56 (nmol/ $\mu$ g/mg).

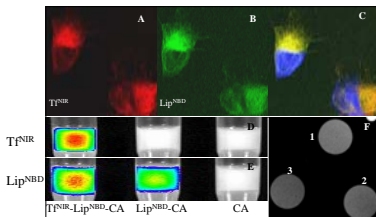
## II. Visualization of Tf- and Lip-mediated cellular uptake

### 1. Confocal microscopic observation of cellular uptake of probe reporters



Cells (MDA-MB-231-luc) were incubated with the probe  $Tf$ - $Lip^{NBD}$ -dye for 5 min to 2 h. Both  $Lip^{NBD}$  (A, D), fluorescent dye (B, E) and co-localization (C, F) were observed to be present in the cell cytoplasm as early as 5 min after incubation with the probe and their fluorescent intensity within the cytoplasm increased gradually, reaching a maximum at about 1 h incubation. Interestingly, the  $Lip^{NBD}$  and dye accumulated again, forming multiple endosomes. These endosomes were mainly located at the peripheral area of the cytoplasm and became more evident at 2 h incubation, suggesting receptor-mediated endocytosis, and release or degradation of the probe reporters through introduction of lysosomal enzymes. Cellular uptake of the dye was not evident in the cells incubated with dye alone.

### 2. Confocal, optical and MRI detection of the reporters in cells



Following 1 h incubation, cellular uptake of  $Tf^{NIR}$  (A) and  $Lip^{NBD}$  (B) were observed in cytoplasm by confocal microscopy and strong fluorescent signal of  $Tf^{NIR}$  (D) and  $Lip^{NBD}$  (E) could be detected using optical imaging in cell pellets incubated with  $Tf^{NIR}$ - $Lip^{NBD}$ -CA, but not in cells incubated with CA alone. Similarly, a stronger signal enhancement and T1 shortening were obtained in cells incubated with  $Tf^{NIR}$ - $Lip^{NBD}$ -CA and in cells incubated with  $Lip^{NBD}$ -CA (F, 1 and 2) than in cells incubated with CA alone (F, 3).

## III. Quantification of Tf- and Lip-mediated cellular uptake

The efficiency of Tf-mediated cellular uptake was evaluated following 1 h incubation of the cells with probes using optical and MR imaging. Cells incubated with the probe  $Tf^{NIR}$ - $Lip^{NBD}$ -CA showed a much greater positive contrast and T1 shortening than the cells incubated with CA alone (table 1). The cellular uptake of NIR dye and  $Lip^{NBD}$  in the cells incubated with  $Tf$ - $Lip^{NBD}$ -dye and with  $Lip^{NBD}$ -dye was significant higher than that in the cells with dye alone (table 2). Pretreatment with 3-fold higher Tf blocked 66% of the dye uptake and 71% of the  $Lip^{NBD}$  uptake (table 3). The fluorescence intensity is expressed as p/s/cm<sup>2</sup>/sr of the cell pellets.

Table 1. Comparison between probe- and CA-mediated signal enhancement

	$Tf^{NIR}$ - $Lip^{NBD}$ -CA	$Lip^{NBD}$ -CA	CA alone
Relative Intensity (10 <sup>3</sup> )	17.7±0.86	15.33±0.86	13.25±0.78
T1 relaxation time (ms)	366.7±17.1	374.3±17.3	408.1±13.8

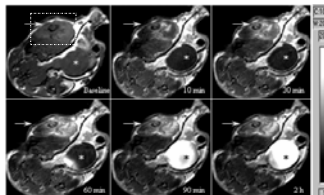
Table 2: Optical quantitation of probe-mediated cellular uptake of reporters

Reporters	$Tf$ - $Lip^{NBD}$ -dye	$Lip^{NBD}$ -dye	dye alone
NIR dye ( $\times 10^9$ )	6.88±0.59	4.99±0.51	0.23±0.006
$Lip^{NBD}$ ( $\times 10^7$ )	2.03±0.14	1.64±0.09	1.10±0.13

Table 3: Blockage of Tf-mediated uptake of reporters by Tf pretreatment

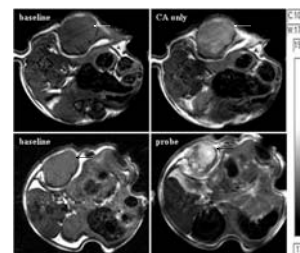
Reporters	$Tf$ - $Lip^{NBD}$ -dye untreated	$Tf$ - $Lip^{NBD}$ -dye pre-treated	$Lip^{NBD}$ -dye alone
NIR dye ( $\times 10^9$ )	3.42±0.17	2.45±0.21	1.94±0.20
$Lip^{NBD}$ ( $\times 10^7$ )	3.45±0.29	2.57±0.21	2.21±0.16

## IV. Probe-mediated signal enhancement of the tumors in vivo



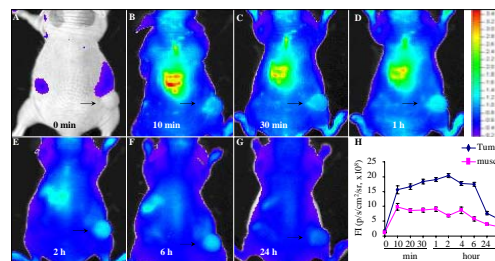
The tumor xenograft was developed by subcutaneous injection of 10<sup>7</sup> cancer cells in the lower back of athymic female nude mice. *In vivo* time course of tumor (bracket) MRI after i.v. administration of the probe  $Tf^{NIR}$ - $Lip^{NBD}$ -CA, showing gradually increased enhancement of the tumor signal (arrow) and heterogeneous enhancement pattern within tumor. \* bladder.

## V. Comparison of signal enhancement by CA alone and by $Tf^{NIR}$ - $Lip^{NBD}$ -CA



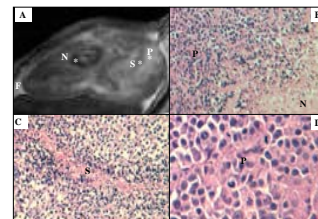
A stronger and heterogeneous signal enhancement of the tumor (arrow) was achieved with  $Tf^{NIR}$ - $Lip^{NBD}$ -CA over CA alone. The MR images were from the same tumor with an interval of 72 h between studies with the probe and with CA alone.

## VI. Optical detection of the tumor after i.v. administration of $Tf^{NIR}$ - $Lip^{NBD}$ -CA



A preferential accumulation of fluorescent signal was observed in tumors. The fluorescence signal was detectable as early as 10 min and reached a maximum at about 2 h and then decreased gradually. FI, fluorescent intensity.

## VII. Comparison between MRI signal enhancement and pathological findings



The probe-mediated enhancement pattern in MRI was well correlated with the pathological findings (HE stain). Panel A is a representative MR image showing heterogeneous enhancement pattern. Panel B shows a region with high proliferation and necrosis (x 250). Panel C shows the stromal tissue (x 250) and panel D shows the proliferating tumor cells with high mitotic activity (x 400). P, proliferating cells; N, necrosis; S, stromal tissue; F, fat tissue.

ACKNOWLEDGMENTS: This work was supported by Grant Number 2G12RR003048 from the National Center for Research Resources (NCRR), a component of the NIH. This study was also supported by the grants: USAMRMC W81XWH-05-1-0291, and NIH 5U54CA091431.





# Targeted DCE-MRI for imaging and characterization of Solid Tumor Xenografts

Alexandru V. Korotcov,<sup>a</sup> Liang Shan,<sup>a</sup> Songping Wang,<sup>a</sup> Tongxin Wang,<sup>a</sup> Rajagopalan Sridhar,<sup>b</sup> Zaver M. Bhujwalla,<sup>c</sup> and Paul C. Wang<sup>a</sup>

<sup>a</sup>Department of Radiology and <sup>b</sup>Department of Radiation Oncology, Howard University, Washington D.C.

<sup>c</sup>Department of Radiology, Johns Hopkins University School of Medicine, Baltimore MD.

## ABSTRACT

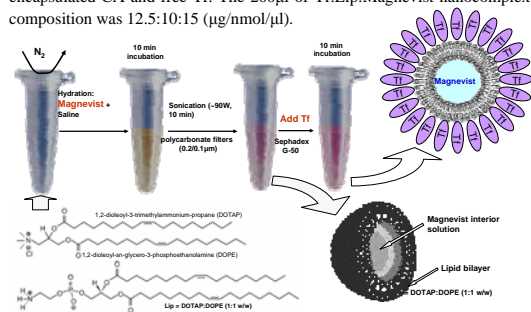
The advances in MRI imaging techniques have led to the increasing use of parametric images, which are designed to display the physiological, pathological and morphological features of tissue in one experiment. The dynamic contrast enhancement MRI (DCE-MRI) involves the acquisition of a series of MR images before, during and after an intravenous (iv) injection of a contrast agent (CA). After iv injection the contrast agent is distributed only in the extracellular space through passive diffusion. Contrast agent doesn't accumulate in normal cells, and is rapidly excreted in the urine. The distribution of CA is generally nonspecific.

The development of liposomes tumor-specific targeting drug delivery has the potential to deliver imaging contrast agents more effectively than is currently achievable. A cell membrane receptor transferrin (TfR) is known to be overexpressed in 74% of breast carcinomas, 76% of lung adenocarcinomas and 93% of lung squamous cell carcinomas. The expression level of TfR receptor is of great value in grading tumors and determining prognosis. There are two goals in this study: (1) to develop a liposome-Tf nanocomplex as MRI probe for systematic delivery of the conventional gadolinium based CA to tumors and (2) to analyze the relationship between MRI dynamic contrast enhancement pattern and tumor pathology after administration of the newly developed probes with CA. We have constructed liposome (Lip) nanoparticles modified with Tf on the surface as a ligand for specific targeting and CA (Magnevist) inside as the payload. These components together formed a liposomal nanocomplex, Tf-Lip-Magnevist, with a diameter less than 100 - 120 nm. *In vitro* analysis demonstrated that the Tf-Lip-Mag nanocomplex dramatically improved the uptake of CA in monolayer cultures of MDA-MB-231-luc human breast cancer and in PC-3-luc cells through both receptor- and Lip-mediated endocytosis. *In vivo*, the probe significantly enhanced the MRI signals, and was superior to the use of clinical MRI CA alone. The DCE-MRI exhibits the heterogeneous signal enhancement by the liposomal nanocomplex probe and it correlates well with the pathology of the tumors.

We have demonstrated that our newly developed probes, Tf-Lip-Magnevist, increases the sensitivity and specificity of MRI. It also shows the ability of identifying the tumor pathological features based on the DCE-MRI pattern. The results indicate that the Tf-Lip-Magnevist nanocomplex has the potential for improving cancer detection and tumor characterization.

### I. Preparation of the liposomal nanocomplex probe

The Tf-Lip-Magnevist complex (~ 100-120 nm) was constructed using human transferrin (Tf), cationic liposome (DOTAP:DOPE) and Magnevist. The Magnevist was encapsulated within liposome particles and the Tf was then tagged on the particle surface. The particle sizes were controlled by sonication and repeatedly passing through polycarbonate filters. Gel-filtration through Sephadex G-50 column was used to remove un-encapsulated CA and free Tf. The 200µl of Tf-Lip:Magnevist nanocomplex composition was 12.5:10:15 (µg/nmol/µl).

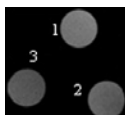


### II. Visualization and Quantification of Tf- and Lip-mediated cellular uptake

The efficiency of Tf-mediated cellular uptake was evaluated following one hour incubation of the cells with nanocomplex probes using MRI. Cells incubated with the Tf-Lip-Magnevist showed a much greater positive contrast and T1 shortening than the cells incubated with Magnevist alone (table 1).

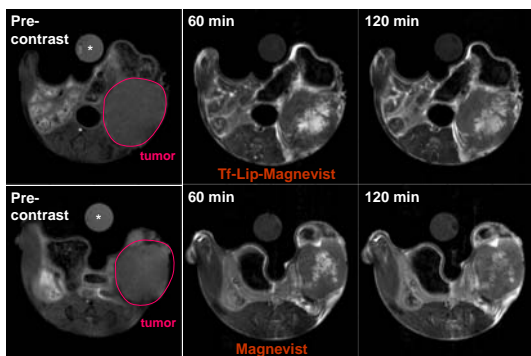
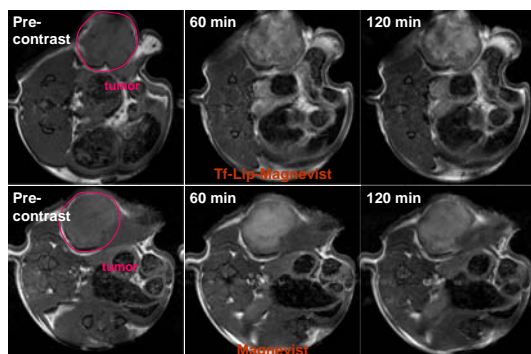
Table 1. Comparison between Tf-Lip-Magnevist, Lip-Magnevist and Magnevist mediated signal enhancement

	Tf-Lip-Magnevist	Lip-Magnevist	Magnevist alone
Relative Intensity (10 <sup>3</sup> ):	17.7±0.86	15.33±0.86	13.25±0.78
T1 relaxation time (ms):	366.7±17.1	374.3±17.3	408.1±13.8



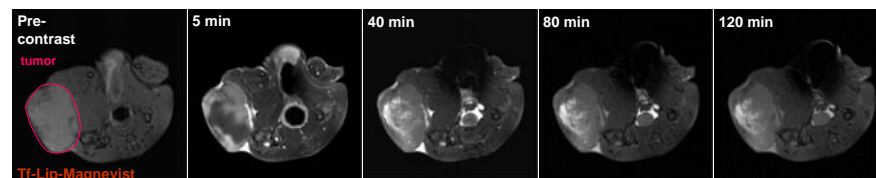
A stronger signal enhancement and T1 shortening obtained in cells incubated with Tf-Lip-Magnevist indicates the importance and specificity of Tf moiety for targeting and illustrating the probe internalization into tumor cells *in vitro*.

### III. Comparison of signal enhancement by Tf-Lip-Magnevist and Magnevist alone



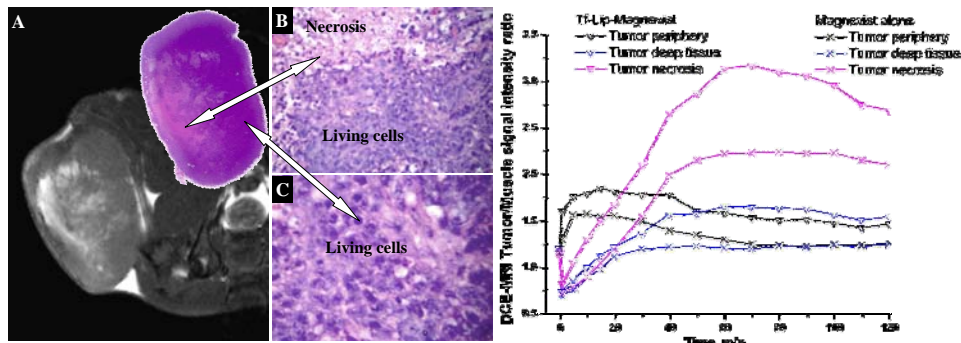
A stronger and heterogeneous signal enhancement of the tumor was achieved with Tf-Lip-Magnevist over Magnevist alone. The MR images were from the same tumors (MDA-MB231-luc and PC-3-luc) with an interval of 48 h between studies with the Tf-Lip-Magnevist nanocomplex and with Magnevist alone. \* 0.9% saline

### IV. Probe-mediated signal enhancement of the tumor in vivo



*In vivo* DCE-MRI followed iv administration of the Tf-Lip-Magnevist nanocomplex shows gradually increased enhancement of the tumor signal and heterogeneous enhancement pattern within tumor. During the first 10 minutes after iv administration of the Tf-Lip-Magnevist nanocomplex the enhancement is observed in the peripherals parts of the tumor and is gradually distributed into the central part of the tumor. Eventually the central part becomes more enhanced than the other parts of the tumor and reaches the maximum enhancement at 60-80 minutes after injection.

### V. Comparison between DCE-MRI and pathological findings



The probe-mediated enhancement pattern in MRI was well correlated with the pathological findings (HE stain, inset on panel A). Panel A is a representative MR image showing heterogeneous enhancement pattern. Panel B shows a region with high proliferation and necrosis (x 250). Panel C shows the proliferating tumor cells with high mitotic activity (x 400). The DCE-MRI curves show the different enhancement patterns correlated with the different pathological features based on specifically enhanced MRI induced by the liposomal nanocomplex and Magnevist alone.

**Research Funded by:** This work was supported by DoD USAMRMC W81XWH-05-1-0291, Charles and Mary Latham Fund (#7023185), and 2G12 RR003048 from the RCMI Program, Division of Research Infrastructure, National Center for Research Resources, NIH.

# Targeted Fluorescent Liposome Nanoparticles for Molecular Imaging of Breast Cancer Xenografts in Mouse

Liang Shan<sup>1</sup>, Songping Wang<sup>1</sup>, Yanfei Zhou<sup>2</sup>, Alexandru Korotcov<sup>1</sup>, Renshu Zhang<sup>3</sup>, Tongxin Wang<sup>1</sup>, Rajagopalan Sridhar<sup>3</sup>, Zaver M. Bhujwalla<sup>4</sup> and Paul C. Wang<sup>1</sup>

<sup>1</sup>Department of Radiology, <sup>2</sup>Oral Diagnostic Service, and <sup>3</sup>Department of Radiation Oncology, Howard University, Washington DC; <sup>4</sup>Department of Radiology, Johns Hopkins University, Baltimore, MD  
<http://www.howard.edu/medicine/radiology/ml/index.html>

**Background and objectives:** Molecular imaging is developed on the basis of the concept that targeted delivery of contrast agents can specifically increase the detection sensitivity by targeting the difference in ‘molecular properties’ between cancer and normal tissues. Transferrin receptor (TfR) is a cell-membrane internalizing receptor, which is overexpressed in various human malignancies including breast cancer. It is a potential target for targeted imaging. Herein, we developed a fluorescent liposome nanoparticles targeting TfR for optical imaging of human breast cancer xenografts in mice. **Methods:** The targeted fluorescent liposome nanoparticles were constructed using near-infrared (NIR) fluorescent transferrin conjugate (Tf<sup>NIR</sup>), NIR fluorescent dyes and fluorescently labeled (NBD) cationic liposomes (Lip<sup>NBD</sup>). NIR dyes were first encapsulated in the Lip<sup>NBD</sup> to yield NIR-loaded liposomes (Lip<sup>NBD</sup>-dye). They were then linked to Tf<sup>NIR</sup> to obtain targeted fluorescent liposome nanoparticles (Tf<sup>NIR</sup>-Lip<sup>NBD</sup>-dye). The binding and internalization of the nanoparticles were first analyzed in MDA-MB-231-luc breast cancer cells using confocal microscopy and flow cytometry. The imaging feasibility was then tested in solid tumor xenografts in nude mice using Xenogen optical imaging system. **Results:** Confocal microscopy showed endocytosis of the fluorescent reporters from transferrin (Tf), liposome particles and encapsulated dyes, separately, following incubation of the MDA-MB-231-luc cells with the nanoparticles. Pretreatment with Tf blocked the cellular uptake of the reporters indicating the importance and specificity of the Tf moiety for targeting. Quantification using flow cytometry revealed a 1.8, 7.0 and 16 fold higher fluorescence intensity in cells incubated for 1 hour with Tf<sup>NIR</sup>, Lip<sup>NBD</sup>-dye, and Tf<sup>NIR</sup>-Lip<sup>NBD</sup>-dye, separately, than in control cells without probes (all p<0.05). Systemic administration of Tf<sup>NIR</sup> alone showed a preferential accumulation of the fluorescent signal in tumor xenografts produced in the lower back of nude mice. The fluorescent signal was clearly detectable at 10 min in tumors and reached the maximum intensity at 90-120 min after injection. The ratio of the signal from tumor to background from muscle ranged from 1.64 to 3.14, depending on the tumor sizes. Application of the Tf<sup>NIR</sup>-Lip<sup>NBD</sup>-dye nanoparticles further increased the signal from tumor to background ratio by up to 30 % compared to Tf<sup>NIR</sup> alone. Importantly, Tf<sup>NIR</sup>-Lip<sup>NBD</sup>-dye system is superior to Tf<sup>NIR</sup> alone for imaging small tumors (<3 mm in diameter). **Conclusion:** Our results indicate that TfR is a promising target for molecular imaging. Both Tf<sup>NIR</sup> and Tf<sup>NIR</sup>-Lip<sup>NBD</sup>-dye are potentially useful for visualizing human breast cancer in clinic. Tf<sup>NIR</sup>-Lip<sup>NBD</sup>-dye is superior to Tf<sup>NIR</sup> alone for imaging small tumors because of better delivery of fluorescent contrast agents to the tumors.

## I. Preparation of the molecular probe: Tf<sup>NIR</sup>-Lip<sup>NBD</sup>-dye complex

The Tf<sup>NIR</sup>-Lip<sup>NBD</sup>-dye complex was constructed using fluorescent Alexa Fluor® 680 conjugate of human transferrin (Tf<sup>NIR</sup>), cationic fluorescent liposome (DOTAP:DOPE+0.1% NBD-DOPE (Lip<sup>NBD</sup>)) and Alexa Fluor® 680. Pre-mixed Lip<sup>NBD</sup> in chloroform (3.607  $\mu$ l) was dried under a nitrogen stream and hydrated by adding 50  $\mu$ l water containing 5  $\mu$ l (2  $\mu$ g/ $\mu$ l) of Alexa Fluor 680 fluorophore. The hydrated Lip<sup>NBD</sup>-dye mixture was homogenized using a vortex generator and incubated for at least 20 minutes (min) for complete reaction. The volume of the mixture was adjusted to 175  $\mu$ l with water. The mixture was then down-sized by sonication (80-90 W, 10 min) in a water bath. The Tf<sup>NIR</sup> was then tagged on the surface of liposomes. Gel-filtration through Sephadex G-50 column was used to remove un-encapsulated free dye and free Tf<sup>NIR</sup>. The final volume for animal use was 200  $\mu$ l and Lip:Tf:dye composition was 10:12.5:10 (nmol/ $\mu$ g/ $\mu$ g). Fluorescent dye-encapsulated liposome (Lip<sup>NIR</sup>) was similarly prepared, but Tf<sup>NIR</sup> was omitted.

## II. Confocal, Flow cytometric, optical and MRI detection of the reporters in culture cells

Breast cancer cells MDA-MB-231-luc were used in this study. The cells are stably transfected with luciferase gene and express high level of luciferase. The efficiency of Tf-mediated cellular uptake was first observed under confocal microscopy. Cells were incubated with the probe Tf<sup>NIR</sup>-Lip<sup>NBD</sup> for 5 min to 2 h. Both Tf<sup>NIR</sup> (Fig. 1A, 1D) and Lip<sup>NBD</sup> (Fig. 1B, 1E) were observed to be present in the cell cytoplasm as early as 5 min. The fluorescent intensity from both Tf<sup>NIR</sup> and Lip<sup>NBD</sup> increased gradually and reached the maximum at about 1 h incubation. Later, they accumulated again to form multiple endosomes which were mainly located at the peripheral area of the cytoplasm and became more evident at 2 h incubation. This process suggests receptor-mediated endocytosis, and lysosomal enzyme involvement in degradation of the probe reporters.

The efficiency was then evaluated using flow cytometry and optical imaging following 1 h incubation of the cells with probes Tf<sup>NIR</sup>, Lip<sup>NBD</sup>-dye, and Tf-Lip<sup>NBD</sup>-dye, separately. Flow cytometry showed that the GeoMean of the cell fluorescent intensity for Tf<sup>NIR</sup>, Lip<sup>NBD</sup>-dye, and Tf-Lip<sup>NBD</sup>-dye was 1.8, 7.0 and 16 folds higher compared with untreated controls (p<0.05) (Fig. 2). Using optical imaging, the cellular uptakes of NIR dye and Lip<sup>NBD</sup> in the cells incubated with Tf-Lip<sup>NBD</sup>-dye and with Lip<sup>NBD</sup>-dye were significant higher than that in the cells with dye alone (table 1). Pretreatment with 3-fold higher Tf blocked 65.6% of the dye uptake and 70.97% of the Lip<sup>NBD</sup> uptake (table 2). The fluorescence intensity is expressed as p/s/cm<sup>2</sup>/sr of the cell pellets.

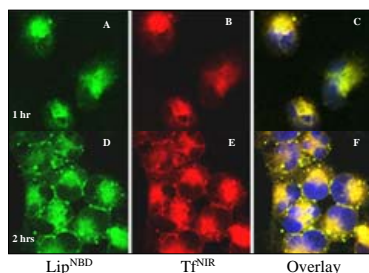


Fig. 1

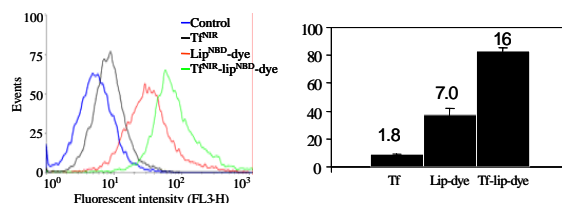


Fig. 2

Table 1: Optical quantitation of probe-mediated cellular uptake of reporters

Reporters	Tf-Lip <sup>NBD</sup> -dye	Lip <sup>NBD</sup> -dye	dye alone
NIR dye (x 10 <sup>6</sup> )	6.88±0.59	4.99±0.51	0.23±0.006
Lip <sup>NBD</sup> (x 10 <sup>7</sup> )	2.03±0.14	1.64±0.09	1.10±0.13

Table 2: Blockage of Tf-mediated uptake of reporters by Tf pretreatment

Reporters	Tf-Lip <sup>NBD</sup> -dye untreated	Tf-Lip <sup>NBD</sup> -dye pre-treated	Lip <sup>NBD</sup> -dye alone
NIR dye (x10 <sup>6</sup> )	3.42±0.17	2.45±0.21	1.94±0.20
Lip <sup>NBD</sup> (x10 <sup>7</sup> )	3.45±0.29	2.57±0.21	2.21±0.16

## III. Dynamics of Tf<sup>NIR</sup>-based fluorescent signals in tumor xenografts

We first checked the imaging efficiency and dynamics of Tf<sup>NIR</sup> alone in 3 animals with tumors in each side of the lower back and in 9 mice with tumors only in the right side of low back to minimize potential influence of two tumors each other from same mouse. A preferential accumulation of the fluorescent signals was clearly detectable as early as 10 min in most tumors and the tumor signal was rapidly increased and then gradually decreased over time (Figure 3, upper panel). The time to reach the maximum fluorescent signal (peak time) varied from 72 to 230 min, showing a significant difference among tumors in different animals. The background fluorescence showed rapid increase and decrease. A similar dynamic change of bioluminescent signal was also observed among tumors. Following intraperitoneal administration of D-luciferin, the signal could be detected within 2 min and showed rapid increase and then decrease (Figure 3, lower panel). In majority of the tumors, the signal became undetectable within 60 min. The peak time reaching maximum signal in tumors varied from 6 to 26 min, which was significantly different among tumors in different animals.

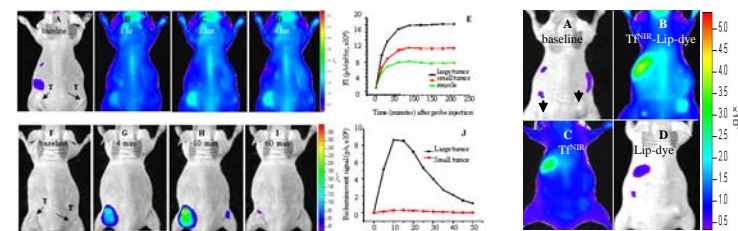


Fig. 3

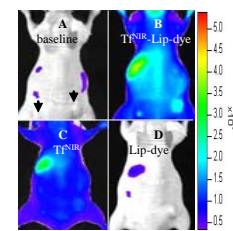


Fig. 4

## IV. Enhancement of tumor signal by application of Tf<sup>NIR</sup>-Lip<sup>NBD</sup>-dye complexes

The fluorescent intensity following administration of Tf<sup>NIR</sup> was related to the tumor sizes. The tumor to normal tissue (contralateral muscle) ratio varied from 1.3 to 3.4, which was related to the size of tumors. For small tumors, it is difficult to be visualized. Increased amount of Tf<sup>NIR</sup> to mice resulted in significantly high background with limited enhancement of the signal in small tumors. To specifically increase the tumor signal, a new strategy using Tf<sup>NIR</sup>-Lip<sup>NBD</sup>-dye complex was applied. Intravenous administration of the complex increased both the tumor signal and background. The dynamics of the signal in tumors was similar to that using Tf<sup>NIR</sup> alone, but use of Tf<sup>NIR</sup>-Lip<sup>NBD</sup>-dye complexes further increased the tumor to normal tissue ratio by 1-30 % (Figure 4). Small tumors (<3 mm in diameter) could be visualized clearly.

## V. Conclusions:

1. We have constructed the fluorescent probes, Tf<sup>NIR</sup> and Tf<sup>NIR</sup>-Lip<sup>NBD</sup>-dye, for optical imaging of breast cancer.
2. Endocytosis of the fluorescent reporters was observed by confocal microscopy following incubation of the MDA-MB-231-luc cells with the probes.
3. Flow cytometry confirmed the targeting effect of Tf and nonspecific enhancement by Lip on the endocytosis of reporters.
4. Pretreatment with Tf blocked the cellular uptake of the reporters indicating the importance and specificity of the Tf moiety for targeting.
5. Tumors were clearly detected by systemic administration of Tf<sup>NIR</sup> using Xenogen optical imaging system. Application of the Tf<sup>NIR</sup>-Lip<sup>NBD</sup>-dye nanoparticles further enhanced the efficacy in tumor detection, particularly for small tumors.

**ACKNOWLEDGEMENT:** This work was supported by the grants: USAMRMC W81XWH-05-1-0291, 2 G12 RR003048 from the RCMI Program, Division of Research Infrastructure, National Center for Research Resources, and NIH 5U54 CA091409-06.





# A Molecular Probe Tf<sup>NIR</sup>-Lip<sup>NBD</sup>-CA for MRI and Optical Imaging of Breast Cancer

Paul C. Wang<sup>1</sup>, Songping Wang<sup>1</sup>, Alexandru Korotcov<sup>1</sup>, Tongxin Wang<sup>1</sup>, Liang Shan<sup>1</sup>, Rajagopalan Sridhar<sup>2</sup>, Zaver M. Bhujwala<sup>3</sup>

<sup>1</sup>Department of Radiology and <sup>2</sup>Department of Radiation Oncology, Howard University, Washington D.C.

<sup>3</sup>Department of Radiology, Johns Hopkins University School of Medicine, Baltimore MD.

<http://www.howard.edu/medicine/radiology/mil/>

**ABSTRACT:** Conventional imaging modalities such as CT and MRI exploit the differences of the physical properties between the normal and malignant tumor tissues. These differences are often insufficient for obtaining good image contrast. In order to improve the image contrast and low sensitivity of MRI, a large amount of contrast agent is often needed. In recent years, several targeted MRI contrast agent delivery systems have been developed to improve the signal-to-noise ratio of image based on exploiting the differences of the molecular properties between cancerous and normal tissues. Another imaging modality, optical imaging, offers several advantages over CT or MRI. It is simple to use, highly sensitive, and no ionizing radiation. Optical imaging has been used for *in vivo* evaluation of gene expression, monitoring of gene delivery and real-time intraoperative visualization of tumor margins and metastatic lesions. Limited depth of light penetration and lack of tomographic information prevent *in vivo* efficiency of optical imaging. We have developed a dual molecular probe with fluorescent and magnetic reporter groups for MRI and optical imaging of tumors. This probe contains a near-infrared fluorescent transferrin conjugate on the surface of a cationic fluorescent liposome, which encapsulates MRI contrast agent. The efficiency of the probe was evaluated by MDA-MB-231-luc breast cancer cells grown as monolayers *in vitro* and as solid tumor xenografts in nude mice. The results from these studies demonstrate that this newly developed dual nano probe enhances the tumor MRI image contrast and it is superior than using MRI contrast agent alone for identifying the tumor pathological features. This probe also provides high sensitivity for near infrared (NIR)-based optical imaging. Due to the superior sensitivity and specificity, this newly developed nano probe has a great potential to be used for early detection of cancers and evaluating drug delivery in general.

## I. Preparation of the molecular probe: Tf<sup>NIR</sup>-Lip<sup>NBD</sup>-CA complex

The Tf<sup>NIR</sup>-Lip<sup>NBD</sup>-CA complex was constructed using fluorescent alexa fluor® 680 conjugate of human transferrin (Tf<sup>NIR</sup>), cationic fluorescent liposome (DOTAP:DOPE+0.1% NBD-DOPE (Lip<sup>NBD</sup>)) and MRI contrast agent (CA), Magnevist. The CA was first encapsulated within liposomes and the Tf<sup>NIR</sup> was then tagged on the surface of liposomes. The size of liposome was dictated by sonication and repeatedly passing through polycarbonate filters (100 nm in diameter). Gel-filtration through Sephadex G-50 column was used to remove un-encapsulated CA and free Tf<sup>NIR</sup>. The Lip:Tf:Magnevist composition was 10:12.5:0.56 (nmol/μg/mg).

## II. Confocal, Flow cytometric, optical and MRI detection of the reporters in culture cells

Breast cancer cells MDA-MB-231-luc were used in this study. The cells are stably transfected with luciferase gene and express high level of luciferase. The efficiency of Tf-mediated cellular uptake was first observed under confocal microscopy. Cells were incubated with the probe Tf<sup>NIR</sup>-Lip<sup>NBD</sup>-CA for 5 min to 2 h. Both Tf<sup>NIR</sup> (Fig. 1A, 1D) and Lip<sup>NBD</sup> (Fig. 1B, 1E) were observed to be present in the cell cytoplasm as early as 5 min. The fluorescent intensity from both Tf<sup>NIR</sup> and Lip<sup>NBD</sup> increased gradually and reached the maximum at about 1 h incubation. Later, they accumulated again to form multiple endosomes which were mainly located at the peripheral area of the cytoplasm and became more evident at 2 h incubation. This process suggests receptor-mediated endocytosis, and lysosomal enzyme involvement in degradation of the probe reporters.

The efficiency was then evaluated using flow cytometry and optical imaging following 1 h incubation of the cells with probes Tf<sup>NIR</sup>, Lip<sup>NBD</sup>-dye, and Tf-Lip<sup>NIR</sup>-dye, separately. Flow cytometry showed that the GeoMean of the cell fluorescent intensity for Tf<sup>NIR</sup>, Lip<sup>NBD</sup>-dye, and Tf-Lip<sup>NIR</sup>-dye was 1.8, 7.0 and 16 folds higher compared with untreated controls ( $p < 0.05$ ) (Fig. 2). Using optical imaging, the cellular uptakes of NIR dye and Lip<sup>NBD</sup> in the cells incubated with Tf-Lip<sup>NBD</sup>-dye and with Lip<sup>NBD</sup>-dye were significant higher than that in the cells with dye alone (Fig. 1G and 1H and table 1). Pretreatment with 3-fold higher Tf blocked 65.6% of the dye uptake and 70.97% of the Lip<sup>NBD</sup> uptake (table 2). The fluorescence intensity is expressed as p/s/cm<sup>2</sup>/sr of the cell pellets.

The cellular uptake of CA was analyzed using MRI. Strong signal enhancement and T1 shortening (table 3) were observed in cells incubated with Tf<sup>NIR</sup>-Lip<sup>NBD</sup>-CA compared with that in cells incubated with Lip<sup>NBD</sup>-CA (Fig. 1I and 1J) and in cells incubated with CA alone (Fig. 1I, 1J).

Table 1: Optical quantitation of probe-mediated cellular uptake of reporters

Reporters	Tf-Lip <sup>NBD</sup> -dye	Lip <sup>NBD</sup> -dye	dye alone
NIR dye ( $\times 10^9$ )	6.88±0.59	4.99±0.51	0.23±0.006
Lip <sup>NBD</sup> ( $\times 10^7$ )	2.03±0.14	1.64±0.09	1.10±0.13

Table 2: Blockage of Tf-mediated uptake of reporters by Tf pretreatment

Reporters	Tf-Lip <sup>NBD</sup> -dye untreated	Tf-Lip <sup>NBD</sup> -dye pre-treated	Lip <sup>NBD</sup> -dye alone
NIR dye ( $\times 10^9$ )	3.42±0.17	2.45±0.21	1.94±0.20
Lip <sup>NBD</sup> ( $\times 10^7$ )	3.45±0.29	2.57±0.21	2.21±0.16

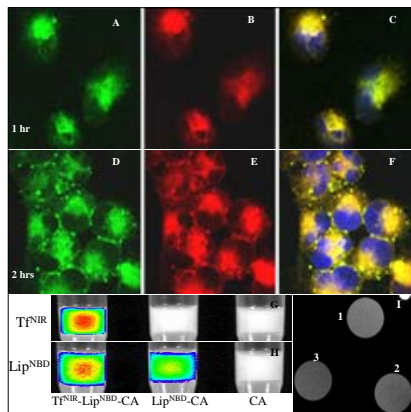


Fig. 1

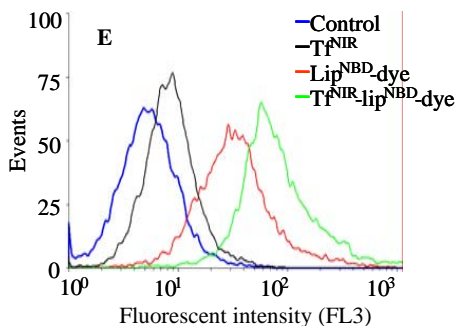


Fig. 2

Table 3. Comparison between probe- and CA-mediated signal enhancement

	Tf <sup>NIR</sup> -Lip <sup>NBD</sup> -CA	Lip <sup>NBD</sup> -CA	CA alone
Relative Intensity ( $10^5$ )	17.7±0.86	15.33±0.86	13.25±0.78
T1 relaxation time (ms)	366.7±17.1	374.3±17.3	408.1±13.8

## III. Probe-mediated MRI contrast enhancement in animal models of human breast cancer

The solid tumor xenograft model was developed by subcutaneous injection of  $1 \times 10^7$  subconfluent cells in 100  $\mu$ l DPBS in the lower back of female athymic nude mice (8-10 weeks old). The probe was evaluated in a total of 10 nude mice bearing tumors from 0.4 to 1.2 cm in diameter.

Intravenous administration of the probe Tf<sup>NIR</sup>-Lip<sup>NBD</sup>-CA significantly enhanced the tumor image contrast. The enhancement was observed as early as 10 min and increased gradually, reaching the maximum at 90 min to 2 h (Fig. 3, lower panel). After that, gradual decrease of the signal enhancement was observed. Interestingly, the enhancement was greatly heterogeneous within the tumors. The signals from strongly enhanced region decreased much slower than the signals from region with weak enhancement. For small tumors, the enhancement was relatively uniform and usually observed starting from peripheral area.

Magnevist alone slightly enhanced the image contrast of tumors compared to the baseline images. The maximum enhancement was observed usually at 30 to 60 min after injection. The image contrast enhancement started from peripheral area to the center of tumors and was relatively uniform within tumors (Fig. 3, upper panel). The signal enhancement decreased rapidly and returned to baseline within 3 h.

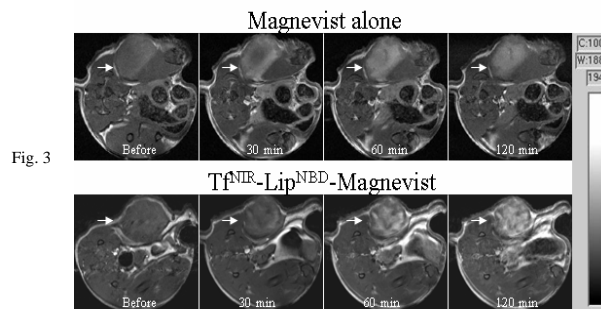


Fig. 3

## IV. Optical detection of the tumor after i.v. administration of Tf<sup>NIR</sup>-Lip<sup>NBD</sup>-CA

Fluorescent imaging: Fluorescent signals of the tumors were clearly detectable as early as 10 min after i.v. injection of the probe Tf<sup>NIR</sup>-Lip<sup>NBD</sup>-CA and reached the maximum intensity at about 90 min to 2 h (Fig. 4, upper panel). The fluorescent intensity was related to the tumor sizes. For large tumors (> 0.8 cm in diameter), significant fluorescent signals were still detectable after 2 days. The background fluorescence showed rapid increase and decrease. The tumor to normal tissue (contralateral muscle) ratio varied from 1.3 to 3.4, which was related to the size of tumors. Fig. 4 lower panel shows the bioluminescent imaging of tumors: The bioluminescent signal intensity from the tumors gradually increased and then decreased over time within 1 hour following administration of D-luciferin.

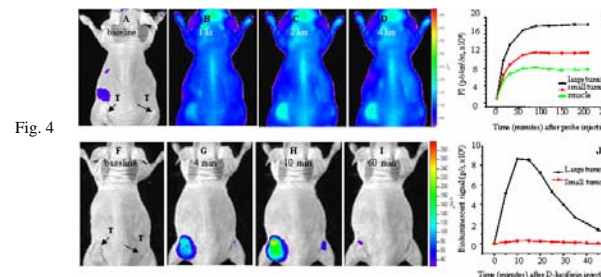


Fig. 4



# Surface Coating and Bioconjugation of Quantum Dots for Non-invasive Detection of Breast Cancer

Tongxin Wang,<sup>a</sup> Liang Shan,<sup>a</sup> Alexandru Korotcov,<sup>a</sup> Songping Wang,<sup>a</sup> Yanfei Zhou,<sup>b</sup> Rajagopalan Sridhar,<sup>c</sup> and Paul Wang<sup>a</sup>

<sup>a</sup>Molecular Imaging Laboratory, Department of Radiology, <sup>b</sup>Oral Diagnostic Service, and <sup>c</sup>Department of Radiation Oncology, Howard University, Washington, DC

**ABSTRACT.** Optical imaging is a promising technique for early diagnosis of cancer. Developing an optical imaging contrast agent with high sensitivity and specificity is critical for early diagnosis. In this research, we designed QDs conjugated with transferrin (Tf) as an optical imaging agent for breast cancer detection with high sensitivity and specificity. QD is chosen to improve detection sensitivity due to its great extinction coefficient and emission of bright light in comparison to the organic fluorescent dyes. Transferrin was used as a ligand specifically targeting the overexpressed transferrin receptors on the MDA-MB-231 breast cancer cells. The two-step carbodiimide chemistry process was used to obtain the QDs-transferrin conjugation. First, Carboxylated QDs were activated by excess EDC and sulfo-NHS at pH 6.5. Then the excess EDC and sulfo-NHS was removed by Sephadex™. Later, the activated QDs were conjugated with transferrin at pH 8.3, and further purified by gel filtration. A controlled experiment from Tf-Alexa Fluor conjugate was used to confirm the conjugation. The successful linkage of transferrin to QDs was demonstrated by SDS-PAGE gel electrophoresis. *In vitro* uptake of QDs-Tf by MDA-MB-231 cells was confirmed by cellular labeling combined with flow cytometry. In addition, novel multi-dentate block copolymers were synthesized via an atom transfer radical polymerization and will be used for surface coating of QDs to improve their stability and biocompatibility under harsh in vivo conditions.

## I. Synthesis of Quantum Dots

ZnS coated CdSe quantum dots were selected for surface coating because of a well-established synthetic approach in literatures. The QD was synthesized via a solution method at high temperature (200-350°C) from cadmium oxide and selenium. TOPO (triethyl phosphine oxide) was used as ligand to stabilize QD. CdSe nanocrystals were nucleated and grown by mixing TOPO-Cd<sup>2+</sup> solution and TOP-Se solution at around 300 °C. Then a thin ZnS layer was grown on the surface of CdSe at around 220 °C. In order to remove the TOPO thoroughly, the prepared QDs were purified by reprecipitation from toluene and methanol. Eventually, the TOPO ligands on the surface of QDs were replaced by tri-block copolymers with multi-dentate thiol groups via surface exchange reactions. The hydrodynamic diameter of QD in solution was characterized around 22.8 nm by dynamic light scattering (DLS). This kind of QD has a relatively high fluorescent intensity when using DsRed excitation and emission filters (Fig. 1).

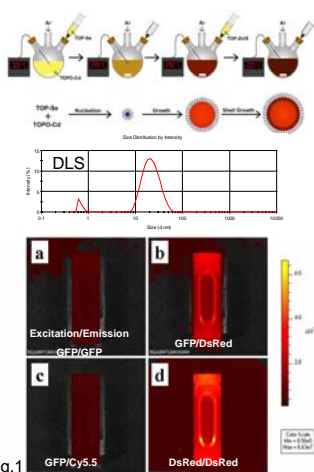


Fig.1

## II. Conjugation of QDs with Transferrin

Transferrin was used as a ligand specifically targeting the overexpressed transferrin receptors on the MDA-MB-231 breast cancer cells. The conjugation of transferrin with QDs was first performed on commercially available QDs. The two-step carbodiimide chemistry process was used to obtain the QD-transferrin conjugation (Fig. 2). Carboxylated QDs were first activated by excess EDC and sulfo-NHS at pH 6.5. Then the excess EDC and sulfo-NHS were removed by Sephadex™. Later, the activated QDs were conjugated with transferrin at pH 8.3, and further purified by gel filtration. Controlled experimentation of Tf-Alexa Fluor conjugate has confirmed the conjugation between QD and Tf. The successful linkage of transferrin to QDs was demonstrated by SDS-PAGE gel electrophoresis. The migration of QD-Tf and QD-Tf-Alexa conjugates are different from free QDs (Fig. 2).

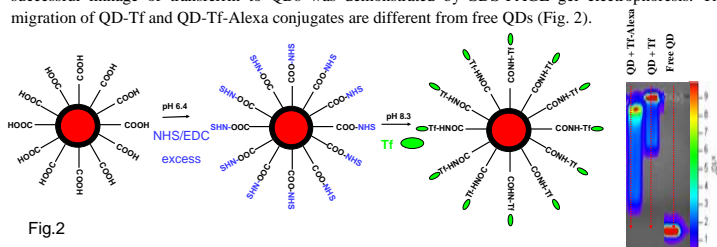


Fig.2

## III. Synthesis of multi-dentate polymer for QDs coating

Bi-dentate thiol was proved to have a better effect to stabilizing QDs than mono-dentate thiol. It is expected that multi-dentate thiol would have a much better stabilizing effect than bi-dentate thiol. In this research, we designed a novel triblock copolymer with multi-dentate thiol groups. The block copolymer has a polycarboxylic acid and polythiol block at both ends and a middle poly(styrene/divinyl benzene) block. The multiple mercapto groups of the polythiol block were used as multi-dentate ligands to stabilize quantum dot nanoparticles, while the polycarboxylic acid block allowed reaction sites to modify or conjugate quantum dots with functional biomacromolecules. The dense and compact hydrophobic intermediate shell formed from a cross-linked poly(styrene/divinyl benzene) block will efficiently prohibit other molecules from diffusing across the macromolecular shell to react with and decompose quantum dots. QD stabilized multi-dentate thiols are expected to be more stable than those coated with mono-dentate thiols (e.g. 11-mercaptoundecanoic acid).

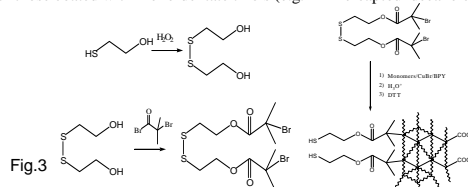


Fig.3

The polymer was synthesized via an atom transfer radical polymerization (Fig. 3). First, a sulfur containing initiator was synthesized. Second, successive polymerization from monomers (i.e. styrene (STR)), divinyl benzene (DVB) and t-butyl acrylate (TBA) was used to generate these blocks. Third, controlled hydrolysis and reduction by DTT (Dithiothreitol) was used to generate carboxylic and thiol groups. Gel permeation chromatography shows that the molecular weights can be controlled by adjusting monomer ratio, polymerization temperature and time (Fig. 4). More DVB monomers and longer polymerization time lead to higher molecular weights, indicated by a shorter elution time, due to the cross-linking effect. The higher molecular weights, indicated by a shorter elution time, are a result of the addition of TBA and confirm the growth of the TBA block from the poly(STR-DVB) block.

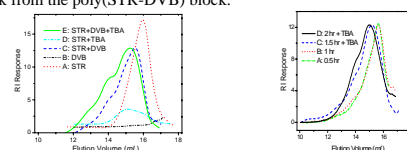


Fig.4

## IV. Labeling of breast cancer cell (MDA-MB-231) with QD-Tf conjugates and flow cytometry

The MDA-MB-231 breast cancer cell line was labeled by QD-Tf and QD-Tf-Alexa Fluor conjugates. *In vitro* uptake of QD-Tf and QD-Tf-Alexa conjugates by MDA-MB-231 cells was confirmed by flow cytometry. The cell lines labeled by QD-Tf and Tf-Alexa conjugates show higher fluorescent intensities in comparison to those labeled by the MDA-MB-231 cell line only.

In addition, dual color flow cytometry confirms the linkage between QD and Tf. Cell line labeled by QD-Tf-Alexa show two colors: red color (FL3H) from QD and green color (FL1H) from Alexa Fluor, while cell line labeled by QD-Tf only show a red color (Fig. 5).

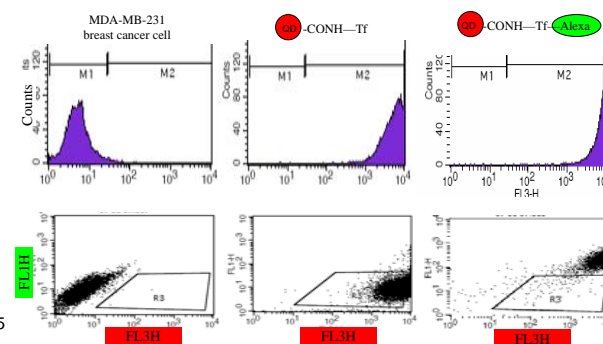


Fig.5

## V. Conclusions

QDs stabilized with TOPO were synthesized via a literature method. A novel tri-block copolymer with multi-dentate thiols was successfully synthesized via atom transfer radical polymerization. Gel permeation chromatography (GPC) shows that the molecular weights of polymers can be controlled via temperature, feeding ratio of reactants and polymerization time. This polymer can be used for surface coating of QDs to improve their stability.

Transferrin was successfully conjugated with QDs via a two-step carbodiimide chemistry process. The successful linkage of transferrin to QD was confirmed by SDS-PAGE gel electrophoresis. Breast cancer cell line, MDA-MB-231, can be labeled by the Tf-QDs conjugates via the interaction between transferrin on the surface of QDs and the overexpressed transferrin receptors on the surface of breast cancer cells. Flow cytometry confirms the *in vitro* uptake of QD-Tf by MDA-MB-231 cells. Flow cytometry of QD-Tf-Alexa Fluor labeled cancer cells shows two colors (red color from QD and green color from Alexa Fluor), indicating the linkage of transferrin and QDs.

**Acknowledgement:** This work was supported by DoD USAMRMC W81XWH-05-1-0291, NIH/NCRR/RCMI G12 RR003048 and NIH 5U54CA091409-06.



# Cytotoxicity, cell cycle effects and mutagenicity of etidronic acid towards MCF-7 human breast cancer cells

Rajagopalan Sridhar<sup>1,2</sup>, Desta Beyene<sup>2</sup>, Yanfei Zhou<sup>1,2</sup>, Alemayehu Kassa, Renshu Zhang<sup>1,2</sup>, Ebrahim Ashayeri<sup>1,2</sup> and Renshu Zhang<sup>1,2</sup>

<sup>1</sup>Department of Radiation Oncology and <sup>2</sup>Cancer Center, Howard University, Washington, DC

## ABSTRACT

Cell cycle effects and mutagenicity of Etidronic acid (1-hydroxyethane-1,1,-diphosphonic acid; 1-hydroxyethylidenediphosphonic acid) (Eti) towards MCF-7 human breast cancer cell line and its multidrug resistant derivative MCF-7 clone 10.3 cell line, were studied in the presence and absence of strontium chloride (Sr). Eti affects calcium metabolism and slows down abnormal bone resorption. The anti osteolytic activity of this first generation bisphosphonate has led to research on the use of bisphosphonates for the treatment of Paget's disease, osteoporosis and cancer metastases to the bone. Strontium, which mimics the *in vivo* behavior of calcium, stimulates bone formation and has been used in the treatment of post menopausal osteoporosis. There have been several reports on anti tumor effects of bisphosphonates. Clonogenicity assays revealed the cytotoxicity of etidronic acid towards these cell lines, while addition of strontium chloride had no effect. Flow cytometry studies showed that Eti caused a decrease in the S-phase population with concomitant increase in G2/M phase population (Table). Again Sr was without any effect. Within the cell cycle, late S-phase cells are the most radioresistant, while G2/M cells are the most radiosensitive. Therefore the decrease in S-phase population with a corresponding increase in G2/M population would position the cells in a more radiosensitive state. Such a shift in cell cycle distribution may be useful if etidronic acid were combined with radioactive strontium (89Sr, metastron), which is a beta emitter used in the treatment of bone metastases. For mutagenicity studies, DNA was extracted from MCF-7 cells treated with Eti (10 mM) according to the QIAamp DNA mini-kit procedure. Amplified PCR products were used to detect p53 mutations using denaturing high pressure liquid chromatography (DHPLC). DHPLC analysis of the conserved region of p53 showed clear alterations in exons 6 and 8 as a result of Eti treatment. It is not known if these p53 mutations will decrease the chemo or radiosensitivity of MCF-7 cells.

## INTRODUCTION

Breast cancer has a strong tendency to spread to bone and about 70% of women with metastatic disease have bone involvement. There is no effective treatment for metastatic disease. Bone is a rich source of a variety of growth factors and serves as a fertile substratum for cancer cells to develop metastases. Breast cancer cells produce cytokines, which support the survival of osteoclasts, which cause erosion of the bone. Bisphosphonates have an affinity for bone and inhibit osteoclast mediated bone resorption. Therefore bisphosphonates can be used in palliation of bone metastases from breast cancer. The calcium mimic <sup>89</sup>Sr is a bone seeking radionuclide that is also used for palliation of symptoms from bone metastases. Interestingly, non radioactive strontium compounds are effective against osteoporosis in postmenopausal women. An understanding of the homing tendencies of these therapeutic agents to the bone as well as their mechanism of action will lead to better therapy of bone metastases. Bisphosphonates are also cytotoxic to breast cancer cells. Therefore it would be useful to study the effect of bisphosphonates with strontium.

## METHODS AND MATERIALS

**Cells:** MCF-7 and MCF-7 clone 10.3 human breast cancer cells were cultured and maintained as exponential monolayers in a humidified 5% carbon dioxide air atmosphere in a 37°C incubator. RPMI 1640 medium fortified with 10% fetal bovine serum, glutamine (2mM), sodium pyruvate (1mM) and 100 units/ml of penicillin and 100µg/ml of streptomycin was used for culturing MCF-7 cells.

**Clonogenicity assay:** Cells were seeded at densities of 1500 and 4500 cells per 100 mm diameter tissue culture dish and the cells were allowed to attach overnight. Control cultures were treated with same volume of medium without drug. After 24 hour exposure to etidronic acid (Eti) (0, 1 and 10 mM) with or without strontium chloride (Sr) (0, 3.5 and 7.0 mM), the medium was removed from each culture dish and the cells were washed with Dulbecco's phosphate buffered saline (PBS), and fresh drug free culture medium (15 ml) was added. The cultures were then returned to the incubator for colony formation to progress for ten days. Any colony containing more than 50 cells was considered to represent a viable clonogenic cell. The colonies in the different dishes were counted after staining with methylene blue. Survival was calculated relative to a 100% value for untreated controls.

**Flow Cytometry Analysis for Cell Cycle:** The effect of etidronate treatment with or without strontium chloride on cell cycle was analyzed using flow cytometry assay. The cells were trypsinized and washed twice with PBS after treatment. The suspended cells were fixed overnight with ice cold 80% ethanol, and then centrifuged for 5 min at 1500rpm. The fixed cells were washed again with PBS two times.

The cells were stained at 37°C in the dark with 1 ml of propidium iodide (PI) and RNase solution. The cell cycle distribution was analyzed by FACScaliber flow cytometry (Becton Dickinson, San Jose, CA) using modfit software. Ten thousand cells were analyzed per sample. PI solution contained 50 µg/ml RNase A and 50 µg/ml PI in PBS.

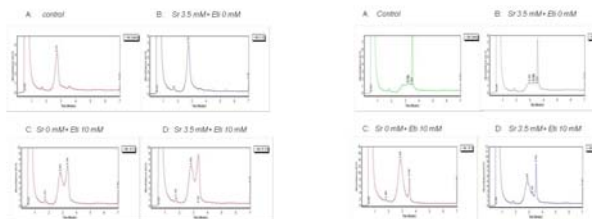
**Mutagenicity of etidronic acid:** After treatment with etidronic acid, the mutagenic effect of etidronic acid on p53 was studied using DHPLC analysis to detect changes (if any) on the highly conserved exon5 to exon 8 regions of the p53 gene. **DNA Extraction and Polymerase Chain Reaction (PCR) Amplification of p53 Gene:** DNA extraction was carried out according to the QIAamp DNA Mini Kit procedure. Amplified PCR products were used to detect p53 mutations using denaturing high-pressure liquid chromatography (DHPLC). The PCR products were denatured for 5 minutes at 95 °C and cooled to 65 °C within a period of 3 minutes. Ten to 15 µl of PCR product were applied to a preheated reverse-phase column (DNA-Sep Transgenomic). Mutational screening was performed according to the method described by Oefner and Underhill (1998) on an automated DHPLC analysis system (Transgenomic, Omaha, NE). The highly conserved exons 5 to 8 of the p53 gene, including the intron/exon boundaries, were amplified by PCR. The primers used are listed in Table 1. The quality and correct size of the PCR products were checked on agarose gel. The temperature for optimal resolution of heteroduplex and homoduplex DNA detection was determined using the predicted *T<sub>m</sub>* from the DHPLC and the temperature recommended by Quintanilla-Martinez *et al.* 2001. The overall sensitivity of this method for the detection of p53 mutations in exons 5 to 8 is expected to be in the range of 95%.

Table 1. PCR primers and PCR conditions.

Exon	Forward primer sequence	Reverse primer sequence	Amplicon length (bp)			Annealing Temperature, °C	
			length (bp)	Predicted	Recommended		
5	ATC TGT TCA CTT GTG CCC TG	AAC CAG CCC TGT CGT CTC TC	239	63	60		
6	AGG GTC CCC AGG CCT CTG AT	CAC CCT TAA CCC CTC CTC CC	197	61	62		
7	CCA AGG CGC ACT GGC CTC ATC	CAG AGG CTG GGG CAC AGC AGG	205	62	56		
8	TTC CTT ACT GCG TCT TGC TT	TGT CCT GCT TGC TTA CCT CG	194	60	56		

## RESULTS AND DISCUSSION

Clonogenicity assays revealed that a 24 hour exposure to etidronic acid (10 mM) was toxic to MCF-7 cells, while the addition of strontium chloride had no effect (Table 2). Flow cytometry studies reveal that etidronic acid caused a decrease in the S-phase population with concomitant increase in G2 phase population (Table 3). Again strontium was without any effect. Within the cell cycle, late S-phase cells are the most radioresistant while G2/M cells are the most radiosensitive. Therefore the decrease S-phase population with corresponding increase in G2/M would position the cells in a relatively more radiosensitive setting. Such a shift in cell cycle distribution may be useful if etidronic acid was combined with radioactive strontium (<sup>89</sup>Sr, metastron), which is a beta emitter used in the treatment of bone metastases from breast cancer.



**Figure 1** DHPLC profiles of exon 6 of p53 from untreated control (A), and treated with strontium chloride (3.5 mM) (B), or etidronic acid (10 mM) alone (C) or etidronic acid (10 mM) in combination with strontium chloride (3.5 mM) (D)

**Figure 2** DHPLC profiles of exon 8 of p53 from untreated control (A), and treated with strontium chloride (3.5 mM) (B), or etidronic acid (10 mM) alone (C) or etidronic acid (10 mM) in combination with strontium chloride (3.5 mM) (D)

Many studies have shown an association between p53 alterations/mutations and clinical outcome in breast cancer. The overall frequency of p53 mutation in breast cancer is approximately 20% . In this study we examined cytotoxicity of strontium and etidronic and the expression of p53 in MCF-7 cells. DHPLC analysis of the conserved region of p53 showed clear alterations in exons 6 and 8 due to treatment with 10 mM etidronic acid and with 10 mM etidronic acid and 7 mM strontium chloride ( Figure 1 and Figure 2 ).

Table 2 Cytotoxicity of etidronic acid

Treatment	MCF-7 Relative Survival(%)
Control	100
Sr 3.5 mM	96
Sr 7.0 mM	100
Sr 0 mM+Et 0.1 mM	87
Sr 0.5 mM+Et 0.1 mM	82
Sr 0.5 mM+Et 1.0 mM	87
Sr 0.5 mM+Et 10 mM	62
Sr 3.5 mM+Et 10 mM	62
Sr 7.0 mM+Et 10 mM	45

Table 3 Table: Cell cycle distribution for MCF-7 and MCF-7/MDR clone 10.3

Treatment	MCF-7			MCF-7/MDR clone 10.3		
	G0/G1	S phase	G2/M	G0/G1	S phase	G2/M
Sr 0.0 mM	68.3	25.3	6.4	64.1	18.8	17.1
Sr 3.5 mM	70.1	23.7	6.1	67.1	20.1	12.7
Sr 7.0 mM	70.7	21.8	7.6	63.3	20.4	16.3
Sr 0.0 mM+Et 0.1 mM	69.5	22.6	7.9	67.0	18.5	14.5
Sr 3.5 mM+Et 0.1 mM	72.1	21.4	6.5	66.2	18.9	14.9
Sr 7.0 mM+Et 0.1 mM	70.8	21.3	7.9	64.6	20.7	14.7
Sr 0.0 mM+Et 10 mM	63.8	16.9	19.3	70.9	7.2	21.9
Sr 3.5 mM+Et 10 mM	59.9	17.4	22.7	70.1	7.2	22.7
Sr 7.0 mM+Et 10 mM	67.1	14.7	18.2	74.7	6.7	18.7

## CONCLUSION

Etidronic acid is cytotoxic to MCF-7 breast cancer cells. Flow cytometry showed inhibition of cell proliferation by etidronic acid. The S phase population decreased while the G2/M population increased slightly. This suggests that etidronic acid may have radiosensitizing effects. This effect appears to be higher in MCF-7 clone 10.3 cells

## ACKNOWLEDGEMENT

This work was supported in part by grant 2 G12 RR003048 from the RCMI program, Division of Research Infrastructure, National Center for Research Resources, NIH and USMRC grants DAMD17-03-1-0123, DAMD17-03-1-0759.





# Bioluminescence Imaging for Monitoring the Response of a Luciferase Transfected Human Breast Cancer Cell Line Subjected to Hyperthermia

Rajagopalan Sridhar, Renshu Zhang, Yanfei Zhou, Liang Shan, Ebrahim Ashayeri and Paul C. Wang  
Departments of Radiation Oncology, Radiology, and Cancer Center, Howard University, Washington DC

## Introduction

Hyperthermia is a useful cancer treatment modality when used in combination with chemicals and/or radiation. Cytotoxic effects of anti-cancer drugs, radiation and hyperthermia are usually studied using cell viability/proliferation assays based on dyes such as neutral red, alamar blue, MTT and XTT. The survival rate measured on the basis of these assays seldom reflects true clonogenic capacity of cells. The gold standard for assessment of cytotoxic effects from tumor control standpoint is the clonogenicity assay. But this assay is time consuming (takes 7 to 15 days) and costs more than dye based assays. In our experience many of the rapid dye based assays underestimated cell viability of cells subjected to hyperthermia, compared to clonogenicity assays. There is a need for more rapid assays which yield results that are closely related to clonogenic survival. In this study, the usefulness of luciferin induced luminescence for estimating cell viability and cell proliferation was studied using MDA MD 231-D Luc cells which are transfected with luciferase gene. Attempts were made to develop assays based on luminescence detection with a view to obtain results that were approximately related to clonogenicity. Three different assays of cell viability were used to study the response of MDA-MB 231-D-Luc cells to 43°C hyperthermia treatment.

## Methods and Material

**Cell line:** MDA-MB-231-luc human breast cancer cell line (Xenogen, Alameda, CA), which is stably transfected with luciferase gene was used for this study. This cell line produces light when incubated with luciferin. Cells were routinely maintained as monolayers in RPMI 1640 medium supplemented with 10% FBS, penicillin (50 units/ml), and streptomycin (50 µg/ml) (Invitrogen) and kept at 37°C in humidified atmosphere containing 5% CO<sub>2</sub> in air.

**Hyperthermia treatment:** **A:** Cells were seeded in 96-well plates at 1x10<sup>4</sup> cells per well and incubated overnight. Hyperthermia was applied by sealing the plates with parafilm, enclosing in a Ziploc bag and immersing into a temperature controlled water bath maintained at 43°C (± 0.1°C). The continuous heating period ranged from 10 to 120 minutes. Controls were sealed in Ziploc bags and immersed in a 37°C water bath. Cell survival was estimated immediately after heating using (i) optical imaging for bioluminescence by incubating with luciferin, (ii) by measuring formazan formation after incubation with MTT solution in medium or (iii) by plating in complete medium for colony formation (clonogenicity assays). Cell survival/cell proliferation was also estimated after allowing the heat treated and control cultures to grow for different periods up to 72 hours at 37°C before incubating the cells with luciferin for (optical imaging) or with MTT for formazan formation. **B:** cells were also seeded in 96-well plates at a range of cell densities (from 10<sup>3</sup> to 5x10<sup>5</sup> cells per well) and incubated overnight. The next day, cells were subjected to heat for 2 hours at 43°C, and the plates were processed for optical imaging and MTT assays.

**Optical imaging:** Luciferase-based bioluminescence was detected using a highly sensitive Xenogen IVIS 200 imaging system (Xenogen, Alameda, CA). After heating, the old medium was removed and 100 µl of D-luciferin solution (150mg/ml in RPMI 1640 medium) were added to each well and then placed on the stage of specimen box (37°C). Images were captured 5 minutes after adding luciferin. Control cells were imaged at the same time as treated cells.

**MTT assay and colony formation assay:** After exposure of the cells to 43°C, and removing old medium, MTT solution (100 µl; 0.5mg/ml) in RPMI 1640 medium (phenol red free) was added. After incubation for 3 hours at 37°C, the absorbance was determined at the wavelength of 560 nm using multi-well spectrophotometer. For colony formation assay, following hyperthermia treatment, cells were trypsinized to obtain a suspension of single cells. The same volume of single cell suspension was plated on 100-mm tissue culture dishes with fresh medium and kept at 37°C, 5% CO<sub>2</sub> incubator for 10 to 14 days. Colonies consisting of more than 50 cells were counted.

## Results and Discussion

Cell viability was measured immediately after heating using clonogenicity, MTT and bioluminescence assays. The MTT assay under estimated cell viability while luminescence over estimated cell viability compared to survival based on clonogenicity assay, which is the preferred method in tumor biology and experimental therapeutics (Fig.1, Fig.2). Survival measured on the basis of MTT assay and the bioluminescence assay were quite different from survival determined using the clonogenicity assay (Fig 2).

The reason for overestimation of cell viability by MTT assay could be due to the retention of mitochondrial succinic dehydrogenase activity in heat damaged non clonogenic cells. The reason for over estimation of cell viability by the luminescence method could be thermal denaturation of luciferase enzyme by heat treatment in clonogenic cells as well as non clonogenic cells.

Both MTT and bioluminescence assays are sensitive for estimating the number of cells over a wide range of cell densities. The variation of luminescence with cell density is also shown (Fig 1 A). Comparison of luminescence from cells were recorded before and immediately after heating shows a dramatic decrease in luminescence of cells heated for 2 hours at 43°C (Fig. 2).

The MTT assay and luminescence assays were delayed so that the viable clonogenic cells were allowed to proliferate (Fig. 3). The delayed responses enable us to obtain results that may be approximately related to clonogenicity. When the MTT assay was delayed by 3 days of incubation at 37°C, after delivery of hyperthermia, the survival estimates were still higher than survival values based on clonogenicity measurements. Cell survival values based on bioluminescence measurement of cells subjected to hyperthermia, were consistently higher when the assay was delayed by 72 hours compared to the results of luminescence carried out immediately after heating.

## Reference

Tomasovic SP, Barta M, Klostergaard J. Neutral red uptake and clonogenic survival assays of the hyperthermic sensitization of tumor cells to tumor necrosis factor. Radiat Res. 1989 Aug;119(2):325-37.

**ACKNOWLEDGEMENT:** This work was supported by the grants: USAMRC W81XWH-05-1-0291.

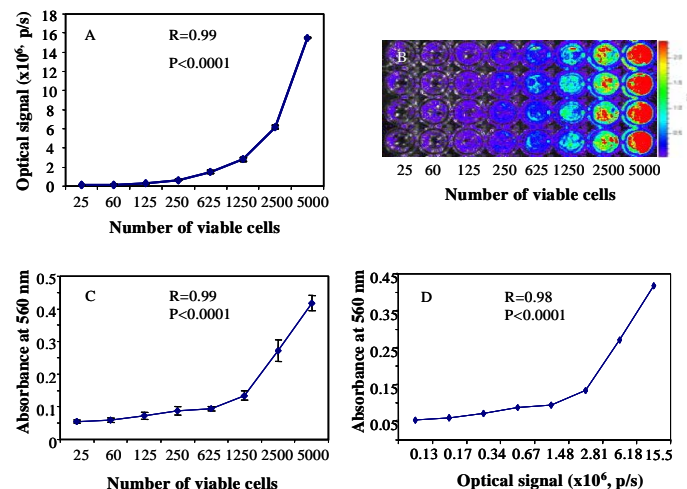


Figure 1. Comparison of MTT and bioluminescence assays for measurement of cell viability in untreated control cells. Relationship of cell numbers to bioluminescence using optical imaging (1A and 1B) and absorbance due to formazan formation in the MTT assay (1C). Correlation between MTT assay and bioluminescence assay (1D).

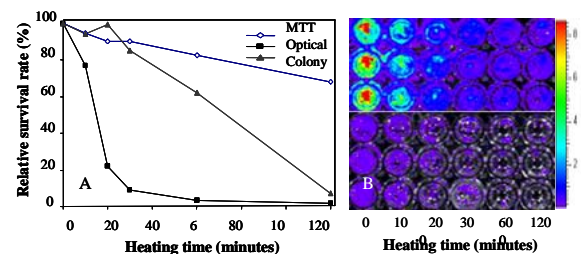


Figure 2

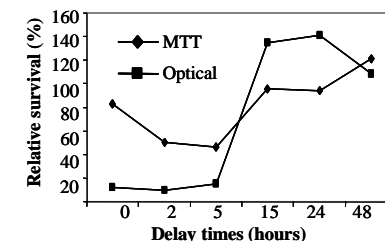


Figure 3

Figure 2. Evaluation of tumor cell response to hyperthermia treatment at 43°C for different durations from 0 to 120 minutes, indicating optical imaging may underestimate and MTT may overestimate cell viability with respect to the clonogenic potential as estimated by colony formation assay (2A). 2B shows the optical images of cells following heat treatment (lower panel) alongside controls (upper panel). The survival rates are reported as percentages relative to 100% survival for untreated controls.

Figure 3. Delayed assessment of the cell viability following 1 hour treatment at 43°C using optical imaging and MTT assay, indicate continued cell damage and recovery of cells from damage.

## Conclusion

The advantage of the delayed MTT is that loss of clonogenicity can be estimated in 3 days compared to the 10-14 days required for colony formation assay. This is similar to the conclusions of Tomasovic *et al.* with respect to the use of neutral red assay for estimating the clonogenicity of cells subjected to hyperthermia. Luminometric assay of response to hyperthermia is rapid in bioluminescent cells, but is not closely related to the clonogenic potential. Caution has to be exercised while interpreting cell viability results based on different assays. Optical imaging is potentially useful for rapid screening of cytotoxic regimens *in vitro* using luciferase-expressing cancer cells.



# MCF-7 breast cancer cells down-regulate macrophage migration inhibitory factor in co-cultured macrophages: Implications for context-specific modulation of tumor-associated macrophages

Giselle T. Burnett, Denise C. Weathersby, Tiffany E. Taylor, and Theodore A. Bremner, Department of Biology, & Howard University Cancer Center, Howard University, Washington, DC, USA

## BACKGROUND

Accumulating evidence implicates tumor-associated macrophages (TAMs) in tumor progression. Recent reports indicate that key modifier genes of tumor progression are expressed in TAMs. Macrophage ablation has been proposed as a therapeutic strategy; however, context-specific targeting of TAMs would be preferable. We used pathway-focused gene array, RT-PCR, and Western blot analyses of inflammation- and angiogenesis-related gene expression in co-cultured MCF-7 cells and macrophages, to determine how interactions between the two cell types are affected by tamoxifen and aspirin. We also sought to identify phenotypic changes that may render TAMs selectively vulnerable to pharmacological agents.

## MATERIALS & METHODS

THP-1 (human monocytic leukemia), MCF-10A (nontumorigenic mammary epithelial), MCF-7 (mammary adenocarcinoma) and MDA-MB-231 (mammary adenocarcinoma) were used in this study. THP-1 monocytes were differentiated to macrophages with PMA (100 nM) for 3 d; differentiated macrophages were activated with LPS (20 ng/ml) for 5 h. THP-1 were cultured in RPMI medium 1640 supplemented with 7.5% FBS, 100 U/ml penicillin, 100 µg/ml streptomycin, and 50 µM 2-mercaptoethanol. Breast cell lines were propagated in MEM supplemented with 8% FBS and antibiotics. 1 x 10<sup>6</sup> THP-1 cells/well were seeded in the inserts (3-µm pore size) of 6-well Transwell™ chambers, and differentiated 1 d later with PMA, and then activated with LPS. 2.5 x 10<sup>5</sup> MCF-7 cells/ml were seeded in a 2-ml volume in lower wells (separately) 2 d after THP-1 cells were seeded. The medium of both cell types was changed and inserts (activated macrophages) were placed in the lower wells. Chambers were incubated for 3 d. Tamoxifen, aspirin, and rhMIF were used at final concentrations of 10 µM (24 h), 1 mM (24 h), and 10 ng/ml (6 h), respectively.

## RESULTS & DISCUSSION

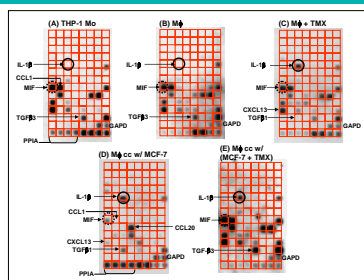


Fig. 1. Gene arrays for inflammatory cytokines and receptors. (A) THP-1 monocytes (Mo). (B) PMA-differentiated THP-1 macrophages (Mφ). (C) Mφ treated with tamoxifen (TMX). (D) Mφ co-cultured with MCF-7. (E) Mφ co-cultured with tamoxifen-pretreated MCF-7. RNA was extracted from THP-1 and used for gene arrays (SuperArray HS-015.2).

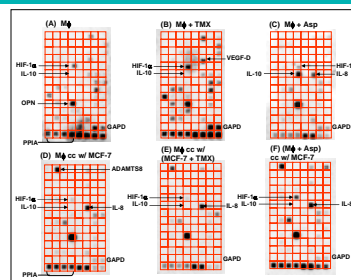


Fig. 2. Gene arrays for angiogenesis. (A) PMA-differentiated THP-1 macrophages (Mφ). (B) Mφ treated with tamoxifen (TMX). (C) Mφ treated with aspirin (Asp). (D) Mφ co-cultured with MCF-7. (E) Mφ co-cultured with tamoxifen-pretreated MCF-7. (F) Aspirin-pretreated Mφ co-cultured with MCF-7. RNA was extracted from THP-1 and used for gene arrays (SuperArray HS-009).

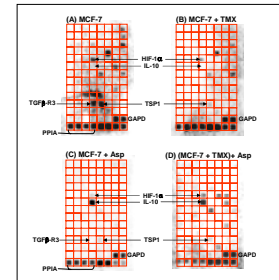


Fig. 3. Gene arrays for angiogenesis. (A) MCF-7. (B) MCF-7 treated with tamoxifen (TMX). (C) MCF-7 treated with aspirin (Asp). (D) Tamoxifen-pretreated MCF-7 treated with aspirin. RNA was extracted from MCF-7 cells and used for gene arrays (SuperArray HS-009).

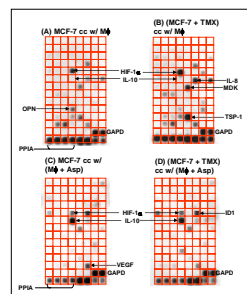


Fig. 4. Gene array for angiogenesis. (A) MCF-7 co-cultured with PMA-differentiated THP-1 macrophages (Mφ). (B) Tamoxifen (TMX)-pretreated MCF-7 co-cultured with Mφ. (C) MCF-7 co-cultured with aspirin (Asp)-pretreated Mφ. (D) Tamoxifen-pretreated MCF-7 co-cultured with aspirin-pretreated Mφ. RNA was extracted from the MCF-7 cells and used for gene arrays (SuperArray HS-009).

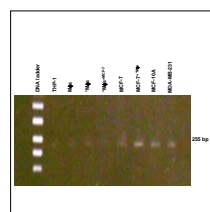


Fig. 5. RT-PCR of MIF mRNA in breast cancer cells and macrophages. In activated macrophages (Mφ) co-cultured with MCF-7 (Mφ+MCF-7), MIF expression was down-regulated when compared with activated macrophages (Mφ).

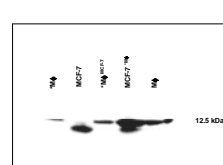


Fig. 6. Western blot of MIF in THP-1 macrophages and MCF-7 cells. Mφ: LPS-activated macrophages; Mφ+MCF-7: activated macrophages (source of RNA) co-cultured with MCF-7; MCF-7+TMX: MCF-7 (source of RNA) co-cultured with activated macrophages; and untreated macrophages were probed for MIF protein. For each sample, 50 µg lysate protein was resolved in 4-20% SDS-PAGE gradient gels, electroblotted on to nitrocellulose membrane and probed with rabbit polyclonal anti-human MIF IgG (Santa Cruz Biotechnology, FL-115, sc-20121). Secondary antibody was horseradish peroxidase-conjugated goat anti-rabbit IgG.

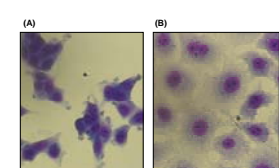


Fig. 7. (A) MCF-7 cells 24 h after seeding. Cells were cultured in MEM supplemented with 7% FBS. (B) MCF-7 after 24 h in co-culture with LPS-activated THP-1 macrophages. Macrophages were differentiated in the inner well (membrane) of a Transwell chamber, activated for 6 h, washed with HBSS, transferred to fresh medium, and co-cultured with MCF-7 cells seeded in the lower well of a Transwell chamber. LeukoStain™ staining.

- All cells expressed MIF RNA. In co-culture, *MIF* expression was upregulated in MCF-7, but downregulated in macrophages (Figs. 1, 5). MCF-7-induced reduction of MIF expression in TAMs may be associated with partial M2 polarization; therefore, co-culture produced macrophage phenotypes that were intermediate between M1 and M2. Reduction of MIF expression may also produce context-specific vulnerability of macrophages to therapeutic agents.
- Aspirin induced *IL-10* expression in both macrophages (Fig. 2) and MCF-7 (Fig. 3) grown separately: MCF-7 cells did not express *IL-10* when grown separately (Fig. 3A) or in co-culture (Fig. 4A); however, aspirin induced *IL-10* expression in MCF-7 (Fig. 3C) and in tamoxifen-pretreated MCF-7 (Fig. 3D). Moreover, aspirin-pretreated macrophages potentially induced *IL-10* expression in MCF-7 cells (Figs. 4C) and pretreatment of MCF-7 with tamoxifen did not prevent this induction (Fig. 4D).
- Two molecular variants of MIF were identified: a larger, macrophage-type and a smaller, MCF-7-type (Fig. 6); both variants were present in co-cultured MCF-7 cells.
- Co-culture of MCF-7 with LPS-activated THP-1 macrophages induced a change in MCF-7 morphology reminiscent of an epithelial-to-mesenchymal transition (Fig. 7).

# Breast Cancer Cells Down-regulate Tristetraprolin in Co-cultured Macrophages: A Possible Mechanism for Sustaining Inflammation and Angiogenesis in the Tumor Microenvironment

Giselle Burnett, Denise Weathersby, and Theodore A. Bremner, Department of Biology, and Howard University Cancer Center, Howard University, Washington, DC



## BACKGROUND

Although inflammation is also an immune response against cancer, research shows that it plays a role in all stages of cancer, including carcinogenesis, tumor progression, and metastasis (1-3). There are several pro-inflammatory cytokines implicated in tumor progression and metastasis including tumor necrosis factor- $\alpha$  (TNF- $\alpha$ ). Usually, these cytokines are not long-lived because their mRNAs are markedly unstable. The mRNAs of these inflammatory cytokines have one or more adenine- and uracil-rich elements (AREs) located in their 3' untranslated regions (3' UTRs), which regulate their stability (4). The consensus sequence of an ARE is A-U-U-U-A. Insertion of an ARE into the mRNA of a gene that does not usually possess it causes that mRNA to become unstable (5). The ARE regulates mRNA stability by recruiting proteins that promote mRNA degradation. A protein that regulates the stability of inflammatory cytokine mRNA through ARE-mediated degradation is tristetraprolin (TTP), the prototype of a CCH tandem zinc finger (TZF) domain protein (6). TTP and related proteins have two conserved tandem Cys-X8-Cys-X5-Cys-X3-His (CCH) zinc fingers, along with divergent N- and C-terminal regions (7). TTP binds to the ARE of mRNAs and recruits poly(A) ribonucleases to deadenylate the poly(A) tail; this is the first step of mRNA degradation.

Inflammation plays a critical role in cancer progression, and one of the ways that cancer cells are able to maintain an inflammatory environment is by stabilizing the mRNA of pro-inflammatory cytokines in order to maintain an inflammatory environment (8). This study investigated the role of macrophages in promoting the development of an inflammatory environment in and around breast cancer cells. The primary objective of this investigation is to identify examine one mechanism by which breast cancer cells may control the inflammatory state by regulating TTP expression in TAMs so that anti-cancer drugs and treatment can be modified to increase their potency and effectiveness in inhibiting metastasis. We measured mRNA levels by RT-PCR and protein levels by Western blot analysis of TTP and TNF- $\alpha$  in MCF-7, MDA-MB-231, and untreated or LPS-treated PMA-differentiated macrophages individually and in co-culture in order to assess the reciprocal interactions between breast cancer cells and macrophages and how the presence of one cell type alters gene expression in the other.

We hypothesized that there would be a decrease in TTP expression levels in macrophages due to their interaction with breast cancer cells in co-culture. Furthermore, it is hypothesized that a decrease in TTP levels will yield an increase in TNF- $\alpha$  mRNA levels as further confirmation that TTP expression has decreased. This proposed effect of breast cancer cells on macrophages would enhance the stability of inflammatory cytokine mRNA in macrophages and create an inflammatory environment that would promote the survival or metastasis, or both, of the breast cancer cells. This study provides evidence that breast cancer cells regulate gene expression in macrophages when in co-culture. Our data show for the first time that the mRNA and protein levels of TTP in TAMs are subject to regulation by breast cancer cells.

## MATERIALS & METHODS

**Cell Culture:** MCF-7 and MBA-MD-231 cells were maintained in Minimum Essential Medium supplemented with 7% fetal bovine serum (FBS), penicillin (100 units/ml), streptomycin (100  $\mu$ g/ml), and glutamine (2 mM). THP-1 cells were maintained in RPMI Medium 1640 supplemented with 7.5% FBS, penicillin (100 units/ml), streptomycin (100  $\mu$ g/ml), and  $5 \times 10^{-5}$  M of  $\beta$ -mercaptoethanol. Cells were incubated at 37°C in a humidified atmosphere of 5% CO<sub>2</sub>/95% air. THP-1 cells were differentiated via treatment with phorbol 12-myristate 13-acetate (PMA) at a final concentration of 100 nM. THP-1 cells differentiated into macrophages over a 72-hour period. After differentiation, THP-1 macrophages were treated with lipopolysaccharide (*Escherichia coli* 055:B5; Sigma, St. Louis, MO) at a concentration of 20 ng/mL for 4 hours. Macrophages were co-cultured with each breast cancer cell line, in fresh media, immediately following differentiation, or after 4 hours of LPS treatment. After two days of co-culture, total RNA or protein was isolated from each type of cell.

**RT-PCR:** Total RNA was isolated using the Versagene RNA Cell Kit (Gentra Systems, Minneapolis, MN) according to the manufacturer's instructions. 1.5  $\mu$ g of RNA was reverse transcribed into cDNA using the Advantage RT-for-PCR kit according to the manufacturer's instructions (BD Bioscience Clontech, Mountain View, CA). For PCR, 3  $\mu$ L of cDNA sample was combined with 12.5 pmol of sense and antisense primers (Invitrogen, Carlsbad, CA), 25 nmol of dNTP mix, 37.5 nmol of MgCl<sub>2</sub>, 37.5 nmol of 10X PCR reaction buffer, 1.25 units of AmpliTaq Gold (Applied Biosystems, Foster City, CA), and distilled water was added up to a final reaction volume of 25  $\mu$ L. PCR primers for TTP were as follows: TTP sense, 5'-CATCCA-CAACCTAGGCGA-3'; TTP antisense, 5'-GATCGGAT TGAAGATGGGGA-3'. The expected amplicon for TTP was 476 base pairs. PCR performed for TTP amplification was 32 cycles with denaturation at 95°C for 30 s, annealing

## RESULTS

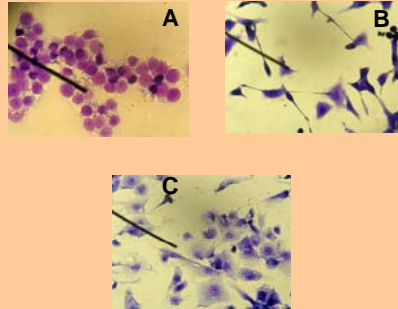


**Figure 1-** LeukoStat™ Staining of each cell line. Magnification: 400 X. (A) MCF-7: tumorigenic, non-metastatic; (B) MDA-MB-231: tumorigenic, metastatic; (C) PMA-differentiated THP-1 macrophages (5 d)

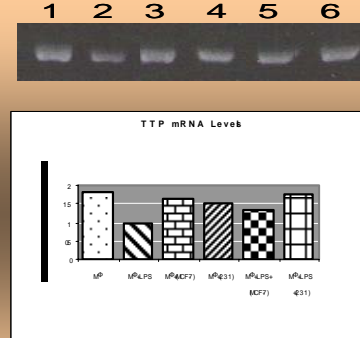


**Figure 2-** THP-1 macrophages showed a 45% decrease in TTP mRNA levels when treated with 20 ng/mL of LPS (Lane 2) compared to controls (Lane 1). Compared with THP-1 macrophages in mono-culture, macrophages in co-culture with MCF-7 and MDA-MB-231 cells showed a 10% (Lane 3) and a 16% (Lane 4) decrease, respectively, in TTP mRNA levels. However, LPS treated THP-1 macrophage expression of TTP mRNA increased by 32% (Lane 5) and 75% (Lane 6) when in co-culture with MCF-7 and MDA-MB-231 cells, respectively.

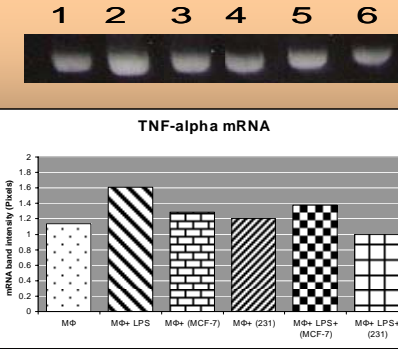


**Figure 3-** Compared to controls, a 40% increase in TNF- $\alpha$  mRNA levels was observed when THP-1 macrophages were treated with LPS (Lane 2) compared to controls (Lane 1). Co-culture of macrophages with MCF-7 and MDA-MB-231 cells yielded increases of 12% (Lane 3) and 5% (Lane 4), respectively, in TNF- $\alpha$  mRNA levels, respectively. When LPS-treated THP-1 macrophages were co-cultured with MCF-7 and MDA-MB-231 cells, TNF- $\alpha$  mRNA levels decreased by 14% (Lane 5) and 38% (Lane 6), respectively.

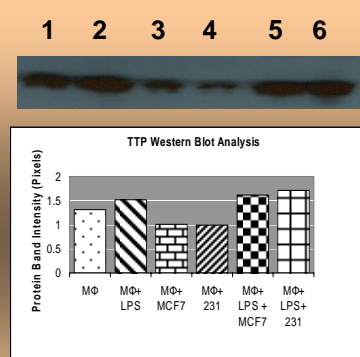


**Figure 4-** THP-1 macrophages showed a 14% increase in TTP protein levels when treated with 20 ng/mL of LPS (Lane 2) compared to controls (Lane 1). Compared with THP-1 macrophages in mono-culture, macrophages in co-culture with MCF-7 and MDA-MB-231 cells showed a 25% (Lane 3) and a 24% (Lane 4) decrease, respectively, in TTP mRNA levels. However, LPS treated THP-1 macrophage expression of TTP mRNA increased by 6% (Lane 5) and 11% (Lane 6) when in co-culture with MCF-7 and MDA-MB-231 cells, respectively.

## MATERIALS & METHODS (cont'd)

**RT-PCR (cont'd)** at 54°C for 30 s, and elongation at 72°C for 45 s (9). PCR primers for TNF- $\alpha$  were as follows: TNF- $\alpha$  sense, 5'-ACGTGACCAAGCCTGTACTCATGR-GTAGCA-3'; TNF- $\alpha$  antisense, 5'-CGAATGATCCCAAGTAGACCTGCCAG ACT-3'. The amplicon for TNF- $\alpha$  was 444 base pairs. PCR performed for TNF- $\alpha$  amplification was 36 cycles with denaturation at 94°C for 45 s, annealing at 60°C for 45 s, and elongation at 72°C for 2 min. The amplified cDNA fragments were separated by gel electrophoresis in 2% agarose gels supplemented with 0.67  $\mu$ g/mL ethidium bromide (10).

**Western Blotting:** Cells were washed twice in Hank's Balanced Salt Solution. 1 mL of hot Hepes-SDS-sodium vanadate (HSSV) lysis buffer (10 mM HEPES, pH 7.5; 1% SDS; 1mM sodium vanadate, activated) was added to lyse the cells. Lysates were transferred to an Eppendorf tube and heated at 100°C for 4 minutes. The lysates were passed through a 26-gauge needle attached to a 1-mL hypodermic syringe 8-10 times. Protein concentrations were determined using the BioRad Detergent-Compatible Protein Assay kit (Bio-Rad Laboratories, Hercules, CA). Western blot was performed using anti-TTP antibody (Santa Cruz, sc-8458) at 1:5000 dilution and visualized by ECL detection.

## CONCLUSIONS

Inflammation plays a critical role in cancer progression, and one of the ways that cancer cells are able to maintain an inflammatory environment is by stabilizing the mRNA of pro-inflammatory cytokines (8). In this study, we examined one mechanism by which breast cancer cells may control the inflammatory state by regulating TTP expression in TAMs. The interactions of tumor cells with TAMs may alter the transcriptional activity of macrophages in such a way as to promote the survival and metastasis of tumor cells. The consequence of such interactions would be consistent with the suggestions that breast tumor cells alter the behavior of TAMs *in vivo*.

This study shows the direct role of TTP and inflammatory cytokines in breast cancer inflammation and breast cancer metastasis. We have shown that MCF-7 and MDA-MB-231 cells can regulate gene expression in macrophages to enhance their own survival and subsequent metastasis by altering TTP expression. TTP mRNA expression decreased when THP-1 macrophages were treated with LPS. Previous research provides evidence that LPS treatment increases TTP expression in THP-1 monocytes (4). This observation is consistent with the suggestion that altered gene expression is an initial response to cell differentiation. An increase in TNF- $\alpha$  mRNA expression was observed in cells that experienced a decrease in TTP mRNA levels and vice versa. However, there was not a perfect correlation between the magnitude in TTP mRNA levels and that of TNF- $\alpha$ . It is possible that the breast cancer cells are regulating the two genes differently in such a way as to increase or decrease the inflammatory response from the macrophages in order to benefit breast cancer cell proliferation. There could also be other underlying factors affecting these differences; therefore, this observation warrants further study so that a mechanistic explanation of this occurrence can be developed.

It is not known whether the observed increase in TTP protein in LPS-treated macrophages influenced their production of TNF- $\alpha$ . Although TNF- $\alpha$  mRNA increased in macrophages after treatment with LPS, it is possible that the cytokine production decreased due to degradation of the mRNA caused by the increase in TTP protein. Microarray studies could be performed in order to determine the regulation of TNF- $\alpha$  translation.

This project illustrated how cells respond differently to external stimuli and mimicked the possible responses of macrophages in response to breast cancer cells *in vivo*. Our study proposes that regulation of gene expression in the stromal cells surrounding breast tumors is a strategy used by breast cancer cells to promote their survival and metastasis. This conclusion warrants further study so that a clear understanding of the underlying pathways can be reached. Moreover, a better understanding of these mechanisms could lead to the development of methods and therapies to abrogate the contribution of macrophages to breast cancer progression.

## REFERENCES

- Executive summary of inflammation and cancer think tank. Division of Cancer Biology, National Cancer Institute, 2004.
- Karin, M. (2005). Inflammation and cancer: the long reach of Ras. *Nature Medicine* 11, 20-21.
- Sparrmann, A., and D. Bar-Sagi. (2004). Ras-induced interleukin-8 expression plays a critical role in tumor growth and angiogenesis. *Cancer Cell* 6, 447-458.
- Brooks, S., et al. (2004). The role of mRNA turnover in the regulation of tristetraprolin expression: evidence for an extracellular signal regulated kinase-specific, AU-rich element dependent, autoregulating pathway. *Journal of Immunology* 172, 7263-7271.
- Suzuki, K., et al. (2003). IL-4-Stat6 signaling induces tristetraprolin expression and inhibits TNF- $\alpha$  Production in Mast Cells. *Journal of Experimental Medicine* 198, 1717-1727.
- Lai, W.S., et al. (2002). Interactions of CCH zinc-finger proteins with mRNA: Non-binding tristetraprolin mutants exert an inhibitory effect on degradation of AU-rich element-containing mRNAs. *Journal of Biological Chemistry* 277, 9609-9613.
- Johnson, B. A. and T. K. Blackwell. (2002) Multiple tristetraprolin sequence domains required to induce apoptosis and modulate responses to TNF- $\alpha$  through distinct pathways. *Oncogene* 21, 4237-4246.
- Chen, J., et al. (2005). Tumor-associated macrophages: the double-edged sword in cancer progress. *Clinical Oncology* 23, 953-964.
- Ogawa, K., et al. (2003). Transcriptional regulation of tristetraprolin by transforming growth factor- $\beta$  in human T-cells. *Journal of Biological Chemistry* 278, 30373-30381.
- Wang, W. and S. Walsh. (1996). TNF- $\alpha$  concentrations and mRNA expression are increased in preclamping placentas. *Journal of Reproductive Immunology* 32, 157-169.